Technische Universität München
TUM School of Natural Sciences

Characterization and Manipulation of Tailored Molecular Systems that Protrude from Surfaces

Tobias J. Weiß

Vollständiger Abdruck der von der TUM School of Natural Sciences der Technischen Universität München zur Erlangung eines

Doktors der Naturwissenschaften (Dr. rer. nat.)

genehmigten Dissertation.

Vorsitz: Prof. Dr. Frank Ortmann

Prüfende der Dissertation:

1. Prof. Dr. Wilhelm Auwärter
2. Prof. Dr. Johanna Eichhorn

Die Dissertation wurde am 26.11.2024 bei der Technischen Universität München eingereicht und durch die TUM School of Natural Sciences am 14.01.2025 angenommen.

Abstract

Understanding well-defined molecular systems on metal substrates and the surface chemistry of these systems is important for the synthesis of materials with pre-designed properties. Additionally, suitable molecular structures can be utilized as model systems for understanding physical and chemical processes on the nanometer scale.
Surface science techniques in an ultra-high vacuum environment enable to characterize chemical, electronic, and topographic properties of the molecular systems. In particular, scanning probe microscopy (SPM) offers imaging in real space with atomic resolution and can also be used as a tool for manipulation experiments at the atomic scale.
Here, four systems are presented. First, borazine molecules are studied on Ag(111). Borazine adsorbs non-dissociatively with the ring aligned parallel to the surface plane. The borazine adsorption configuration can be modified via voltage pulses from the SPM tip. These pulses induce dehydrogenation of borazine at the boron position and result in an upright standing adsorption geometry. These borazine fragments are rotatable by further voltage pulses.
The next chapter reports on molecular model systems which are designed for azimuthal rotation. This chapter is split into two parts. The first part describes tuning the adsorption geometry of a hemithioindigo-based motor molecule through supramolecular assembly and a covalent organic framework (COF). The COF prevents island formation of the motor molecules by isolating individual molecules. The motor molecules adsorb in a flat-lying adsorption geometry. The second part presents results on the controlled rotation of Thorium-Naphthalocyanine double-decker molecules via the tip of an atomic force microscope (AFM). Quantification of the force, via frequency shift measurements, yields a lower limit for the necessary torque of rotating the top napthalocyanine moiety of a modified double-decker species.
The final section discusses carpyridines on surfaces. Carpyridines are formed by two pyridine and carbazole units and are part of a class of inherently saddle-shaped molecules featuring a central coordination site. Interaction with the Au(111) surface slightly distorts the saddle-shape. Note that the distinctive protruding tilt of the pyridine groups persists, which is characterized by AFM and near-edge x-ray absorption fine structure spectroscopy measurements. Further properties such as self-assembly, local density of states, and chemical composition are investigated via means of scanning tunneling microscopy (STM) and x-ray photoelectron spectroscopy(XPS). Experiments aimed at functionalization of the central coordination site with Copper or Iron show distinct changes in the results of the XPS and STM measurements.
As a result, the presented experiments advance the understanding of molecules on surfaces, particularly of systems with three-dimensional geometries whose characteristic features extend beyond planar geometries of molecules on surfaces. Specifically, the detailed characterization of carpyridines may serve as a reference for their future implementation in molecular structures on surfaces.

Zusammenfassung

Das Verständnis wohldefinierter molekularer Systeme auf Metallsubstraten und deren Oberflächenchemie ist wichtig für die Synthese von Materialien mit vorher konzeptionalisierten Eigenschaften. Außerdem können geeignete solcher Strukturen als Modellsysteme für das Verständnis von physikalischen und chemischen Prozessen im Nanometerbereich verwendet werden.
Methoden der Oberflächenwissenschaften in einer Ultrahochvakuumumgebung ermöglichen die Charakterisierung von chemischen, elektronischen, und topographischen Eigenschaften. Insbesondere Rastersondenmikroskopie (SPM) bietet ein bildgebendes Verfahren im Realraum mit atomarer Auflösung und kann auch als Werkzeug für Manipulationsexperimente auf atomarer Skala eingesetzt werden.
Im Folgenden werden vier Systeme vorgestellt. Zuerst werden Borazinmoleküle auf Ag(111) untersucht. Borazin adsorbiert non-dissoziativ mit dem Ring parallel zur Oberflächenebene ausgerichtet. Die Adsorptionskonfiguration des Borazinmoleküls kann durch Spannungspulse von der SPM Spitze modifiziert werden. Diese Pulse induzieren Dehydrogenierung des Borazinmoleküls an der Bor-Position und haben eine aufrechtstehende Adsorptionsgeometrie zur Folge. Diese Borazinfragmente sind durch weitere Spannungspulse drehbar.
Das nächste Kapitel berichtet über molekulare Modellsysteme, welche für azimutale Rotation konzipiert sind. Dieses Kapitel teilt sich in zwei Teile. Der erste Teil beschreibt das Anpassen der Adsorptionsgeometrie eines hemithioindigo-basierten Motormoleküls durch supramolekulare Assemblage und durch eine kovalente organische Gerüstverbindung (COF). Die COF verhindert Inselbildung der Motormoleküle durch Abgrenzen einzelner Moleküle. Die Motormoleküle adsorbieren in einer flachen Adsorptionsgeometrie. Der zweite Teil präsentiert Ergebnisse der kontrollierten Rotation von Thorium-Naphthalocyanin Doppeldeckermolekülen durch die Spitze eines Rasterkraftmikroskops (AFM). Quantifizierung der Kraft, durch Frequenzverschiebungsmessungen, ergibt eine untere Grenze für das erforderliche Drehmoment für die Rotation der oberen Naphthalocyanin Hälfte einer modifizierten Doppeldeckerspezies.
Der letzte Abschnitt diskutiert Carpyridine auf Oberflächen. Carpyridine bestehen aus je zwei Pyridin- und Carbazolgruppen und sind Teil einer Klasse von an sich sattelförmigen Molekülen mit einem zentralen Koordinationsplatz. Die Wechselwirkung mit der Au(111) Oberfläche deformiert die Sattelform leicht. Man beachte, dass der markante hervorstehende Kippwinkel der Pyridingruppen bestehen bleibt, was durch AFM und Röntgen-Nahkanten-Absorptions-Spektroskopie Messungen charakterisiert wurde. Weitere Eigenschaften wie Selbst-Assemblage, lokale Zustandsdichte, und chemische Zusammensetzung wurden durch Rastertunnelmikroskopie (STM) und Röntgenphotoelektronenspektroskopie (XPS) untersucht. Experimente mit dem Ziel den zentralen Koordinationsplatz mit Kupfer oder Eisen zu funktionalisieren zeigen deutliche Änderungen in den Ergebnissen der STM und XPS Messungen.

Als Ergebnis halten wir fest, dass die vorgestellten Experimente das Verständnis von Molekülen auf Oberflächen weiterentwickeln, insbesondere von Systemen mit dreidimensionalen Geometrien deren charaktischen Merkmale aus den planaren Geometrien von Molekülen auf Oberflächen herausragen. Insbesondere die detaillierte Charakterisierung der Carpyridine kann als Referenz für deren zukünftige Anwendung in molekularen Strukturen auf Oberflächen dienen.

Contents

1. Introduction

Molecules exist in a plethora of constitutions and conformations leading to a seemingly infinite variation of physical and chemical properties. Research revolving around characterization of molecules greatly advanced by the invention of the scanning tunneling microscope (STM) in 1981 [1] and its following technical improvements [2], enabling imaging of individual molecules in real space with sub-molecular resolution [3].
As part of the scanning probe microscopy (SPM) family, STM focuses on the electronic properties, while atomic force microscopy (AFM) [4], another SPM technique, is sensitive to local forces, allowing to acquire information on e.g. the topographic features. In combination with further specialized techniques [5], SPM has enriched research focusing on understanding properties of molecules and concomitantly boosting nanotechnology. One of the more pictorial examples is directly imaging the molecular structure of pentacene. The striking visual similarity between its drawn skeletal structure and the data in this experiment visualizes the power of SPM for identifying molecular structures [6].
SPM has numerous areas of application, including for example setups related to electrochemistry [7, 8], molecules at the solid/liquid interface [9], spin-polarization [10], electron spin resonance [11], luminescence [12, 13], catalysis [14], biology [15, 16], and materials science [17–20].
Since SPM is an inherently surface sensitive technique, a common prerequisite for SPM experiments is to fix the object of interest on a surface. However, this apparent restriction also provides an opening to study structures that are stabilized on surfaces and would be otherwise challenging to realize. This way characterization of single isolated molecules is readily accessible.
Going beyond their characterization, molecules can also be used in on-surface reactions, expanding the synthesis options from solution-based chemistry [21]. The surface provides an inherent restriction in these reactions and also offers stabilization of reaction products. In particular polymerization reactions are common in on-surface synthesis where the resulting products are stabilized for example via adatoms [22–24]. Covalent polymers are also possible to obtain [25]. Among many on-surface reaction schemes for C-C coupling [25–29], surface assisted Ullmann coupling reactions stand out for their widespread use and have proven reliable [30]. Typical for these Ullmann reactions are halogenated carbon-based precursor molecules that are deposited on the surface. Heating of the surface dissociates then the halogen-carbon bond such that the molecules become activated for carbon-carbon coupling at the previously halogenated carbon positions. Examples for the achieved structures range from linear chains [31, 32] and ribbons [33] towards extended networks [34–36].
Moreover, due to the very high resolution, SPM immediately supports the idea to study model systems on the molecular scale. These system can be even reduced to the atomic

limit, transferring concepts like switches [37] or transistors [38] to the nanometer scale. Research in this direction also highlights the necessity for technical developments in the instrumentation. In order to maintain an atomically clean samples an ultra-high vacuum (UHV) environment is necessary. In addition, thermal diffusion needs to be suppressed by measuring at cryogenic temperatures, achieved by cooling with liquid nitrogen or liquid helium.
Going beyond its imaging capabilities, SPM can also be utilized as a tool. Reactions at specific positions of single molecules can be induced by tip mediated voltage pulses [39–42]. Current experiments have progressed considerably, compared to the early dissociation experiments, granting access to special structures such as for example cyclocarbons [43, 44]. Recent reports on tip-induced single molecule chemistry also show that is possible to steer the reactivity by the polarity and magnitude of the voltage pulses [45] and by the molecular assembly around the target molecule [46]. Covalent organic nano structures were also achieved by manipulation of individual molecules and subsequent voltage pulses [47].
Using the STM tip to arrange atoms [48, 49] and molecules [50, 51] into pre-designed, non-covalent bound geometries, was found as a powerful method to build artificial model lattices. While these experiments were conceived to probe phenomena such as scattering of the surface state of the electrons in these geometries, the created structures also highlight the precision of using the STM tip as a tool.
Next, the tip in SPM experiments can also be used as a tool and as a probe simultaneously. In particular AFM experiments were employed to quantify forces on the atomic scale. An important example is measuring the forces needed to move a Co atom on the surface [52]. The reported manipulation procedure allows to extract forces in the manipulation direction in addition to the vertical tip-sample potential. Only few experiments are reported where the force was quantified for moving single molecules with the AFM tip. These publications discuss moving H2Pc [53], PTCDA [54, 55] and tetra(4-bromophenyl)porphyrin molecules [56]. They highlight that many factors such as interactions in self-assembled structures, manipulation path, possible additional rotational movements, and conformation of the molecule need to be carefully considered for a quantitative analysis. Related to these experiments on quantification of the lateral manipulation of molecules are also reports on modified AFM setups used to measure friction phenomena of single molecules on surfaces [57].
Furthermore, the AFM tip was also used to transfer a metal atom from the tip apex into the cavity of a phthalocyanine molecule [58]. In this report they also extracted the force and energy between tip and molecule during this single molecule metalation reaction.

A common theme of the systems in this thesis are the tailored protruding molecular structures. On the one hand, as seen in the examples above SPM is well suited to characterize planar molecules. Moreover, the family of SPM technique is also in widespread use in the field of extended two dimensional materials such as graphene or transition metal dichalcogenides. For a brief overview see references [59, 60]. On the other hand, going beyond planar molecules and planar structures towards protruding molecular structures offers to explore new phenomena. Extended three dimensional molecular architectures

are found for example in metal coordinated metal organic frameworks(MOF). For an introduction into this topic see the reviews and examples in references [61–68]. The basic idea is that cage like structures are built by linking organic spacer molecules via metal atoms. The resulting MOFs are investigated for their promising in electrocatalytic reactions.

In the present study we focus on protruding molecular structures which are on a intermediate scale relative to the examples given above. Here, the protruding molecular structures encompass single molecules in an upright adsorption geometry, double-decker systems sticking out of self-assembled molecular layers and inherent non-planar structural features in the molecules . Selected tailored structures are used to probe phenomena such as the adsorption geometry of molecules, molecular rotation and the stability of inherent geometric properties of molecules.

The adsorption of molecules is one of the central topics in surface science [69]. It also is closely related to surface chemistry, a field relevant for numerous applications such as catalysis or fuel cells. The importance is also highlighted by the Nobel prize in chemistry 2007 awarded to Gerhard Ertl "for his studies of chemical processes on solid surfaces" [70].

Closely related to the adsorption of molecules is also their conformation on the surface. In particular in the field of molecular motors on surfaces the combination of adsorption geometry and switchable conformations is important for their function [71]. The investigation of molecular rotation also ties in with the study of adsorption geometries of molecules. In order to probe azimuthal rotation of molecular subunits a suitable adsorption geometry is necessary. Specifically a protruding geometry of the rotor unit is required for unblocked rotation. This protruding structure depends on the investigated molecule and the rotation mechanism. Recent examples for directional rotation of protruding molecular structures studied with STM include acetylene molecules adsorbed on a chiral surface [72], a chemically anchored molecule [73, 74] and a platform anchored ethoxy group [75].

Another protruding molecular system for probing rotation are double-decker molecules. Double-decker systems on surfaces have attracted interest for example in their use as single molecule magnets [76]. It was also shown that the two molecular units coordinated to the metal atom are rotatable, demonstrating their use in molecular rotors on surfaces [77–81].

In addition, the protruding features can also be inherent to the specific constitution of the respective molecule. This is in contrast to the previously mentioned examples where the protruding structure originates from the adsorption geometry of the molecule or the stacking of the planar subunits in the double-decker complexes. Porphyrins are a well-studied class of molecules on surfaces [82, 83] which feature non-planar conformation in solution [84]. On surfaces the macrocycle of the porphyrin can adapt a rather planar geometry [85] or up to strong deformations [86]. This raises the question to investigate how much non-planar molecules maintain their conformation when deposited on the surface. From solution chemistry examples for non-planar molecules are found in saddle- and bowl-shaped molecules such as carpyridines [87–90] and subporphynoids [91, 92]. Both carpyridines and subphthalocyanines [93, 94] are reported to self-assemble in solution

into intriguing structures such as columnar stacks. This demonstrates their potential as model systems to study if their protruding molecular geometries are maintained on the surface, and thus potentially providing starting points to grow three dimensional molecular structures extending from the surface.
In summary, SPM opened a variety of research directions. Here, this thesis integrates into the SPM field by reporting on systems related to on-surface synthesis, rotation on the molecular scale and inherently non-planar molecules.
This thesis starts with an overview of the employed surface science techniques in a methods section, followed by three chapters on the experimental results.
The four molecular systems focus on self-assembly and single molecule manipulation, measuring torque on the single molecule level and characterization of intrinsically saddle-shaped molecules, as briefly described in the following.
In chapter 3, the self-assembly of a small molecule, namely borazine is investigated, including characterization of its single molecule chemistry by means of a tip induced dehydrogenation reaction. The surface chemistry of borazine is essential for synthesis of the extended atomically thin insulators hexagonal boron nitride [95]. Furthermore, the dehydrogenated borazine species was observed to be rotatable by voltage pulses.
Next, in chapter 4 we continue our focus on the rotation of molecular systems. The first section describes efforts to control the adsorption geometry of a hemithioindigo-based motor molecule. This molecule exhibits unidirectional rotation by visible light and is designed to maintain this behavior when adsorbed on the surface [96]. The second section reports on using the SPM tip as a tool to measure the torque needed to rotate a naphthalocyaninces based double-decker molecule. The aim with this model system is to extend the methodology from moving atoms [52] such that it is suitable to quantify rotation of molecules.
Finally, chapter 5 presents a detailed multi-method characterization of carpyridines on surfaces. In solution carpyridines are an inherently non-planar, saddle-shaped type of molecule. Understanding their properties on the surface paves the way for their use in future on-surface experiments. They may offer a way to induce controlled corrugation via on-surface synthesis to extended polymers.
A summary of the results and possible directions for future experiments are presented in the conclusion in chapter 6.

2. Methods

2.1. Scanning Probe Microscopy

Scanning probe microscopy (SPM) techniques are powerful methods in surface science. They provide real space imaging at the atomic scale and can also be used as a tool to manipulate molecules on surfaces with atomic precision. A plethora of specializations of SPM techniques are used to investigate a variety of (time-resolved) phenomena such as for example electric, magnetic, topographic, chemical and optical properties. For a concise overview see Ref. [5]. In the experiments for this thesis, scanning probe microscopes are operated in ultra high vacuum (UHV, $\approx 2{\cdot}10^{-10}$ mbar) and at low-temperatures (LT, ≈ 6 K). Specifically, scanning tunneling microscopy (STM) and atomic force microscopy (AFM) are used to characterize the electronic structure as well as the topography of organic molecules on surfaces. Features of the electronic structure of the interface are measured by means of scanning tunneling spectroscopy (STS). A brief overview of the operating principles is given here. For detailed derivations see for example the textbooks [97, 98].
In this thesis, scanning probe microscopy data is analyzed with WsXM [99], Gwyddion [100], Spectrafox [101] and SpmImage Tycoon [102].

2.1.1. Scanning Tunneling Microscopy

The STM is based on the quantum mechanical tunneling effect. The atomically sharp tip is brought in close proximity to the surface (≈ 1 nm). Applying a bias V to this tip-sample junction enables electrons to tunnel through the vacuum gap, resulting in the tunneling current. Scanning the tip across the surface yields a typical STM image. Selected equations from Ref. [97, 98] relevant for discussing STM experiments are provided in the following.
In the Bardeen model the tunneling current between tip and sample is given by:

$$I = \frac{4\pi e}{\hbar} \int_0^{eV} \rho_{tip}(\varepsilon - eV)\rho_{sample}(\varepsilon)|M|^2 d\varepsilon \tag{2.1}$$

with the matrix M given by

$$M = \frac{\hbar}{2m} \int_{S_{tip/sample}} \left[\psi_{tip}(\mathbf{r})\nabla\psi^*_{sample}(\mathbf{r}) - \psi^*_{sample}(\mathbf{r})\nabla\psi_{tip}(\mathbf{r})\right] \cdot d\mathbf{S} \tag{2.2}$$

We note that the current depends on the wave functions of the sample and tip ($\psi_{sample/tip}$) and the density of states in the sample and tip ($\rho_{sample/tip}$), respectively.

For the one-dimensional (1D) case of the tunneling junction, the matrix element can be approximated by the transmission factor $T(\varepsilon, V, d)$ with Φ the respective work function:

$$T(\varepsilon, V, d) \propto \exp\left[-2d\sqrt{\frac{2m}{\hbar^2}\left(\frac{\Phi_{tip}+\Phi_{sample}}{2}+\frac{eV}{2}-\varepsilon\right)}\right] \tag{2.3}$$

The basic principles of the STM tunneling junction are illustrated with help of the sketch of the 1D tunneling junction in Fig. 2.1. The tip and sample are separated by a distance d, and feature a characteristic density of states. At T=0K these states are occupied until the Fermi energy E_f. The work function $\Phi_{tip/sample}$, states how much energy is required to lift an electron from the respective Fermi energy into the vacuum.
For the tunneling process we first discuss the transmission factor Eq. 2.3. It depends on the average tip/sample work function and also the energy ε of the electron. Electrons with energies closer to eV have a higher probability for tunneling, also illustrated by the different arrow lengths. Most importantly, the transmission factor depends exponentially on the distance d between tip and sample. This is one of the requirements for the very high spatial resolution.
Next, we focus on the Bardeen equation (see Eq. 2.1). The total tunneling current is given by a combination of the density of states in the tip and sample integrated over the range of the bias window eV. Consequently, STM data show a combination of tip and sample density of states. In Fig. 2.1 a positive sample bias leads a relative downwards shift of $E_{f,sample}$ with respect to $E_{f,tip}$ resulting in tunneling of the electrons from the occupied states of the tip into the unoccupied states of the sample.

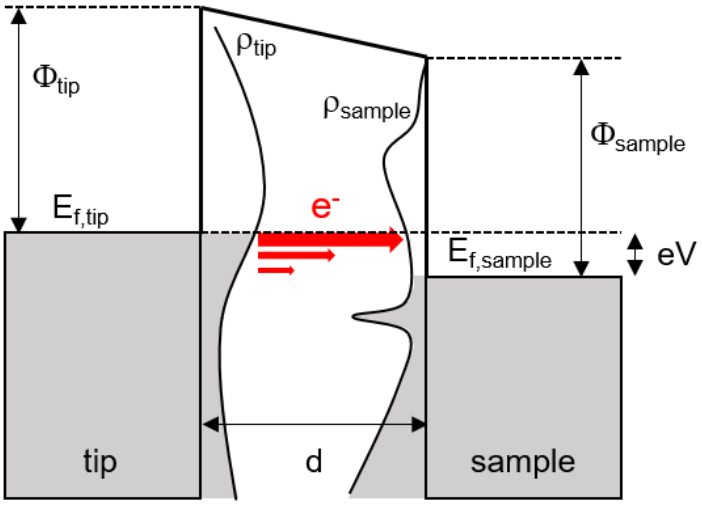

Figure 2.1.: Scheme of the tunnel junction. At T=0K electrons occupy states in the tip and sample up until the respective Fermi energy, $E_{f,tip/sample}$ (shaded area). The energy to remove an electron to the vacuum is given by the work function $\Phi_{tip/sample}$. A positive sample bias voltage V allows electrons to tunnel from the occupied states in the tip into the unoccupied states of the sample (red arrows). Figure adapted from Bert Voigtländer, Scanning Probe Microscopy: Atomic Force Microscopy and Scanning Tunneling Microscopy, Springer, 2015, p.297 [98].

STM images are acquired by scanning the tip across the surface. Piezo elements control the translation and extension of the tip. The specific geometry and arrangement of these piezo elements depend on the type of scanner in the STM head.
For typical STM experiments two types of image acquisition modes are employed, constant current and constant height mode. In constant current mode the tip is held at a fixed tunneling current set point (pA to nA) and the movement of the piezo elements is controlled via a current-feedback loop. The tip-sample separation is extracted from the voltage required to drive the piezos. In the constant height mode the tip is moved at a fixed height above the surface and the current signal is recorded. This mode is typically used in small scale images with little height variation.
In summary, the topography STM images show a combination of the tip and sample density of states.

2.1.2. Scanning Tunneling Spectroscopy

STS is a technique to gain information on the local density of states. To this end, the differential conductance is measured. Taking the derivative of Eq. 2.1 is instructive for the relation between differential conductance and local density of states:

$$\frac{dI}{dV} = \frac{4\pi e^2}{\hbar}\rho_{tip}(0)\rho_{sample}(eV)T(eV,V,d) + \int_0^{eV} \rho_{tip}(\varepsilon - eV)\rho_{sample}(\varepsilon)\frac{dT(\varepsilon,V,d)}{dV}d\varepsilon$$
$$\approx\propto \rho_{sample}(eV) \tag{2.4}$$

Here, the approximations from the 1D case are applied, and in the last step $\frac{dT(\varepsilon,V,d)}{dV} \approx 0$ is used. From Eq. 2.4 we see that the density of states in the sample contributes to the dI/dV signal, enabling charaterisation of the electronic structure. In order to exclude effects from the tip, reference spectra of the surface state and multiple data sets with different tips need to be recorded.

2.1.3. Atomic Force Microscopy

In AFM experiments the tip-sample interactions at close distances depend on the local forces, which are used to extract information about the surface topography or work function [5]. During the work of this thesis, non-contact frequency modulated AFM (in the following nc-AFM) is used, mainly focusing on identifying topographic features. Moreover, the AFM tip is also used as a tool to rotate a molecule on the surface and quantify the required torque via lateral manipulation.
The general working principle of nc-AFM is sketched here, for a detailed derivation see Ref. [98, 103]. Details on quantitative torque measurements are discussed in the next section.
In nc-AFM experiments, the atomically sharp tip is located on a cantilever and this combined system oscillates while recording the data. The tip-sample interaction can be modeled by two connected springs as sketched in Figure 2.2. The resonance frequency of the tip-cantilever system $f_0 = \frac{1}{2\pi}\sqrt{\frac{k}{m^*}}$, is given by the effective tip-cantilever mass m^* and stiffness k. Interaction with the surface can be separated in long and short ranged phenomena. Electrostatic and van der Waals forces are longe ranged, while Pauli repulsion is short ranged. The combination of these tip-sample interactions is modeled with a second spring k_{TS} (red in Figure 2.2 a). This causes a change in the resonance frequency, termed frequency shift, which is the typical signal measured in nc-AFM experiments.

$$\Delta f = \frac{1}{2\pi}\sqrt{\frac{k+k_{TS}}{m^*}} - \frac{1}{2\pi}\sqrt{\frac{k}{m^*}} \approx \frac{f_0}{2k}\cdot k_{TS} \tag{2.5}$$

Consequently, the tip-sample force F_{TS} and potential U_{TS} can be extracted from the frequency shift with the following relation:

$$k_{TS} = -\frac{\partial F_{TS}}{\partial z} \Rightarrow \Delta f = -\frac{f_0}{2k}\frac{\partial F_{TS}}{\partial z} = -\frac{f_0}{2k}\frac{\partial^2 U_{TS}}{\partial z^2} \tag{2.6}$$

Accurate calculation of F and U is not straightforward, however for small oscillation amplitudes, methods for deconvolution have been reported by Sader and Jarvis [104] ("Sader-Jarvis Method") and Gießibl [105]("Matrix-Method").

An instructive description of the approximate tip-sample forces is given by the Lennard-Jones potential U_{LJ}. It combines the attractive van der Waals interaction and an empirical repulsive component. Additional tip-sample forces are briefly summarized after the discussion of the Lennard-Jones potential.

$$U_{LJ} = U_0 \left(\left(\frac{r_a}{r} \right)^{12} - 2 \left(\frac{r_a}{r} \right)^{6} \right) \tag{2.7}$$

with $-U_0$ the minimum energy at the equilibrium distance r_a, r denotes the distance between the two particles.
Eq. 2.7 is plotted in blue in Figure 2.2 b) ($U_0 = 5.8\,\mathrm{meV}$, $r_a = 3.6\,\text{Å}$, the parameters model the O-atom of a CO-tip above a C atom from the sample, values taken from Ref. [106]). The force and relative frequency shift are calculated via $F = -\nabla U$ and Eq. 2.6 ($k = 1800\,\mathrm{N\,m^{-1}}$), respectively.
At distances far away from the sample, the potential is attractive, then it reaches a minimum at $r = r_a$ and becomes repulsive at closer distances (shaded region). The force and relative frequency shift curves display similar qualitative shapes. The change from attractive to repulsive regime and can be easily identified in the force curve by the sign change. In a typical experiment, the frequency shift over one oscillation period is measured. Consequently, at oscillation amplitudes of typically 60 pm, contributions from the repulsive regime are present close to the minimum/sign switch region of the frequency shift. These repulsive effects give rise to the bond-resolved contrast.

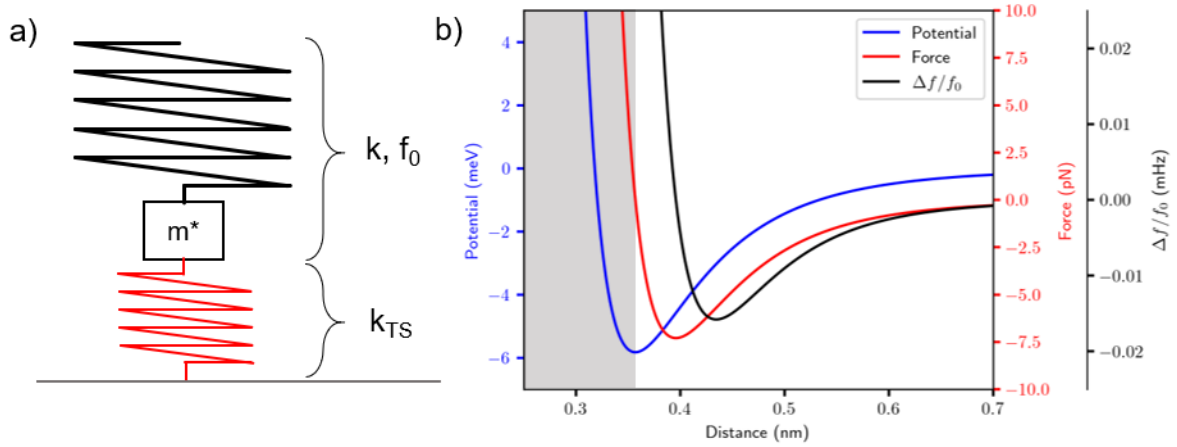

Figure 2.2.: Scheme of the tip-sample interaction in AFM experiments. a) The tip-cantilever system oscillates with f_0, represented by the black spring. The interaction with the surface is modeled with a second spring k_{TS} (red). b) Plot of the Lennard-Jones potential (blue) and extracted force (red) and frequency shift (black). The repulsive regime is marked with the shaded area. Figure adapted from [98, 107].

A brief overview of forces relevant for nc-AFM measurements is given in the following. Attractive van der Waals forces originate from induced dipole moments and scale with r^{-6}. They are classified as long range forces and contribute with a large fraction to the

forces observed at distances > 1 nm. At close distances the electron wave functions of tip and sample atoms overlap, leading to a repulsive force due to the Pauli exclusion principle. This repulsive term can be approximated for example with the r^{-12} term in the Lennard-Jones potential. Moreover, the tip-sample system represents a capacitor, and consequently a long-range electrostatic force $\propto 1/r$ is present.
In the experiments the influence of the long range van der Waals component can be compensated by subtracting a suitable reference data set. For this, a spot of the sample featuring the bare surface is investigated covering the same distance range as the data set that features the region of interest. The electrostatic component is suppressed by minimizing the potential difference $\Delta V = V_{TS} - \Delta\Phi/e$, where $\Delta\Phi$ is the work function difference. Explicitly, a sample bias V_{TS} is chosen, where the lowest absolute value of the tunneling current is observed.

Torque measurement

In order to employ the AFM as tool and measure the torque required to rotate a molecule, we adapt the procedure for measuring forces needed to move an atom [52]. The tip is moved in constant height above the movable object and from the simultaneous recording of the frequency shift the interaction potential U is calculated. See also Figure 2.3. Before going into details of the calculation a brief summary of the experimental procedure is given here.
The tip is moved across a Co atom on Pt(111) along the path marked in blue in Figure 2.3 a). This procedure is repeated at decreasing tip-sample distance while simultaneously recording the frequency shift. At a sufficiently strong interaction, i.e. a short tip-sample distance, the Co atom moves to the position highlighted by a red circle in 2.3 a). The frequency shift signal is approximately proportional to the vertical stiffness (equation 2.5), which is plotted for different tip-sample distances in 2.3 b). Far away from the Co atom (purple curve) the signal is featureless. Upon going closer to the amplitude of the signal increases, with the minimum located above the Co atom. In the green curve a discontinuity appears at the position marked by the red arrow. This is followed by a copy of the signal where a similar signal appears again with a constant x-offset. This behavior is attributed to the Co atom moving in x-direction.
The tip-sample potential can be extracted as a function of tip-height via equation 2.6 and is plotted in Figure 2.3 c). From this data the lateral force is calculated by taking the negative gradient in x-direction (see Figure 2.3 d).

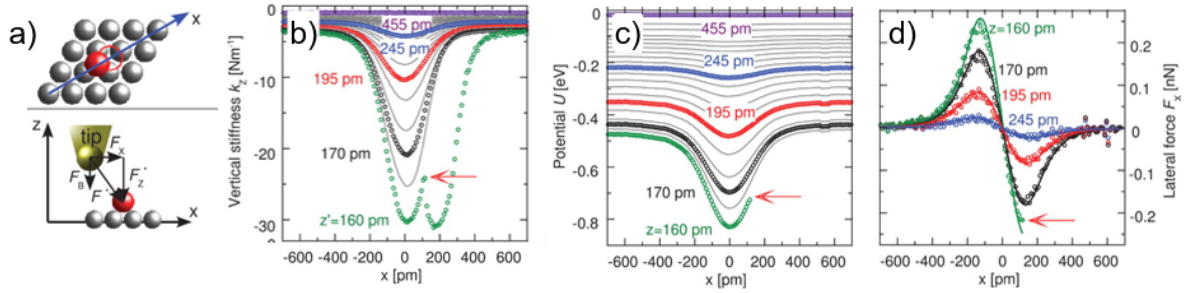

Figure 2.3.: Lateral manipulation protocol for extracting lateral forces in nc-AFM measurements at the example of moving a Co atom on Pt(111). a) Scheme of a Co atom (red sphere) on Pt(111). The AFM tip is moved laterally across the atom at different tip heights. b) The vertical stiffness is approximately proportional to the measured frequency shift (Equation 2.5). For closer tip-sample distances (decreasing z) the signal intensity increases. The red arrow marks the position where the Co atom moved. c) Tip-sample potential for different tip-heights extracted from the vertical stiffness. d) Lateral force obtained by taking the negative derivative in x-direction of the potential in c). Figure adapted from Markus Ternes et al., The Force Needed to Move an Atom on a Surface. Science 319, 1066-1069 (2008) [52]. Reprinted with permission from AAAS.

This procedure is adapted for extracting the torque necessary to rotate a molecule. Therefore the torque is calculated via

$$\overrightarrow{M} = \overrightarrow{r} \times \overrightarrow{F} \tag{2.8}$$

with r the distance from the center of rotation, easily accessible from the STM images. The force $|\overrightarrow{F}|$ is obtained by taking the derivative in the manipulation direction of the potential U. U is extracted from the frequency shift data via the Sader-Jarvis method [104, 105], specifically the following formulas and correction terms are implemented in a python code:
Equation (9) from Ref. [104] states:

$$F(z) = 2k \int_z^\infty \left(1 + \frac{a^{1/2}}{8\sqrt{\pi(t-z)}}\right) \Omega(t) - \frac{a^{3/2}}{\sqrt{2(t-z)}} \frac{d\Omega(t)}{dt} dt \tag{2.9}$$

where $\Omega(z) = \Delta\omega(z)/\omega_{res}$ with $\omega(z)$ the measured frequency shift, z the tip-sample distance and ω_{res} the resonance frequency. The experiment is performed with $\omega_{res} = 2\pi \cdot 30900$ Hz, an oscillation amplitude $a = 60$ pm and for the stiffness k a value of 1800 N/m is assumed.
The measured frequency shift and tip-sample distance are discrete data sets allowing to use the implementation from Ref. [105]:

$$F(z) = \underbrace{2k\left[\left(1+\frac{a^{1/2}}{8\sqrt{\pi(t-z_j)}}\right)\Omega(t) - \frac{a^{3/2}}{\sqrt{2(t-z_j)}}\frac{d\Omega(t)}{dt}\right]}_{\text{from eqn 2.9, to be integrated along t with composite trapezoidal rule}} \\ \underbrace{+2k\left[\Omega_j(z_{j+1}-z_j) + 2\frac{\sqrt{a}}{8\sqrt{\pi}}\Omega_j\sqrt{z_{j+1}-z_j} + \frac{-2a^{3/2}}{\sqrt{2}}d\Omega_j/dz\sqrt{z_{j+1}-z_j}\right]}_{\text{corrections terms for integrable singularity at t=z}} \tag{2.10}$$

z is the distance to the sample, with z_j closer to the sample than z_{j+1} and $z_j < z_{j+1}$, j counts the height steps, $d\Omega_j/dz$ denotes the derivative along z until z_j for each data point along the line.
The interaction potential U between tip and sample is calculated via numerical integration (composite trapezoidal rule) of the first part in Eq. 2.10 and then adding the correction terms. The lower limit for j is set by the closest continuous frequency shift curve to the molecule prior to discontinuities in closer constant height frequency shift sweeps.
The axis along the manipulation direction is labeled with x, and the potential is obtained by integration of the force:

$$U(x,z) = -\int_z F(z')dz' \tag{2.11}$$

U is smoothed with a Savitzky-Golay filter, for details see the related plots in section 4.2.2 and Figure 4.20.
Finally the force required for evaluating eq. 2.8 is extracted by taking the derivative along the manipulation direction:

$$F_x = -\frac{dU(x,z)}{dx} \tag{2.12}$$

Now F_x and r are available, allowing the calculation of M via Eq. 2.8.

2.2. Photoelectron Spectroscopy and Related Techniques

Photoelectron spectroscopy is a space averaging technique and allows to measure properties such as the chemical environment of the atoms in the sample. From this, we can draw conclusions on the chemical composition of the compound. In the present study this technique is used to check whether the molecules adsorb intact on the surface and to identify possible reaction products upon sample treatments.

2.2.1. X-ray Photoelectron Spectroscopy

X-ray photoelectron spectroscopy (XPS) yields information on the chemical environment of the elements. A short introduction is given here, for a detailed derivation see references [108–112]. XPS is based on the photoelectric effect, where upon absorption of a photon an electron ("photoelectron") is released. X-rays with energies $\approx$ 300-1500 eV excite core-level electrons. The released electrons have a mean free path of a few nm in the material, leading to the inherent surface sensitivity of this technique. The kinetic energy of the electron in the vacuum is related to the photon energy $\hbar\omega$, binding energy E_{bin} and work function Φ via

$$E_{kin} = \hbar\omega - E_{bin} - \Phi \tag{2.13}$$

Consequently measuring the kinetic energy of the electrons yields information about the binding energy, which in turn depends on the chemical environment of the atom from which the electron originates. The shift in binding energy is called chemical shift and is typically used to characterize the oxidation state. Electronegative (electropositive) substituents at the atom decrease (increase) the screening effect of the resulting core-hole resulting in a shift towards higher (lower) binding energies. Additional effects on the peak shape and further contributions to the XP spectra, which are present in the data shown in this work, are briefly listed in the following. A more detailed discussion on the signal shape and resulting peak fitting is found in references [111–114].
Spin-orbit splitting results in peak splitting with an intensity ratio of $l + 1/l$ with l the orbital angular momentum quantum number. Auger peaks appear when the core hole e.g. in the K-shell is filled with an electron from a higher energy level e.g. L-shell and results in the release of a third electron (e.g. L_2). This so called Auger electron has a specific kinetic energy related to the energy level of the core hole and energy levels of the two other involved electrons.

$$E_{Auger,kin} \approx E_{bin,K} - E_{bin,L_1} - E_{bin,L_2} - \Phi \tag{2.14}$$

Plasmon peaks occur frequently when investigating metal substrates. The photoelectron transfers transfers a part of its kinetic energy to a plasmonic excitation resulting in plasmon loss peaks at higher binding energy compared to the main peak from the metal.
In summary, XPS is employed here to probe the occupied core levels and, with the chemical shift as main criterium, to identify the elements and their chemical environment.
The XPS data in this thesis is processed with CasaXPS and Matlab. Linear or Doniach-Sunjic [115] backgrounds are subtracted from the data and peaks are modeled with a Gauss-Lorentz lineshape.

2.2.2. Near-Edge X-ray Adsorption Fine Structure Spectroscopy

NEXAFS spectroscopy probes the unoccupied states and provides information about the electronic structure and the geometric orientation of adsorbates with respect to the surface. The basic principle is introduced here, for details see references [116, 117].

The process is sketched in Figure 2.4 a). Photons from a tunable ($\approx 200 - 700$ eV) linearly polarized light source excite a core level electron into an unoccupied state. This excited state decays releasing either another photon (radiative decay, fluorescence) or an electron (non-radiative decay, Auger electron). In a typical spectrum three features appear. First, when the photon energy matches the energy difference between the core level and a π^* state, a sharp peak appears. Next, with increasing photon energy, a step-like feature occurs when the photon energy matches the ionization potential. Above this step, broad resonances occur from short-lived σ^* states.
The sensitivity to the geometry stems from the dependence of the photoabsorption cross section on the polarization of the electric field $\overrightarrow{E}$ and orbital orientation $\overrightarrow{O}$ (p.71 in reference [116]).

$$I \propto |\overrightarrow{E} \cdot \overrightarrow{O}|^2 \tag{2.15}$$

Consequently from the scalar product above, the signal is the most intense for a parallel geometry of the electric field and the orbital orientation. This allows to determine the orientation of adsorbates on the surface. The case of a π^* and σ^* resonance in a six-membered ring, e.g. benzene is illustrated in Figure 2.4 b) and c). For grazing incidence of the light, $\overrightarrow{E}$ is parallel to the π^* orbital, leading to a strong signal of the π^* resonance. For normal incidence, $\overrightarrow{E}$ is not orientated along the direction of the π^* orbital, but now matches the direction of the σ^* orbital, resulting in an spectrum with a small π^* signal and a strong σ^* signal. The intensities of specific orbital transitions as a function of substrate symmetry and incidence angle of the light are tabulated, allowing to calculate the orientation of the orbital [118, 119]. Thus, the orientation of rigid building blocks in the adsorbate, e.g. phenyl groups in a molecule, can be determined.

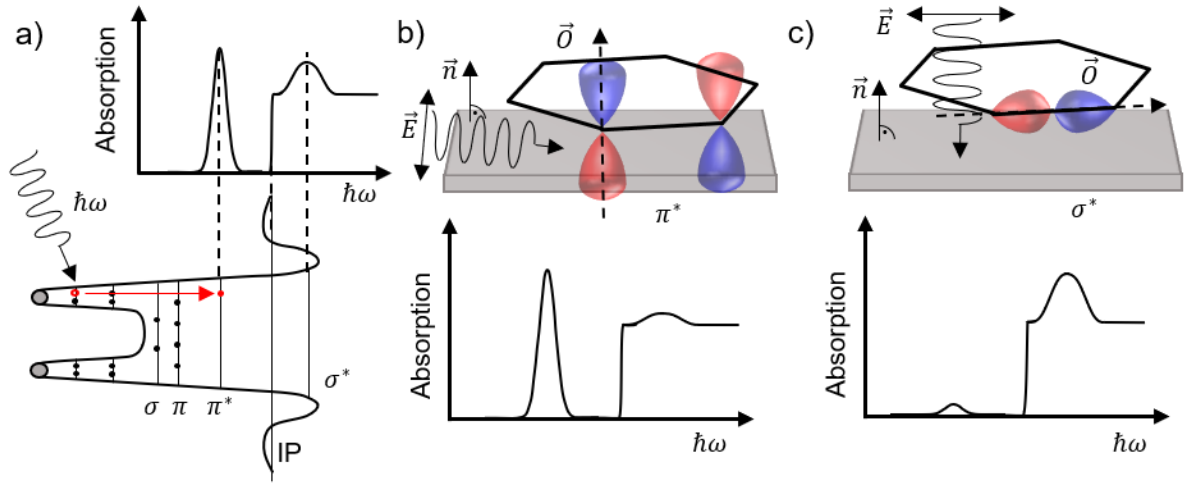

Figure 2.4.: Scheme of processes relevant in NEXAFS spectroscopy. a) When the photon energy $\hbar\omega$ matches the energy difference between the binding energy of the electron and an unoccupied orbital, a resonance appears in the spectrum. b,c) Sketch of a six membered molecule to visualize the angle dependency between the orientation of the orbital $\vec{O}$ and polarization direction of the electric field $\vec{E}$ of the photon. In grazing incidence $\vec{E}$ is orientated roughly parallel to the surface normal $\vec{n}$. Maximum intensity is observed for a π^* transition, while the signal from σ^* transitions is suppressed. For normal incidence the σ^* orbital is now orientated parallel to $\vec{E}$, leading to a intense σ^* signal, while the π^* intensity vanishes. Figure adapted from [116, 117].

In this work the NEXAFS data are taken at the PEARL endstation at the Swiss Light Source and treated according to literature procedures [118, 119]. The intensity was recorded via the N KVV Auger region in the fixed energy mode with a pass energy of 200 eV. The uncalibrated photon energy was swept in 0.1 eV increments from 395 eV to 415 eV. For each incidence angle the signal of the clean Au(111) substrate was also recorded. Each measured signal, i.e. molecules on Au(111) and bare Au(111), is normalized to the reference current, which is proportional to the photon flux. This compensates for minor photon flux variations during the photon energy scan. The normalized spectra of the molecules is then divided by the normalized spectra of the substrate. The resulting curve is then normalized to an edge jump of 1. This process is done for each incidence angle. The π^* resonance was modeled by subtracting and a linear background with a step and approximating the peak with a gaussian function. For determining the orientation of the molecular orbital, the (111)-symmetry of the substrate was considered according to equation (11) of [119]. The extracted peak areas are normalized to the value of the peak area measured at the magic angle 53.5° and then compared to equation (11), whilst taking into account a polarization factor of 0.9.

2.3. Simulation

Density Functional Theory

Density functional theory (DFT) calculations and STM simulations presented in chapter 3 are performed by Georg S. Michelitsch.
Dispersion corrected DFT calculations were performed in the FHI-aims simulation package [120–122]. The exchange and correlation terms were described using PBE functionals [123]. Spin polarized calculations were employed to account for the behavior after homolytic bond separation in dehydrogenated species. For the adsorption energy calculations, a 3x3x3 unit cell was modeled, where the bottom layer was exempt for geometry optimization while the remaining atoms were allowed to relax until residual forces on each atom were $< 1.0 \cdot 10^{-3}$eV/Å. Tersoff-Haman STM simulations were performed by summing all the states within an energy-window at the Fermi level of size determined by the experimental bias voltage [124].

Probe-Particle model

The Probe-Particle model is used to simulate the nc-AFM contrast of 2H-Car-C1 presented in section 5.1.3. A brief overview of the Probe-Particle model is given here, for a detailed description see Ref. [106, 125, 126]. An open-source implementation is available[1].
In this model the tip is separated into a fixed anchor point and an additional spherical probe particle attached to it. This probe particle represents the tip apex, e.g. the oxygen atom in the CO tip. The forces on this probe particle contain forces from the tip and forces from the sample. Tip-related forces are modeled with a radial spring. Forces originating from the sample include Pauli repulsion, van der Waals interactions and electrostatic interaction. The data is obtained by simulating scanning the tip across the surface and at each position the probe particle is allowed to move until the forces are below a chosen threshold (typically 10^{-6} eV/Å).
In section 5.1.3, the simulation is based on a gas-phase DFT optimized structure of 2H-Car-C1 provided by Joseph Woods [127]. The images were generated with CO-tip parameters ($k_{xy} = 0.25$ N/m) and without an electrostatic potential.

2.4. Experimental Setup

Experiments are performed in various ultra-high vacuum (UHV) chambers located at the Technical University of Munich (TUM) and the Paul Scherrer Institut (PSI). UHV environment is necessary to ensure cleanliness of the samples. The base pressure of $\approx 2 \cdot 10^{-10}$ mbar is maintained through a series of standard vacuum pumps. Typically a roughing pump in series with two turbo molecular pumps is utilized with additional ion pumps as well as a titanium sublimation pump. In specific cases cold traps are activated.

[1] https://github.com/Probe-Particle and https://nanosurf.fzu.cz/pprmodel.php

The LT-STM chamber at TUM features a base pressure of $< 2 \cdot 10^{-10}$ mbar in the measurement chamber and one order of magnitude larger in the preparation chamber. It is equipped with standard surface science sample preparation techniques such as sputter gun, leak valves (Ar, CO, Borazine), LEED. The CreaTec Fischer commercial STM is equipped with a bath cryostat (liquid nitrogen (lN_2) and liquid helium (lHe)) allowing operation at 6.8-8.3 K. The STM stage is decoupled through mechanical springs and an eddy current damping. A Besocke-Beetle type and a Slider-type scanner are used and controlled through a CreaTec or Nanonis electronics. The STM tips are etched from a 0.25 mm tungsten wire and sputtered with argon prior to use. An additional high voltage power supply for field emission between tip and sample ($\approx$ 100 V, 7 µA) is available for conditioning the tip.
The nc-AFM chamber at TUM is built with a comparable geometry as the above mentioned LT-STM chamber. The AFM operates by using a tungsten tip mounted on a qPlus sensor and is also controlled with Nanonis electronics. STM mode is also possible with this setup. Typical measurement temperatures, achieved with a bath cryostat (lN_2, lHe), are $\approx$ 5.3 K.
The XPS chamber at TUM is equipped with a Specs XR50 dual anode x-ray source and a Phoibos 100 analyser. Mg K-α radiation at 1253.6 eV is used in the experiments.
Synchrotron based experiments are carried out at the PEARL endstation at the Swiss Light Source in Villigen. A detailed description is given in ref. [128], some aspects are summarized here. The UHV system features an interconnected preparation chamber, STM chamber and XPS chamber allowing characterisation with complimentary techniques on the very same sample without breaking UHV. The STM (Omicron) was operated at 4.5 K with a PtIr tip. The XPS chamber is equipped with a Scienta EW 4000 analyser. XPS measurements were performed at room temperature.
Molecules are deposited on the samples via organic molecular beam epitaxy (OMBE) using commercial (Dodecon) and home-built Knudsen cell systems. Metals such as Fe, Cu, Th are evaporated from e-beam evaporators or home built systems as described below.

2.5. Sample Preparation

Single Crystal Cleaning

The single crystal samples are mounted on sample holders (TUM: CreaTec metal sample holder with resistive heating, PSI: flat flag style) and introduced into the UHV systems followed by standard cleaning procedures.
Atomically clean Ag(111) and Au(111) surfaces (MaTeck, SPL) were prepared by repeated cycles of sputtering with Ar^+ ions at 800-1000 V and annealing to 450-470°C and 500-550°C respectively.

Borazine

Borazine (99%, Katchem) is purified by freeze-thaw cycles before dosing via a leak valve equipped with a nozzle resulting in a sample-nozzle distance of $\approx$ 10 cm. The reported exposure is calculated with the signal at the pressure gauge located $\approx$ 45 cm away from the sample.

Thorium-Naphthalocyanine Double-Deckers

Naphthalocyanine molecules (95%, Porphychem) are loaded in a commercial Dodecon OMBE system and carefully stepwise degassed in UHV until only a negligible concentration of non-naphthalocyanine species was observed in STM images. The used temperature and times are: 400 °C for 6 h, 410 °C for 1 h, 450 °C for 9.5 h, 470 °C for 7 h, 485 °C for 21.5 h. They are then evaporated at 485 °C for 8 h onto Ag(111) held at room temperature. Elemental Thorium is dosed from a home built evaporator by heating (19.2 W) a Tungsten wire (0.3 mm) with a Thorium wire (0.1mm) wrapped around it onto Nc/Ag(111) at room temperature. A coverage of 3 pm of Th was detected via a quarz microbalance, located opposite the wire and positioned at a distance comparable to the wire-sample distance. Lastly, the Thorium-naphthalocyanine system is annealed at 350 °C for 10 min.

Molecular Motors

The motor 1 and motor 2 molecules provided by the group of Prof. Henry Dube [129] and are evaporated from a Dodecon OMBE at 218-250°C. The TBB-based covalent framework is prepared by dosing 1,3,5-Tris-(4-bromphenyl)-benzene ("TBB", 97%, Sigma Aldrich) at 178°C (225°C) on Ag(111) (Au(111)) held at room temperature for 40s (45s) followed by annealing to 250°C and 460°C (375°C) for 5 min each. C_{60} molecules are evaporated at 390°C. Figure 4.8 shows the structure of TBB, TBB-COF and C_{60}. All substances were degassed up to 1h prior to usage in preparations.

Carpyridines

Carpyridine molecules were provided by Joseph Woods and Lucia Gallego from the group of Prof. Michel Rickhaus located at University of Zurich in 2022. After degassing, 2H-Car-C2 (2H-Car-C1) molecules are evaporated at 305 °C (330-340°C) for 5-12 min onto the substrate at room temperature resulting in sub-monolayer coverages. For details on preparations related to 2H-Car-H see section "carpyridines without alkyl side chains and with ethyl side chains" 5.2.
Preparation details of Cu/2H-Car-C1/Au(111): Small amounts of Cu were dosed with a home built evaporator, equipped with a Cu wire. The 2H-Car-C1/Au(111) sample held at room temperature was exposed to the Cu beam for 7 s at a distance of $\approx$ 10 cm.
Preparation details of Fe/2H-Car-C1/Au(111): The sample for the XPS measurements was prepared with the following parameters: 1) evaporate 2H-Car-C1 at 340°C for 10

min onto Au(111) held at room temperature 2) dose Fe from e-beam evaporator (flux 8 nA, 60s, U=900 V, emission 10 mA) on 2H-Car-C1/Au(111) at room temperature 3) annealing steps at 100°C, 205°C and 300°C for 10 min each. The two discussed samples for STM measurements were prepared with: a1) evaporate 2H-Car-C1 at 340°C for 6 min onto Au(111) held at room temperature a2) dose Fe (flux 5 nA, 90s, U=900 V, emission 10 mA) a3) anneal to 100°C for 10 min. b1) evaporate 2H-Car-C1 at 340°C for 6 min onto Au(111) held at room temperature b2) dose Fe (flux 3.5 nA, 150s, U=900 V, emission 10 mA) b3) anneal to 200°C for 10 min.

3. Adsorption, Self-Assembly and Single-Molecule Manipulation of Borazine on Ag(111)

This chapter includes content published in: T. Weiss, A. Baklanov, G. Michelitsch, K. Reuter, M. Schwarz, M. Garnica and W. Auwärter, "Adsorption, Single-Molecule Manipulation, and Self-Assembly of Borazine on Ag(111)" in Advanced Materials Interfaces, 11, 2300774 (2023) [130].

Borazine, $(HBNH)_3$, the isostructural and isoelectronic analogue to benzene, keeps attracting considerable interest in modern science, even nearly a century after its first synthesis, reported in 1926 by Stock and Pohland [131]. Fundamental conceptual issues, such as aromaticity in borazine and its relation to benzene, are still debated, pointing to its relevance as model system [132, 133]. Furthermore, borazine is heavily employed in material science applications [134], including low-dimensional materials [135, 136], ceramics [137], and optoelectronic devices [138, 139]. However, only few studies address pristine borazine adsorption on metal surfaces under ultrahigh-vacuum (UHV) conditions well below room temperature. Specifically, borazine adsorption was experimentally studied on Re(0001) [140], Ru(0001) [141], Rh(111) [142, 143] , Ir(111) [144] , Pt(111) [145, 146] , hBN/Pt(111) [145], Pt(110) [147], and Au(111) [146] with space-averaging surface science methods, revealing intricate behavior. Borazine might adsorb flat, i.e., with the $(BN)_3$ ring aligned in parallel with the surface plane, or upright, even in the (sub)monolayer regime. Thereby, non-dissociative adsorption can compete with dissociative adsorption, where the latter might feature B- or N-terminal dehydrogenated borazine. For example, on Pt(110), a borazine monolayer adsorbed at 110 K includes intact, flat lying borazine as well as upright borazine species that underwent H abstraction [147].

Additionally, the adsorption of pristine borazine on metal surfaces gained considerable attention in the last decades due to eminent role of borazine as precursor for chemical vapor deposition (CVD) growth of hexagonal boron nitride (hBN) monolayers [95, 135]. hBN is an important representative of the two-dimensional (2D) materials library, where reliable synthesis protocols are indispensable in order to achieve high quality and durability [135, 148–151]. In this context, borazine is usually dosed at high temperatures (> 800 K) on catalytically active metal supports [95], thus complementing the low

temperature adsorption studies addressed above. In particular, the UHV-based CVD synthesis route to hBN can involve different adsorption configurations of the borazine precursor (i.e., orientations of the borazine ring relative to the metal surface plane), as well as dehydrogenation and dissociation [142, 144, 147, 152]. Whereas dissociation of the $(BN)_3$ ring is reported for hBN growth on Re(0001), Ir(111), and Rh(111), [143] dendritic hBN morphologies on Cu(111) were attributed to intact $(BN)_3$ rings during growth [153] . As recently reported for Ru(0001), intermediate porous phases constituted by dehydrogenated borazine might exist during hBN synthesis [154].
Furthermore, considerable organic synthesis efforts gave access to a variety of borazine derivatives [134, 155] , covering structures ranging from halogenated borazines [156] to complex functionalized borazines [157–159]. These serve as versatile building blocks, integrating the $(BN)_3$ ring into carbon scaffolds [160]. On solid supports, self-assembly protocols and on-surface reaction schemes have been applied to functionalized borazines, yielding patterned surfaces exposing polar BN bonds [160–163] and BN-doped covalent carbon nanostructures on metal supports [164].
Considering all the aspects introduced above, the adsorption configuration and self-assembly of unsubstituted borazine on coinage metal supports, as well as its multi-facetted chemistry yielding to borazine decomposition, is of general interest. On the one hand, borazine with its C3 symmetry and minimal size is a promising building block, anticipated to form self-assembled honeycomb-like structures with regular pores [165, 166]. On the other hand, individual borazine molecules represent a model system to investigate adsorption characteristics and single-molecule chemistry.
Here, we provide real-space imaging of surface-supported pristine borazine molecules. Specifically, we report on distinct self-assembled borazine structures on Ag(111) and demonstrate controlled dehydrogenation of single borazine molecules. A detailed characterization of individual molecules and two distinct self-assembled phases, namely a porous phase and a dense-packed phase, is accomplished via low temperature STM measurements. The different assemblies are achieved by adjusting the borazine dosage and each of the structures exhibit domains of organizational chirality formed by intact, flat lying borazine molecules. Insights about the interaction with the substrate are obtained through scanning tunneling spectroscopy (STS). Furthermore, the adsorption geometry is modified by manipulation of individual borazine molecules via tip-induced voltage pulses, promoting dehydrogenation. This reaction yields an upright standing configuration of the molecule. DFT calculations are employed to explore the adsorption energies and sites of the intact borazine molecules on the Ag(111) support and to identify a main manipulation product as dehydrogenated borazine species bound via B to Ag. For an overview see also Figure 3.1.

3.1. Self-Assembly and Adsorption Configuration

Figure 3.2 a)-d) presents STM data upon adsorption of a small amount of borazine (dose: $5 \cdot 10^{-4}$ L) on the Ag(111) substrate at 150 K. The overview image in Figure 3.2 a) shows extended molecular islands featuring regular arrays of pores with a periodicity of (25.4

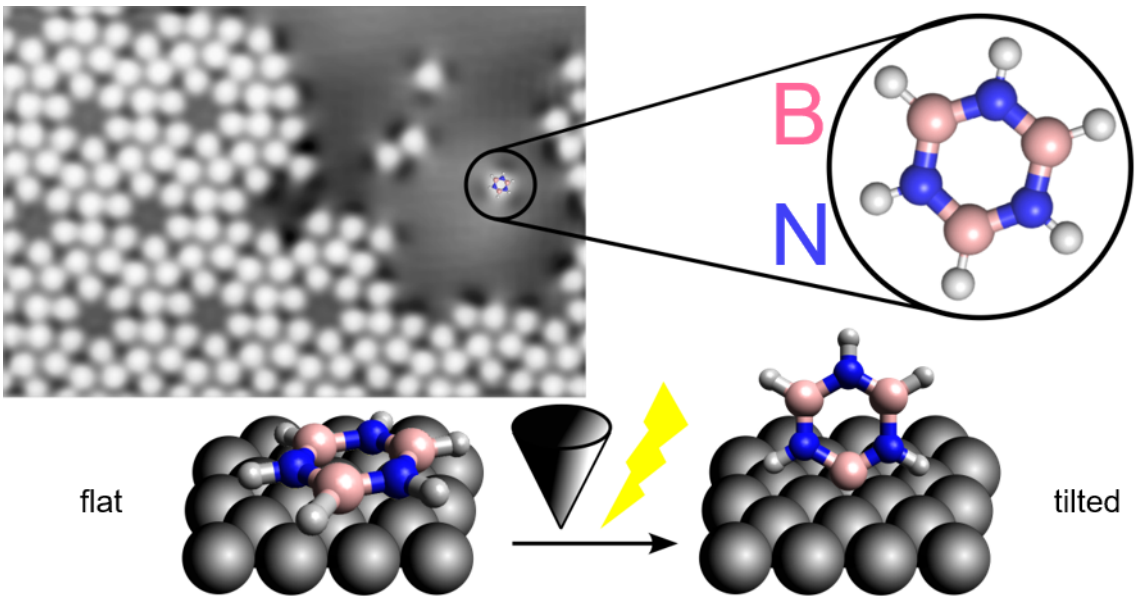

Figure 3.1.: Borazine molecules are imaged on a solid support in real space via low-temperature scanning tunneling microscopy. The intact molecules form a porous and a dense-packed phase. Individual borazine molecules are manipulated with voltage pulses. The manipulation products are identified, in combination with density functional theory calculations, as dehydrogenated and tilted borazine fragment.

± 0.5) Å. The pores constitute a hexagonal lattice and the image reveals coexisting domains with distinct orientations. A more detailed examination (see intermediate scale image in Figure 3.2 b) indeed shows two distinct domains and resolves each borazine molecule as individual protrusion. The red and blue rhombi in Figure 3.2 b) highlight the respective unit cells of the two domains and enclose an angle of (32 ± 4)°. The unit cells are rotated by ± (16 ± 4)° with respect to the [1-10] and equivalent Ag(111) crystal directions. Figure 3.2 c) shows the image obtained by the fast Fourier transformation (FFT) routine applied to the STM image in Figure 3.2 b). It emphasizes the two hexagonal patterns, where the spots originating from each of the domains are encircled in red and blue, respectively. Reflecting the STM images, the two sublattices are rotated by 32° towards each other. Interestingly, few pores inside the regular porous structure are filled with an additional molecule (see Figure 3.2 b), marked with black arrow).
The high-resolution image shown in Figure 3.2 d) reveals additional insights into the molecular packing scheme. Each unit cell includes twelve molecules that are arranged into two triangular subunits of six molecules, as highlighted by the black triangles in Figure 3.2 d). Particularly, any two neighboring triangular subunits are arranged with a small lateral offset along their common side of the triangles. The direction of this shift is specific to each of the domains and thus expresses the chirality of the system. Note that the [1-10] and equivalent Ag(111) directions are identified as mirror axes for these chiral domains. Moreover, the characteristic hexagonal assembly arises from grouping six triangular subunits around a central pore. This architecture features three molecules

along the side of each triangular subunit and is thus classified as N=3 porous honeycomb-like structure following the notation for C3-symmetric molecules in Ref. [166].
After dosing larger amounts of borazine (about $4 \cdot 10^{-3}$ L) onto the substrate held at 150 K, an additional dense-packed phase is observed (see overview image in Figure 3.2 e). In contrast to the low exposure case, this dense-packed phase is characterized by striped patterns. This assembly differs from the porous structure, even if all its central pores were filled by additional borazine molecules. Domains with distinct orientations of the stripes coexist, as can be seen on the adjacent terraces in Figure 3.2 d).
High-resolution imaging (Figure 3.2 f) reveals a grouping of molecules into pairs (with dumbbell-like appearance), highlighted by white ellipses. The different alignment of the pairs gives rise to the striped pattern, which includes rows with a width of two or three borazine molecules. Alternating pairs lead to the two-striped pattern (marked by green arrows). Stacking two pairs with the same orientation and one pair of the alternative orientation results in the three-striped configuration (yellow arrows).

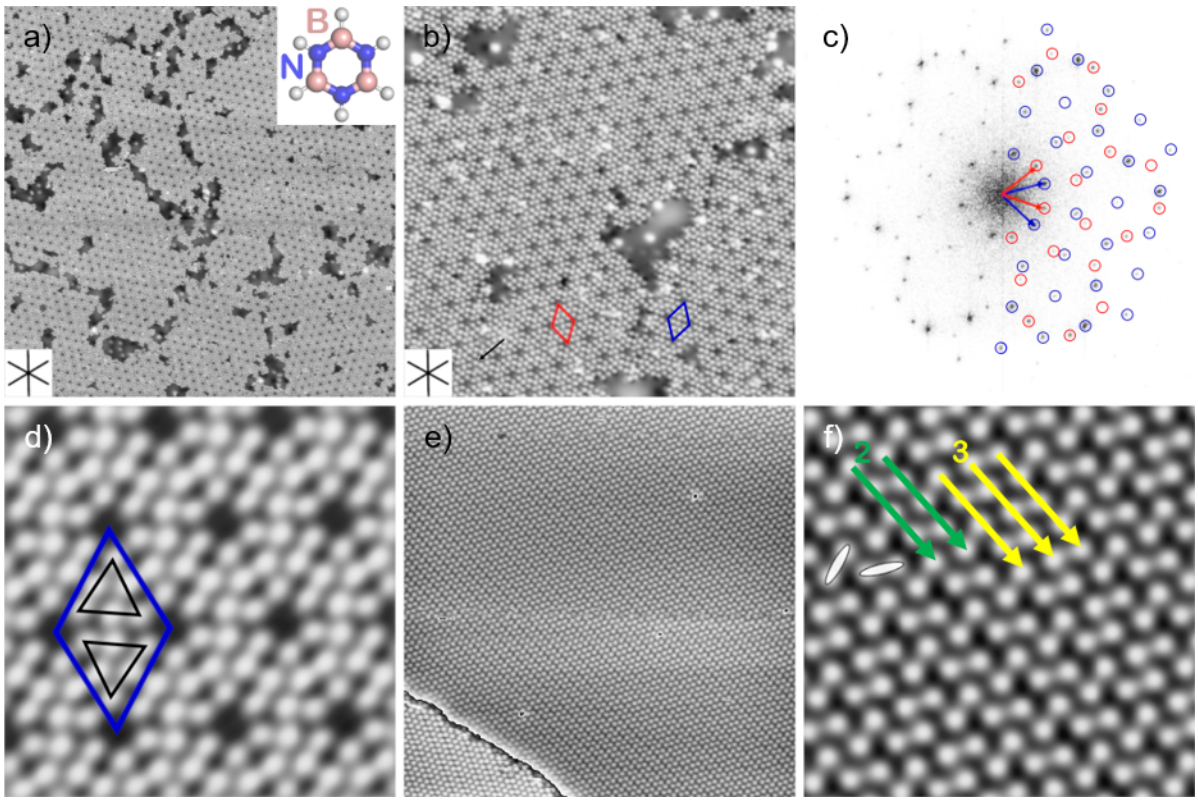

Figure 3.2.: Characteristic structures formed by borazine molecules on Ag(111): a)-d) Porous honeycomb-like assembly and e)-f) dense-packed assembly. a) Overview STM image of the low exposure phase. The molecular structure of borazine is shown in the top right corner. b) Intermediate scale image showing two chiral domains each consisting of a hexagonal arrangement, where the respective unit cells are highlighted with red and blue frames. c) Corresponding FFT image featuring a superposition of two hexagonal patterns each originating from one of the chiral domains. Blue and red circles, superimposed on the right half of the image, indicate the spots attributed to the marked domains in b). The unit cell vectors in reciprocal space are k=0.45 1/nm long (k=1/wavelength convention). d) High-resolution STM image. The blue rhombus highlights the unit cell and each triangle (marked in black) shows the arrangement of six molecules. e) STM image of the dense-packed phase featuring a striped pattern, which exhibits distinct orientations on adjacent terraces (contrast adapted for visibility). f) Zoomed-in image unveiling the striped pattern, which comprises of rows of two (green arrows) and three (yellow arrows) molecules, respectively. The white ellipses mark shorter intermolecular distances. The black cross in the inset of a,b) mark the [1-10] and equivalent Ag(111) directions. Imaging parameters: a) 107.5 x 107.5 nm^2, 0.05 V, 0.5 nA b) 43.7 x 43.7 nm^2, -0.05 V, 0.5 nA d) 8.6 x 8.6 nm^2, -0.1 V, 0.5 nA e) 36.6 x 36.6 nm^2, 0.05 V, 0.5 nA f) 8.6 x 8.6 nm^2, 0.25 V, 1 nA.

After this rather general description of the porous network and the dense-packed striped borazine assembly, we now proceed to a more detailed characterization of these borazine

architectures and their interaction with the supporting Ag(111) lattice, also discussing individual borazine molecules. To this end, Figure 3.3 presents additional STM data and complementary DFT-based STM image simulations. The overview image including a border of a porous assembly and adjacent individual species (Figure 3.3 a) resolves distinct borazine molecules and their orientation. As emphasized in Figure 3.3 b), individual borazine molecules appear as triangular-shaped protrusions with a depression at each side of the triangles, allowing to identify the orientation of the molecules. Judging from the STM data, the borazine molecules adsorb "flat" on Ag(111) (i.e., with the borazine ring aligned parallel to the Ag surface plane), show a threefold symmetry (C3, reflecting the molecular structure), and occur in two distinct orientations, rotated to each other by 180° (see Figure 3.3 b).
To rationalize these observations, we performed STM image simulations based on DFT-optimized interface structures of borazine on a Ag(111) slab. These STM simulations (Figure 3.3 c)) reveal a triangular shape of individual borazine molecules, where the corners and sides of the triangle are attributed to the positions of boron (represented in pink in the model) and nitrogen (blue in the model). The agreement between the simulated STM images and the contrast in the STM data, both showing a triangular outline, indicates a non-dissociative adsorption of borazine molecules on Ag(111) (Figure 3.3 b,c, see discussion section).
Characterization by complementary XPS measurements, shows different binding energies compared to hexagonal boron nitride on Ag(111) [167] and does not indicate (partial) borazine dissociation or decomposition (see Figure A.1).
The calculated triangular shape persists for different packing densities (Figure A.2) and for fcc and hcp adsorption sites (Figure 3.3 c). However, these two distinct adsorption sites yield two configurations that differ by rotation of 60° (and integer multiples thereof) around the C3-symmetry axis of the molecule. In both cases the B-B and N-N axes are aligned with the [1-10] and equivalent Ag(111) directions. Accordingly, we assign the two distinct borazine orientations observed experimentally to fcc and hcp adsorption sites. Calculations for the alternative adsorption sites Figure A.3 yield orientations not compatible to the experimental observations. To highlight the molecular orientation, a pink-colored triangle (with its sides connecting the boron atoms) is superimposed jointly with a structural model on the STM data of a borazine molecule in Figure 3.3 b).
Next, the azimuthal orientation of the borazine molecules in the porous phase is deduced from their triangular-shaped appearance and the depressions at the borders of an island (compare Figure 3.3 a). The characteristic alignment of the borazine molecules with the [1-10] and equivalent directions observed for individual molecules is maintained in this assembly. The twelve molecules in the unit cell (blue rhombus, compare Figure 3.2 b,c) feature two distinct orientations (Figure 3.3 e), marked by blue and pink triangles.
As mentioned above, chiral domains in this porous phase originate from the chiral assembly in the unit cell, featuring a lateral shift of the two triangular unit cell halves. Interestingly, a specific arrangement of borazine molecules is observed within each half of the unit cell. Three molecules of the same orientation are grouped into a triangle and are surrounded by three molecules of the opposite orientation located at the corners of the triangular half unit cell. The borazine orientations are reversed for the respective

other half of the unit cell.
Moreover, adjacent molecules of different orientations are grouped into pairs by shorter intermolecular distance of (6.4 ± 0.5) Å , as highlighted by white ellipses in Figure 3.3 e), compared to the distance to the other molecules that is measured as (7.3 ± 0.5) Å. These pairs represent the building blocks of the assemblies. The lateral offset between the two molecules induces a chiral nature of the pair, which translates to the chirality of the assembly, introduced above. Potential driving forces for the pair formation are addressed in the discussion section.
The unit cell of the porous phase has dimensions of $a_1 = b_1 =$ (25.4 ± 0.5) Å and encloses an angle of $\gamma_1 =$ (119 ± 3)°. Compare also Figure A.4 for a tentative structural model of the assembly and matrix notation [168].
For the dense-packed phase, high-resolution imaging (Figure 3.3 f) reveals discernible repeating units (which we refer to as unit cells) of the two- and three-stripe patterns as illustrated in Figure 3.3 f) with green and yellow frames, respectively. The dimensions of the two-stripe unit cell are $a_2 =$ (12.3 ± 0.4) Å and $b_2 =$ (13.6 ± 0.3) Å with an enclosed angle of $\gamma_2 =$ (87 ± 4)°. Whereas the three-stripe unit cell is spanned by $a_3 =$ (18.4 ± 0.5) Å and $b_3 =$ (13.1 ± 0.2) Å with an angle $\gamma_3 =$ (102 ± 4)°. Similar to the low exposure case, the molecules show distinct orientations relative to the [1-10] and equivalent Ag(111) directions in this phase (Figure A.5).
Additionally, in both stripe patterns the molecules are arranged in pairs by their intermolecular distance, as highlighted by white ellipses in Figure 3.3 h). In particular, the short distances for the two- and three- stripe patterns are (6.1 ± 0.5) Å and (5.7 ± 0.5) Å, respectively. The long distances amount to (7.1 ± 0.5) Å and (7.0 ± 0.5) Å.
The packing densities ρ of the three assemblies are $\rho_{porous} =$ (2.1 ± 0.1) molecules nm^{-2}, $\rho_{two-stripe} =$ (2.4 ± 0.1) molecules nm^{-2}, and $\rho_{three-stripe} =$ (2.5 ± 0.1) molecules nm^{-2}, showing that the striped patterns are denser than the porous structure, in accordance with the preparation.

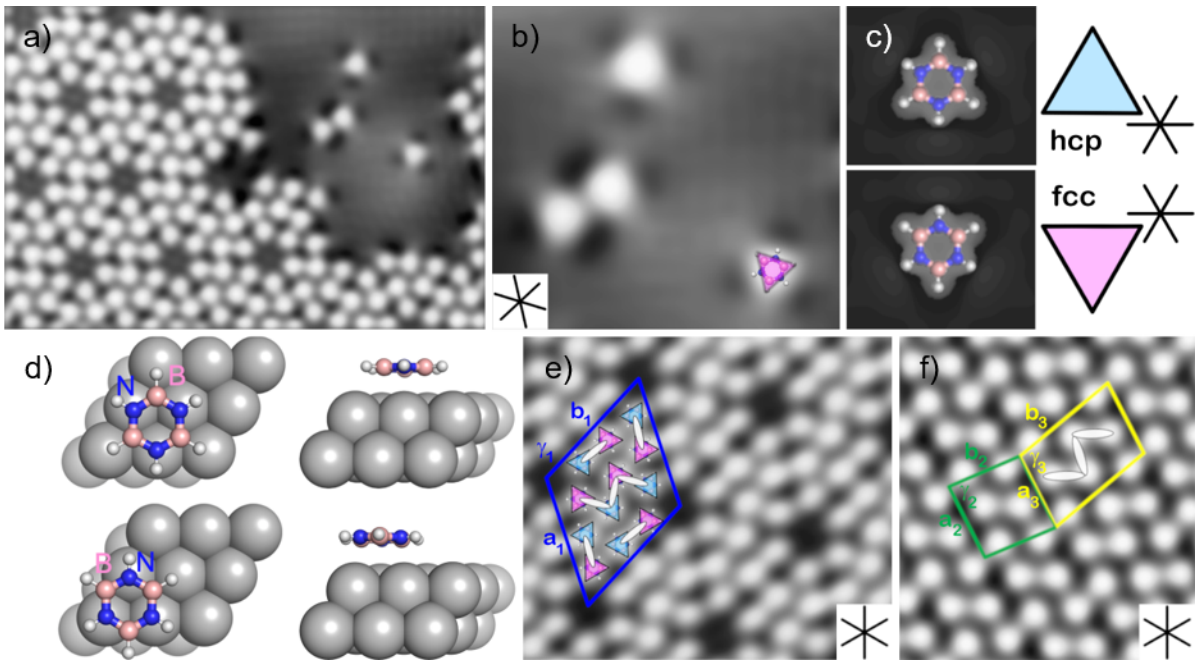

Figure 3.3.: a) High-resolution STM image of individual borazines near a border of a porous assembly on Ag(111). b) Individual molecules appear as triangular protrusions surrounded by three depressions. A molecular model (B: red, N: blue) is superimposed. c) Simulated STM images of borazine molecules adsorbed on fcc and hcp sites of a Ag(111) slab. d) Corresponding DFT-optimized structural models for the fcc (top panel) and hcp sites (bottom panel) with top and side views, respectively. e) The unit cell of the porous phase comprises twelve molecules, gathered into two triangular subunits of six molecules each. The two orientations of borazine are color-coded (blue and pink, respectively), shorter intermolecular distances are highlighted in white. f) The unit cells of the two- and three- stripe patterns are marked by green and yellow frames. Both unit cells involve pairs of molecules with two distinct orientations that are located at their corners and centers. The three-stripe pattern features two parallel pairs in the center of the unit cell, while the two- stripe pattern hosts only one pair. The black crosses in the insets mark the [1-10] and equivalent Ag(111) directions. Imaging parameters: a) 12.7 x 8.6 nm^2, -0.1 V, 0.5 nA b) 4.0 x 3.8 nm^2, -0.1 V, 0.5 nA e,f) 4.6 x 3.0 nm^2, -0.1 V, 0.5 nA g,h) 5.0 x 5.0 nm^2, 0.25 V, 1 nA

The STM data clearly signal an influence of the Ag(111) support on the borazine orientation and position. To understand the interaction of borazine with the substrate, the adsorption energetics of the molecules are addressed by DFT calculations. The analysis of adsorption height and energy for different adsorption sites (Table A.1) reveals that the adsorption energy for borazine molecules on high-symmetry sites is about 0.8 eV at an average distance of 3.3 Å from the metal facet, indicating physisorption. Considering the alignment of the borazine molecules with the [1-10] and equivalent Ag(111) directions in the porous phase, we identify the fcc and hcp sites as the energetically most favorable positions compared to the on-top and bridge sites. However, the differences

observed in the adsorption energies are very small, with the largest deviation being 0.06 eV (see discussion). Accordingly, the occupation of additional adsorption sites (beyond fcc and hcp) can not be excluded for the dense-packed phase (see Figure A.5).

3.2. Electronic Interface Structure

To probe the interfacial electronic structure of borazine on Ag(111), STS measurements and bias-dependent imaging were performed (Figure 3.4 and Figure A.6). A series of STM images of the porous phase recorded at bias voltages between – 1.8 V to + 1.8 V reveals that the appearance of molecules and the contrast of the pores in the assembly are bias-dependent (Figure 3.4 a-e).
At negative sample bias voltages, the pores are imaged as depressions and all molecules appear as single protrusions, which is emphasized at low negative voltages (Figure 3.4 b). At positive sample bias voltage around 0.3 V, the pores appear with a brighter contrast (Figure 3.4 c). Around 0.7 V prominent "connections" occur between distinct molecules (Figure 3.4 d), resulting in a characteristic “z”-like appearance, involving four molecules. The apparent "merging" of these four molecules is correlated with three pairs of molecules with shorter intermolecular distances.
To further address the electronic structure at different parts of the porous assembly, dI/dV spectra are taken above the pores and the center of two selected molecules that exhibit different orientations. The corresponding spectra are shown in black, blue and red in Figure 3.4 f), respectively. At negative bias voltages all three spectra appear featureless, while at positive voltages the spectra reveal electronic resonances at 0.5 V. This characteristic peak is most pronounced in the spectrum measured above the pore and is attributed to confinement of the Ag-derived surface / interface state [169, 170], thus explaining the bright appearance of the pores in the STM images at 0.3 V (Figure 3.4 c). The spectrum acquired above the borazine molecule close to the center of the unit cell (red curve) shows a broad feature in the unoccupied states region with its maximum at 0.98 V. Whereas, for the molecules closer to the pore (blue in Figure 3.4 f) the signal intensity at this energy is decreased. This is also reflected in the molecular appearance in STM images at 0.7 V (Figure 3.4 d), where the molecules closer to the pore feature a lower apparent height than the central ones. Overall, the strongest signature in the STS data is attributed to confinement of the Ag-derived electronic surface/interface state in the pores of the assembly. Borazine electronic states might contribute around 1 and 2 V.

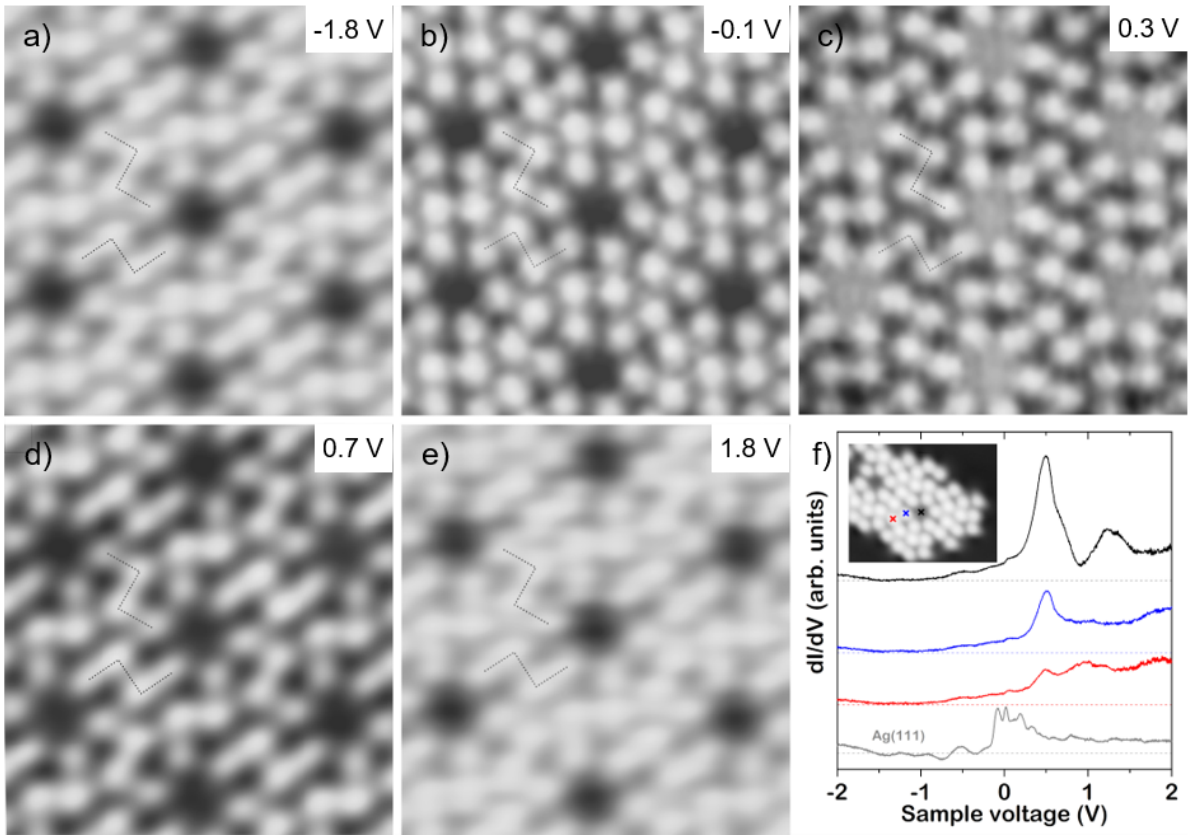

Figure 3.4.: Interfacial electronic structure of the porous borazine phase. a)-e) Bias dependent STM images. At negative sample bias voltage each molecule appears as a single lobe. Around 0.3 V, the pores appear "filled" c), which correlates with the main peak in the corresponding spectrum f). Around 0.7 V, the lobes appear connected, leading to a “z”-shape contrast comprised of four molecules d) that persists at higher voltage e). f) Scanning tunneling spectra recorded at the pore and above two selected positions of molecules in the assembly are marked with black, red and blue crosses respectively. A reference spectrum on bare Ag(111) is provided for comparison. The spectra are vertically offset for better visibility, dashed lines mark the respective zero intensity. Imaging parameters: a) 5.7 x 6.0 nm^2, 0.3 nA b) 5.7 x 6.0 nm^2, 0.3 nA c) 5.7 x 6.0 nm^2, 0.2 nA d) 5.7 x 6.0 nm^2, 0.3 nA e) 5.7 x 6.0 nm^2, 0.3 nA f) 7.6 x 6.0 nm^2 -2.0 V, 0.21 nA.

3.3. Modification of the Adsorption Configuration by Single Molecule Manipulation

So far, we demonstrated the "flat" adsorption configuration of pristine borazine on Ag(111), both in assemblies and for individual molecules. Considering the different adsorption behavior reported on other substrates (see above), we venture to demonstrate that even on Ag(111), tilted adsorption configurations can be achieved. To this end, we

focus on individual borazine units as a model system.
Application of voltage pulses to individual molecules reproducibly results in distinct modifications in contrast, symmetry and apparent height of the molecules (Figure 3.5, A.7). These changes can be accompanied by translational and rotational movements. Figure 3.5 summarizes the manipulation sequence and the properties of one characteristic product.
The STM images in Figure 3.5 a) and c) show the very same area of the Ag(111) surface including one borazine molecule, before and after applying a voltage pulse (2.5 V, 5 s) near a boron position of the molecule (position marked in Figure 3.5 a). The current-time trace (Figure 3.5 b) recorded during the voltage pulse shows discrete steps, pointing to several sequential processes during the manipulation (such as chemical modification and displacements). Upon manipulation, the borazine molecule changed its appearance from the characteristic threefold symmetric contrast (discussed above) to an elongated shape featuring a bulge on one side.
Additionally, the apparent height is increased from 0.7 Å to 1.9 Å (see inset in Figure 3.5 a) and the molecule is displaced laterally. The long axis of this bulge-shaped manipulation product is aligned with one of the [1-10] and equivalent Ag(111) directions. This preferred alignment is visualized in the image sequence shown in Figure 3.5 d-f), displaying rotation and further translation of this manipulation product.
First, a voltage pulse leads to rotation (d $\rightarrow$ e). A subsequent pulse then results in a combined rotation and translation (e $\rightarrow$ f). After each step the product retains its characteristic appearance and its alignment with the primary crystal directions. Such movements can be triggered by voltage pulses up to 3 nm away from the affected molecule, indicating a remote effect on the dynamics of the manipulation product either by the electric field between tip and sample or by hot electrons. No modifications were observed for bias voltages below 2.5 V, consistent with non-perturbative STM imaging at such voltages (see Figure 3.4).
In order to identify this characteristic manipulation product, DFT simulations were performed for various B- and N-terminal dehydrogenated (Figure 3.5, Table A.2 , Figure A.8) and deprotonated borazine fragments (Table A.3 , Figure A.9) as well as for doubly dehydrogenated borazine species (Table A.4 , Figure A.10) on distinct adsorption sites of the Ag(111) surface.
For the B-terminal, single dehydrogenated species adsorbed on the fcc (Figure 3.5 g) and hcp (Figure 3.5 h) sites, the simulated STM images are in good agreement with the experimental observations. Notably, the alignment with the crystal directions and the elongated, rod-like appearance with a bulge are reproduced. None of the other configurations matches the experimental observations well (Figures A.8 - A.10), the B-terminal adsorption sites are preferred over the N-termination (Tables A.2 , A.3). Thus, the manipulation product is assigned to such an upright standing, singly dehydrogenated borazine molecule, exposing a B atom to the Ag support.
The increase of the apparent height in STM images upon manipulation is consistent with an upright standing geometry. The calculated adsorption energy at the fcc and hcp sites is nearly identical for this singly dehydrogenated B-terminal species (see Table A.2), pointing to the possible occupation of fcc and hcp sites.

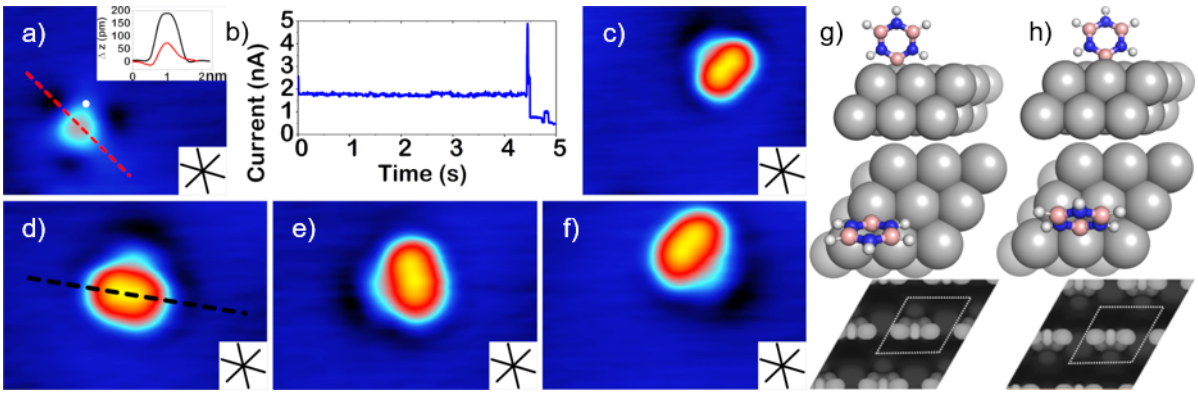

Figure 3.5.: Manipulation of single borazine molecules. The voltage pulse of 2.5 V applied to an isolated borazine molecule at the position marked with a white dot a) causes a drastic change in the molecular appearance c). The corresponding current-time sequence recorded during this process reveals several intermediate steps b). The resulting manipulation product exhibits an elongated shape oriented along one of the [1-10] and equivalent Ag(111) directions. The apparent height changes from 0.7 Å to 1.9 Å, shown by the line profiles in inset in panel a). Subsequent voltage pulses result in translation and rotation of the manipulation product d-f), maintaining the alignment with the crystal high symmetry directions. The STM images a,c) and d-f) show the same region of the surface respectively, illustrating the translational part of the movement. DFT simulations of a tilted, B-terminal dehydrogenated borazine molecule adsorbed on fcc (g, top) or hcp (h, top) sites, and the corresponding calculated STM signatures at -0.1 V (g-h, bottom) match the experimental observations of the manipulation product. The dashed rhombi represent the sections of the top panels. Black crosses in the insets mark the [1-10] and equivalent Ag(111) directions. Imaging parameters: a), c) 2.9 x 2.5 nm^2, -0.1 V, 0.5 nA, z-scale 0.0-1.9 Å d-f) 2.7 x 1.9 nm^2, -0.1 V, 0.5 nA, z-scale 0.0-1.9 Å.

3.4. Discussion

We first discuss the adsorption behavior of borazine. The STM data complemented by an XPS analysis and STM image simulations show that borazine adsorbs intact on Ag(111) at low temperatures, with the plane of the borazine molecule parallel to the Ag surface (i.e., flat). This is not unexpected, as even on more reactive (111) surfaces, dehydrogenation only starts at elevated temperatures (e.g., ≈ 300 K for Ni(111)[23]). The "footprint" of one borazine derived from the molecular areal density of the dense-packed assemblies amounts to about 42 $Å^2$, closely matching values reported for the flat adsorption of intact borazine on Ru(0001) (41.3 $Å^2$) [11] and clearly exceeds the 18.5 $Å^2$ deduced for tilted, dehydrogenated borazine on Pt(111)[11]. This corroborates a non-dissociative, flat adsorption, which thus seems characteristic for rather inert supports (such as Au and hBN) [145, 146]. In contrast to several other metal supports (including Rh(111), Ir(111), Pt(111)), we did not observe a combination of flat and upright

adsorption configurations on Ag(111) for intact borazine in the achieved coverage range. In this study, the self-assembled borazine structures are formed on Ag(111) by adjusting the borazine dose at substrate temperatures below 150 K. After warming up to room temperature, borazine completely desorbed from Ag(111), consistent with the absence of borazine after room temperature exposure. On Pt(111) [146] and Au(111) [146] a multilayer desorption routine in the temperature range 135 K to 150 K was applied to achieve monolayers of borazine. Thus, similar - and low - temperatures are needed to adsorb intact borazine on these different unreactive metal supports.

The STM data demonstrate two distinct azimuthal orientations of intact borazine on the Ag(111) lattice, which are identical for individual borazine species and molecules constituting the porous self-assembled structure. As borazine shows a triangular appearance in high-resolution STM images, these two orientations are represented by triangles pointing in opposite directions. Individual borazines on Ag terraces and molecules at borders of islands exposing a side of triangle to the bare Ag areas show distinct depressions in STM images recorded at low bias voltage. These depressions are tentatively attributed to electron density depletion near the N-H positions, due to the localization of negative charge at the nitrogen atoms, reminiscent of earlier STM findings on molecules featuring terminal N on Ag(111) [171]. This STM contrast is thus consistent with the assignment of the N positions of the borazine ring to the sides of the apparent triangle. The STM image simulations do not reproduce the depressions near the molecules, which we attribute to limitation of the modeling approach (e.g., s-wave tip character) in properly describing localized electronic features.

A precise evaluation of the molecular positions and intermolecular distances in the porous honeycomb phase (see Figure 3.3 b) and Figure A.4) reveals that borazines occupy two different adsorption sites of the Ag(111) lattice. These two adsorption sites are reflected in the two opposite borazine orientations. A statistical analysis of 138 individual molecules reveals an fcc:hcp ratio of 59:41 between the two orientations, whereas in the islands the orientations of the molecules are equally distributed (50:50). By comparison to the DFT calculations, we assign the two adsorption sites to configurations with the center of the borazine ring on fcc and hcp hollow sites, respectively. Whereas the calculations for other symmetric adsorption sites, such as on-top or bridge, yield similar adsorption energies (compare Table A.1) the alignment of the triangular outline of the borazine with the [1-10] and equivalent Ag(111) direction observed in the STM data matches only the two hollow sites. In both adsorption configurations, the nitrogen atoms (colored blue in the model) are located (roughly) on-top of Ag atoms (see Figure 3.3 d). Such a configuration with nitrogen above on-top and boron above hollow sites is known as stable configuration for hBN on Ni(111) [172] and predicted to be the favorite registry for hBN on other transition metals [173, 174]. For Ag(111), however, hBN is calculated to be repelled even in this configuration [167] and to be only weakly bonding in a rotated 2 x 2 hBN unit cell [174]. Experiments indeed do not reveal preferred azimuthal orientations of hBN domains [167]. Accordingly, our findings for individual borazines and self-assembled borazine films on Ag(111) reveal an adsorption behavior distinctly different from hBN/Ag(111) [167].

The calculated adsorption energies for borazine on Ag(111) confirm a weak adsorption,

and do not suggest considerable site-specific interactions between individual borazine and Ag(111). Nonetheless, the STM imaging revealed an important role of the substrate, inducing two distinct adsorption sites / orientations, yielding the intricate honeycomb network. Also, the assembly into striped arrays reveals distinct molecular orientations. A common feature of these assemblies is the grouping of molecules into apparent pairs with short intermolecular distance, which originate in the two coexisting adsorption configurations. In the porous case, two adjacent pairs appear as z-shape, while for the dense-packed cases, the pairs appear as separated dimers or z-shaped structures (see Figure 3.3 e,f). Computational modeling of isolated borazine dimers was reported to yield several minima in the potential energy landscape, including a configuration with laterally displaced borazines in an antiparallel alignment and a center-to-center distances of 6.5 Å (not representing the global minimum in gas phase, though) [175, 176]. Electrostatic interactions emerging from the polar BN bonds might contribute to stabilize the on surface-assemblies. Due to the short H···H distances, dihydrogen bonding was recognized to stabilize these configurations [175, 176]. With such pair geometries being similar to the ones observed in our experiments, dihydrogen bonding - rather unusual in literature - might contribute to stabilize the on-surface assemblies.

Interestingly, the transition from the porous assembly to the dense-packed phases follows a different scheme than previously reported for other C3-symmetric molecules [166], where honeycomb assemblies with an increasing number (N) of molecules along the side of the triangular subunits were formed upon increasing the coverage. Here, only a single honeycomb-like pattern (with N=3) is observed for all borazine exposures resulting in the porous phase. The arrangement of the molecules in two chiral domains in the porous phase resembles indeed reported chiral assemblies of other C3-symmetric molecules [165, 177, 178]. The lateral shift between the triangular subunits can be used to categorize the assemblies. A shift of a complete triangle would result in a Kagome-lattice, while no shift would yield a perfect honeycomb lattice. The present porous borazine assembly is thus recognized as an intermediate structure between a Kagome and honeycomb lattice, labeled honeycomb-like.

The porous borazine assembly leads to surface state confinement effects in the pore areas exposing bare Ag, thus tailoring the surface electronic landscape [169]. The electronic signature of the pores persists in spectra recorded above adjacent borazines, indicating a weak interaction of the pristine molecule with the metal. Contributions from an electronic interface state in borazine covered areas are not evident in our STS data. In contrast, an interface state was observed for borazine derivatives on Cu(111) and Ag(111), which were functionalized to reduce molecule - substrate interactions and to promote network formation [161]. An interface state slightly upshifted from to the pristine Ag(111) surface state was also reported for hBN/Ag(111) [179]. The apparent absence of borazine-derived electronic states near the Fermi level and down to binding energies of at least 2 eV (i.e., - 2V sample voltage, see Figure 3.4 f) is consistent with photoemission results of borazine on Pt(110) [147].

We now proceed to address the characteristic product achieved by STM manipulation of individual borazines, briefly expanding on the results obtained by DFT. Spin-polarized calculations were performed for a neutral borazine-fragment and an anionic borazine-

fragment adsorbed on different positions of a 3x3x3 Ag(111) supercell. Different adsorption sites (on-top, fcc, hcp, bridge) in a B-terminal or N-terminal configuration were screened for a dehydrogenated/deprotonated reaction product (Figures A.8 - A.10).
In agreement with previously reported studies of a dehydrogenated borazine reaction product on Pt, the B-terminal adsorption site is preferred over N-terminal [147]. No stable adsorption position in the N-terminal studies apart from on-top was obtained. In conjunction with the experimental evidence for alignment along the [1-10] and equivalent Ag(111) directions and the asymmetric appearance in STM imaging (rod-like shape with a bulge on one side), the manipulation product is identified as a singly dehydrogenated B-terminal borazine. It adsorbs upright with a minor tilt and might occupy fcc and hcp sites (see Figure 3.5 g,h). Other adsorption configurations including deprotonated and ortho- and para-doubly dehydrogenated borazine molecules on various adsorption sites do not provide a better match with the experimental findings (see discussion in the Appendix, Figures A.8 - A.10, Tables A.2 - A.4).
While this singly dehydrogenated upstanding borazine fragment was achieved reproducibly from pristine borazine and could be rotated and laterally transferred by STM manipulation, STM allows one to induce and detect additional states. On the one hand, an intermediate, flat configuration was observed (see Fig. A.7). On the other hand, additional voltage pulses can yield additional products, presumably inducing multiple dehydrogenations or even decomposition of the $(BN)_3$ ring. An identification and classification of all potential products is beyond the scope of this work. However, we envision further studies aiming for the construction of distinct nanoscale h-BN aggregates exclusively by STM manipulation of borazine, e.g., by promoting intermolecular bond formation, to be rewarding.
Finally, the structural analogy of the 6-membered ring in borazine to the well-studied benzene molecule [180–183] allows for a comparison of these two systems. Benzene molecules adsorb in a flat geometry on (111) facets of coinage metal substrates, including Ag, at the hcp-hollow sites [184]. The effective surface area for intact benzene was estimated to about 50 $Å^2$ [141], which is close the value we deduced from the striped borazine phase (42 $Å^2$). The azimuthal orientation of benzene on Ag(111) is fixed such that a superimposed triangle with corners at every other C atom is aligned with the [1-10] and equivalent crystal directions [182], analogous to the alignment of the B-B axes in the case of borazine on Ag(111).
The adsorption position of benzene can be controlled by introducing functional groups with either electron donating or withdrawing effect [182], a strategy that also might be applicable to functionalized borazines.
The adsorption height of benzene on Ag(111) amounts to 3.04 Å [184]. The theoretical value derived in this study for borazine (3.26 Å) is slightly larger, but both findings are consistent with a physisorption character of benzene and borazine on Ag(111).
Dehydrogenation of benzene via voltage pulses with an STM was achieved on Cu(100) [185, 186]. The benzene manipulation product was identified via inelastic electron tunneling spectroscopy and DFT simulation as C_6H_5 fragment and shows an increased apparent height and a symmetry reduction in STM imaging. These findings were rationalized by a transition from a flat benzene adsorption geometry to an upright standing

configuration upon dehydrogenation, similar to the case of borazine dehydrogenation introduced in this work.

3.5. Conclusions and Outlook

We provide a detailed real space characterization of individual borazine molecules on a solid support and demonstrate the self-assembly of distinct, highly ordered borazine architectures on Ag(111). With increasing exposure, a chiral, porous honeycomb-like network and dense-packed, striped arrays are achieved. Borazine is shown to adsorb non-dissociative with its ring aligned in parallel to the surface. The low temperatures ($< \approx$ 150 K) requested for adsorption, STS revealing the surface state, and the small calculated adsorption energies signal a weak interaction of pristine borazine with Ag(111).
Nonetheless, distinct adsorption sites (fcc and hcp hollow) are determined by our combined STM and DFT approach. With the N atoms consistently residing near on-top sites of the Ag(111) lattice, these two adsorption sites result in two distinct azimuthal borazine orientations.
Furthermore, controlled dehydrogenation of single borazine molecules by STM manipulation using voltage pulses is demonstrated. The resulting borazine fragment features an upright standing adsorption geometry, corroborated by DFT calculations.
Our results elucidate the characteristics of pristine borazine adsorbed on Ag(111) and thus provide a reference system for many advanced BN-doped interfacial systems, including surfaces patterned by functionalized borazines or graphene-like systems incorporating $(BN)_3$ units. Additionally, the controlled dehydrogenation demonstrates a single molecule level access to the multi-facetted chemistry of this seemingly simple molecule, opening prospects for the controlled, sequential synthesis of nanoscale hBN aggregates by STM manipulation protocols.

4. Adsorption of Molecular Motors and Torque Measurements on Double-Decker Molecules

The potential applications of "tiny machines" were already anticipated in Richard Feynmans visionary talk "plenty of room at the bottom" in 1959 [187]. Nowadays, in the broad field of nanotechnology examples are found where the interpretation of "tiny" is pushed even to the single atom level [38]. Considering the term "machines" molecular motors feature sizes of tens of atoms [188, 189]. This particular research field around molecular motors gained considerable public interest with the Nobel Prize in Chemistry 2016 awarded to Jean Pierre Sauvage, Sir J. Fraser Stoddart and Bernard L. Feringa for the "design and synthesis of molecular machines" [190].
The term molecular motors encompasses a broad spectrum of definitions among different length scales and purposes of the motor. The common property is that the molecular motors "harness various energy sources to generate unidirectional mechanical motion" [189].
In particular the Feringa-type motors [191] are an important class of molecules. They feature an unidirectional rotation triggered by light. A promising aspect to take advantage of these light-driven molecular motors is to fix them on a surface [192]. Energy can be readily supplied to the motors by illumination, avoiding the problem of electrically contacting each molecule. Furthermore, since one part of the molecule is fixed on the surface, the performed work achieved by relative motion within the molecule might be possible to harness [193].
Here, we investigate a hemithioindigo motor molecule specifically designed for adsorption on surfaces [96]. The hemithioindigo motor molecules feature sulfur based anchoring groups, rationalizing the choice for a Au(111) support. For comparison, Ag(111) as a substrate is also explored. Previous experiments showed that protective groups at the sulfur positions can be cleaved by thermal activation, resulting in clusters of motor molecules. In these clusters the motors adapt a flat lying geometry, unfortunately hindering the movement of the rotor part. The first section of this chapter describes efforts to isolate motor molecules in unrestricted adsorption geometries via means of self-assembly and covalent organic framework templates.
Ultimately, the motor molecules are designed to have their motor unit rotate in an azimuthal configuration. While this is challenging for the Feringa-type motors [194, 195], it is readily accessibly for molecules featuring a double-decker geometry [77, 81, 196]. Thus, to gain insights into quantitative aspects such as torque measurements, we

shift our focus in the second section of this chapter to double-decker systems.
Adapting a method used to measure forces required to move single atoms across a surface [52], we employ nc-AFM to acquire the torque required for rotation. Porpyhrin-based double-decker system have already been successfully rotated by lateral manipulation using an STM tip [81, 196]. However, for a quantitative analysis via AFM, these system are not suitable, due to inherent steric interaction of upper and lower moieties of tetraphenylporphyrin based double-deckers. A more rigid and decoupled system is employed by using naphthalocyanine based double-deckers. The naphthalocyanine moieties offer a planar building block, aimed at minimizing the steric interaction between the two double-decker halves. Furthermore, a large metal atom, namely Thorium, is also used to minimize the steric hinderance between the bottom and top half of the double-decker molecules. Preparing the isolated double-decker molecules on surfaces via direct evaporation of the double-decker molecules is experimentally challenging. Studies which use thermal evaporation to sublime the double-deckers onto the sample frequently report dissociated species [197–200]. Since naphthalocyanine (NPc) molecules evaporate at 485°C in UHV, decomposition of potential double-decker species during sublimation experiments of these double-deckers is likely. Consequently, we turn towards methods of on-surface synthesis to prepare Thorium-Naphthalocyanine (Th(NPc)2) double-deckers. Adaptation of on-surface synthesis protocols from other phthalocyanine- and porphyrin-based double-decker species [81, 196, 201] are promising to solve challenges inherent to a double-decker system designed for rotation experiments. Preparation with these protocols result in a dense-packed layer of the participating phthalocyanine/porphyrin species with islands of double-decker species. Isolated double-deckers and multi-decker sandwich complexes were also observed. The dense packed bottom layer is a particular interesting feature, since it is likely to prevent rotation of the lower half during rotation experiments on top half of the double-decker species.
The second section of this chapter addresses quantification of rotational movement. A model system, Th(NPc)2 double-deckers, is successfully prepared via on-surface synthesis and subsequently investigated via non-contact atomic force microscopy. The rotation of the top NPc unit is probed via lateral manipulation with the tip. For a modified double-decker species, a lower limit for the necessary torque is determined.
A sketch of the investigated systems in this chapter, and their anticipated rotation, is shown in Figure 4.1.

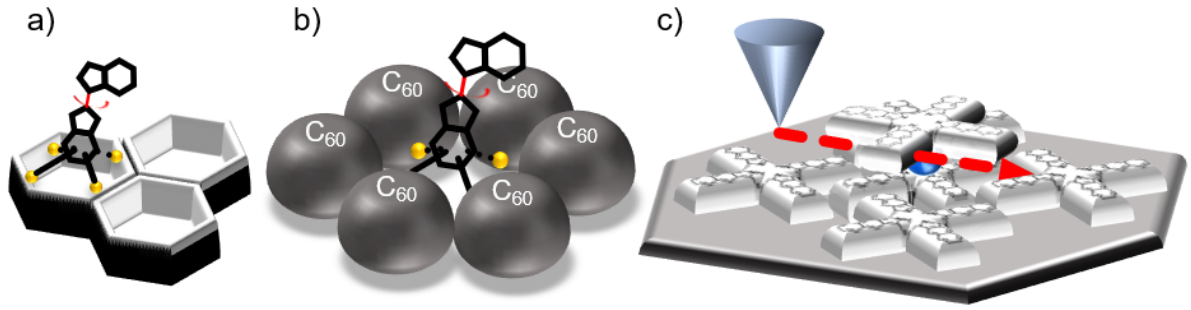

Figure 4.1.: In the first part of this chapter an upright standing geometry of molecular motors is targeted via a porous organic network (a) and supramolecular assemblies (b). The top half of the molecule is rotatable around the C-C double bond marked in red. The second part discusses tip-induced rotation of double-decker molecules and the quantification of the related torque via AFM. Panel c) shows a sketch of a double-decker molecule embedded in a dense packed layer of cross-shaped molecules.

4.1. Hemithioindigo Motor Molecules on Surfaces

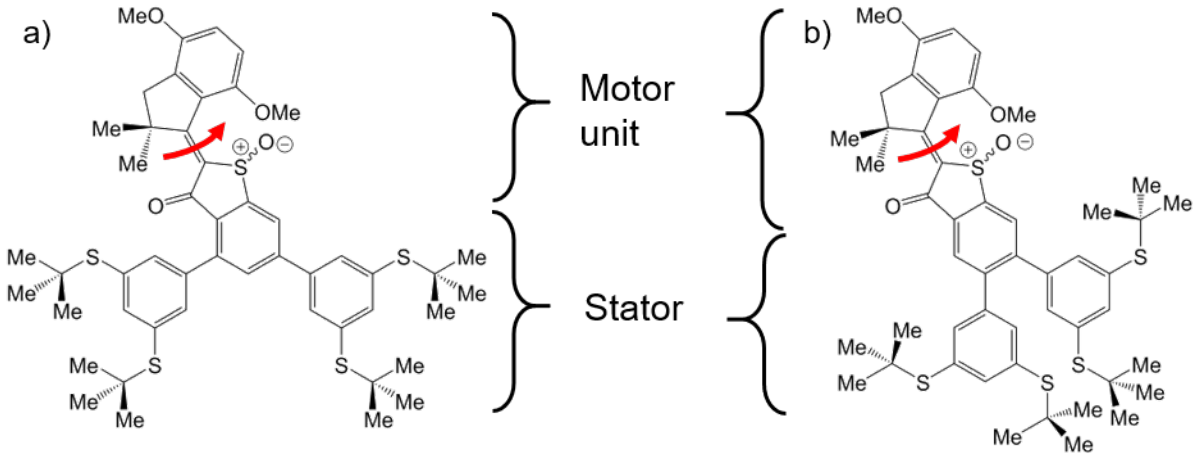

Figure 4.2.: Structure of motor 1 a) and motor 2 b). Motor 2 features a vicinal position of the anchoring groups at the central phenyl ring. The red arrow mark the rotation direction of the top motor unit around the rotatable C-C double bond.

The appearance of motor molecules, referred to as motor 1 and motor 2, in STM measurements is documented in a previous PhD study [129]. A brief summary of this collaboration is given here. The structure of both molecules is shown in Figure 4.2, each featuring a motor unit and a stator part. The unidirectional motion of the motor part is indicated by red arrows [202, 203]. Both molecules are drawn in the Z configuration, where the methoxygroup is located on the same side like the sulfoxide group with respect to the C-C double bond relevant for rotation. The anchoring groups, so-called "feet",

in the stator unit feature sulfur groups. These groups are known for a strong interaction with the surface, in particular after cleaving the t-butyl groups [204]. Both motor molecules adsorb in a flat adsorption configuration on metal substrates, as summarized in the following section. This geometry stands in contrast to the desired standing upright configuration needed for azimuthal rotation of the rotor unit. A reason for the flat-lying adsorption of motor 1 molecules was found in their structure. The phenyl groups in the feet can rotate into a plane with the phenyl group of the hemithioindigo-resembling moiety, leading to a large planar subunit of the molecule. This configuration where the three phenyl groups are in the same plane is also sketched in the structure in Figure 4.2 a).
In the motor 2 molecules this issue is addressed by a vicinal arrangement of the feet in the stator unit. This arrangement is anticipated to increase steric hindrance between the phenyl groups in the feet due to the proximity of the hydrogen atoms. Therefore an out-of-plane configuration of the phenyl groups is expected which in turn facilitates an upright standing adsorption geometry.
The adsorption of motor 1 on Ag(111) and Au(111) is investigated via LT-STM and shown in Figure 4.3. Image a) shows a single molecule after deposition at room temperature and an overlay of the molecular model. The STM signature exhibits four bright lobes and a less intense feature in the top left corner. Comparing the STM-topograph with a model, indicates an adsorption-geometry with all phenyl rings parallel to the surface, resulting from a flat-lying configuration of the molecule. The four bright lobes are assigned to the position of the butyl groups.
Annealing to 200 °C induces a change in the molecular appearance as shown in Figure 4.3 b). The molecules now feature a single protrusion and assemble in ordered islands. A molecular model without the butyl groups matches the dimensions of the observed contrast in STM. The molecules remain in a similar flat lying geometry as described above. The protrusion observed within each molecule is attributed to the methyl group in the motor unit. The apparent height of the molecules is below 0.5 nm, corroborating a flat adsorption configuration.
The right column in Figure 4.3 displays the results of motor 1 molecules on the Au(111) substrate. Image 4.3 c) shows an isolated motor 1 molecule after deposition on the substrate held at room temperature. The molecule exhibits a similar contrast as on Ag(111), indicating a comparable flat adsorption geometry. The effects of annealing to 200 °C are depicted in panel 4.3 d). The molecules now form chain-like structures with individual protrusions. A comparison with the molecular model yields similar conclusions as before. The butyl groups are cleaved from the sulfur positions and the molecule adsorbs flat with the protrusion assigned to the methyl groups in the motor unit.

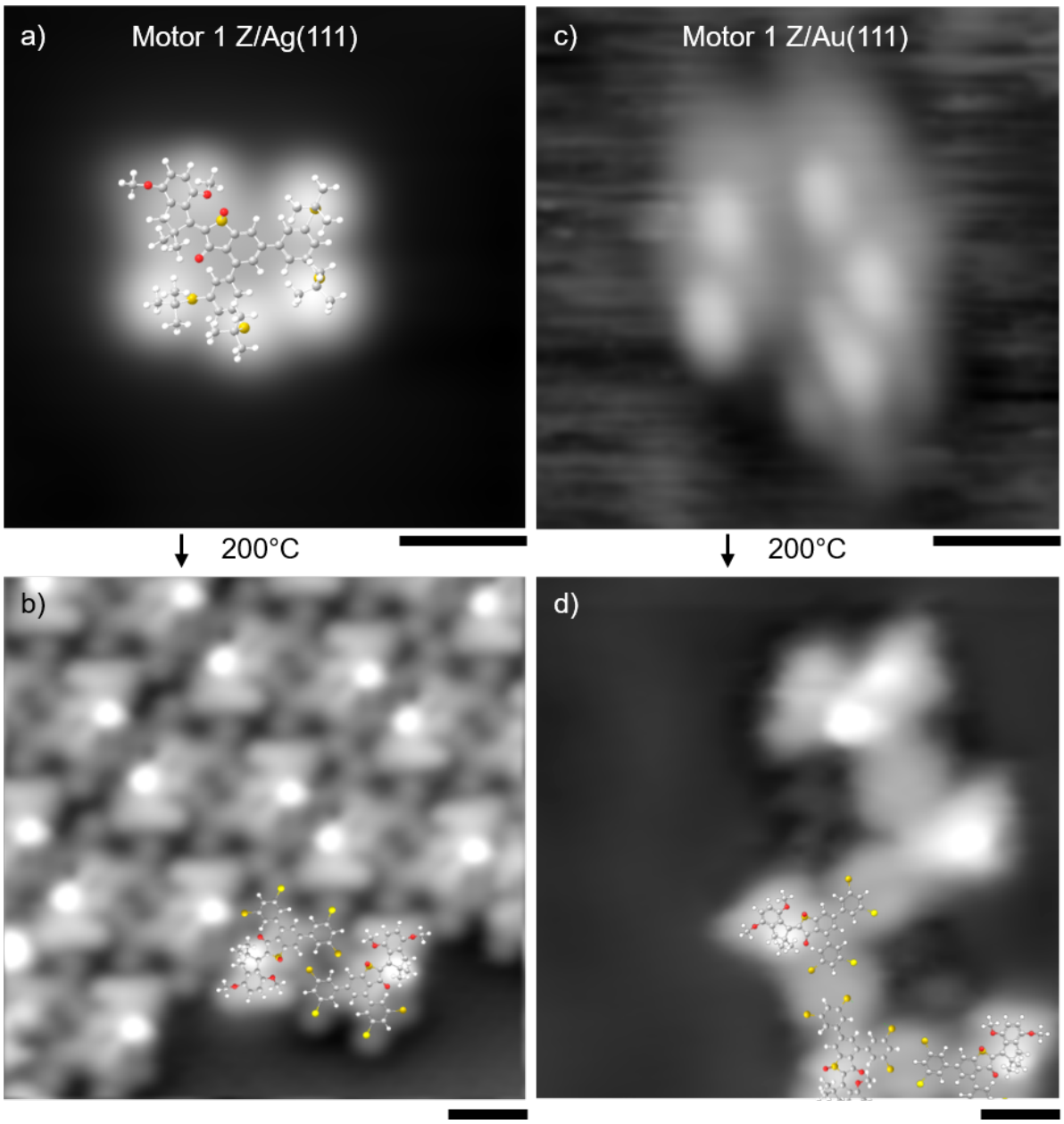

Figure 4.3.: STM images of Motor 1 Z deposited on Ag(111) and Au(111) at room temperature and after annealing to 200 °C, respectively. a) Motor 1 after deposition at room temperature on Ag(111). A molecular model is overlayed. The four bright protrusions are assigned to the position of the butyl groups, indicating a flat lying geometry. b) Annealing to 200 °C leads to island formation. A molecular model with the butyl groups removed from the anchoring groups is shown. c) Motor 1 after deposition at room temperature on Au(111) shows similar contrast as on Ag(111). d) The molecules form chain structures on Au(111) after annealing to 200 °C. Imaging parameters, scale bar: a) 0.15 V, 400 pA, 1 nm; b) -15 mV, 100 pA, 1 nm; c) 1.0 V, 100 pA, 1 nm; d) -59 mV, 55 pA, 1 nm. Figure adapted from Ref. [129]

The results of depositing motor 2 with the modified position of the anchoring groups are presented in Figure 4.4. On Ag(111) the motor 2 Z molecules feature a bright protrusion (Panel a). Overlay of a model suggests that it is related to the upstanding butyl groups of the anchoring groups. The left and right molecule can't be transformed into each other by rotation. The difference stems from the two orientations, Z and E, of the motor unit in the molecule. Prior to evaporation the molecules are in the Z configuration, however isomerization during sublimation is possible.
Heating to 200 °C induces disordered island structures. Since the butyl groups in motor 2 are bound in a similar way as in motor 1, they are predicted to separate from the anchoring group at this temperature.
Images 4.4 c) and 4.4 d) show the results of the corresponding experiment on Au(111). After adsorption at room temperature, different configurations exist with several protrusions. These configurations are assigned to different stacking of the butyl groups. For both cases the molecular model fits the experimental data in a flat-lying configuration. After cleaving the butyl group, trimer-like structures are observed.
The apparent height of the molecules for all four combinations of motor 1 and 2 on Ag(111) and Au(111) is lower than 0.5 nm, suggesting a flat-lying adsorption [205]. On some motor 2 molecules on Au(111) are mobile during scanning and variations in the contrast occur. These changes are tentatively attributed to different configurations of the methyl groups in the feet. Restricted switching of E/Z configuration is also possible.

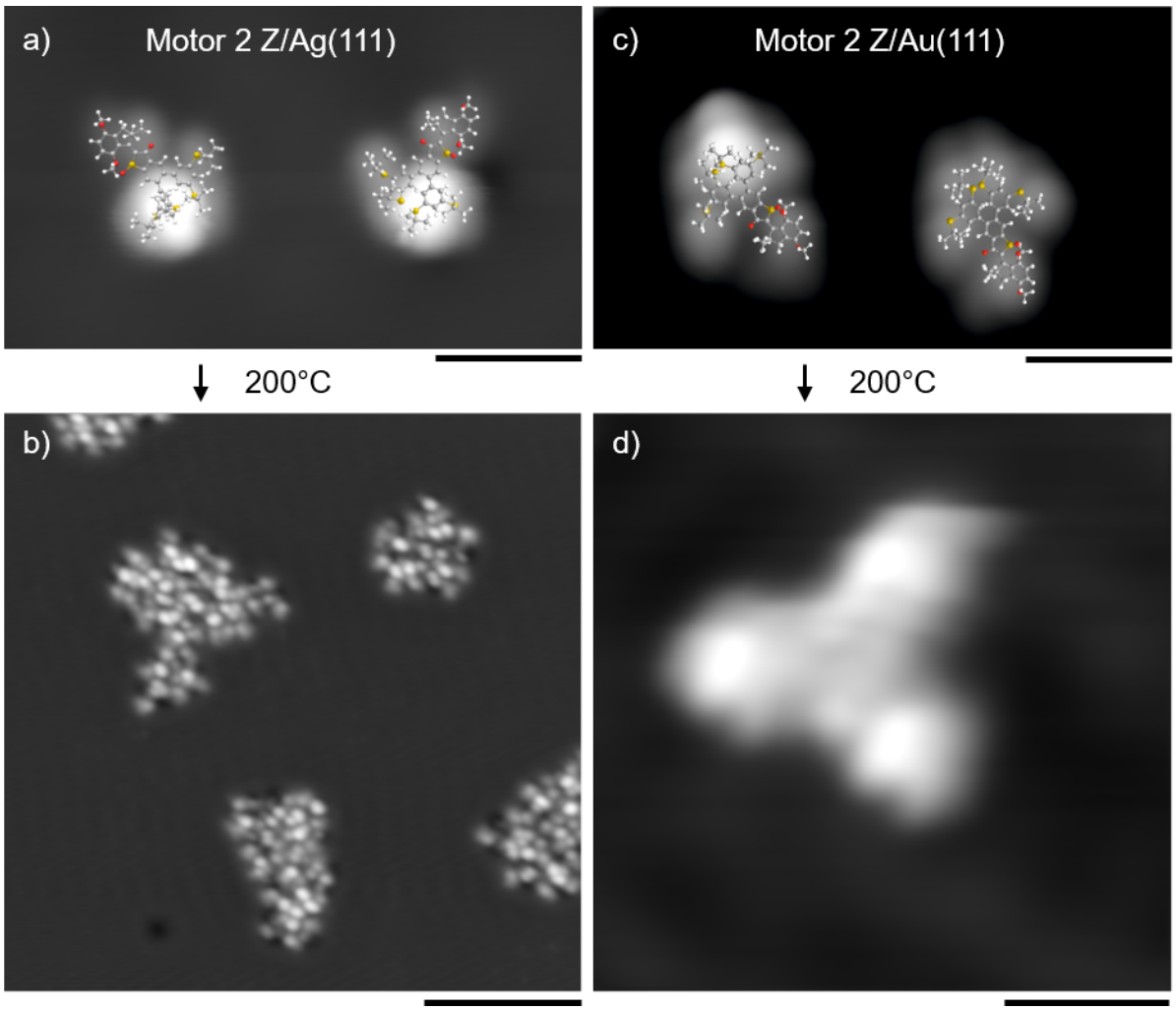

Figure 4.4.: STM images of motor 2 Z deposited on Ag(111) and Au(111) at room temperature and after annealing at 200 °C, respectively. a) Motor 2 adsorbs in two configurations on Ag(111). In both cases the bright protrusion is assigned to the butyl groups. b) Annealing at 200 °C results in agglomerates containing molecules of different apparent height. c) Motor 2 Z molecules were adsorbed at room temperature on Au(111). d) Heating to 200 °C leads to formation of trimer-like structures. Imaging parameters, scale bar: a) 0.05 V, 91 pA, 2 nm; b) 0.25 V, 67 pA, 10 nm; c) 0.33 V, 140 pA, 2 nm; d) 0.05 V, 58 pA, 2 nm. Figure adapted from Ref. [129]

4.1.1. Interaction with Molecular Assemblies

In order to achieve an upright standing adsorption configuration, we aim for a system with C_{60} molecules as a spacer, similar to self-assembled structures of a comparable motor and spacer system [195]. Figure 4.5 shows a comparison of the motor 1 and C_{60} molecular models. The plotted van der Waals radii suggest that in a mixed assembly of upright standing motor molecules and C_{60} molecules, the motor unit is still free to

rotate. Furthermore, the rather bulky C_{60} molecules are chosen to facilitate intermolecular interactions between the C_{60} and the lower, fixed unit of the motor molecules. Note that motor 2 features similar dimensions as motor 1, see also Figure A.11.

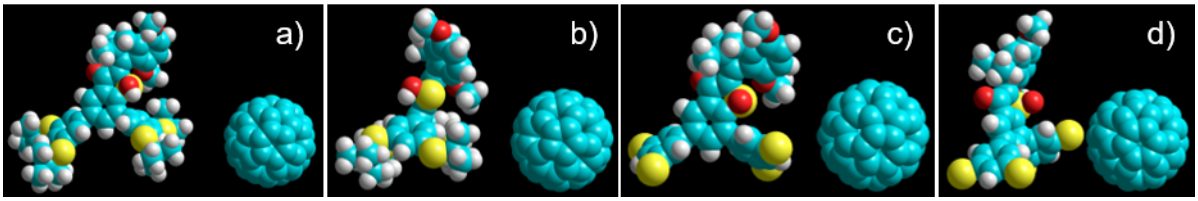

Figure 4.5.: Front and side view comparison of motor 1 and C_{60} van der Waals radii. a,b) Motor 1 with butyl groups and C_{60}. c,d) Motor 1 without butyl groups and C_{60}. Models are created with the Hyperchem 8 software package.

The experiments are based on the annealed motor 1/Ag(111) system. Figure 4.6 shows the results of adding C_{60} molecules. Upon deposition at room temperature the C_{60} molecules form separated islands (yellow arrows). The motor 1 molecules (red arrows) remain in assemblies similar as seen in Figure 4.3 b). The C_{60} islands feature molecules of different contrast, related to the respective rotational orientation and adsorption site of C_{60} [206]. The zoom-in image 4.6 b) at the border region between the two islands reveals that the motor molecules exhibit a lower apparent height than the C_{60} island. In order to exclude coverage dependent effects, where free Ag(111) still allows the species to diffuse into separated islands, a high coverage system is also investigated. Figure 4.6 c) and 4.6 d) show the corresponding results after dosing additional C_{60} molecules. Both species continue to assemble in separated islands. Some C_{60} molecules are located within the motor islands and exhibit a more blurred contrast compared to the molecules in the C_{60} island. The motor molecules appear with the same signature as without the C_{60} molecules. No indication for upright standing motors is found.

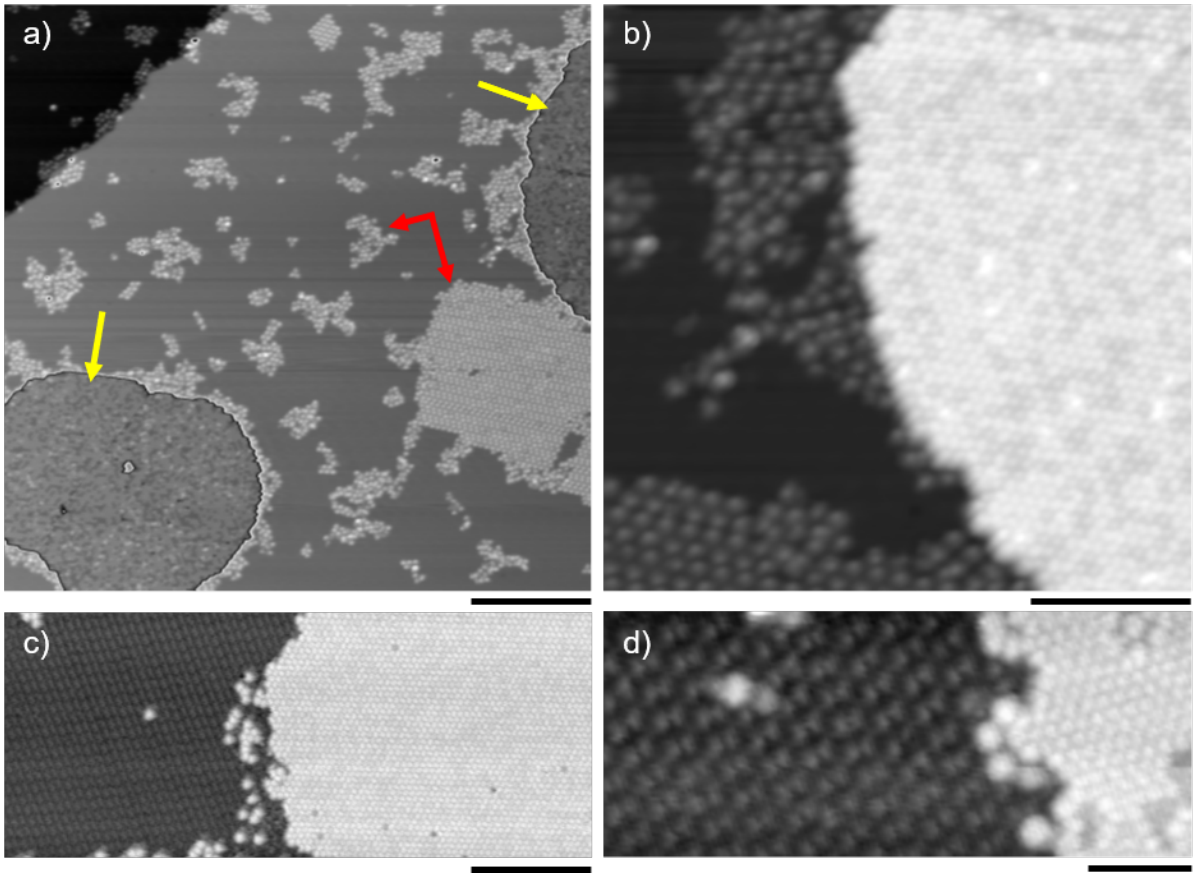

Figure 4.6.: STM images of C_{60}/motor1/Ag(111). a) C_{60} molecules (yellow arrow) and motor 1 molecules (red arrows) assemble in separated islands. The contrast in the C_{60} islands is adjusted better visibility. b) Border region between motor 1 and C_{60} molecules. c) Fully covered Ag(111) surface after additional dosage of C_{60}. d) Zoom-in at a motor 1/C_{60} border region. Imaging parameters, scale bar: a) 0.96 V, 110 pA, 30 nm; b) 0.7 V, 100 pA, 10 nm; c) 0.4 V, 100 pA, 15 nm; d) 1.15 V, 100 pA, 5 nm.

Additional annealing to 240 °C is applied to the C_{60}/motor1/Ag(111) system in order to increase the diffusion rate and allow the molecules to overcome energy barriers in the potential phase mixing. Figure 4.7, recorded after the annealing process shows a drastic decrease in motor 1 molecules on the surface assumed to be due to desorption. The C_{60} virtually cover the complete surface as seen in image 4.7 a). Some protrusions are present in the layer, as it would be expected for the mixed system. However, closer investigation via lateral manipulation, reveals that the protrusions are adsorbates in the second layer. Images 4.7 b) and 4.7 c) show the state before and after manipulation along the path marked in red. The yellow encircled molecule serves as position marker. The bright protrusion is not visible anymore after the manipulation, but instead a C_{60} molecule is revealed below, embedded in the C_{60} layer. Since no vacancy is visible in the bottom C_{60} layer, which would be expected if the bright protrusion stems from upright standing motor molecules, this indicates that the protrusions do not originate

from upright standing motor molecules. They are instead attributed to C_{60} molecules adsorbed in the second layer.

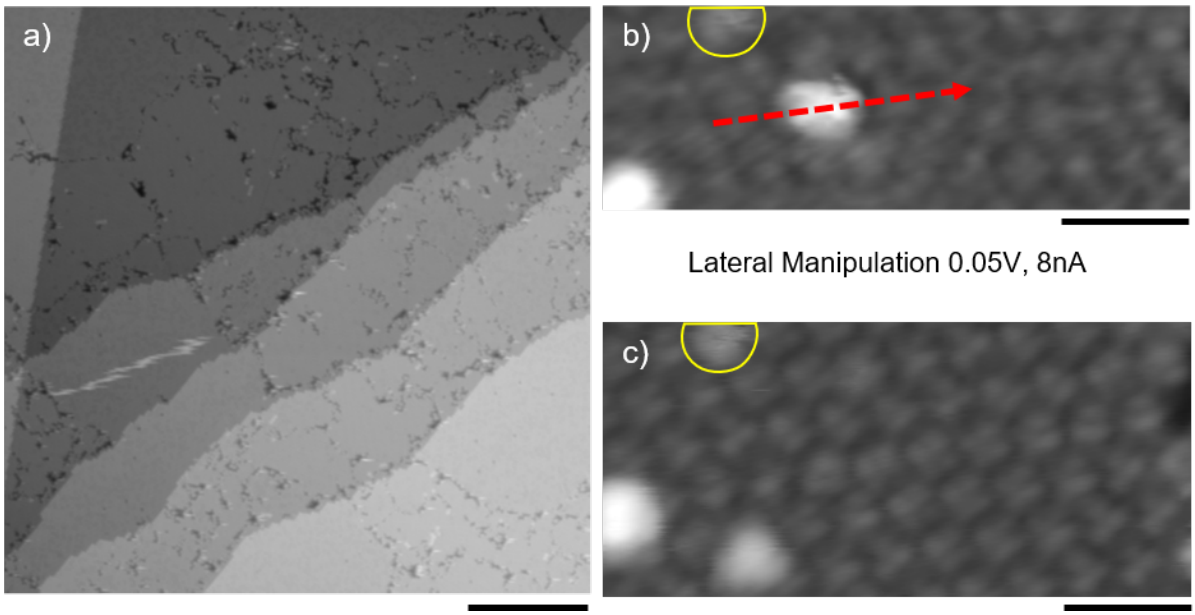

Figure 4.7.: Lateral manipulation of C_{60}/motor1/Ag(111) annealed to 240 °C. a) Near complete coverage of C_{60}. b,c) Lateral manipulation of a protrusion in the C_{60} layer shows a C_{60} molecules remaining below. The manipulation path is marked in red, the molecule highlighted in yellow serves as position marker. Imaging parameters, scale bar: a) 0.45 V, 130 pA, 30 nm; b,c) 1.3 V, 120 pA, 2 nm.

The inverted system with Motor 1 molecules dosed on C_{60} on Ag(111) is also investigated. The C_{60} and motor 1 molecules formed separate phases. Protrusions in the C_{60} islands could be removed by tip manipulation revealing a dense packed C_{60} layer below. For details see Figure A.12 and Figure A.13.
In conclusion, no indication for upright standing motor molecules was found in the motor 1/C_{60} system.

4.1.2. Interaction with Covalent Organic Frameworks

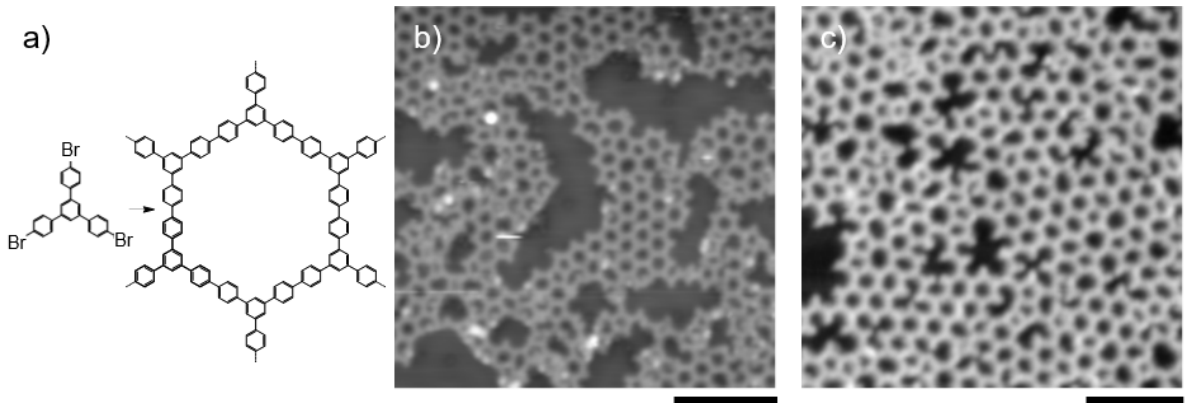

Figure 4.8.: a) Structure of a TBB molecule (left) and the structure of a typical hexagonal pore in the resulting TBB-based covalent organic framework (right). Overview STM images of a TBB-based COF on Ag(111) and Au(111) are shown in b) and c), respectively. Imaging parameters, scale bar: b) -0.44 V, 210 pA, 10 nm; c) 1 V, 100 pA, 10nm.

Covalent organic frameworks (COFs) can serve as a template to guide adsorption of molecules [35]. The number of guest molecules in a pore of a 1,3,5-tris-(4-bromophenyl)-benzene (TBB) based COF could be controlled by the pore size. The inherent inhomogeneities in a TBB-based COF, resulting from different pore sizes, offer here a promising chance to simultaneously test adsorption of motor molecules in different pore sizes. A TBB-based COF is prepared via Ullmann coupling on Ag(111) [36] and Au(111) [35]. Figure 4.9 shows STM images after dosing motor 1 molecules on a TBB-COF on Ag(111). The overview image in 4.9 a) reveals that motor molecules adsorb on the network as well as on the free metal. The molecules appear with a larger apparent height than the network. Single molecules fit into the pores of the network as visible in image 4.9 b). They feature three to four bright protrusions, attributed to butyl groups pointing away from the surface. This implies, that the motor 1 molecules adapt a similar flat-lying configuration as on bare Ag(111). The amount of bright protrusions decreases with annealing to 210 °C as seen in 4.9 c). Upon closer inspection several coexisting species are present, as highlighted by the arrows in 4.9 d). On areas of bare Ag(111) the molecules assembly in the same way as discussed above for the motor 1/Ag(111) system (yellow arrow). Inside the pores motor molecules can be classified into a bright species with one protrusion and a dark species without a protrusion (red and blue arrows respectively).

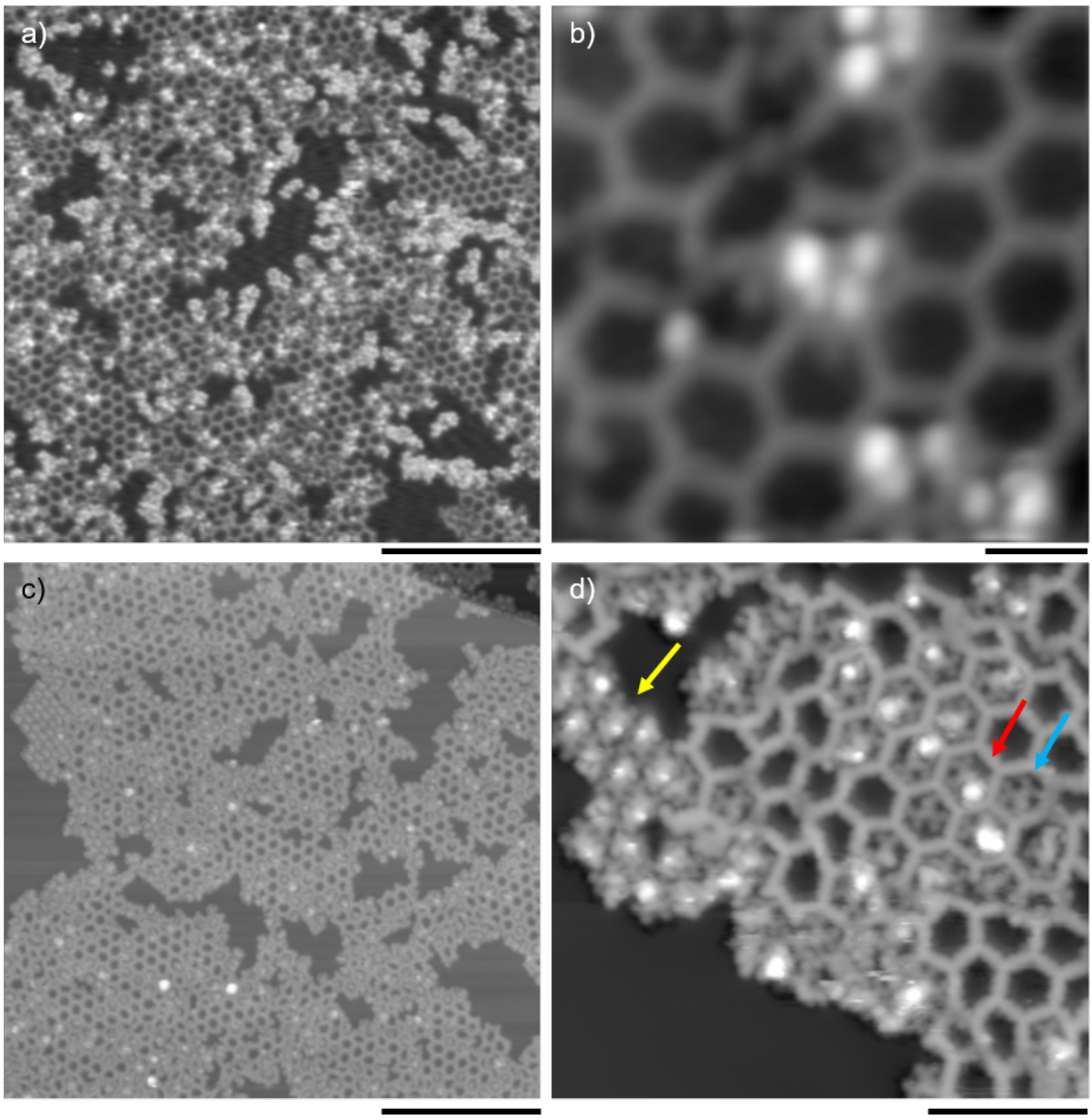

Figure 4.9.: Motor 1 molecules on the TBB-based covalent organic framework on Ag(111). a) Overview image after dosing motor 1 molecules on TBB-COF/Ag(111) at room temperature. b) Zoom-in image of a motor 1 molecule adsorbed in a hexagonal pore. c) After annealing the sample, motor 1 molecules remain on the sample with an intact TBB-COF. d) The motor 1 molecules assemble in island-like structures at the borders of the network (yellow arrow) and are also found in the pores (i.e. red and blue arrow). The molecules inside the pores can be classified into two species, depending on the presence of the bright protrusion. Imaging parameters, scale bar: a) 0.66 V, 120 pA, 25 nm; b) -0.05 V, 230 pA, 2 nm; c) -0.91 V, 110 pA, 25 nm; d) -0.38 V, 100 pA, 5 nm.

The differences between the species are highlighted in Figure 4.10. In 4.10 a) the molec-

ular model indicates that the dimensions of the bright species match a configuration with the motor unit close to the edge of the pore. The spherical features with similar apparent height like the COF are attributed to the sulfur groups. Similar spherical features are observed at the position of the sulfur groups on the motor 1 on bare Ag(111) system. The zoom-in image 4.10 b) displays the dark species. The central part of the motor molecule features similar brightness as the anchoring part. For both cases, bright and dark, the molecular footprint implies that the molecules are adsorbed in a flat-lying configuration.

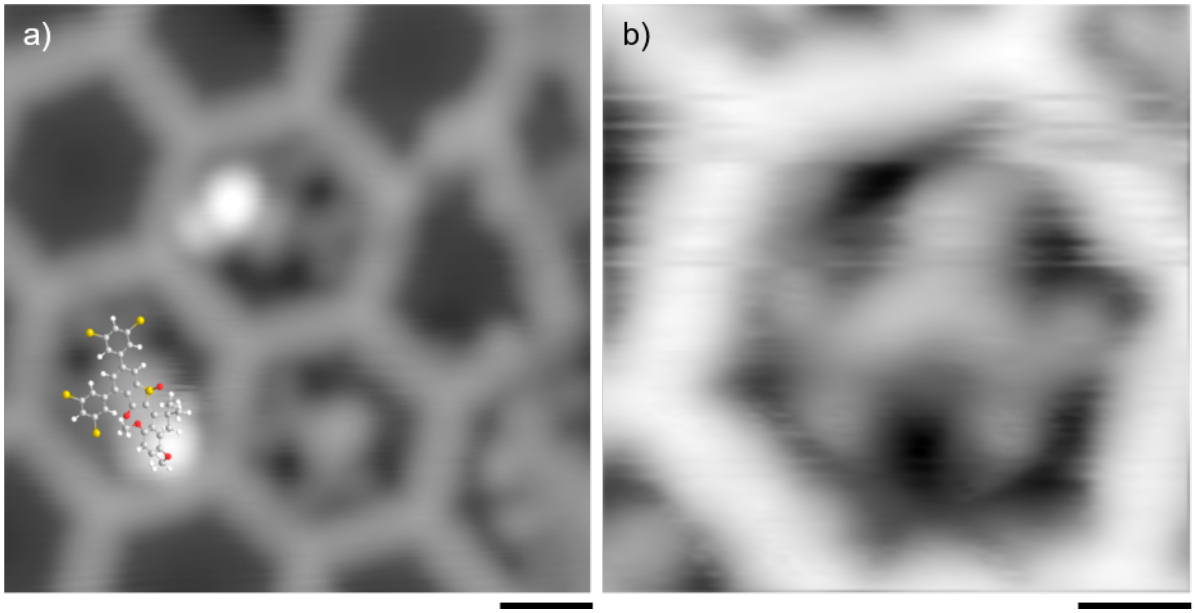

Figure 4.10.: Motor 1 molecules adsorbed inside the pores of the TBB-COF on Ag(111) after annealing to 210 °C. a) Several species with and without protrusions are present. A molecular model is overlayed on the bright species with the protrusion. b) Zoom-in of the dark species. The lower part appears with a similar shape as in the motor molecules with dissociated butyl groups. Imaging parameters, scale bar: a) -0.25 V, 1 nA, 1 nm; b) -0.05 V, 100 pA, 0.5 nm.

Modifying the system to motor 2 on a TBB-COF on Au(111) offers promising characteristics to achieve upright standing motor molecules. As discussed above, the anchoring units are located in vicinal positions in motor 2, designed to provide a higher energy barrier potentially hindering rotation into a flat configuration. Furthermore, the TBB network on Au(111) exhibits a larger variety of pore geometries, ranging from square-like to octagon-like pores. Compared to Ag(111), the pore geometries on Au(111) deviate more from regular polygons and feature a broader distribution. This allows to probe the motor 2 molecules in multiple pore sizes within the same preparation.
Figure 4.11 a) shows a TBB-COF with a few pores occupied with motor 2 molecules, identifiable as bright protrusions. A minority of the molecules also adsorbs on the free metal. Image 4.11 b) displays a zoomed-in region with a motor 2 molecule in a

heptagon-like pore. The four bright protrusions indicate a flat-lying motor geometry with the butyl groups pointing away from the surface, similar to the experiment on Ag(111). After annealing at 200°C virtually all molecules are located in the network, as shown in image 4.11 c). Note that the increase in total amount of motor 2 molecules is related to an additional dosing of molecules prior to annealing. Motor 2 molecules occur as a bright (red arrow) or dark (blue arrow) species as seen in the zoom-in image 4.11 d). They adsorb in differently sized pores, while two molecules can fit in larger sized pores such as the heptagonal ones. The bright species is further separated into molecules adsorbed on or very close at the edge of the pores with an apparent height of 3.2 ± 0.5 Å and more centered adsorbed molecules with an apparent height of 2.2 ± 0.3 Å.

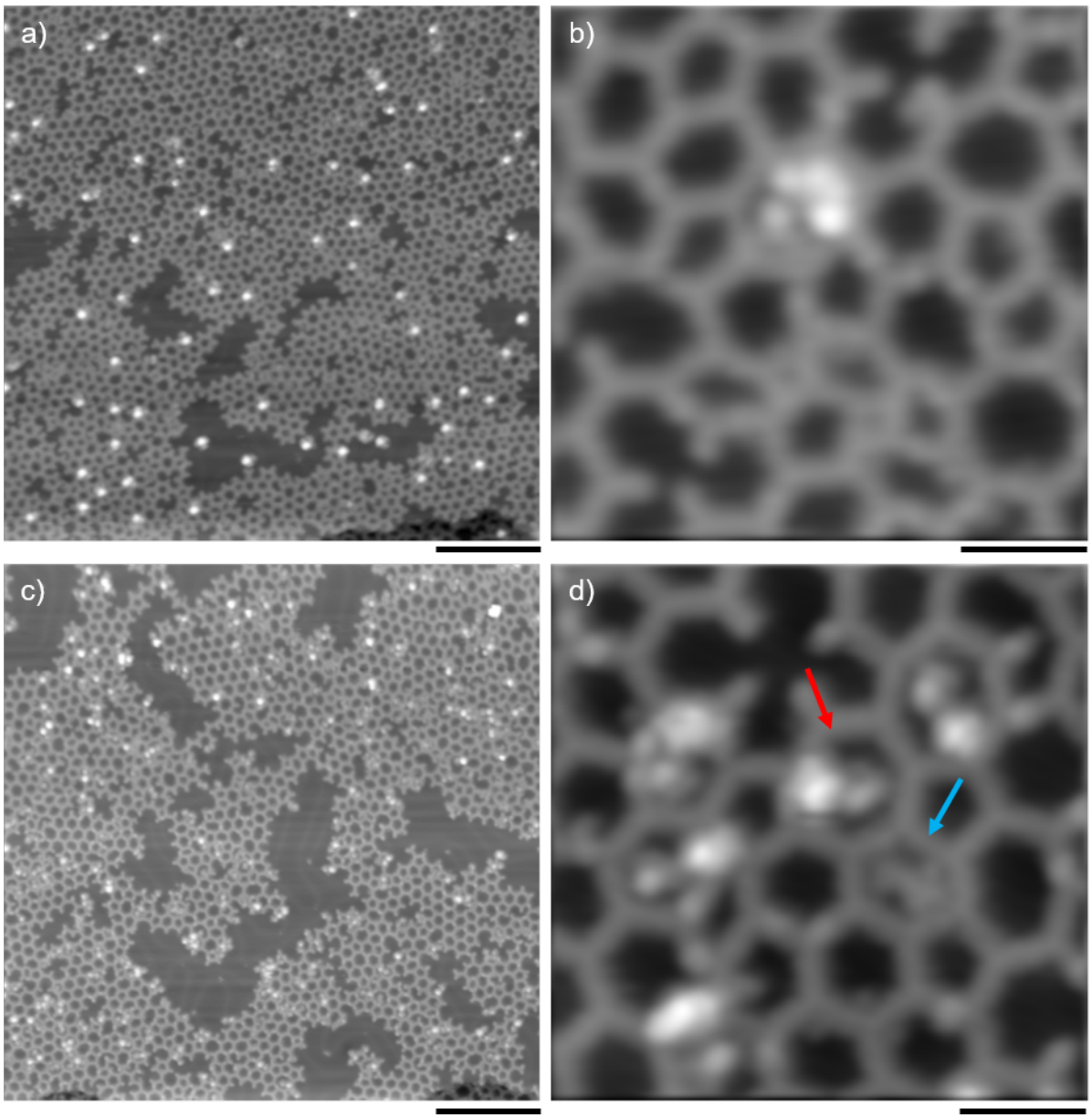

Figure 4.11.: STM images of motor 2 molecules adsorbed on the TBB-based covalent organic framework on Au(111). a) Overview image after dosing motor 2 molecules, appearing as bright protrusions. b) Motor 2 molecule adsorbed in a heptagonal pore. c) After additional dosing of motor 2 molecules and annealing to 200 °C, the majority of motor 2 molecules is located in the pores. d) Bright (red arrow) and dark (blue arrow) species adsorb in hexagonal and heptagonal pores. Imaging parameters, scale bar: a) 0.90 V, 87 pA, 20 nm; b) 0.69 V, 137 pA, 3 nm; c) 0.66 V, 171 pA, 20 nm; d) -0.66 V, 171 pA, 3 nm.

To identify a potential preferred adsorption driven by the pore size, the amount of filled and empty pores is investigated. A total of 2586 pores are inspected for this analysis.

To compare the ratio of filled-to-empty pores across different pore types, the pore areas are approximated by regular polygons respectively.
The bar plot in Figure 4.12 a) summarizes the results. The network consists of square (3%), pentagon (34%), hexagonal (49%), heptagonal (13%), and octagonal (1%) pores, with the majority of 83% comprised of pentagonal and hexagonal pores. This distribution of the pore types is comparable to previous studies on Au(111) [35]. The filled pores are represented with a solid fill while the empty species are marked with the dashed pattern. A total of 10% of all pores are filled with molecules, including doubly occupied pores.
Interestingly, the filled pores are distributed with a tendency towards larger pore sizes. In order to test for a correlation between pore size and filling ratio, the area of the pore is compared with the filling ratio in 4.12 b). The area of each pore type is approximated by the area of the respective regular polygon. The blue markers show the areas of regular polygons, ranging from square to octagon, normalized to the area of the hexagon. The red markers display the ratio of filled-to-empty pores for each pore type, normalized to the filling ratio of the hexagonal pores. The filling ratio exhibits different behavior with increased pore size than the area of the polygons. Almost no filled square or pentagonal pores are observed. Next, 10% of hexagonal pores are filled, and the heptagonal and octagonal pores are filled with a greater ratio at 37% and 42%, respectively. This increase exceeds the hexagon case by roughly a factor four, which stands in contrast to the factor of 1.4-1.9, projected from the polygon area increase with pore size.
This increase is attributed to the preference of the motor molecules to adsorb on areas of bare metal compared to directly on the network. For case of the square and pentagonal pores there is not enough space to accommodate a motor 2 molecule. Starting from hexagonal pores, the pore area is sufficient to host a motor 2 molecule. From heptagonal pores and larger, up to two motor 2 molecules can fit in a single pore. During sample preparation the motor molecules are heated to elevated temperatures (300 K - 480 K) which facilitates diffusion within the pores and across the network. For organic molecules in phenyl-based pores 160 K are sufficient to diffuse across the edges pores [207].
Furthermore, when two motor molecules are located in the same pore, attractive intermolecular interactions between the motor molecules decrease the probability of a molecule to diffuse out of the pore. Attractive interactions between the motor molecules are clearly present, as seen by their island formation in previous experiments.

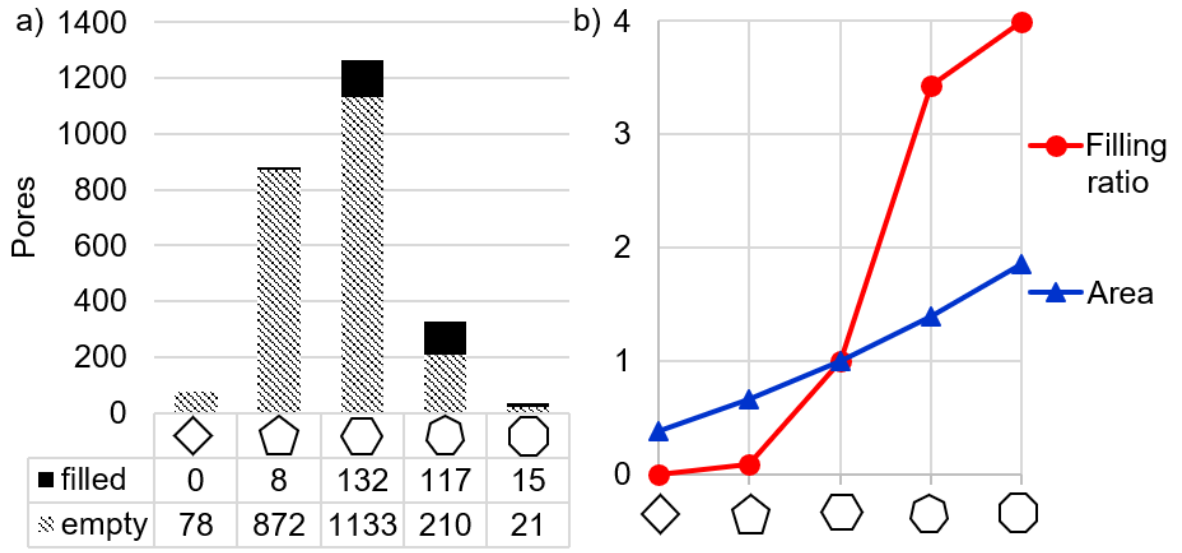

Figure 4.12.: Analysis of the amount of occupied pores of motor 2/TBB-COF/Au(111). a) The network features mainly pentagonal and hexagonal pores. Heptagonal and octagonal pores are occupied preferably relative total the number of available pores. b) The filling ratio with increasing pore size grows faster than expected from the respective polygon area. Filled ratio and polygon area are each normalized to the hexagon case.

In order to clarify the if the motor molecules exist in a flat or upright standing adsorption geometry, we compare the apparent height between the two constitutional isomers of motor 1 and 2 on the two substrates and within the covalent organic framework. The results are summarized in Figure 4.13. The apparent height measurements are calibrated against atomic steps of the respective substrate. Height-related artefacts originating from electronic features are excluded by measuring at the same energy. Panel 4.13 a) shows different motor 1 species on a TBB-covered Ag(111) surface. Bright species (red circle) located at the edge of the pore exhibit an apparent height of 2.2 ± 0.3 Å while the dark species (blue circle) in the center of the pore the molecules are 0.8 ± 0.2 Å high. On motor 1 molecules located next to the network on bare Ag(111) (yellow circle) an apparent height of 1.8 ± 0.2 Å is observed. On Au(111) (b) the molecules feature a similar apparent height of 2.0 ± 0.2 Å even though they form chain-like structures.
Next, the motor 2 molecules on Au(111) are discussed. After annealing they form trimer-like clusters with an apparent height of 2.8 ± 0.2 Å. These agglomerates can be prevented by using a TBB-based covalent organic framework. Depending on the pore size one or two motor molecules are isolated in the pores as shown in images 4.13 d)-g). The apparent height is evaluated for each pore size and whether the molecule is located in the center or on the edge of the pore 4.13 d)-f). For all pore sizes, molecules at the edge appear with a larger apparent height than molecules in the center. In the case of the pentagonal pores (4.13 g) the contrast of the motor molecules is difficult to unambiguously distinguish from the edges of the pores. Thus it is also possible that the pentagonal pores hosting motor molecules are actually irregular or incomplete

pores. Considering all pore sizes, the molecules have a lower apparent height than 4 Å, pointing to a flat-lying geometry. Even though an unambiguous assignment with a molecular model is not possible, the geometries are tentatively assigned to a similar configurations as for the case of motor 1 without butyl groups on Ag(111) as shown in Figure 4.3 b).

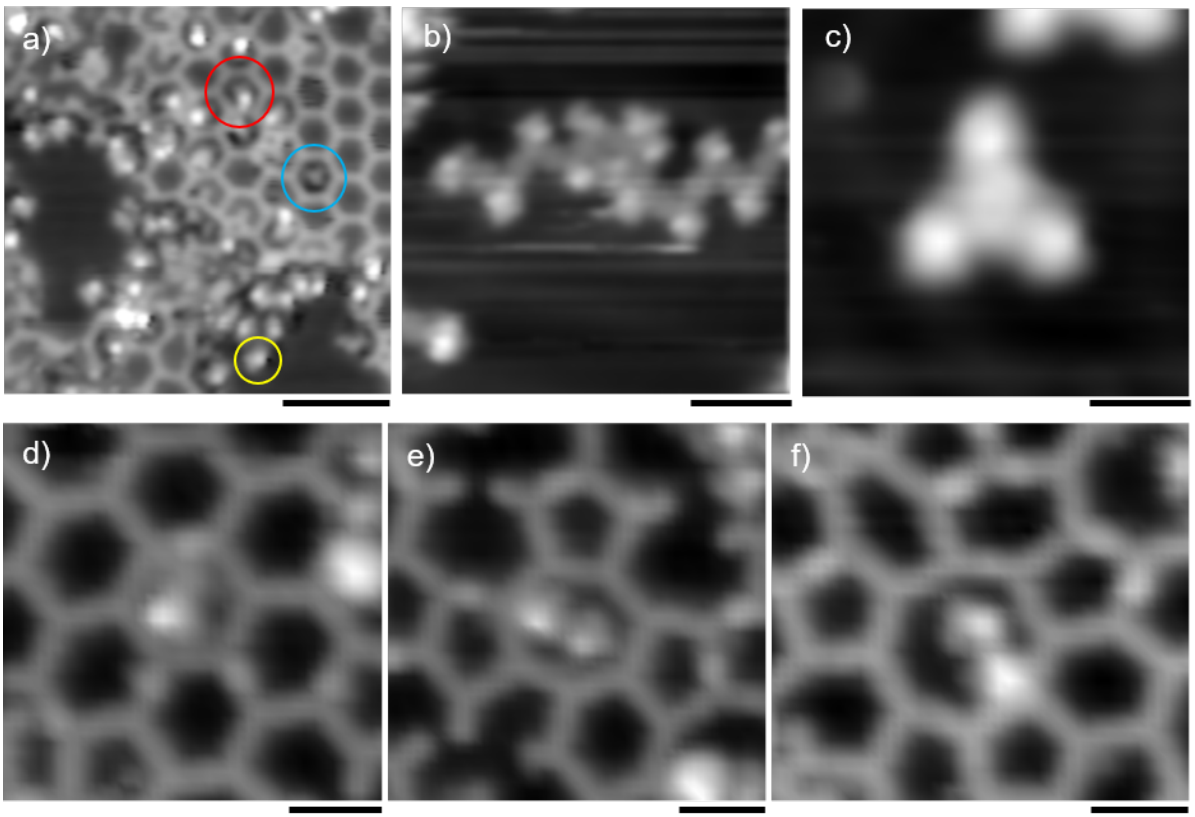

Motor 1	Height [Å]
a) Ag(111)	(blue) 1.8 ± 0.2
a) TBB-COF/Ag(111)	Pore: 0.8 ± 0.2 (yellow) Edge: 2.2 ± 0.3 (red)
b) Au(111)	2.0 ± 0.2

Motor 2/Au(111)	Height [Å]
c) Bare Au(111)	2.8 ± 0.2
d) TBB-COF hexagon	Pore: 2.3 ± 0.3 Edge: 3.0 ± 0.3
e) TBB-COF heptagon	Pore: 2.1 ± 0.2 Edge: 3.1 ± 0.3
f) TBB-COF octagon	Pore: 2.4 ± 0.1 Edge: 3.3 ± 0.5
g) TBB-COF pentagon	Edge: 3.8

Figure 4.13.: Apparent height comparison between motor 1 and motor 2 molecules, after cleaving the butylgroups, on Ag(111) and Au(111) and within different pores of a TBB based covalent organic framework at constant bias. a) Motor 1 molecules on bare Ag(111) (yellow), as well as dark(blue) and bright(red) species in the pores. b) Motor 1 molecules on bare Au(111). c) Motor 2 molecules on Au(111). d-f) Motor 2 molecules in 6-, 7-, and 8-sided pores. g) Motor 2 molecule presumably adsorbed on the edge of a 5-sided pore. The tables list the apparent heights which are all below 4 Å, consistent with a flat-lying adsorption geometry. Imaging parameters, scale bar: a) 0.5 V, 100 pA, 5 nm; b) 0.53 V, 86 pA, 3 nm; c) 0.5 V, 28 pA, 2 nm; d-g) 0.5 V, 123 pA, 2 nm.

Summary and Discussion

In this section the effect of mixed self-assembly and covalent networks on the configuration of motor molecules is shown. For the case of co-adsorption with C_{60} molecules, the assembly and adsorption configuration motor 1 molecules are unaffected. The separation of C_{60} and motor islands is unaffected by the order in which the molecules are deposited. The TBB-based covalent organic framework influences the assembly of motor molecules on both substrates, Ag(111) and Au(111). The previously observed cluster formation upon annealing is successfully prevented and individual motor molecules are isolated in the pores. The thermally induced deprotection reaction of the sulfur groups in the motor molecules is still possible in the network. After cleaving the butyl groups several coexisting configurations of motor molecules are observed in the pores. For both molecules, motor 1 and motor 2, the template effect of the TBB-based COF is clearly present. In the statistical analysis of motor 2/TBB-COF/Au(111) we observe that the filling ratio of motor molecules depends on the pore size. Large pores such as heptagonal and octagonal pores are filled with a higher ratio, while smaller pores such as hexagonal pores have a lower filling ratio.

Both motor molecules exhibit apparent heights below 4 Å in the network. This is compatible with a flat-lying adsorption configuration. Further details of the adsorption configuration are difficult to access in STM experiments. A characterization with nc-AFM measurements in combination with DFT simulations can provide further information how the motor molecules adsorb in the pores.

In order to achieve an upright standing configuration a different geometry of the anchoring group might prove successful, for example a tripodal design [208–212] or a platform based anchoring group [213, 214]. Note, a tripodal design is not a sufficient condition for an upright standing geometry. For example disubstituted naphthalene-1,4,5,8-tetracarboxdiimide (NDI) molecules attached to a tripodal base adsorb in a flat-lying configuration [215]. However, a decoupling affect on the functional moiety in similar molecules was achieved using a tripodal base and tip-induced single molecule manipulation [216].

Furthermore, a modification of the covalent organic framework could be utilized to direct the motor molecules into an upright standing configuration. For example introduction of inert, bulky groups in the network precursor could lead to taller edges of the resulting pores. These steric constraints might help to create a cylinder-like mesh which would prevent flat-lying adsorption. Another plausible option is to introduce functional groups in the network. These functional groups would need to exhibit attractive interactions with the stator part or repulsive intermolecular interactions with the motor part. Insights from DFT simulations of the present carbon-based covalent organic network could help to suggest how to design the precursor for the network. However, in both cases of modification of the network there is the possibility that the free rotation of the motor unit is affected by interactions with the network.

Another option could be to change the substrate to a corrugated surface. A stepped surface was already reported to exhibit a templating effect on self-assembled molecular structures [217–219] and to drive selective synthesis of graphene nanoribbons [220]. A

curved crystal would provide an option to test multiple facets within the same experiment [221]. Moreover, a Cu(110) surface, which is oxidized in a controlled way, features a striped pattern of oxide layers and bare Cu, which was used to direct the self-assembly of molecules [222–226]. Additionally via the width of the Cu-O stripes the structure of organometallic polymers is controllable [227]. A similar system might be applicable to tune the adsorption geometry of the motor molecules. Furthermore the exploration of semiconducting surfaces such as TiO_2 for adsorption of molecular motors is promising, since, in contrast to metal substrates, quenching of excited molecular states is less anticipated [228].
In summary, a templating effect of the TBB-based COF on the adsorption geometry of the motor molecules was demonstrated. Although the molecules are successfully separated into individual units, they still adsorb in a flat-lying geometry. While many options on the choice of substrate are still unexplored, based on the observation that the motor units adsorb parallel to the metal surfaces on Ag(111) and Au(111) a change to other metal substrates might result in similar flat adsorption geometry. A promising approach could be to modify the structure of the molecule.

4.2. Thorium-Naphthalocyanine Double-Decker Molecules

Quantative measurements of energy barriers and forces as well as torque on the molecular scale have been reported for rotations in biomolecules such as in DNA or ATPase [229]. Various techniques allowed to determine the torque in DNA on the order of 15-45 pN·nm, depending on the specific state of the DNA. However, in order to probe torque on the single molecule scale, a reduction to a smaller model system is desirable since DNA is a rather large macromolecule, complicating the analysis. Previously atomic force microscopy has been employed to probe rotational phenomena within a molecule. Examples include: rotation around a C-C double bond [230], rotating a butyl-phenyl leg in a porphyrin derivative [231], rotating porphyrin molecules by tip approach [232], and rotation of a Copper-phthalocyanine molecule via lateral force microscopy [233]. These examples demonstrate a concomitant deformation of the molecule, requiring to carefully consider side effects such as dissipation. Overall the combination of STM and AFM is found to be a powerful technique to study rotation of single molecules or their subunits [234, 235].
A suitable molecular system is needed for probing the rotational movement. A suitable system includes properties such as accessible rotatability, identification of the rotated states and robustness against non-rotational motion during the experiment. Double-decker systems [236] provide a promising starting point. The possibility of rotation of top ligand in double-decker molecules was observed and documented in on-surface experiments [81, 196, 237]. Double-deckers can be separated in heteroleptic and homoleptic systems, depending if the two sandwiching molecules are different species or the same species.

Examples for heteroleptic double-deckers systems include porphyrin-based double-deckers with alkyl chains on the lower molecule [77, 79] as well as phthalocyanine based systems with sulfur groups [238, 239] in the lower molecule. Recently a cogwheel-like molecule, consisting of a phthalocyanine and functionalized naphthalocyanine ligand, was synthesized with the purpose of studying its rotational behavior on the surface [240]. Even though heteroleptic double-decker molecules can be deposited via sublimation, the preparation of suitable geometries, where rotation of an isolated double-decker can be probed, is challenging [241]. A system with isolated double-decker molecules protruding from a dense packed layer would be suitable. The dense packed bottom layer is envisioned to block unwanted rotation of the lower half during rotation experiments on the top half of the respective double-decker molecule.
Common on-surface synthesis protocols of homoleptic double-decker molecules provide such a geometry [81, 196]. Here, we investigate Thorium-Naphthalocyanine (Th(NPc)2) double-decker molecules. Compared to the studied examples of tetraphenylporphyrin (TPP) based double-deckers, the following improvements are anticipated in the naphthalocyanine double-decker. The naphthalocyanine ligands are planar, minimizing steric hinderance during rotation. The geometry of the naphthalene units in the arms is more rigid than for example the rotatable phenyl groups in the TPP based species. This minimizes inelastic effects during tip-induced rotation. The larger dimensions of the naphthalene arms also facilitate probing the distance dependency to the center of rotation of the measured torque.
Naphthalocyanine double-deckers are also interesting from a on-surface synthesis perspective. While some double-deckers with naphthalocyanine moieties have been documented [242–244], these compounds are so far only reported via solution-based synthesis and limited to lanthanide metal centers. To the best of our knowledge, Th(NPc)2 double-decker molecules are the first naphthalocyanine-based double-decker species incorporating an actinide. Furthermore, it is also the first report of a homoleptic naphthalocyanine double-decker molecule achieved via on-surface synthesis.
The following section describes the synthesis and structure of Th(NPc)2 on Ag(111). Th(NPc)2 is then used as a model system to study tip-induced rotational movements. Quantification of the required torque on a modified Th(NPc)2 system is also reported.

4.2.1. Synthesis and Structure of Th(NPc)2 on Ag(111)

The on-surface synthesis of Th(NPc)2 double-decker molecules follows a similar procedure as already known for other double-decker type molecules [81, 196, 201]. The synthesis encompasses three subsequent steps: dosing of an excess of a monolayer of NPc on Ag(111), dosing small amounts of elemental Thorium and annealing to 350 °C in order to induce the 2 NPc + Th $\rightarrow$ Th(NPc)2 reaction and desorb multilayer components. For details see the methods section 2.5.
On the resulting sample, several species are present as shown in Figure 4.14 a). The Ag(111) surface is covered with a dense packed layer of NPc molecules. Second layer NPc molecules (green arrow) are identified by their similar orientation and appearance as molecules in the first layer. The contrast of the molecules in the first and second layer

agrees with the contrast pf free-base naphthalocyanine molecules on Ag(111) as found in reference [245] and the control experiment without Thorium, see Figure A.14.
The contrast of the species marked with circles exhibits additional submolecular features, and is identified as Th(NPc)2 double-decker molecules as detailed in the following. This species appears in two distinct orientations, with the majority rotated by 45° with respect to the first layer (yellow circle). A minor amount is orientated similar to the molecules in the first layer (red circle). Image 4.14 b) reveals that under different imaging conditions the central macrocycle appears with a uniform contrast, while the four naphthalene arms show two protrusions each (yellow arrow). Here, second layer molecules appear with double C shape (green arrow).

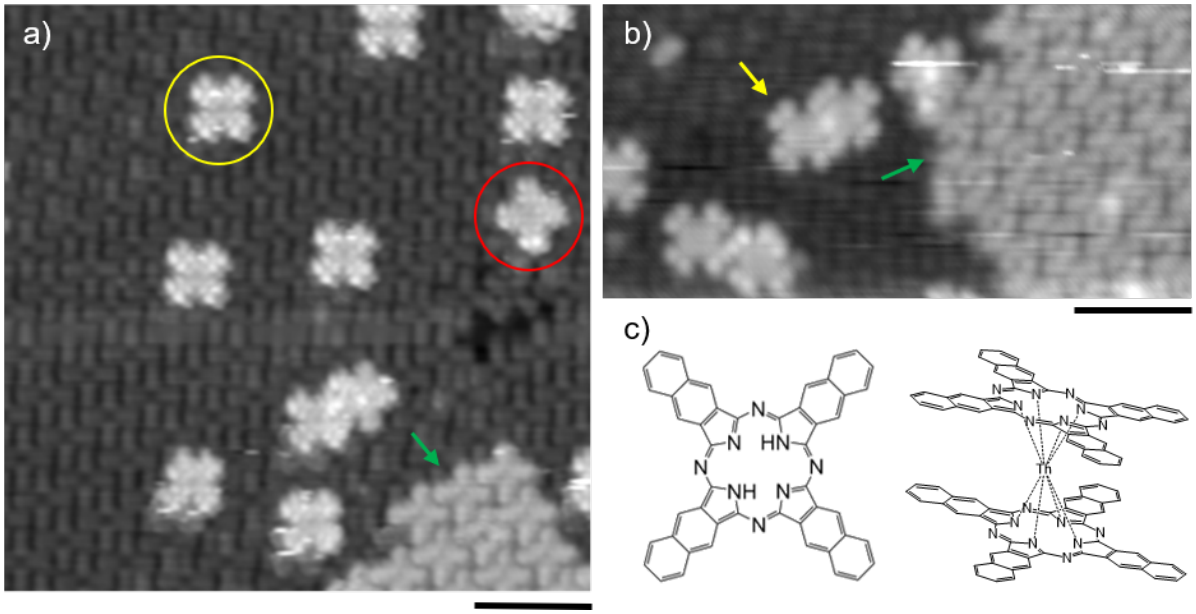

Figure 4.14.: STM images of Th(NPc)2 double-decker molecules embedded in a dense-packed naphthalocaynine layer on Ag(111). a) Double-decker molecules (yellow and red circles) show intramolecular contrast, while NPc molecules in the second layer appear with an uniform contrast in addition to the central depression. b) Under different tip conditions, the double-decker molecules (yellow arrow) remain discernible from second layer molecules (green arrow) by additional intramolecular contrast. c) Structure of Naphthalocyanine (NPc, left) and sketch of the Th(NPc)2 double-decker structure (right). Imaging parameters, scale bar: a) -1.0 V, 20 pA, 4 nm; b) -1.2 V, 4 pA, 4 nm.

A more detailed presentation of the tip-dependent appearance is given in Figures 4.15 and 4.16. The bias series in Figure 4.15 shows that this species exhibit a cross-shape contrast over a wide bias range. At voltages < -0.75 V the cross shape broadens and two additional lobes are discernible at the ends of the arms. When imaging the molecules with a functionalized tip, as displayed in Figure 4.16, submolecular features are clearly distinguishable.
Reports of a heteroleptic Terbium double-decker molecule with phthalocyanine and

naphthalocyanine moieties on Au(111) show similarities to the species observed here [241]. In particular the Terbium double-deckers with the naphthalocyanine unit pointing away from the surface and exhibit similar contrast, see also Figure A.15 a,b).
When comparing the contrast of the Th(NPc)2 species with NPc molecules on NaCl [246] we find indications for electronic decoupling of the top half of the double-decker. Gross et al. imaged NPc molecules on 2ML NaCl on Cu(111) with metal (Cu) and CO-tips, see also Figure A.15 d,e). The contrast on this decoupled NPc/NaCl system resembles the contrast observed here. The images in Figure 4.15 look similar to the Cu-tip data while the data in Figure 4.16 match the CO-tip data in Figure A.15 d), respectively. Furthermore, the data in Figure 4.16 at -1.7 V and 0.75 V shows features which resemble the positive ion resonance (PIR) and negative ion resonance (NIR) of NPc/NaCl. The PIR (-1.65 V) and NIR (0.60 V) of NPc/NaCl correspond to the HOMO and LUMO respectively, compare Figure A.15 e). The similarities in the appearance and the respective energies indicate decoupling of the top half of the double-decker from the substrate in the present Th(NPc)2/Ag(111) system. Furthermore, the differences of the appearance of the Th(NPc)2 double-deckers and the NPc molecules indicate a modification of the electronic structure. A modification of the electronic structure is expected, since it was also observed in Tetraphenylporphyrin-based double-deckers upon Thorium coordination [196].

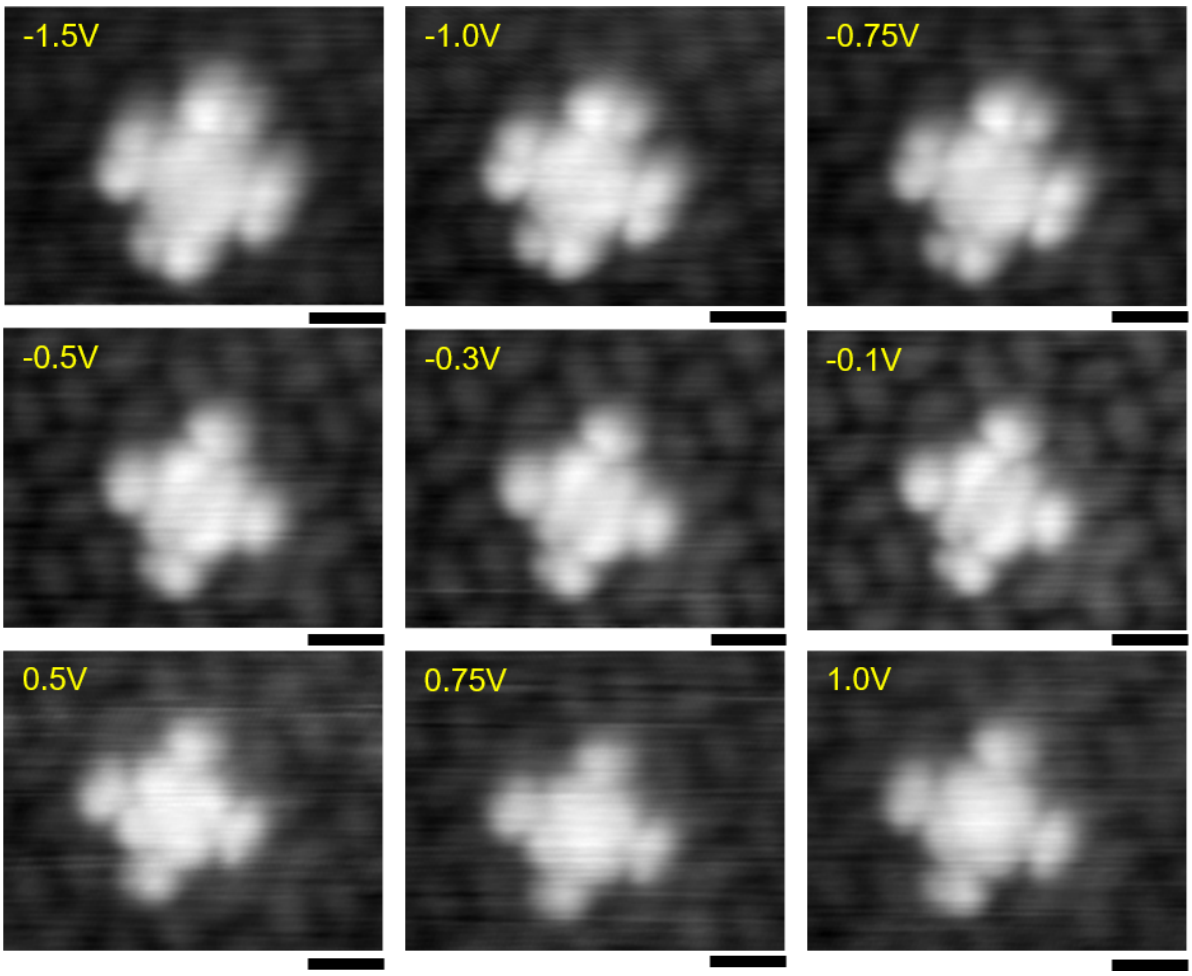

Figure 4.15.: Bias dependent STM imaging of Th(NPc)2 double-decker molecules. A clear cross-shape is visible over a wide bias range. At voltages < -0.75 V the molecules display a two-lobe substructure at the end of the cross. Imaging parameters, scale bar: 20 pA, 1 nm.

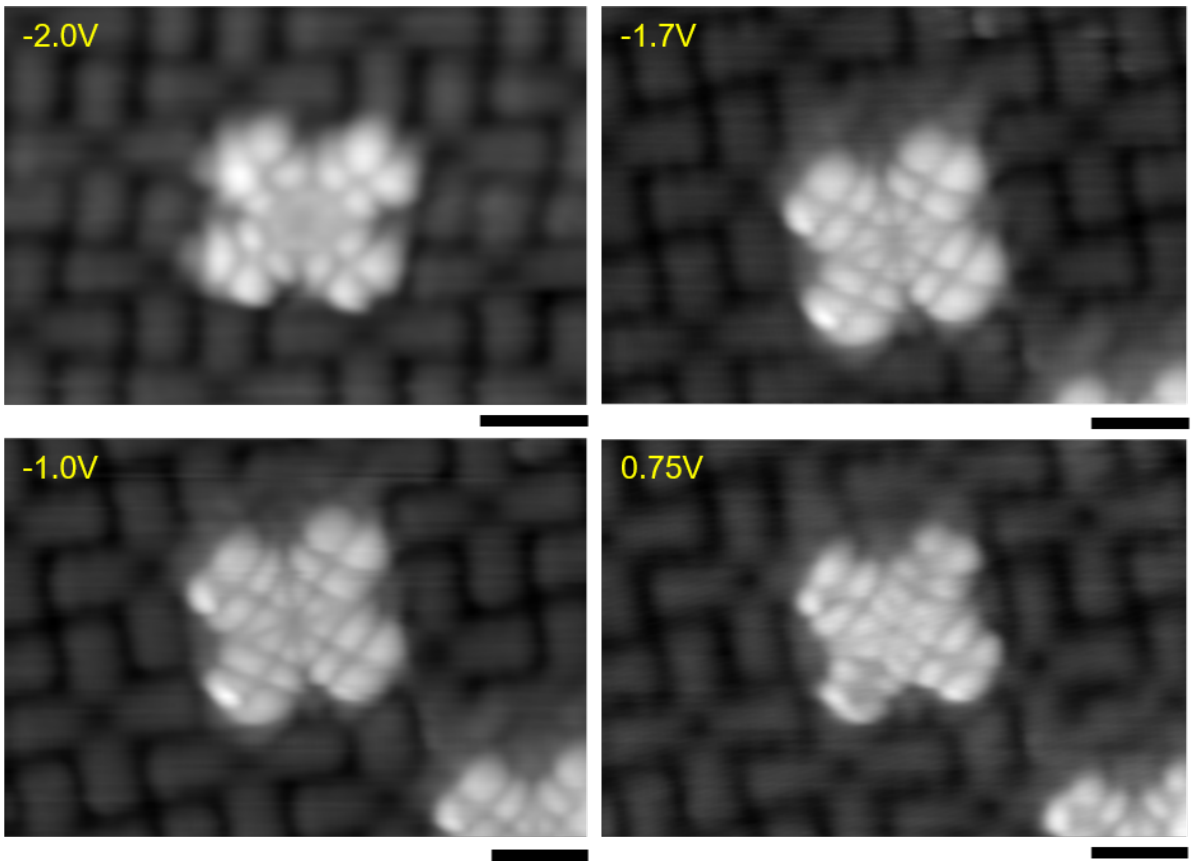

Figure 4.16.: STM images of Th(NPc)2 double-decker molecules with a functionalized tip. Distinct molecular orbitals appear for bias values < -1 V, 0.75 V, 2 V. Imaging parameters, scale bar: 20 pA, 1 nm.

A further argument for the synthesis of Th(Nc)2 double-deckers is given by the centering of the top half above NPc centers in the dense packed bottom layer. In Figure 4.17 a lattice corresponding to the bottom layer of NPc is superimposed on the image, showing that the top halves of the double-decker molecules are centered above molecules in the first layer. Since unreacted second layer NPc molecules are offset, as visible in the bottom right corner of 4.17 a), a centered appearance is pointing towards a Th coordinated double-decker species.
Additionally, a control experiment of a sample without Thorium deposition showed only molecules with an offset in the second layer. The molecules on the edges of 2nd layer islands and isolated molecules are easily moved during scanning, see Figure A.14 a). This behavior is not observed with the Th(NPc)2 double-decker species.

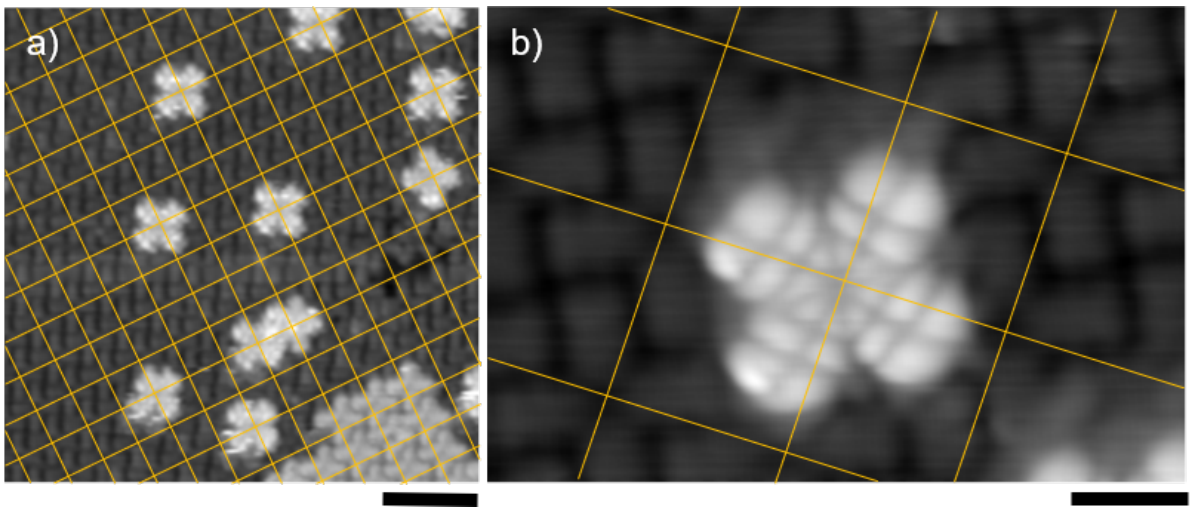

Figure 4.17.: Th(NPc)2 double-decker species are identified by the top NPc centered on NPc molecules of the bottom layer. A grid is overlaid with the periodicity of the dense-packed NPc molecules in the bottom layer. a) The top NPc half in the Th(NPc)2 double-decker molecules follows the periodicity of the grid. b) zoom-in image of a single Th(NPc)2 double-decker. Imaging parameters, scale bar: a) -1.0 V, 20 pA, 4 nm; b) -1.7 V, 20 pA, 1 nm

To summarize, the successful synthesis of Th(NPc)2 double-deckers is confirmed via 1) the appearance in STM contrast, which matching with the contrast of the NPc half of heteroleptic NPc-containing complexes, 2) centering of the top half NPc on the first layer NPc molecules, 3) absence of this species in control experiments without Thorium. Th(NPc)2 molecules are the first homoleptic naphthalocyanine double-decker molecules achieved by means of on-surface synthesis. To date, naphthalocyanine is the largest molecule used among comparable on-surface synthesis reactions.

4.2.2. Tip-induced Rotation of Th(NPc)2

Next, we focus on this Th(NPc)2 double-decker system as model system for torque measurements on the single molecule level. As a first step, suitable parameters for rotation are explored. The manipulation procedure employed here consists of moving the tip at constant height in a linear trajectory across a naphthalene arm of the the double-decker, with incremental closer tip-molecule distances. This procedure is referred to as lateral manipulation. A rotation event is anticipated to be visible in the frequency shift signal. In particular the appearance of a discontinuity and a copy of the signal leading up to the discontinuity is expected. For a detailed description of this method see subsection Torque Measurement 2.1.3 in the atomic force microscopy methods section. For the present Th(NPc)2 double-decker system we found successful rotation to be challenging. Two common outcomes upon closer tip approach are displayed in Figure 4.18. Molecules from the bottom layer can be removed, which is particularly often observed at the start and end of the manipulation path. Image 4.18 b) shows that the double-decker can

also be completely removed from the dense packed layer. Quantitative analysis of the rotation is not feasible for these events.

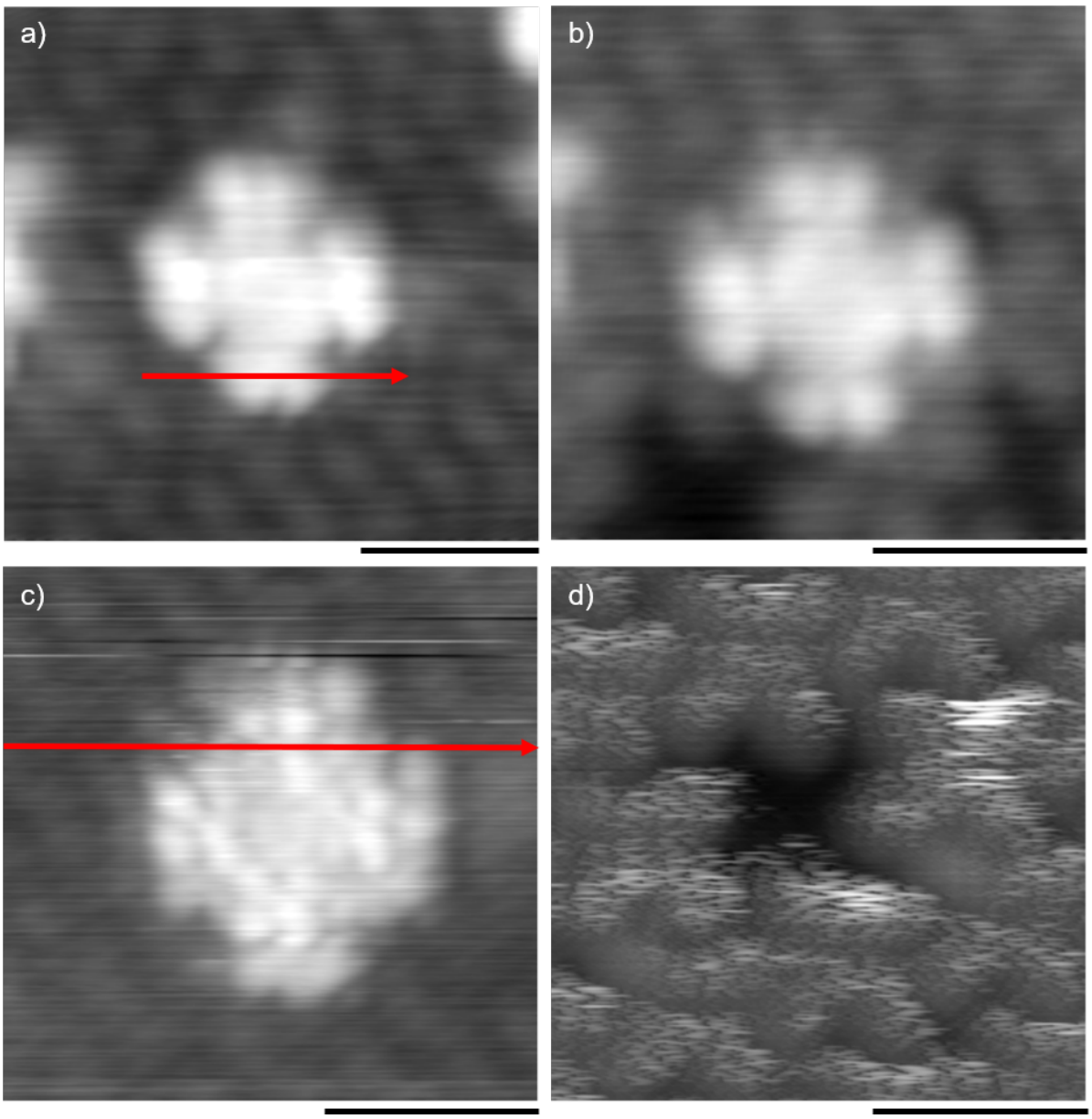

Figure 4.18.: STM images before (left column) and after (right column) rotation attempts via a lateral manipulation protocol. The tip was moved at constant tip-heights along the path marked in red. The tip-height was incrementally decreased until a change was observed in the STM image after the respective movement along the red path. A modification of the Th(NPc)2 double-decker system was observed during these experiments. a)-b) NPc molecules from the bottom layer are removed. c)-d) The Th(NPc)2 double-decker is pulled out from the assembly. Imaging parameters, scale bar: a,b) -1.0 V, 20 pA, 2 nm; c) -0.6 V, 20 pA, 2 nm; d) -1.0 V, 20 pA, 2 nm.

The inherent four-fold symmetry of the double-decker hinders easy identification of rotations by 90°. In order to image these 90° rotational events, a double-decker molecule is modified with a voltage pulse to reduce the four-fold symmetry. Figure 4.19 shows the appearance in STM after applying a > 2 V pulse on the naphthalene unit at the position marked with the yellow arrow. This modified species exhibits one modified naphthalene unit ("arm"), appearing distinctly brighter, and three unmodified naphthalene arms.

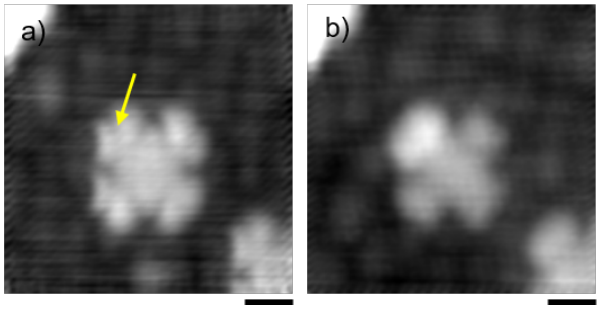

Figure 4.19.: STM images before (a) and after (b) applying a bias pulse of > 2 V at a regular double-decker molecule. a) The yellow arrow marks the location of the bias pulse. b) The modified species features three equal and one modified arm. Imaging parameters, scale bar: a,b) -1.2 V, 4 pA, 1 nm.

The resulting species has been succesfully rotated with three different tips, as shown in Figure 4.20. The left column displays STM images of the molecule before and after rotation. During the manipulation procedure, see also in methods section 2.1.3 Torque Measurement , the tip is moved in constant height across one of the arms of the molecule. This path is marked in red in the STM images of Figure 4.20. The tip-molecule distance is gradually decreased and the corresponding frequency shift (df) signal for each tip height is plotted in the center column. Here, $z_{rel} = 0$ corresponds to the tip-sample distance above the double-decker in constant-current mode, larger z_{rel} values are closer to the molecule. The df-curves are each offset for clarity by 10 Hz (set a-d), 3 Hz (set e-f), 2 Hz (set i-j) and where necessary a 6 Hz gap is introduced. A rotation is expected to alter the frequency shift signal in a similar way as moving an atom [52]. That is, a discontinuity appears and a copy of the original signal shape continues from the point of the discontinuity. This concept was demonstrated by laterally moving an atom, see Figure 2.3 b).
The STM images acquired before and after the set of df-curves (left column in Figure 4.20) clearly show a rotation of the molecule. Considering these three rotation events, a common feature is that the minimum in the df-curves increases in magnitude and one to two additional minima form upon tip approach. The expected clear discontinuity and appearance of a copy is not observed, however a change in the signal shape is present at closer tip-molecule distances. The black arrows mark the closest df-curve prior to the change. Considering that the frequency shift signal across a molecule is more complex than across an atom, it is possible that the rotation is also reflected in a more complex signal. Consequently, the heights of the df-curves directly after the marked curves are

assigned to the tip-heights where the respective rotation occurred. Thus, the marked curves represent a lower limit on the tip-molecule approach to rotate the molecule for the given tip-molecule system. The tip-sample potential is extracted from the df-data set up to the marked curves via the Sader-Jarvis method [104, 105] and plotted on the left axis in 4.20 d), h), l) for each of the three rotation sets. The potential is smoothed via a Savitzky-Golay filter (red curve, degree 3). The lateral force is given by the derivative of the smoothed potential and displayed in blue on the right y-axis.
In the first set (panels 4.20 a-d), the double-decker is manipulated at the modified arm along the path marked in red in alternating directions, starting at $z_{rel} = 0$ in the top-right direction. After a total approach of 130 pm the rotation of the molecule is confirmed via STM imaging. At 100 pm the signal shape develops a discontinuity at a lateral displacement around 3.2 nm. This step is attributed to the minimum approach needed for a rotation. Accordingly, the integration along the z-axis for calculating the potential includes the df-curves obtained from 0 to 90 pm. In diagram 4.20 d) a maximum force of 95 pN is extracted from the potential, presenting a lower limit for the rotation when manipulating the modified arm.
Next, in the second (panels 4.20 e-f) and third set (panels 4.20 i-j) the double-decker is rotated via manipulation at the unmodified naphthalene unit. It is located on the opposite side of the molecule as the modified naphthalene unit. In the second set there is a clear transition in signal shape between z_{rel}=350 pm and z_{rel}=360 pm, where in the closer frequency shift curves the signal even approaches the repulsive regime. When calculating the potential up to including the z_{rel}=350 pm step (marked by the black arrow), a force of 14 pN is extracted.
In the third set, the double-decker is rotated backwards into the the initial position of the second set. Note that here the manipulation path is offset by 3° from the previously used perpendicular path. Again a distinct transition in the frequency shift curves is visible. In this case, a change is observed at z_{rel}=470 pm relative tip height. Integration up until one step before, as marked by the black arrow, results in the potential shown in 4.20 l). Here, a force of at least 6 pN is necessary to rotate the top half back.
When comparing the three events, we note that the force necessary (14 pN, 6 pN) to rotate at the unmodified arm is about one order of magnitude smaller than the force required on the modified arm (95 pN). This is carried over to the torque, where average torque to rotate at the unmodified arm is 9 ± 8 pN·nm while the modified arm requires 40 pN·nm.

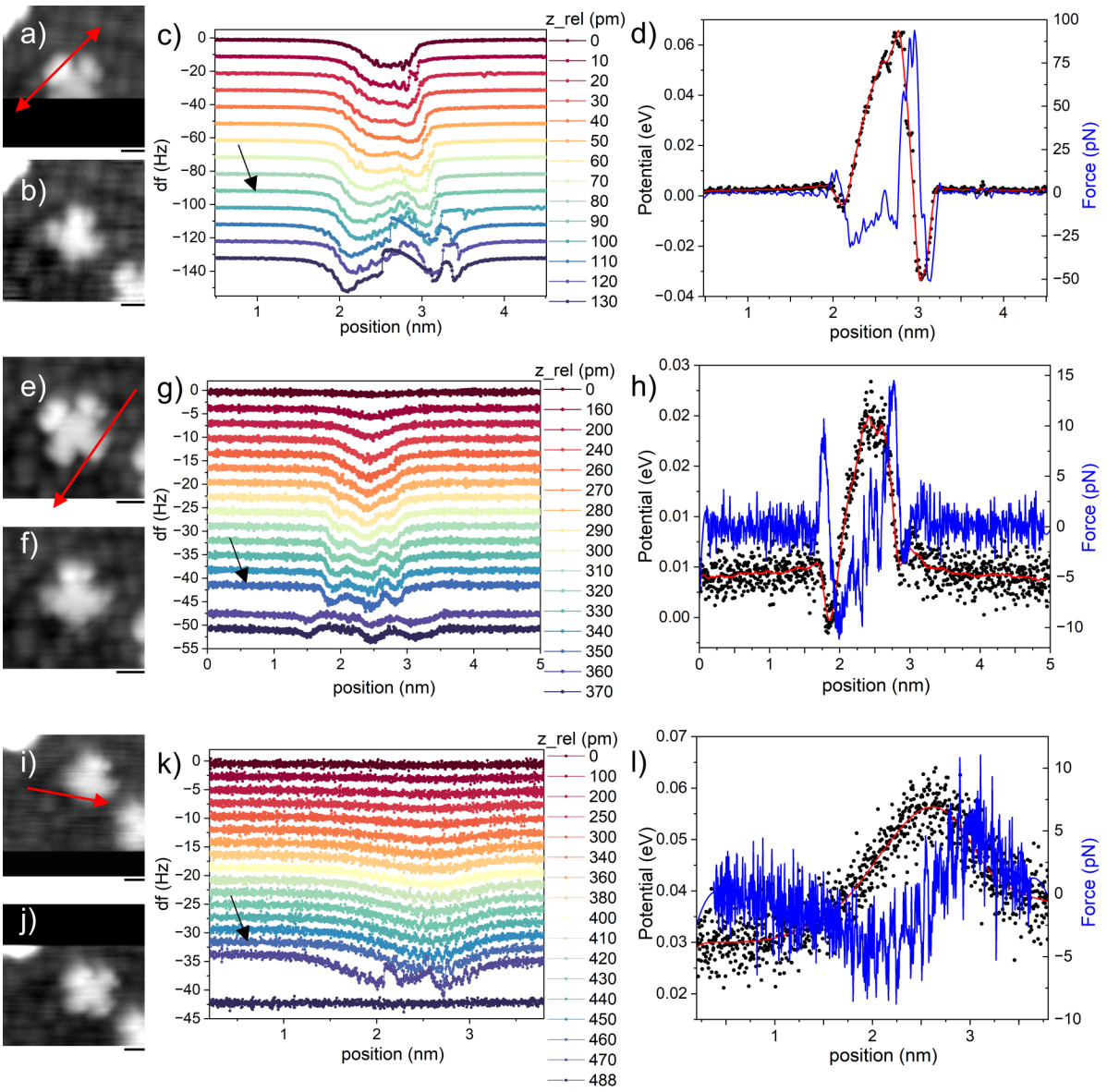

Figure 4.20.: Three sets of successful rotation experiments with a modified Th(NPc)2 double-decker molecule by lateral manipulation. Left column: STM images before and after the lateral manipulation along the path marked in red. Center column: Frequency shift signal measured along the manipulation path for stepwise decreasing tip heights. Black arrows mark the frequency shift curves related to the closest tip-molecule distance before the rotation event. Right column: Calculated potential from the frequency shift curves (black, left y-axis) with the filtered potential in red. The lateral force (blue, right axis) is extracted from the filtered potential. The rotation in set a-d) is induced by manipulation at the modified arm. In set e-f) and i-j) the manipulation along the arm opposite the modified arm requires a much smaller force for rotation. Imaging parameters, scale bar: a,b) -1.2 V, 4 pA, 1 nm; e,f,i,j) -1.2 V, 15 pA, 1 nm.

Summary and Discussion

First, the appearance of the unreacted NPc molecules is discussed. As seen in Figure 4.14 b), NPc molecules can appear either with a cross-shape, as observed in the bottom layer, or with a "double C" resembling contrast, found in the second layer. The change between the cross-shape and double C like contrast in NPc molecules is analyzed in detail by Wu and colleagues [245]. They rationalize these two appearances with different positions of the hydrogen atoms in the macrocycle.
Depending on the equilibrium of the switching rate between a trans- and cis-isomer, differences in the appearance in STM measurements arise. The switching rate is faster then typical STM imaging times, which means that a superposition between the isomers is observed. If the equilibrium is more towards the trans-isomer, a cross shape appears, while two cis-isomers relate to the double C type contrast. The four-fold degeneracy of the cis-isomers is reduced to two isomers due to the interaction with the substrate. In the present case, the C-shape appears in second layer molecules already at bias voltages about $\pm$ 0.3 V, while in the study of Wu the C-shape appears in the monolayer only at voltages < -2 V. This indicates that hydrogen transfer is facilitated in second layer NPc's. In the submonolayer and monolayer regime we observe exclusively a cross shape, even at higher negative bias (-3 V). Considering the present data is recorded at 5 K, this is in agreement with their statement that elevated temperatures (100 K, 300 K) enable a higher cis-isomer ratio.
The synthesis of Th(NPc)2 double-deckers is supported by three main points, 1) a modified contrast compared to the bottom layer NPc, 2) centering of the top NPc on the lattice of the bottom layer and 3) in the control experiment without Thorium the double-decker species is not observed. These double-deckers can be further modified by a voltage pulse, reducing the four-fold symmetry. The brighter contrast on the modified naphthalene arm is tentatively assigned to a dehydrogenation. Voltage pulses are known to induce dehydrogenation at the C-H bond in phthalocyanines [247].
In the rotation experiments the unmodified double-deckers proved difficult to rotate, since the bottom layer was often modified or the double-decker was removed entirely. Intermolecular interactions between the top and bottom ligand may also be resulting in a high rotational barrier. For Cerium based double-decker molecules consisting of a bottom phthalocyanine and top phthalocyanine or tetraphenylporphyrin ligand, a higher rotational barrier was proposed for the phthalocyanine-terminated molecule (C_8OPc)Ce(Pc) compared to the tetraphenylporphyrin-terminated molecule (C_8OPc)Ce(TPP) [80].
Another challenge is the inherent four-fold symmetry. In STM images it is not possible to discern configurations which are rotated by 90°. In the corresponding frequency shift data, recorded between the STM images, no clear indication for such 90° rotation events is found. The corresponding analysis is documented in the appendix in Figure A.16.
In contrast, the modified species behaves differently. This species can be rotated easily without influencing the bottom layer of NPc molecules and STM images reveal geometries where the top half is stable in a 45°-rotated configuration. A rotation back into the initial position is also possible.
This data set is then used as a starting point to test the extraction of the magnitude of

the lateral force from height-dependent frequency shift data. Similar to the method used in the experiment of moving a cobalt atom on Pt(111) [52], the Sader-Jarvis algorithm is implemented [104, 105]. Immediately obvious is the small signal-to-noise ratio (SNR) in the frequency shift, potential and in the extracted lateral force. While in data set one, frequency shift values of -10 Hz up to -20 Hz lead to a reasonably good SNR in the potential, the frequency shift data in the data sets two and three feature only a magnitude of about -7 Hz. In the next step the lateral force is extracted by taking the negative derivative in the manipulation direction. As a prerequisite, the potential curve needs to be smoothed in order to obtain a derivative where the signal is clearly larger than the noise. Several paths for smoothing are explored, such as filtering the raw df-data or applying different filters to the potential. While smoothing the raw df-data with a moving average results in the desired better SNR in the potential and force, the value of the maximum potential and force are too variable with the filter settings. Increasing filter width leads to smaller values in both potential and force. In contrast, using the raw df-data and applying the filter solely to the potential leads to a smaller improvement in the SNR in the potential and force. A moving average, butterworth and Savitzky-Golay filter are varied and tested for SNR improvement and creation of artefacts. The best compromise was achieved with the Savitzky-Golay filter of polynomial degree three and width of $4 - 10\%$ of the line length.
Next, we relate the obtained values of the double-decker rotation to similar force measurements. Moving Co atoms requires 210 ± 30 pN on Pt(111), 17 ± 3 pN on Cu(111) and moving CO molecules on Cu(111) requires 160 ± 30 pN [52]. Few examples of moving larger, organic molecules are reported. For moving H2-Pc molecules on Pb(111), 5-17 pN are found, note that these values vary due to many possible molecule/substrate configurations and additional contributions from rotational movement [53]. PTCDA molecules can be pushed on Ag(111) with a force of 170-210 pN [54]. For specific conformers of tetra(4-bromophenyl)porphyrins on Cu(111) 200-340 pN are necessary for lateral displacement [56]. The wide range of values indicates that the manipulation process of adsorbates is complex and many factors such as molecule-substrate interaction, conformation, and concomitant rotation need to be considered.
Copper phthalocyanine (CuPc) molecules are rotatable on Cu(111) by overcoming a barrier of $17 - 26$ meV, although this rotation is concomitant with a change in geometry [233]. DFT calculations, assuming no geometry change, predict an energy barrier of ≈ 70 meV [248]. For tilting a NO molecule on Cu(110) a torque of 100 pN·nm is reported [249]. Here, forces between 6 and 95 pN are obtained for the double-deckers, which are within a similar range as the examples above. The largest value of 95 pN might contain artefacts originating from the non-zero frequency shift signal at the farthest distance [104, 250]. Nevertheless this outlier is listed for completeness. Furthermore, the measured values for the torque on the double-deckers, 4.7 pN·nm and 13.0 pN·nm, show a large deviation, which results mainly from the differences in the measured force. The difference in the force values is in part attributed to the manipulation positions, i.e. the rotational barrier can differ depending if the force is applied on a modified naphthalene arm on the double-decker or on a unmodified arm. Further influences on the force measurements are discussed below.

The tip shape and termination influence the extracted force values, as shown by a comparison of Cu, CO, Xe and CuOx tips[251]. Ternes et al. found deviations about 5 % related to tip effects [52]. For CO-terminated tips it is also documented that the shape of the metal tip behind the front metal atom affects force measurements [252]. CO-tips are also not stiff and exhibit lateral flexibility[253]. The exact tip termination in the present case is unknown, most likely it is not a CO-tip but a metal tip. Distortions of the tip shape might be present during manipulation and influence the force measurements. Moreover, the present system is more complex than an isolated atom, allowing for additional effects to influence the rotation. In particular since the molecule was modified, the assumption of a NPc unit rotating in a strictly parallel plane might not hold anymore. Instead, a "wobbly" motion might take place. Furthermore, the interaction between the modified naphthalene arm and the bottom layer NPc is anticipated to differ to the interaction between pristine naphthalene and NPc. This could play a role in the difference in the force of about one order of magnitude, when rotating the modified double-decker at these two different naphthalene arms.
A more accurate measurement of the force can be achieved by increasing the statistics and by additionally subtracting the long range component in the tip-sample interaction. Moreover, DFT calculations regarding the geometry and rotation behavior might shed light on additional phenomena. For example bowl shape geometries were found in Tb(Pc)2 [254] and Th(TPP)2 [196], pointing to potentially more complex rotation paths.
Overall the method of lateral manipulation and simultaneously recording the frequency shift was successfully transferred to rotating a molecular unit. This way a lower limit for the necessary torque was also extracted.
The current data and analysis on rotation experiments with Th(NPc)2 double-decker molecules reveal important specifications that need to be considered for a precise quantification of the torque. These specifications are: 1) rigid rotating unit, 2) rotation of isolated molecules and 3) distinguishable rotated states, which will be discussed in the following.
First, the molecular unit should only rotate upon manipulation. A possible geometry distortion in a non-rigid molecule would drastically increase the complexity of the analysis when separating the effects from rotation and distortion. For this purpose structures containing sp^2-hybridized carbon moieties such as benzene rings are suitable. These are anticipated to feature a rigid motion, due to inherent limitation of rotational degrees of freedom between the C-C bonds. On the contrary, sp^3-hybridized groups are difficult to use, since rotation around a C-C axis within a molecule was observed upon lateral manipulation with the tip [255].
The second argument is closely related to the first one, as interactions of molecules in the vicinity to the rotatable unit can affect the rotation. Considering double-decker systems of tetraphenylporphyrins, the phenyl groups of the two double-decker halves are not co-planar, which can lead to unwanted interactions between the two halves during rotation experiments [196]. Moreover while interlocked molecular gear systems are interesting for their own aspects [256–258], the interaction of the molecular gears would interfere with the purpose of quantifying rotation of single molecular units, or even

lead to blocking of the rotation [258]. The rotation of isolated molecules also relates to the underlying support. To exclude a rotation of the whole system and only probe the relative rotation of the molecular unit, the supporting structure needs to be fixed. In the case of double-decker type systems, this means that the lower half needs to be fixed against rotation. This is typically achieved the double-decker molecules embedded in a dense packed assembly. The employed on-surface synthesis protocol provides an elegant solution since it yields both a fixed lower half in a dense packed layer and a lateral separation of the double-deckers suitable for unblocked rotation.
Third, final states that are clearly distinguishable in STM images from the initial state before the rotation are necessary for a direct confirmation of the rotation. The double-decker system in the present study demonstrates this by serving as a counter-example. With the four-fold symmetric top half, rotations by 90° are indistinguishable in STM images. Furthermore possible rotated states that differ only slightly from 90° rotations and tip-related changes, which result asymmetric imaging conditions, are difficult to separate. While in the Th(NPc)2 case this issue was solved by modifying a molecule as described above, another option is to use an already marked molecule during the on-surface synthesis. In this case, one has to carefully check that the asymmetric precursor still results in a dense packed bottom layer. Otherwise, a sufficiently strong interaction with the metal support would be required to anchor the bottom half such that only the top half is rotating. A linear molecule, anchored to the surface via an O-Au bond, clearly fulfills these symmetry criteria and is probed for rotation [73, 259]. However, difficulties may arise when treating this rotation as a rigid body phenomenon.
In summary a double-decker molecule is a promising system to quantify torque on the single-molecule level. With consideration of the aspects above an improved model system can be developed for future studies.

4.3. Conclusions and Outlook

The first section 4.1 documents the adsorption and temperature-induced reaction of hemithioindigo molecular motors on Ag(111) and Au(111). An upright adsorption geometry is necessary for unhindered rotation of the motor unit. The motor molecules are designed to anchor to the surface via sulfur groups. Previous experiments confirmed that t-butyl groups can be cleaved from the sulfur groups upon annealing. In these experiments the motor molecules in form clusters instead of the anticipated upright standing individual units.
Two approaches are investigated in this thesis to achieve isolated, upright adsorbed motor molecules. On the one hand, supramolecular assemblies with C_{60} result in separated phases with the motors assuming a similar adsorption geometry as without the C_{60} molecules. On the other hand, a TBB-based covalent organic framework prevents island formation and guides the molecules into pores of the network, resulting in isolated species. On both network-systems, TBB-COF on Ag(111) and TBB-COF on Au(111), the motor molecules adsorb in a flat-lying geometry in the pores. Consequently, the network is a suitable template to steer the motor molecules into individual units.

In order to simultaneously achieve an upright standing configuration a different set of "feet", which connect the motor to the surface, might be beneficial. Although the precise structure of the connecting unit is difficult to predict, tripodal structures are employed in combination with tip-induced manipulation for changing the adsorption geometry of molecules with comparable size [216]. A similar tripodal structure as molecular feet in the motor molecules could result in an upright standing adsorption geometry.
In the second section 4.2 we demonstrate the successful on-surface synthesis of Th(NPc)2 double-decker complexes embedded in a dense packed NPc layer. The double-deckers feature a different electronic structure and the top half than NPc molecules in the bottom layer. The top half is orientated with a 45° offset with respect to the molecules in the bottom layer. Rotation via lateral manipulation is challenging for the pristine double-deckers. Modifying the double-decker via a voltage pulse facilitates subsequent rotation and allows us to extract a lower limit of the required torque of 9 ± 8 pN·nm. Finding and controlling a model system with satisfactory specifications is challenging but a necessary step towards quantitative characterization of torque in the rotation of single molecules.

5. Characterization and On-Surface Metalation of Carpyridines

Understanding the shape-property relation is fundamental to many processes on the molecular scale. For macromolecules such as proteins the correctly folded structure is necessary to perform their biological function. For smaller molecules shape-property relations manifest themselves for example in their stereochemistry, a subfield of chemistry with wide implications for the reactivity of molecules. Further shape-property relations are found in light absorption/emission [260] and host-guest interaction [261]. For molecules on surfaces the spin state in spin-crossover complexes depends on the conformation of the molecule [262, 263]. In regards to magnetic phenomena efforts have been taken to expand metallo-porphyrins and -phthalocyanines, a rather planar group of molecules, to non-planar magnetic complexes [264].
These examples span many topics, highlighting that is is necessary to define the term "shape". Starting from the sum formula, the molecule can have different constitutional structures, i.e. different connectivity between the atoms, or different stereochemical formulas [265, 266]. These classifications and their subcategories are described by the different types of isomerism. A subcategory, conformation isomers, are important for the shape of porphyrins, a class of molecules which have a plethora of essential applications, e.g. heme is responsible for the oxygen-binding in blood [84]. In particular the out-of-plane distortions of these macrocyclic molecules are relevant for the shape-property relations.
Gaussian curvature K is a criterion to classify the out-of-plane distortion molecular systems [267]. The three cases of $K = 0$, $K > 0$, $K < 0$ and their implications for rotational and translational freedom have been instructively sketched by Woods [88]. A scheme of these cases is also presented in Figure 5.1 a). Specifically, molecules with negative curvature, as found in a saddle shape conformation, are restricted in rotation and translation such that, ordered columns are anticipated.
In this chapter, a saddle-shaped class of molecules, so called carpyridines, is investigated. The structure features similarities to porphyrins, but due to their constitution carpyridines feature an inherent saddle shape. Their structure is shown in Figure 5.1 b). First reported in 2011 by the group of Prof. Klaus Müllen [87], substantial synthetic efforts are currently performed by the group of Prof. Michel Rickhaus. They focus on synthesizing curved organic molecules and are creating a library of different carpyridine molecules accompanied by a systematic characterization and their application in self-assembled structures. See for example references [88–90, 127, 268, 269].
The name carpyridine originates from the subunits in the macrocycle, namely two carbazole and two pyridine groups, see also Figure 5.1 b). As the naming scheme 2H-Car-R

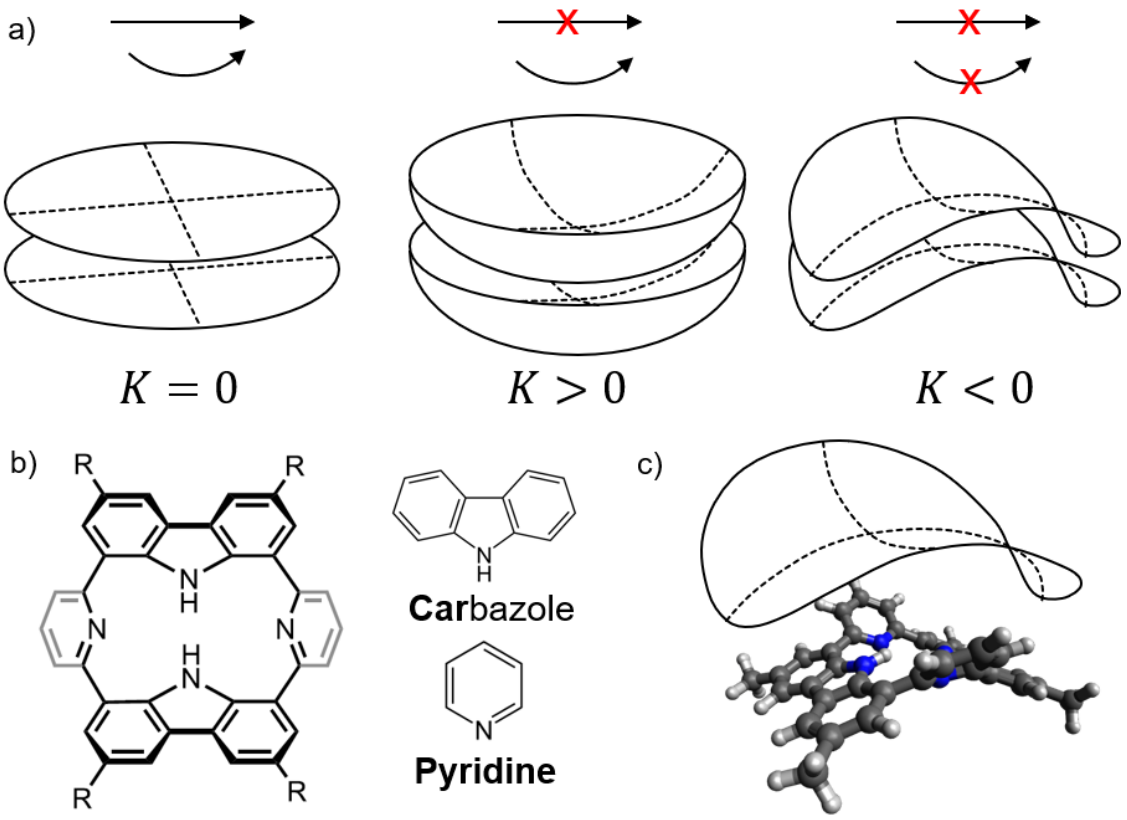

Figure 5.1.: Sketch of molecules with different gaussian curvature in self-assembled stacks and general structure of carpyridine molecules. a) Disc-shaped molecules ($K = 0$) are free to translate and rotate, bowl-shaped molecules ($K > 0$) can only rotate and saddle-shaped molecules ($K < 0$) are fixed against translation and rotation. b) 2H-Car-R carpyridine molecules consist of 2 carbazole and 2 pyridine subunits with R= -H, -tBu, -Ph, -alkyl chain, etc. c) Sketch of the inherent saddle shape on top of a gas phase model of 2H-Car-C1, shown in a "pyridine-up" orientation. Figure adapted from Ref. [88].

suggests, a variety of substituted carpyridine species have been synthesized. Numerous unmetalated (2H-Car-R) and metalated (M-Car-R) molecules have been synthesized in the Rickhaus group, typically substituted with 4 alkyl chains of equal length. A common feature is the inherent saddle shape, caused by the specific way the four subunits are connected. This illustrated by the saddle shape diagram and molecular model in Figure 5.1 c).

Carpyridines assemble in impressive long range ordered structures, for example micrometer long sheets are achieved by depositing 2H-Car-C6 from toluene on a C/Cu grid [88]. In this case, the saddle shape locks the molecules in position and prevents translation and rotation. The hexyl side chains allow interaction between the columns via van der Waals interactions [88, 89]. Further control on the self assembled structures could be achieved by adding two additional substituents. Employing 2H-Car-C6-C6, which features a total of 6 side chains, the molecules form bundled fibers instead of columnar sheets [90]. The driving intermolecular forces in these processes are attractive pi-pi interactions between the individual carpyridine cores and van der Waals interactions between the respective alkyl side chains. The saddle shape was identified as necessary to prevent rotation of the carpyridines in the stacks. These are two examples of so called shape-assisted self-assembly (SASA), where the conformation of the molecules aids to direct the self assembly into extended structures [88].
Furthermore, carpyridines feature similar dimensions as porphyrins. Porphyrins have been intensively studied on surfaces [82, 83] with numerous chemical and physical properties characterized in great detail, providing reference systems for the on-surface characterization of carpyridines. A particular interesting property for comparison is the saddle shape. On most metal surfaces porphyrins adsorb with a saddle shape [270–274], while on Cu(111) tetraphenylporphyrins adapt an inverted saddle shape with their pyrrole rings pointing upwards, demonstrate the influence of the surface [275]. In the crystal structure free-base porphyrins exhibit a slight saddle shape [84]. On the contrary, the carpyridines feature a stronger saddle shape deformation in the crystal structure than the porphyrins, providing a different starting point for the on-surface investigations.
Here, these carpyridine molecules are investigated in an UHV environment on noble metal surfaces with scanning probe microscopy and complementary X-ray photoelectron spectroscopy techniques. Specifically the methyl substituted species 2H-Car-C1 (i.e. -R = -CH_3 in Figure 5.1 b) on Au(111) is discussed in detail in the first section. Comparisons are drawn to 2H-Car-C2 (i.e. -R = -C_2H_5 in Figure 5.1 b) on Au(111) and Ag(111). Additional results from on-surface metalation experiments of 2H-Car-C1 with Cu and Fe are presented in the second section. The comprehensive characterization serves as reference for future studies of carpyridines on surfaces. Figure 5.2 provides an overview of this chapter. The following key questions are addressed 1) Is the saddle shape maintained on the surface ? 2) What is the orientation of the molecule on the surface? 3) What is the behavior in metalation experiments?
Detailed answers are reported in this chapter. In particular the following properties are observed: Upon adsorption on the surface the carbazole units orientate in a planar geometry to the surface. The pyridine groups maintain their tilt angle, resulting in a saddle-shape on the surface. This geometry is quantified by NEXAFS measurements. The saddle-shape orientation, i.e. "up" or "down", is indistinguishable by NEXAFS, however it is unambiguously clarified by tip-sample distance dependent AFM experiments in combination with simulated AFM data. Additional characterization of electronic molecular features is provided by STM and STS measurements.

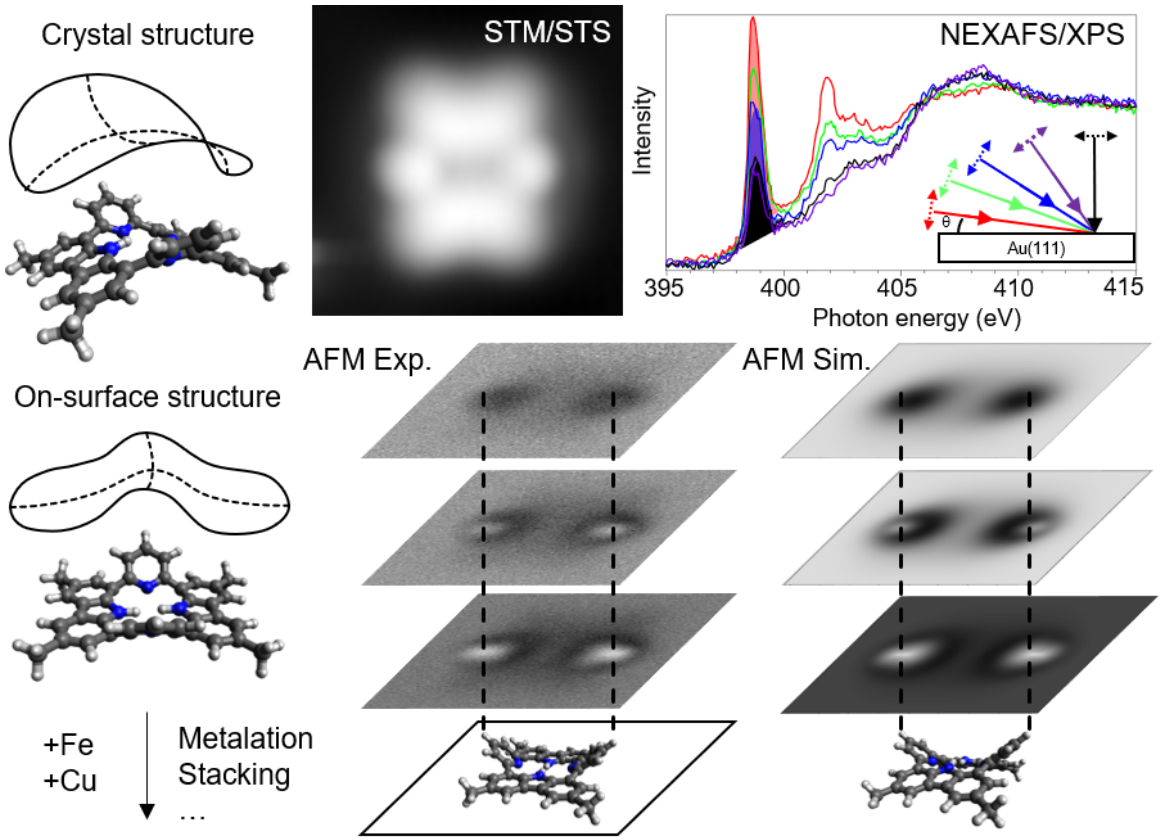

Figure 5.2.: Overview of the characterization of carpyridines on surfaces. In the crystal structure the molecules feature an inherent saddle shape. Upon evaporation on the surface, the molecules adsorb in a slighty flattened geometry with the pyridine groups pointing up. Various surface science techniques including STM, STS, NEXAFS, XPS, AFM are employed to characterize the electronic and geometric structure on the surface. Potential use of carpyiridines in metalation reactions is also investigated.

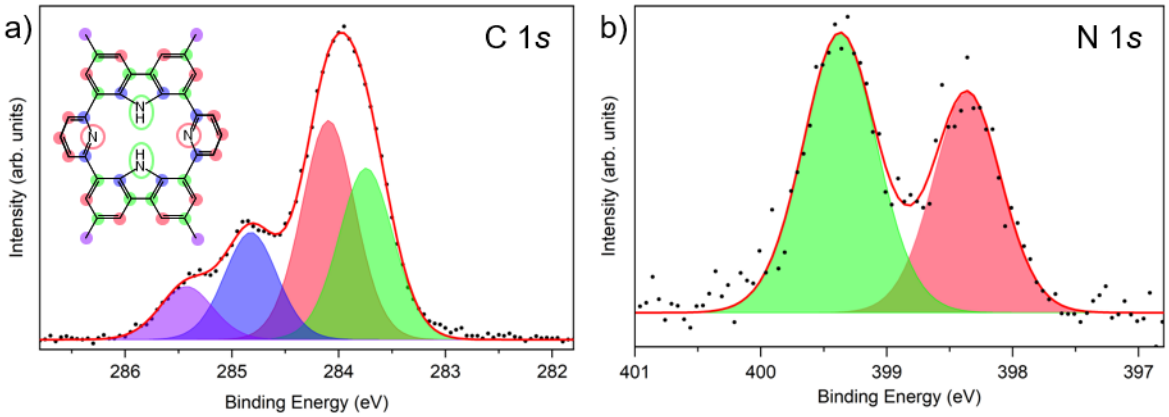

Figure 5.3.: X-ray photoelectron spectra of the a) C 1s and b) N 1s region of 2H-Car-C1 on Au(111). A model with the corresponding assignment of the carbon and nitrogen species is shown in the top left.

5.1. On-Surface Characterization of 2H-Car-C1

5.1.1. Chemical Composition

Information about the chemical structure of 2H-Car-C1 is gained via X-ray photoelectron spectroscopy. The molecules are evaporated at 340°C onto the Au(111) surface, held at room temperature. The corresponding spectra of the C 1s and N 1s region are displayed in Figure 5.3.

The carbon spectra is modeled with 4 peaks, guided by the different chemical environments of the carbon atoms in the molecule. The area and peak positions are given in Table 5.1 with colors corresponding to the model in Figure 5.3 a). The carbon species are grouped by their next neighbours into carbon connected to 1) only other carbon atoms (C-C,C,C green), 2) carbon and hydrogen (C-C,C,H red), 3) carbon and nitrogen (C-C,C,N blue) and 4) the sp^3 hybridized carbon in the methyl groups (C-C,H,H,H violet). The modeled area ratios in the spectrum agree with the expected area ratios. The peak positions are comparable with reported values from literature: sp^2-hybridized carbon C-C,C,H and C-C,C,C are found at 284.2 eV and 284.6 eV on Au(111) [276]. sp^3 C-C,H,H,H in the ethyl group of octaethylporphyrins on Au(111) is located at 285.6 eV [277]. In porphines on Cu(111) the C-C,C,N signal is observed at 285.2-285.8 eV [278].

Next, we focus on the N 1s spectrum in Figure 5.3 b). Two peaks are present, located at 398.3 eV and 399.3 eV. In comparison with free-base porphyrins, the low binding energy component is attributed to iminic -N= nitrogen in the pyridine moiety and the high binding energy peak to the pyrrolic -NH nitrogen in the carbazol moiety [278]. Interestingly, the energy separation between the species is 1 eV, which is considerably smaller than typical separation of around 2 eV found in porphyrins [83, 278–281]. In porphyrins a shift of the iminic component towards the pyrrolic component at higher binding energies is attributed to a stronger interaction of the iminic nitrogen with the substrate. In the present case of 2H-Car-C1/Au(111) the iminic component is located

	C-C,C,C	C-C,C,H	C-C,C,N	C-C,H,H,H
Model	32%	37%	21%	11%
Experiment	(32 ± 3) % 283.7 eV	(40 ± 3) % 284.1 eV	(19 ± 1) % 284.8 eV	(10 ± 1) % 285.4 eV

Table 5.1.: Peak areas and peak positions corresponding to the XPS data in Figure 5.3.

at 398.3 eV, which is close to values 398.1 - 398.4 eV [278, 281] observed for porphines and porphyrins on Cu(111). However, Au(111) is an inherently less reactive substrate than Cu(111), indicating that the different interaction between the pyridine groups in the carpyridine and the surface is not only an effect from the substrate. A stronger interaction could be due to a different geometry, as expected from the intrinsic saddle shape of the carpyridines.
From the C 1s and N 1s XPS data we conclude that the 2H-Car-C1 molecules adsorb intact on the surface. Intact molecules are essential to probe further properties such as their electronic structure and conformation.

5.1.2. Self-assembly and Electronic Structure

Additional information about the assembly and electronic structure is provided by scanning tunneling microscopy and spectroscopy measurements. The overview STM image in Figure 5.4 a) reveals molecules self-assembled in linear patterns. The herringbone reconstruction remains partially observable after molecular deposition, pointing to a moderate molecule-substrate interaction. Upon closer inspection three species are observed: a symmetric species (yellow circle), an asymmetric species with one additional protrusion (blue arrow) and a symmetric species with two additional protrusions (red arrow), see also panel 5.4 b). The majority of molecules belong to the symmetric species, constituting 81% of all molecules. The relative concentrations of the species with one or two additional protrusions amount to 18% and 1%. On lower coverage samples, the two species with additional protrusions are found predominantly at elbow sites of the herringbone reconstruction. The molecular islands on these low coverage samples follow the high-symmetry directions of the reconstruction. For the data in Figure 5.4 we focus first on the majority species. In the zoom-in image 5.4 c) the shape of a single molecule is highlighted in yellow. The carbazole units appear with a C-shaped contrast, while each pyridine group is related to a round protrusion between the two C-shapes. The nearly rectangular unit cell measures a_1=(1.71 ± 0.05) nm $\cdot$ b_1=(1.20 ± 0.04) nm and encloses an angle of $(88 \pm 2)^\circ$.
In order to disentangle electronic and geometric effects on the STM signature we address the electronic properties and non-planar shape of the molecules separately, starting with the electronic properties. Bias dependent imaging with a CO-terminated tip, as displayed in Figure 5.5, shows the molecules with similar STM signatures. Across the measured bias range the general features persist, where the carbazole units appear with

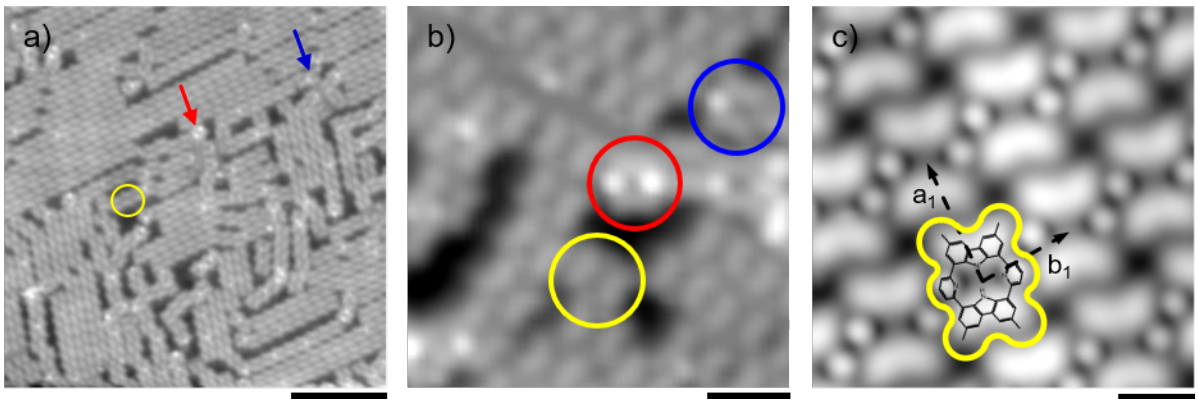

Figure 5.4.: STM images of 2H-Car-C1 on Au(111). The overview image a) shows 2H-Car-C1 molecules in self assembled stripes. Blue and red arrows mark minority species with one or two additional protrusions. These species are also highlighted in the intermediate scale image b). In the zoom-in image of the dominant species (c) a single molecular unit is highlighted by the yellow frame and the structure formula is overlaid. Imaging parameters, scale bar: a) 58 pA, 1.0 V, 10 nm; b) 58 pA, 1.0 V, 2 nm; c) 500 pA, 50 mV, 1 nm.

an elongated shape. At energies close to 0 V, the C-shape contrast of the carbazole unit appears with a subtle splitting at the ends. At lower negative voltages, the pyridine groups feature a greater intensity than the carbazole groups. In this regime the shape changes to a shorter C-shape, orientated perpendicular to the C-shape of the carbazole units.
A bias series of 2H-Car-C1 assembled in a linear way is shown in Figure A.17, also recorded with a CO-tip. The molecules in the assembly exhibit virtually the same contrast as the isolated molecules, excluding assembly-related effects on the contrast. On the contrary, when imaging the molecules with a metal tip, differences appear as displayed in Figure A.18. The circular protrusion, located at the pyridine groups, is most prominent in the intermediate bias range in Figure A.18 ($\approx$1 V until ≈ -1 V). Furthermore, upon closer inspection of the carbazole unit, subtle differences are observable. At large positive bias values, the carbazole units exhibit a straight line as contrast. The characteristic C-shape occurs at smaller voltages with the arch pointing towards the center of the molecule. Then, at more negative bias the C inverts the direction with the arc now pointing away from the center.

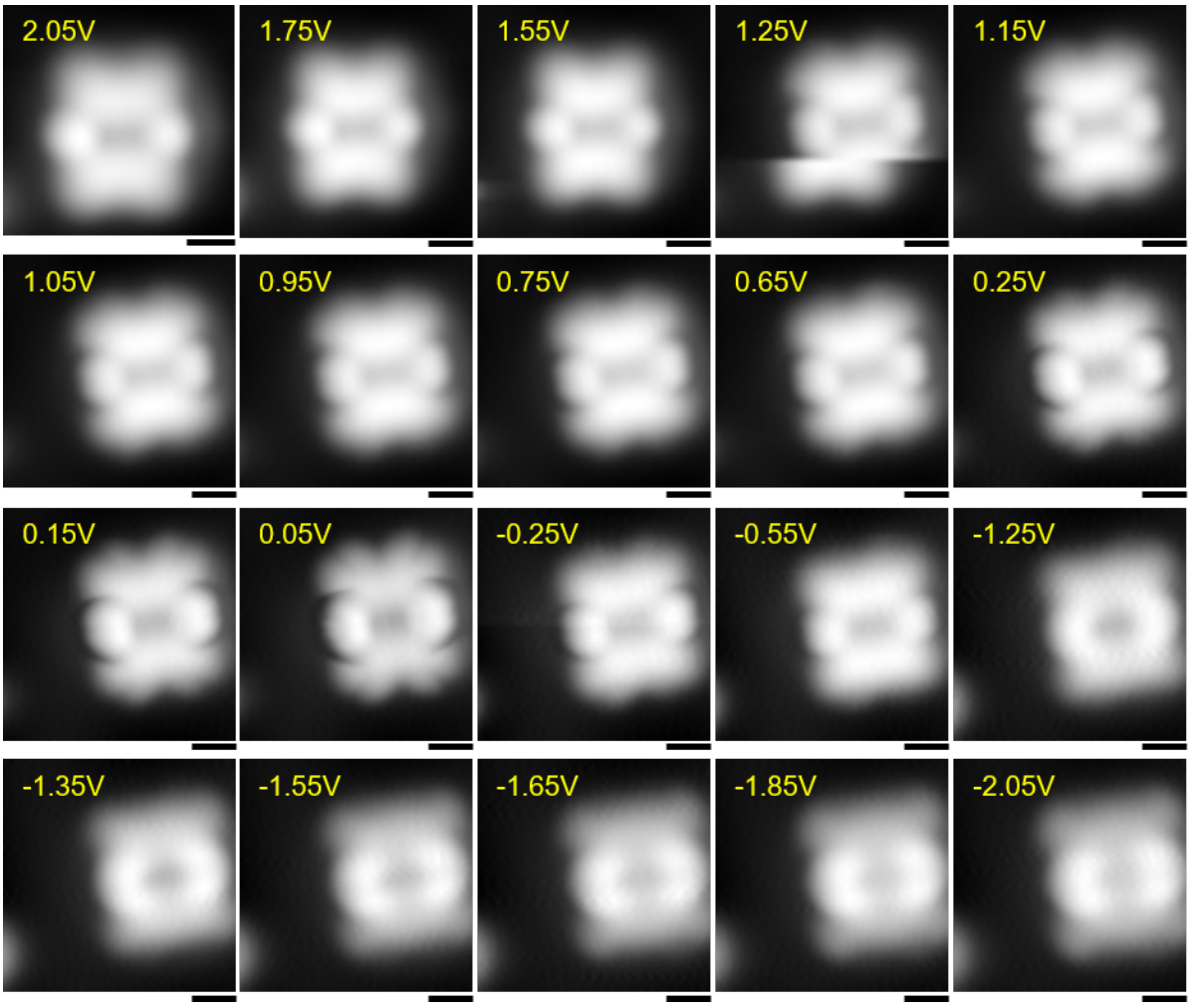

Figure 5.5.: Bias series of an isolated 2H-Car-C1 molecule on Au(111) imaged with a CO tip. The molecule moved during scanning at 1.25 V. Imaging parameters, scale bar: 3.0 pA, 0.5 nm.

More details about the electronic structure are extracted from the STS measurements, shown in Figure 5.6. Two molecules, one on the edge and one in the assembly are compared. Spectra are recorded on the marked position on each molecule and displayed in b) for the edge molecule and c) for the molecule in the assembly. The spectra are vertically offset for clarity, dashed horizontal lines mark the respective zero intensity. The respective reference above Au(111) is plotted in black. For both molecules molecular states are clearly discernible in the occupied states region at -1.35 V and -1.6 V. Above the pyridine group (position 6) and close to the center of the molecule (position 4) both states contribute to the STS signal. On top of the carbazole unit (position 3) mainly the higher energy state is present. In the unoccupied states region a broad slope is present for both molecules. A difference between the two molecules is observed in the spectra recorded near the methyl groups (position 2). The contribution from both the occupied and unoccupied states to the total signal is larger for the molecule in the assembly. A similar effect occurs at position 5 on the assembly-molecule, where the intensity of the unoccupied state is larger than at a similar position on a edge-molecule. These differences appear between the molecules and are attributed to superposition of non-interacting states at these interstitial sites [282].
The spatial extensions of the states, with their respective energies marked with vertical lines in Figure 5.6 b-c), are displayed in the constant height dI/dV maps in panels 5.6 e-g). The state at -1.35 V is located mainly in the center of the molecule with a nodal plane through the pyridine groups. The unoccupied state mostly follows the geometry of the molecule. In Figure 5.6 g) the contrast near the pyridine groups and methyl groups differs between the assembly and the pyridine and methyl groups at the edge, in agreement with the data in Figure 5.6 b,c). Additional maps in constant current mode are shown Figure A.19. Note, that in constant-current maps artefacts, originating from the variable tip-sample distance, might obscure features in the density of states [283, 284].
In summary, distinct molecular states are identified in the occupied states region and a broad feature is observed in the unoccupied states region. For an extended discussion of these molecular states and comparison to porphine and porphyrin species see discussion in section 5.3.

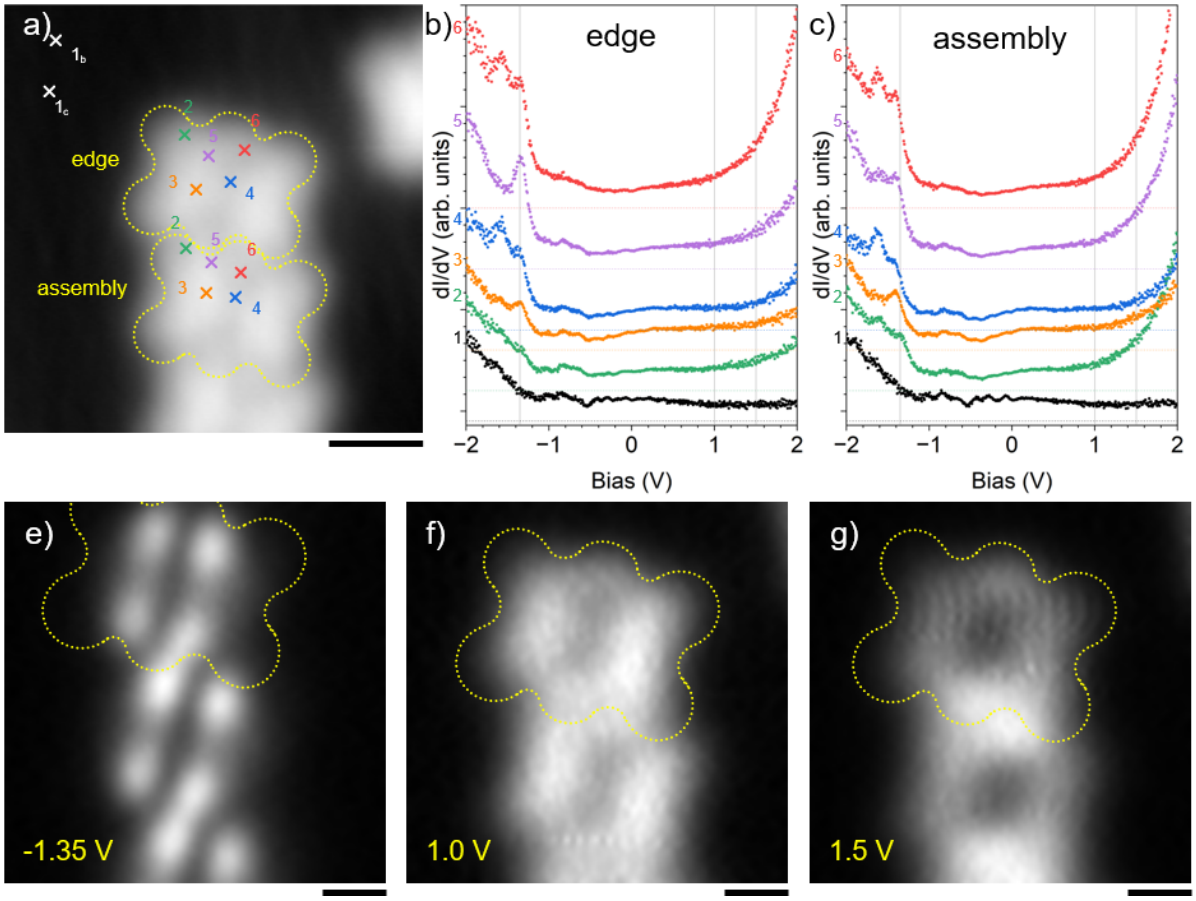

Figure 5.6.: dI/dV measurements on 2H-Car-C1/Au(111). a) STM image of 2H-Car-C1 molecules at the edge and in the assembly. The marked locations correspond to the position of the spectra shown in b) and c) respectively. b,c) STS spectra of 2H-Car-C1 at the edge (b) and in the assembly (c). e-g) Constant-height dI/dV maps at the energies marked with vertical lines in graphs b,c). Imaging parameters, scale bar: a) 20 pA, 0.6 V, 1 nm; e-f) 0.5 nm.

5.1.3. Saddle Shape Geometry

The non-planar geometry of the carpyridines on the surface is probed via NEXAFS and nc-AFM measurements. The results of the NEXAFS experiments at the N K-edge are displayed in Figure 5.7. The angle dependent spectra (Θ = 30°, 42°, 53°, 70°, 90°) in panel 5.7 a) feature a prominent peak a 398.7 eV, attributed to a π^* resonance in the pyridine-nitrogen [285–287]. The second feature at around 402 eV is attributed to the π^* resonance in the carbazole-nitrogen [285, 288–290].
First, we focus on the pyridine-related feature. The intensity decreases with increasing incidence angle of the linearly polarized light. The peak has its maximum intensity in the red spectrum, recorded at 30°. At 90° (black curve), where the light is polarized parallel to the surface, the peak does not vanish. This behavior indicates a tilted geometry of the pyridine ring. Quantitative analysis of the pre-edge region allows to plot the peak area (red markers) in an array of theoretical curves [118, 119] for different orientations of the pyridine moiety (Figure 5.7 b). Details on the analysis are provided in section 2.2.2. The curves are labeled with the angle of the pyridine ring to the surface, i.e. 0° denotes an orientation parallel to the surface and 90° a perpendicular geometry. The experimental data points are compatible with an orientation of $(35 \pm 10)°$.
Second, we focus on the carbazole-related signal. At grazing incidence of the light the signal features maximum intensity, while it vanishes at normal incidence. This behaviour indicates that the carbazole unit is orientated nearly parallel to the surface.

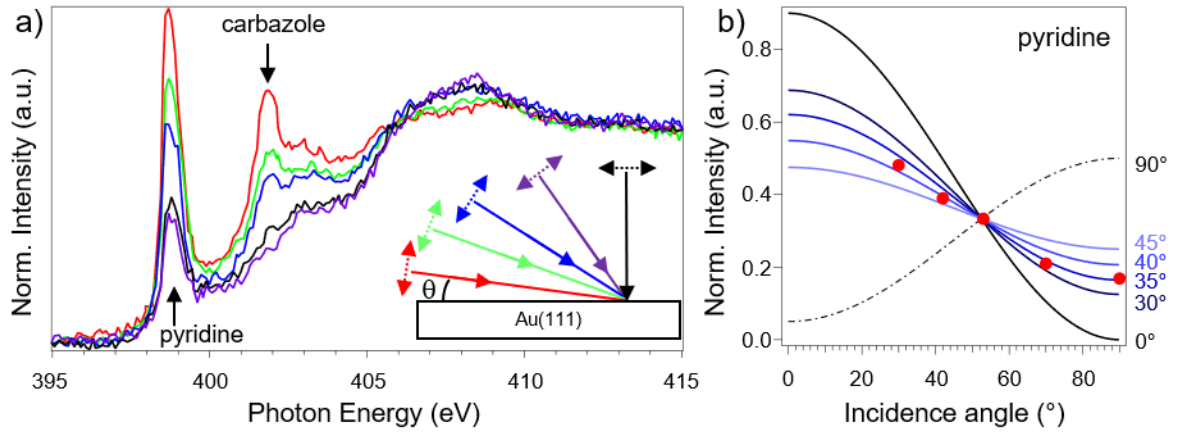

Figure 5.7.: N K-edge NEXAFS spectra of 2H-Car-C1/Au(111) for varying incidence angles Θ = 30°, 42°, 53°, 70°, 90°. a) The π^* resonance around 399 eV, originating from the nitrogen in the pyridine group, shows non-zero intensity at normal incidence. The signal of the carbazole group vanishes at normal incidence. The inset in the bottom right depicts the polarization direction of the electric field (dashed lines) of the incoming light (solid lines). b) The normalized peak area is plotted for each incidence angle (red markers), allowing to determine a tilt of the pyridine group with respect to the surface of $(35 \pm 10)°$.

From this NEXAFS data set we know that the carpyridines do not change into a com-

pletely planar geometry upon adsorption on the surface, but the macrocycle retains a saddle-shape. Specifically the pyrdine groups are tilted by about 35° from the surface and the carbazole units are nearly parallel to the surface. This limits the adsorption geometry to two cases: a pyridine-up and a pyridine-down configuration. Nc-AFM measurements are employed to clarify which of these two cases is present on Au(111).
Figure 5.8 shows height dependent frequency shift images of 2H-Car-C1/Au(111) and simulated frequency shift images of the pyridine-up geometry. For comparison, panel 5.8 a) displays the STM contrast with a model overlaid. Next, in constant height frequency shift images the tip-sample distance is decreased sequentially. Starting with the tip located at the maximum height in the constant-current STM image, two features appear at the position of the pyridine groups in the constant height frequency shift image in panel 5.8 b). Upon approaching (panels 5.8 c-d) a protrusion appears above each pyridine group, indicating a pyridine-up geometry. The protruding features are related to the repulsive regime, indicating a larger distance of the pyridine groups to the surface as compared to the other parts of the molecule. Images of the bottom part of the molecule, marked by the yellow frame in image 5.8 e), are recorded at lower tip heights (panels 5.8 f-h). In this region another pair of protrusions appears, attributed to the two methyl groups bound to the carbazole group. Having now located the protruding pyridine and methyl groups, further zoom-in images (5.8 i-k) are measured above the carbazole group (red frame in image 5.8 h). The contrast in images 5.8 j) and k) resembles closely the five- and six-membered rings in the carbazole.
In order to correlate the recorded frequency shift data with the orientation of the saddle shape, probe-particle model simulations are performed for a pyridine-up geometry (Figure 5.8 l-s) and pyridine-down geometry (Appendix Figure A.20). The simulated frequency shift images reveal that, on the one hand the pyridine-up geometry features two central protrusions, while on the other hand four protrusions are present in the pyridine-down geometry. Following this, the saddle-shape orientation of the carpyridines is identified as pyridine-up.

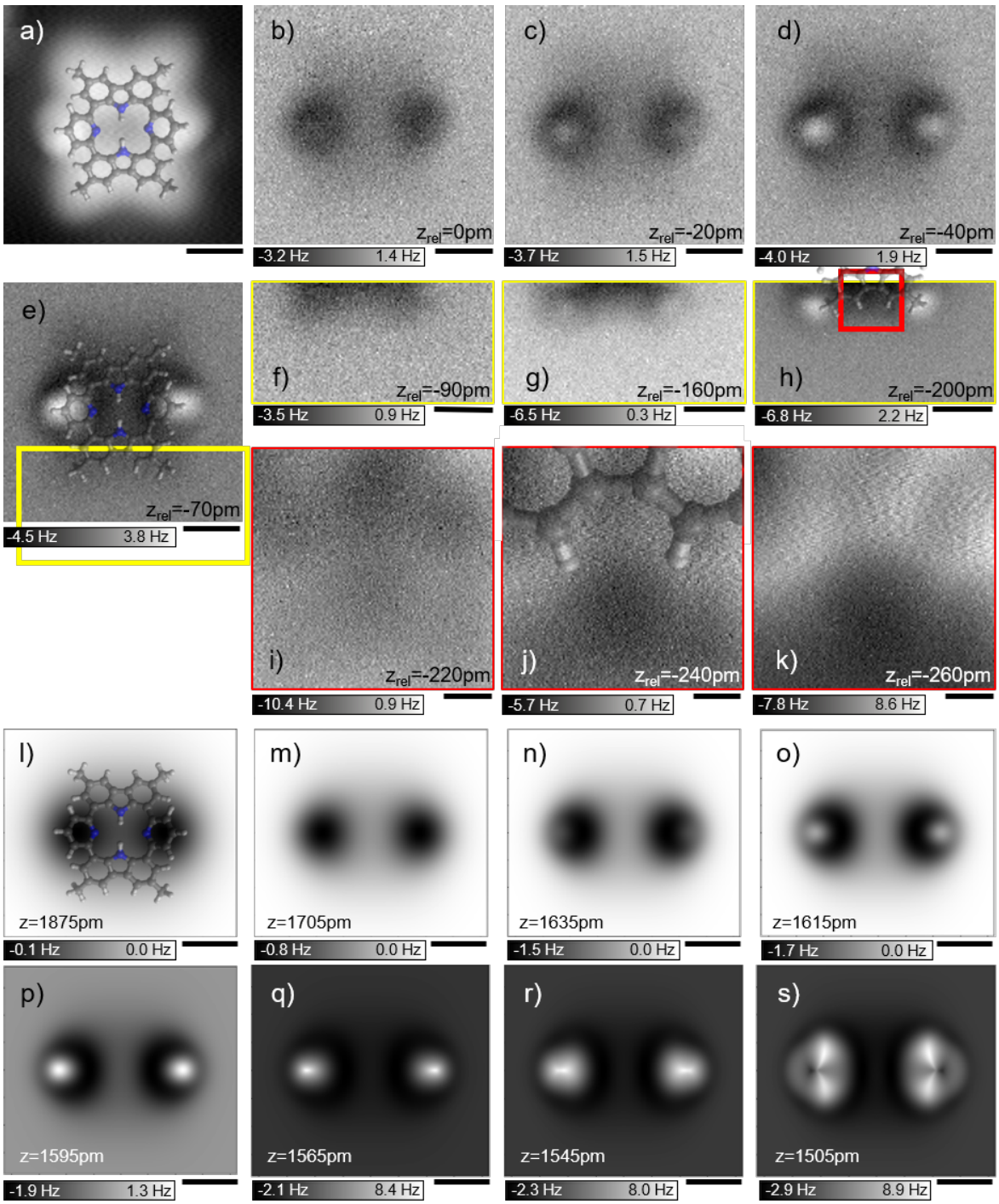

Figure 5.8.: Experimental (b-k) and simulated (l-s) NC-AFM contrast of 2H-Car-C1 upon decreasing tip-sample distance. a) STM image with a molecule overlaid. b-e) constant-height frequency shift images show that upon tip approach the pyridine groups appear as protrusions. f-h) zoom-in on the yellow marked region above the positions of the methyl groups. i-k) zoom-in on the carbazole region marked in red in h), revealing the 5- and 6-membered rings. l-s) The pyridine groups appear first in a probe-particle simulation. Imaging parameters, scale bar: a) 3 pA, 100 mV, 0.5 nm; b-h) 1.7 mV, 0.5 nm; i-k) 1.7 mV, 0.1 nm; l-s) 0.5 nm.

In order to highlight the topography of the molecule, selected frequency shift images are treated with a gaussian filter and stacked in Figure 5.9. Here, panel 5.9 a) and b) show an isolated molecule and a molecule in a staggered, self-assembled phase, respectively. Both molecules persist in the pyridine-up orientation. On the molecule in the self-assembly the same order of pyridines-methyl-carbazole appearing upon tip approach is observed. The corresponding molecular models, optimized in gas phase, are overlaid in Figure 5.9 c,d). When comparing the model to the experimental data, the model appears too short in both cases. This is assigned to a slight elongation of the molecule on the surface, maximizing the interaction of the π-system in the carbazole moieties with the surface.

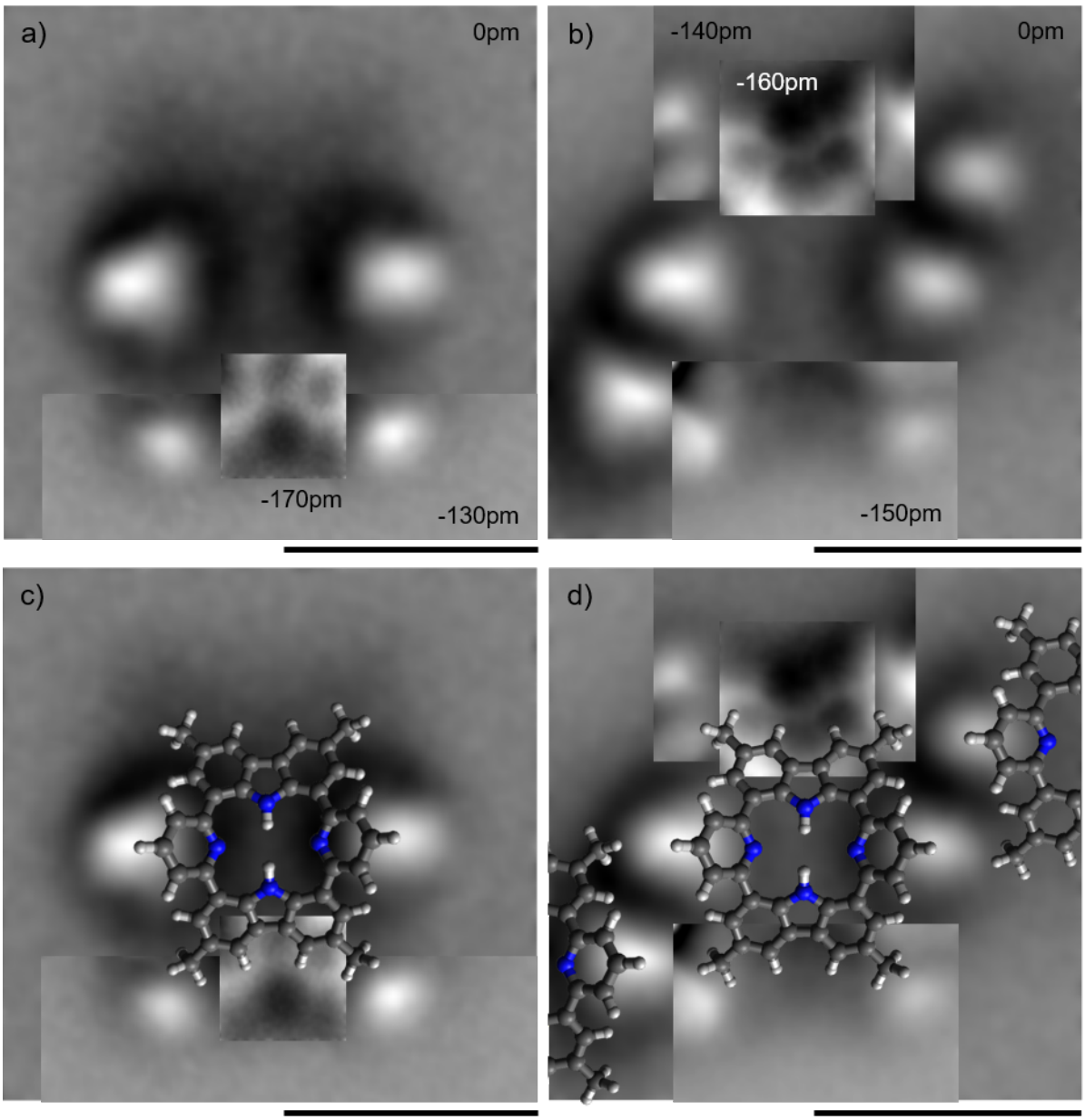

Figure 5.9.: Stacked frequency shift images at different heights of 2H-Car-C1/Au(111). Isolated molecules a) and self-assembled molecules b) adsorb in a pyridine-up orientation. Corresponding molecular models are overlaid on these images and shown in the panels c) and d). Imaging parameters, scale bar: a,c) 1.7 mV, 1 nm; b,d) 5.3 mV, 1 nm. The data was smoothed via Gaussian filtering. Relative tip heights are given in the insets, negative values are closer to the surface.

In intermediate scale images only the pyridine-up geometry was found for carpyridines without additional protrusions, in agreement with their uniform appearance in STM experiments, e.g. Figure 5.4. Details on the two minority species will be addressed next. As observed in the STM images (Figure 5.4) discussed above, two additional species

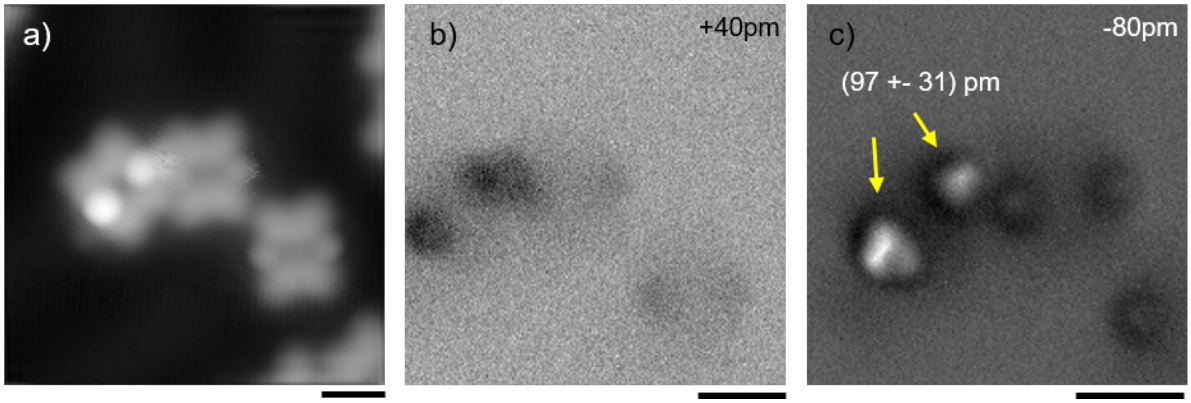

Figure 5.10.: Comparison of the different 2H-Car-C1 species via AFM. In the STM image a) the molecule on the left appears with two bright protrusions compared to the majority molecule in the center. b,c) The frequency shift images reveal the same orientation of the saddle shape, i.e. pyridine up. The bright species protrudes about 100 pm more from the surface than the majority species. Imaging parameters, scale bar: a) 2.7 pA, 300 mV, 1 nm; b,c) 0.4 mV, 1 nm. $z_{rel} = 0$ pm is set to the maximum z value in a).

are present, one species with two bright protrusion at the pyridine group and the other species with only one of the two pyridine groups appearing brighter. They are characterized by AFM measurements shown in Figures 5.10 and 5.11. In the left columns STM images are shown for comparison. The center and right column display the frequency shift signal, with the right column showing images closer to the surface.
A molecule of the bright-bright species is investigated in Figure 5.10. It appears with similar contrast in the frequency shift signal as the majority species. The height dependent images 5.10 b,c) display, that both pyridine groups of the modified species occur at larger tip-sample distances than the majority species. Recording frequency shift vs z curves allows to compare the maximum heights of the pyridine groups in this bright-bright species to the height of the pyridine group in the majority species. The pyridine groups in the bright-bright species are located (97±31) pm farther away from the surface than the pyridine groups in the majority species. Additionally, the bright-bright species is slightly asymmetric with the left protrusion being higher. The values are determined by the location of the minimum in the df vs z curves and averaged over several tips. For an example data set see Figure A.21.
Further species are characterized in Figure 5.11. In addition to the bright-bright species, a bright-dark species is investigated. The bright-bright species consistently exhibits an asymmetric contrast in the frequency shift images 5.10 as well as 5.11 b,c) and 5.11 e,f). In the STM image 5.11 g) a molecule is observed with an additional protrusion in the center. In the frequency shift images 5.11 h) and i) the center also exhibits a protruding feature, pointing towards a possible modification of the center. On this particular species measurements could be performed at closer distances than on the majority species. While molecules of the majority species were pushed away at comparable tip-molecule distance,

the asymmetric molecule here could be imaged easily in the repulsive regime, see panel 5.11 i), pointing to a stronger molecule-substrate interaction. The left pyridine group features additional lobes perpendicular to the pyridine-pyridine direction. These features are also predicted by the probe particle simulation at close distances, see Figure 5.8 s). The increased intensity at the pyridine groups, either bright-bright or bright-dark, is tentatively attributed to geometric effects, see also the discussion at the end of this section.

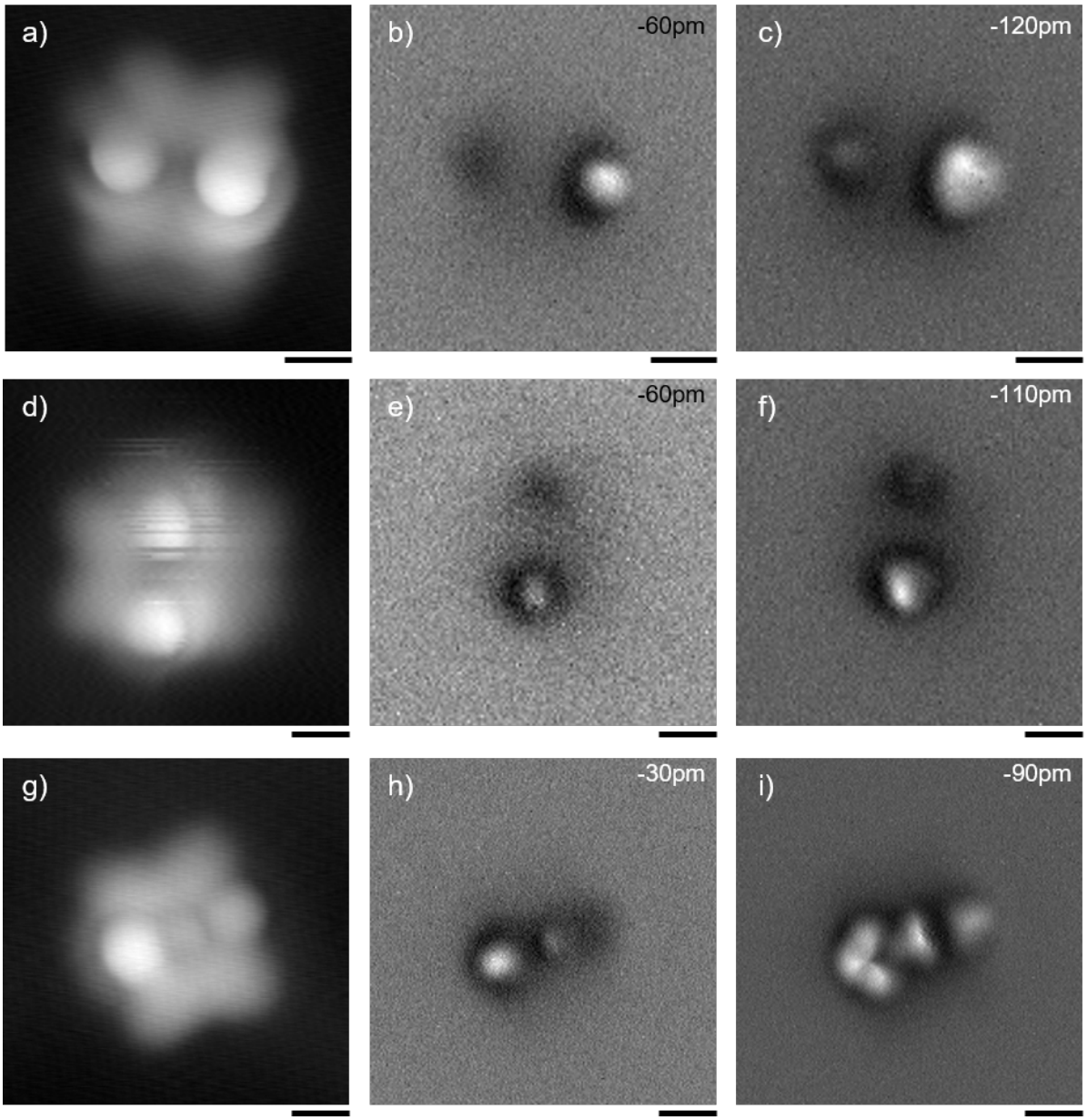

Figure 5.11.: Additional 2H-Car-C1 species characterised by AFM. The left column shows the contrast in STM images, while the center and right column display frequency shift images at different heights. All species adsorb in the pyridine-up geometry. The species in the bottom row features a functionalized center. Imaging parameters, scale bar: a) 3.0 pA, 20 mV, 0.5 nm; b,c) 0.5 mV, 0.5 nm; d) 3.0 pA, 100 mV, 0.5 nm; e,f) 1.3 mV, 0.5 nm; g) 3.0 pA, 100 mV, 0.5 nm; h,i) 1.3 mV, 0.5 nm.

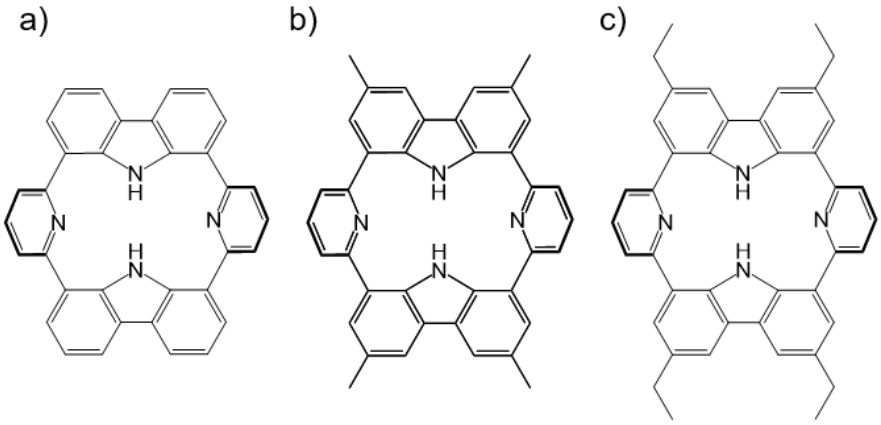

Figure 5.12.: Structural formulas of carpyridine derivatives: a) 2H-Car-H, b) 2H-Car-C1, c) 2H-Car-C2.

5.2. Carpyridines without Alkyl Side Chains and with Ethyl Side Chains

The hydrogen- (2H-Car-H) and ethyl- (2H-Car-C2) terminated carpyridines are also investigated on Ag(111) (2H-Car-H and 2H-Car-C2) and Au(111) (only 2H-Car-C2) substrates. The corresponding structural formulas are shown in Figure 5.12.
First, the evaporation temperature of 2H-Car-H is estimated from the presence of carbon and nitrogen signals in XPS measurements. Deposition experiments on Ag(111) held at room temperature with crucible temperatures stepwise increased from 295°C to 365°C showed a reasonable C 1s signal, indicative of deposition of a carbon containing species, see Figure 5.13 e). While the peak shape resembles the 2H-Car-C1/Au(111) signal, modelling of the 2H-Car-H related signal was not feasible.
STM experiments reveal different species present on the surface for experiments with evaporation temperatures between 295°C and 365°C. Images of the sample related to 330°C evaporation temperature are shown in Figure 5.13. In the overview image 5.13 a) only a minor amount of molecules, some are marked by red arrows, resembles a contrast similar to 2H-Car-C1. In the zoom-in image 5.13 b), this species exhibits a similar contrast to the 2H-Car-C1 molecules, e.g. as visible in Figure 5.4. Thus, this species is attributed to 2H-Car-H molecules. Depending on the tip condition, the molecules can be imaged with inverted contrast as shown in Figure 5.13 c). Here, the protrusions at the pyridine positions appear brighter than the carbazole unit, as opposed to the appearance in b).
Comparable depositions of 2H-Car-H at 295°C, 315°C, 365°C, 410°C yield lower concentrations of species that could be attributed to 2H-Car-H. On samples prepared with 365°C crucible temperature and above, no indication of 2H-Car-H was found.
Interestingly, during deposition experiments at 315°C crucible temperature the molecular substance transitioned from a powdered material before heating (panel 5.13 d, left) to a molten substance (panel 5.13 d, right). In contrast, both 2H-Car-C1 and 2H-Car-C2

remained in their powdered phases after heating to 330°C.
In summary, we could deposit the unsubstituted species 2H-Car-H, however their identification is more challenging compared to the methyl- and ethyl- substituted carpyridines. This is attributed to the presence of multiple species of molecules on the surface and the lack of a characteristic self-assembly pattern of 2H-Car-H molecules.
Next, results of the ethyl-functionalized species 2H-Car-C2 are described. In XPS experiments of 2H-Car-C2/Au(111), see Figure 5.14, a similar signal as for 2H-Car-C1/Au(111) is found.
STM characterization of the ethyl species is summarized in Figure 5.15. On both substrates Au(111) (panels 5.15 a,b) and Ag(111) (panels 5.15 c,d) the molecule assemble in stripe-like islands. Similar to the 2H-Car-C1 molecules, they align with their alkyl chain facing each other. For the similar 2H-Car-C2 molecule, differing by ethyl instead of methyl side chains, the assembly is shown in Figure 5.15. The unit cells of these ethyl-substituted carpyridines have similar geometry, namely on Au(111): a_2=(1.56±0.04) nm, b_2=(1.26±0.03) nm, $\Theta_2 = (94\pm3)^\circ$ and on Ag(111): a_3=(1.58±0.03) nm, b_3=(1.25±0.03) nm, $\Theta_3 = (91 \pm 3)^\circ$. Interestingly, the carbazole-carbazole direction is shorter for the C2 species compared to the C1 species, for a tentative explanation see the discussion section at the end of this chapter. The dimensions of the unit cell are summarized in Table 5.2.

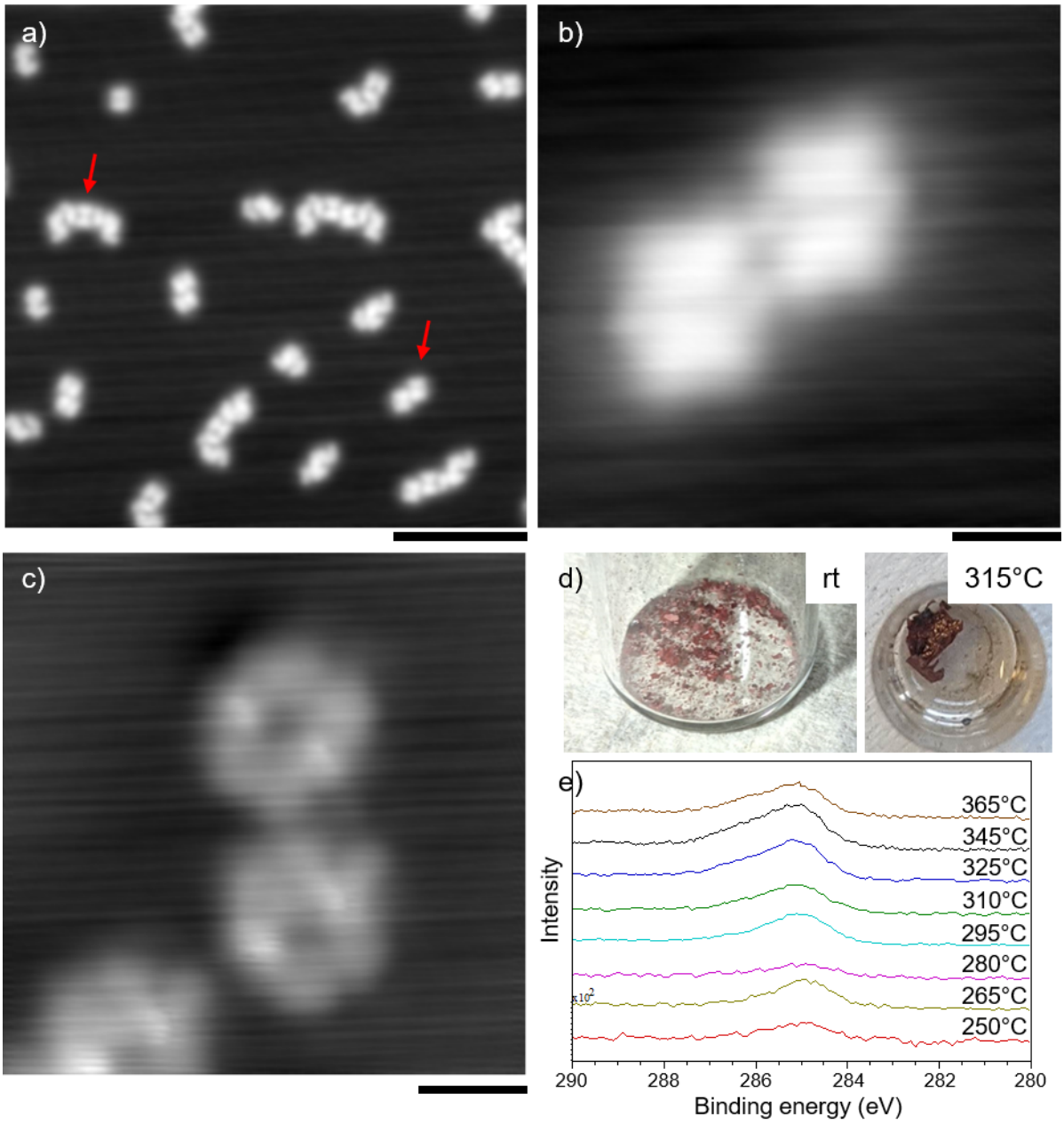

Figure 5.13.: STM characterization of 2H-Car-H/Ag(111) evaporated at 330°C. a) Overview image showing multiple species. Red arrows mark molecules resembling the contrast of 2H-Car-C1. b,c) zoom-in images of the marked species. It is attributed to 2H-Car-H. The "pyridine-down" (b) and "pyridine-up" (c) suggesting contrast depends on the tip condition. d) The photograph of the 2H-Car-H sample after heating to 315°C, reveal a change from a powdered material before heating (left) to a molten substance (right). e) C 1s XP-spectra corresponding to different evaporation temperatures. Imaging parameters, scale bar: a) 94 pA, 0.42 V, 10 nm; b) 200 pA, 0.05 V, 1 nm; c) 290 pA, 0.05 V, 1 nm.

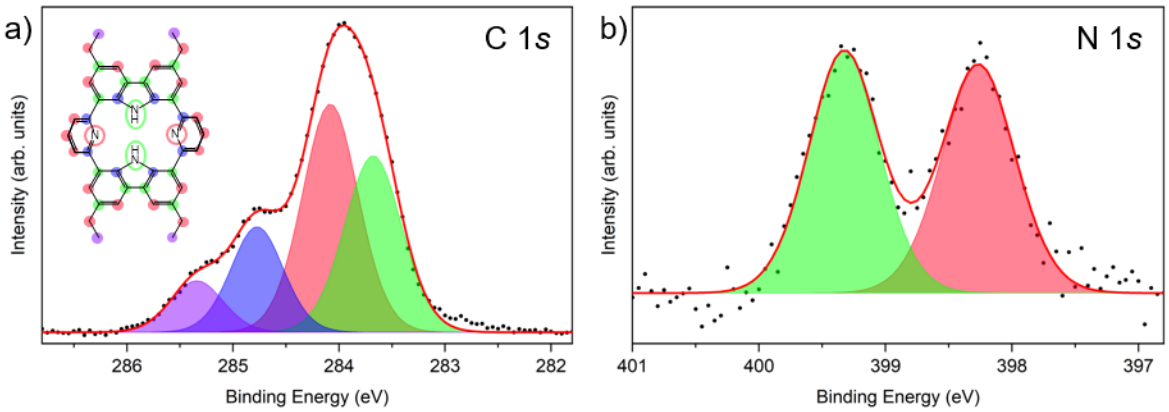

c)

	C-C,C,C	C-C,C,H	C-C,C,N	C-C,H,H,H
Model 2H-Car-C2	29%	43%	19%	9%
Experiment	(32±4)% 283.7 eV	(41±4)% 284.1 eV	(18±3)% 284.8 eV	(9±2)% 285.3 eV
Model 2H-Car-C1	32%	37%	21%	11%
Experiment	(32±3)% 283.7 eV	(40±3)% 284.1 eV	(19±1)% 284.8 eV	(10±1)% 285.4 eV

Figure 5.14.: XPS characterisation of 2H-Car-C2 on Au(111). The C 1s region (a) and N 1s region (b) show similar features as in the 2H-Car-C1/Au(111) system. The corresponding peak parameters and a comparison to 2H-Car-C1 are listed in table c).

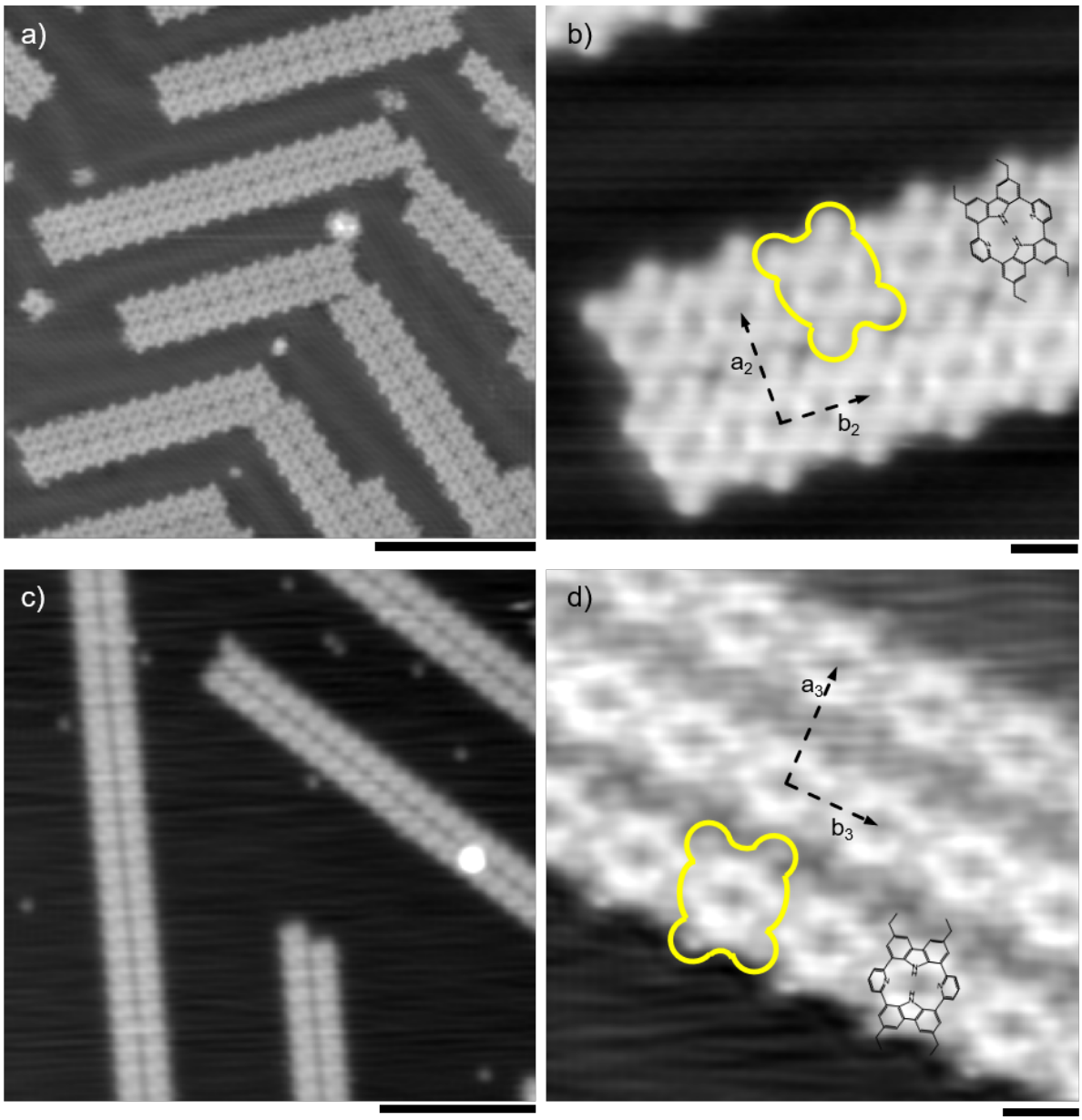

Figure 5.15.: STM characterisation of 2H-Car-C2/Au(111) (a,b) and 2H-Car-C2/Ag(111) (c,d). The molecules assemble on both substrates in linear islands. The unit cells measure on Au(111): a_2=(1.56±0.04) nm, b_2=(1.26±0.03) nm, Θ_2 = (94±3)° and on Ag(111): a_3=(1.58 ± 0.03) nm, b_3=(1.25 ± 0.03) nm, Θ_3 = (91 ± 3)°. Imaging parameters, scale bar: a) 100 pA, 0.2 V, 10 nm; b) 100 pA, 0.7 V, 1 nm, CO-tip; c) 80 pA, 1 V, 10 nm; d) 100 pA, -50 mV, 1 nm.

In the STM images of the ethyl species four round protrusions are visible at the corner of each molecule. They are imaged with multiple tips and are also bias independent, see for example Figure 5.16. Since they are not observed in the methyl- and hydrogen terminated species, these round protrusions are attributed to the ethyl groups.

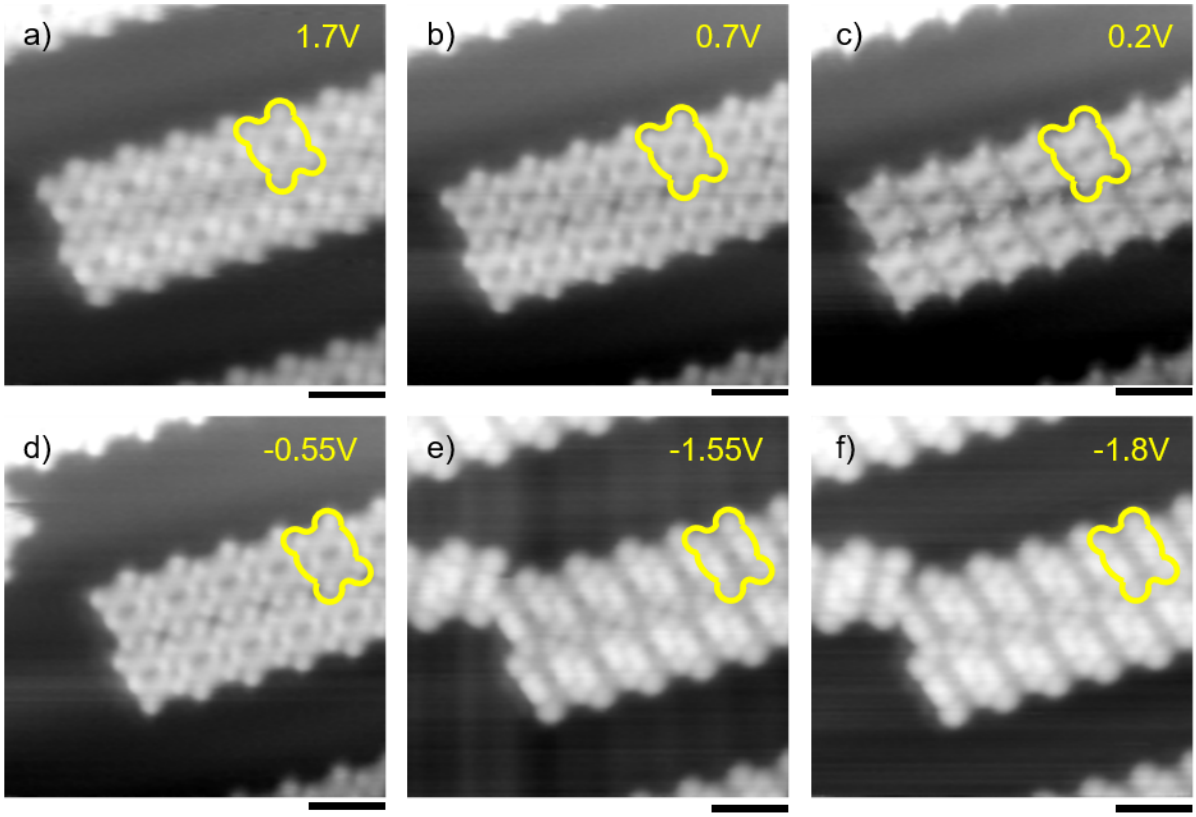

Figure 5.16.: Bias series of self-assembled 2H-Car-C2 molecules on Au(111) imaged with a CO tip. Imaging parameters, scale bar: 100 pA, 2 nm.

	2H-Car-C1/Au(111)	2H-Car-C2/Au(111)	2H-Car-C2/Ag(111)
a	(1.71 ± 0.05) nm	(1.56 ± 0.04) nm	(1.58 ± 0.03) nm
b	(1.20 ± 0.04) nm	(1.26 ± 0.03) nm	(1.25 ± 0.03) nm
Θ	$(88 \pm 2)^\circ$	$(94 \pm 3)^\circ$	$(91 \pm 3)^\circ$

Table 5.2.: Unit cell dimensions of methyl- and ethyl-substituted carpyridines

Overall the STM contrast is similar to the 2H-Car-C1 carpyridines, pointing to a similar "pyridine-up" geometry in the 2H-Car-C2 species. N K-edge NEXAFS measurements of 2H-Car-C2/Au(111) support a non-planar geometry of the pyridine groups, see also Figure A.22. The pyridine signal (399 eV) has its largest intensity at grazing incidence of the light and maintains a residual intensity at normal incidence. The carbazole related peak (402 eV) features a similar trend intentsity when going from grazing to normal incidence, but additionally the signal vanishes at normal intensity. A quantitative evaluation, similar to the 2H-Car-C1/Au(111) system in Figure 5.7, was prevented by the linear increasing background in the region 396-399 eV. This feature is attributed to an unknown artefact, and causes a relative uncertainty of $\approx 75\%$ in the extracted angle of the pyridine group. Consequently, a detailed analysis is omitted. Note that the qualitative trend of the NEXAFS data is comparable to the data taken on 2H-Car-C1/Au(111), indicative of similar geometry of the pyridine and carbazole groups.

5.3. Comparison and Discussion of 2H-Car-H, -C1, -C2

This section addresses non-metalated carpyridines with hydrogen-, methyl- and ethyl-terminations.
First, we focus on the influence of the alkyl chains. In the self-assembled patterns the molecules align with their alkyl chains facing each other, allowing attractive van der Waals interactions. In experiments with carpyridines in solution, performed by the Rickhaus group, van der Waals interactions between the sidechains influence the lateral interaction between molecules [88]. Self-assembled structures on surfaces were investigated by electron microscopy and AFM. The samples were prepared by depositing carpyridines from solution on a C/Cu or C/Ni grid. The authors found an optimum in the ordered self-assembly for an alkyl chain length of n=6. For carpyridines with n=12 and n=0 (2H-Car-H) less ordered assemblies were found. In the present data of 2H-Car-H/Ag(111) no ordered islands are observed. Although the 2H-Car-H experiments are in the low coverage regime, the data indicates that some alkyl side chains are necessary for ordered self-assembly on the surface, similar to the experiments in solution chemistry. The differences in the unit cell dimensions of the 2H-Car-C1 and 2H-Car-C2 species can be explained with attractive intermolecular interactions mediated by the alkyl chains. The distance in the carbazole direction is shorter for the C2-case, an initially counter-intuitive observation where the larger molecule assembles in a more compact way. This

trend is tentatively attributed to attractive intermolecular interactions originating from van der Waals interactions from the alkyl chains, with longer alkyl chains resulting in stronger interactions due to the larger induced dipole moment. A threshold of the chain length, where the unit cell dimensions increase again, is expected. At this point the steric hindrance of the alkyl chains has a significant influence on the assembly.
Next, for the methyl- and ethyl-terminated carpyridines, three species are found. Besides the symmetric majority species, molecules exhibiting a bright-dark and bright-bright type of contrast at the pyridine protrusions are found. An external contamination effect is unlikely, since they are observed in different UHV chambers. A striking similarity is that the "bright-bright/dark" species follow the elbow sites of the Au(111) reconstruction, see for example Figure A.26 a). In previous studies these positions have been identified as potential sources of Au adatoms [291]. Adatom induced bright contrast has been previously identified for TPP on Au(111) [292] as solely an electronic effect. However, here the "bright-bright/dark" contrast is identified via frequency shift measurements as a geometric effect with the pyridine group being further away from the surface as in the majority species (compare also Figure 5.10). This could be related to an elevated position of the carpyridine, caused by an adatom located below. The asymmetry might also be related to a rigid tilt of the molecule or an asymmetric position of the adatom below.
During STM measurements on all three carpyridines (-H, -C1, -C2) on both substrates Au(111) and Ag(111), the molecules are easily movable with the tip. Frequent pushing and pulling of molecules occurs during scanning.
Remarkably, a saddle shape geometry persists on the surface. DFT calculations of a 2H-Car-H stack show a tilt angle of 37.7° of the pyridine group and 19.1° of the carbazole group [88]. In the on-surface experiment the pyridine groups in 2H-Car-C1 feature a comparable tilt angle of $(35 \pm 10)°$. The situation at the carbazole groups is different. In the experiment we observe an angle close to 0°. This way the π-system in the carbazole group is orientated parallel to the surface, maximizing the interaction.
Attempts on inverting the saddle shape via approaching the SPM tip result in lateral movement of the molecule or picking up of the molecule. No indication of a "pyridine-down" geometry was found.
We also draw comparisons to porphyrins, since both molecules, the carpyridines and the porphyrins have 16 atoms in their central macrocycle. Two porphyrin systems are considered, porphine (2H-P) since it is similar in molecular structure to the carpyridines, and H2-TPP/Cu(111) because it assumes an "inverted saddle shape", resembling partially the geometry of carpyridine. In order to quantify the planarity we compare the tilt angles of the pyrrol or pyridine groups with respect to the surface plane. On the one hand, 2H-P/Cu(111) represents a system with a weak saddle shape geometry, where the pyrrolic groups are tilted 7° from the macrocycle [293, 294]. On the other hand, 2H-TPP/Cu(111) shows a strong distortion where an angle of 99° is found between the pyrrole rings and Cu(111) surface [86, 294, 295]. The investigated 2H-Car-C1/Au(111) system lies in between these two cases with a pyridine tilt angle of about 35° with respect to the Au(111) surface. The three cases are illustrated in Figure 5.17.
Now we focus the discussion on the electronic structure. Scanning tunneling spectra

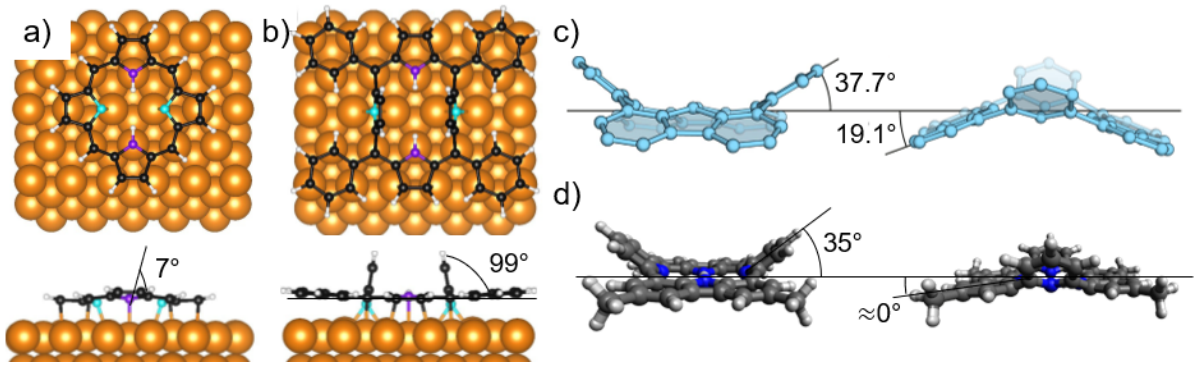

Figure 5.17.: Comparison of the geometry of selected macrocyclic molecules. a) in porphine (2H-P) on Cu(111), the pyrrol groups are tilted by 7°. b) In the inverted saddle shape geometry of tetraphenylporphyrin (H2-TPP) on Cu(111), the pyrrol groups are tilted by 99°. c) DFT simulation of 2H-Car-H reveal tilt angle of 37.7° for the pyridine and 19.1° for the carbazole group. d) Sketch of the 2H-Car-C1 geometry on Au(111), the pyridine groups are tilted by 35° while the carbazole groups are basically parallel to the surface. Panels a,b) are adapted from P. T. P. Ryan, P. L. Lalaguna, F. Haag, et al., Validation of the inverted adsorption structure for free-base tetraphenyl porphyrin on Cu(111), Chemical Communications, 2020, 56, 3681 [294]. Panel c) is adapted from Woods, J.F., Gallego, L., Pfister, P. et al. Shape-assisted self-assembly. Nature Communications, 2022, 13, 3681 [88].

of 2H-P/Cu(111) are reported in Ref. [296]. The spectrum on 2H-P/Cu(111) displays broad features in both the occupied and unoccupied region starting from -1.5 V and 1.0 V, respectively. For 2H-TPP/Cu(111) the LUMO resonance is located at around 0.6 V and a broad feature starts around 1.5 V. In the occupied region a broad peak is observed around -1.5 V [297]. The signal is similar to 2H-TPP/Ag(111) where the pyrrol rings are not pointing away from the surface [37, 298]. In the 2H-Car-C1/Au(111) system the clear feature at -1.35 V (Figure 5.6) in the occupied states region is attributed to the HOMO. In the unoccupied states region the broad feature starting around 1 V is attributed to the LUMO.
Moreover the dI/dV maps provide information on the spatial extend of the molecular orbitals and their symmetry. As reference we compare the measurements to gas phase DFT calculated orbitals from 2H-Car-tBu [87] (see Figure A.23). The LUMO and LUMO+1 are degenerate in energy. A simple overlap of the molecular orbitals reveals intensity along the whole macrocycle except at positions close to the carbazole-nitrogen. In the unoccupied states region the spatial extension of the signal in the dI/dV map at 1.5 V is concentrated along the macrocycle and no intensity is observed among the methyl groups. This is compatible with a superposition of the calculated LUMO and LUMO+1. The calculated HOMO features a charge density also spreading around the macrocycle, but a nodal plane perpendicular to the macrocycle is present connecting the pyridine-nitrogen atoms. This nodal plane is also observed in the experiment, see Figure 5.6 e). The zero intensity along the axis connecting the pyridine-nitrogen atoms supports the

assignment of this state at -1.35 V to the HOMO.
The calculated orbitals corresponding to 2H-P and 2H-TPP are shown for example in Ref. [297, 299]. Compared to the calculated carpyridine orbitals we notice some differences. In the 2H-P and 2H-TPP HOMO, there is non-zero contribution on all nitrogen positions, which is not the case in the carpyridine. The LUMO in 2H-P and 2H-TPP features carbon atoms with zero intensity, located at the edge of the iminic groups. In the carpyridine the wavefunction includes all carbon atoms at the edge of the macrocycle.
Summarizing the electronic structure, we found that 2H-Car-C1 features differences in the electronic structure compared to porphine and tetraphenylporphyrin. They are attributed to differences in the connectivity of the atoms and the resulting non-planarity in the carpyridine species. Furthermore, the specific constitution of the molecule also prevents an extended pathway of alternating single and double bonds. Conjugated bonds are a common criterion to identify possible aromatic pathways in molecules including porphyrinoid macrocycles [300, 301]. This indicates that while the building blocks of the carpyridines, pyridin and carbazol, are aromatic, the macrocycle does not fit this prerequisite for aromaticity.
Finally we discuss the geometric structure of 2H-Car-C1/Au(111). Here, the "pyridine-up" geometry was characterised via a multi-method approach, including STM, AFM and NEXAFS. To date, only one study reports on carpyridines by means of STM. Specifically Co-Car-tBu is investigated with a focus on magnetic exchange coupling with a Ni thin film [264]. In the reported STM image, the molecules appear with a comparable aspect ratio to 2H-Car-C1/Au(111), indicating that the macrocycle is orientated parallel to the surface. However, in the published DFT+U simulation of Co-Car-tBu/Ni(001) interesting differences to the geometry of 2H-Car-C1/Au(111) are revealed. In Co-Car-tBu/Ni(001) the pyridine rings orientate parallel to the surface and the carbazole units are pointing slighty away from the surface resulting in a U-shaped molecule. This is in contrast to the persistent "pyridine-up" saddle-shape found for 2H-Car-C1/Au(111).
In summary we have answered two of the questions posed in the introduction at the beginning of this chapter. First, the 2H-Car-C1 carpyridine molecules maintain their saddle shape when adsorbed on a Au(111) surface. Second, the combination of NEXAFS and nc-AFM measurements reveals that the molecules adsorb with the pyridine groups pointing away from the surface. The third question on the metalation behavior will be addressed in the next section.

5.4. Application of Carpyridines in Self-Assembled Structures and On-surface Metalation Reactions

5.4.1. Stacking

Drop casting carpyridines from solution yields stacks and 2D sheets on the micrometer scale. The interactions in the corresponding self-assembled structures are guided by the intrinsic saddle-shape [88]. Here, the stacking behavior of 2H-Car-C2/Au(111) in high

coverage experiments is investigated by sublimating an amount of 2H-Car-C2 resulting in a coverage between 1 and 2 ML. The corresponding STM images are shown in Figure 5.18. Panel 5.18 a) reveals second layer molecules appearing with two protrusions. Imaging these second layer molecules is difficult, since they can be easily moved with the tip during scanning. See for example the streaks in the bottom left corner. The stacking is elucidated by the adjusted contrast in Figures 5.18 b) and 5.18 c). First, in panel 5.18 b) a grid is overlaid on the bottom layer, marking the periodicity. The position of the second layer molecules with respect to this layer is then compared in panel 5.18 c). The molecules are positioned in a non-commensurate way and feature multiple orientations. Two roughly perpendicular orientations occur, indicating a directed interaction with the molecules in the rectangular assembly in the bottom layer. However, the off-center arrangement of molecules in the second layer excludes extended sheets via columnar growth for this particular system.

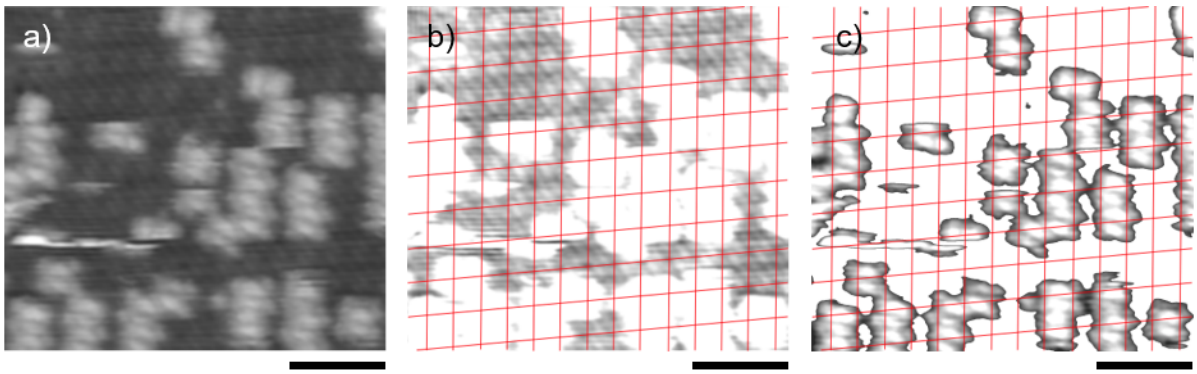

Figure 5.18.: STM measurements of 2H-Car-C2 molecules on Au(111) exceeding 1 ML. a) untreated data. b) Contrast adjusted to the bottom layer molecules with the grid representing the periodicity. c) Contrast adjusted to the second layer molecules, revealing a non-commensurate adsorption. Imaging parameters, scale bar: 28 pA, 1.52 V, 5 nm.

5.4.2. On-Surface Metalation

On surface metalation of porphyrin systems is well studied and variation of the metal center offers control on the properties of the resulting species [302]. Metalloporphyrins are recently envisioned also in quantum information science [303].
Metalation of carpyridines is a method to change the saddle surface area and was investigated via in-solution synthesis [127, 268]. On the contrary to porphyrins, carpyridines have only been metalated with a few elements through means of solution chemistry. In particular, Cobalt-metalated tert-butylcarpyridine species have been reported [87, 264]. In addition, 2H-Car-H, 2H-Car-C6 and 2H-Car-C12 were metalated in solution with Co, Cu and Zn, respectively [127]. For these species stability was found only on the order of hours to days, before demetalation. Carpyridines substituted with 6 side chains such as 2H-Car-C4-C4 and 2H-Car-C6-TIPS have been metalated also with Co, Cu and Zn,

and in addition also with Ni. Nickel-species were even less stable than the other three transition metal carpyridines [268].
The cavity size is determined by the position of the nitrogen atoms of the carbazole and pyridine groups, respectively. The dimensions of the cavity in free-base species are reported on the basis of X-ray diffraction data [87, 268]. The $N_{pyridine}$-$N_{pyridine}$ distance amounts to 3.8 - 3.9 Å and the $N_{carbazole}$-$N_{carbazole}$ are separated by 4.7 - 4.9 Å. For comparison porphyrins feature a size of 4.2 Å.
In the next sections the results of on-surface metalation experiments of 2H-Car-C1 with Cu and Fe are presented. Copper and Iron are both known to readily metalate porphyrins on Au(111) on other surfaces [83, 304, 305].

2H-Car-C1 and Cu

A small amount of Cu is dosed on 2H-Car-C1/Au(111) and the sample is subsequently characterised by XPS and STM. The XPS results are shown in Figures 5.19 and A.24. The N 1s region changes from a distinct two peak line shape into a complex line shape, involving five peaks (Figure 5.19 a). The position of the two species related to the pyridine-(brown, 398.4 eV, 9%) and carbazole-(green, 399.4 eV, 12%) nitrogens are extracted from the unreacted species and are fixed in the modeling of the signal after Cu dosing. Three additional peaks are required to model this signal. The blue species (399.8 eV, 57%) is attributed to NH in the carbazole coordinated to Cu. This position lies close to the binding energy found for coordination between Cu^0 and NH in Tetrapyridylporphyrin/Au(111) at 400.0 eV [304]. Next, the central peak (orange, 398.8 eV, 8%) is attributed to Cu-metalated carpyridine molecules. This value is in the range for reported Cu-TPP (398.5 - 398.8 eV) [306–310], Cu-TBrPP (398.8 eV) [311] and Cu-Pc (398.7 eV) [312] species, synthesized via self-metalation on Cu substrates. For Cu metallated tetrapyridylporphyrins on Au(111) the N 1s peak is located at 398.2 eV [304]. In this study, Cu is present in the +2 oxidation state, while in the present data Cu is in a neutral state, as identified by the Cu 2p 3/2 peak at 931.9 eV (Figure A.24). The assignment of the yellow component (397.3 eV, 13%) in Figure 5.19 remains unclear.
The C 1s spectrum in Figure 5.19 b) only features one additional component after Cu addition. This peak at (285.8 eV, 7%) could be related to a shake-up feature.
Complementary STM measurements on the same sample yield additional insights on the Cu/2H-Car-C1/Au(111) system. The overview image a) in Figure 5.20 shows the surface after Cu deposition. In the zoom in image 5.20 b), three species are distinguishable by the number of bright protrusions per molecule. Similar to the situation prior to Cu-dosing, a species without bright protrusions exists (yellow frame), labeled "dark-dark". Furthermore, molecules can appear with one "bright-dark" (blue arrow) or two protrusions "bright-bright" (red arrow). However, now the relative concentrations have changed with most of the molecules exhibiting bright protrusions.
A bias series of STM images is shown in Figure 5.21. The molecular contrast, specifically round protrusions at the pyridine position and an elongated shape above the carbazole units, persists across the measured bias range. Furthermore, some of the bright-bright species are transformed into the bright-dark type, as marked by the red arrows in Figures

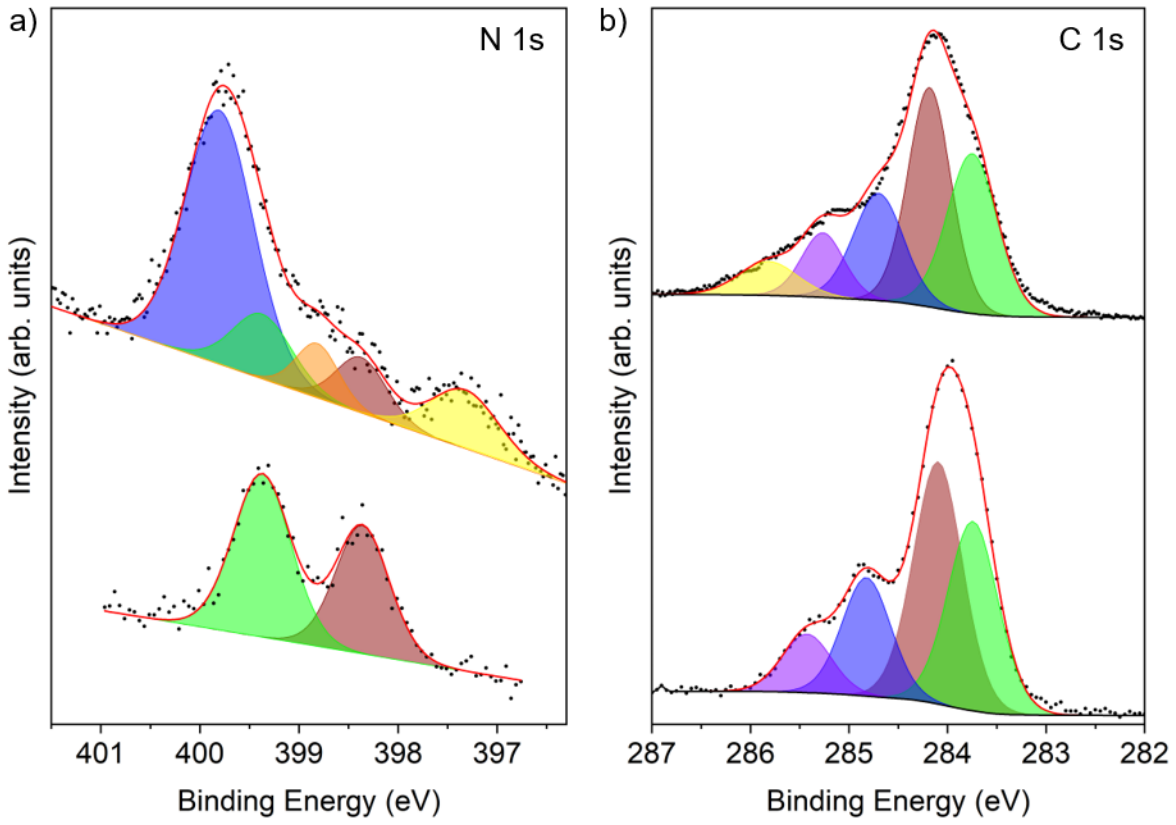

Figure 5.19.: XPS data before (bottom) and after (top) dosing Cu on 2H-Car-C1/Au(111) at room temperature. After dosing, the N 1s signal (a) features a major component at 399.8 eV, while in the C 1s region only a minor change is observed.

5.21 b) and 5.21 d). This switching occurs during scanning at 1.7 V. An unstable molecule is visible in the top right corner of panel 5.21 a). Switching in the other direction was not observed.
The distribution of the three species before and after Cu dosing is given in the table in Figure 5.21 g). The amount of the bright-bright species increases significantly with Cu, while the dark-dark type decreases concomitantly. The concentration of the bright-dark species roughly doubles with addition of Cu. During all of the measurements, with different tips and imaging parameters, no indication of a feature at the center of the molecule was observed.
Dosing copper atoms affects the self-assembly of 2H-Car-C1 molecules. For a comparison between the two systems see Figure A.25. In both cases the majority of molecules are aligned with the carbazole groups facing each other. After dosing Cu, two effects are observed on the self-assembled structures. First, the size of the ordered islands decreases. In particular, the concentration of the assembly featuring the staggered type of carbazole-carbazole alignment (blue and green in Figure A.25 g,h) shrinks in favor of the assembly where the carbazole groups are aligned without offset (red in Figure A.25 g,h). Second, more single-molecule-wide chains and disordered structures (black in Figure A.25 g,h)

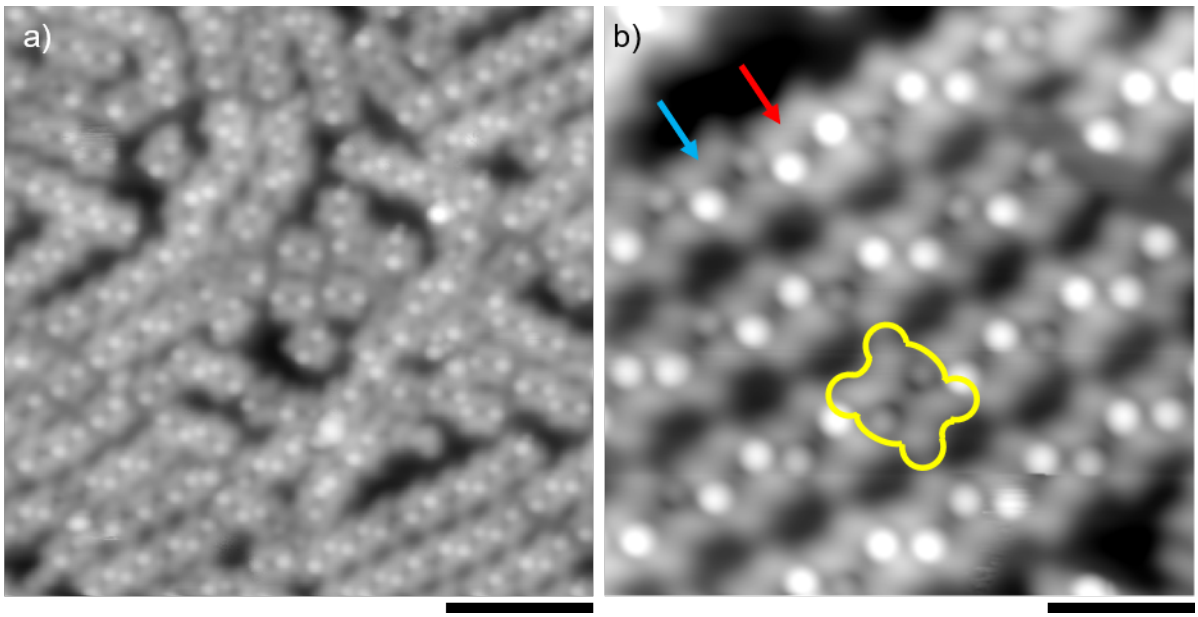

Figure 5.20.: Overview STM image (a) and zoom-in (b) of Cu/2H-Car-C1/Au(111). Three species are present, characterized by the amount of bright protrusions: 0 protrusions "dark-dark" (yellow frame), 1 protrusion "bright-dark" (blue arrow) and 2 protrusions "bright-bright" (red arrow). Imaging parameters, scale bar: a) 35 pA, 0.7 V, 5 nm; b) 500 pA, 50 mV, 2 nm.

are present.
In summary, the aforementioned data clearly supports a modification of 2H-Car-C1/Au(111) with Cu at room temperature. The complex XPS signal in the N 1s region points to a coordination of a majority of the molecules with Cu^0. In STM measurements the bright-bright species is attributed to these Cu-coordinated carpyridines, featuring similar concentrations (STM: 62%, XPS 57%). A possible geometry is that the copper atom is located below the molecule, similar to Cu below TPyP molecules on Au(111) at 300 K [304]. The presence of the bright-bright species in experiments without Cu could be due to the molecules located on Au adatoms. In particular, the striking location of the bright-bright and bright-dark species on elbow sites on low-coverage samples, indicates a relation to adatoms (see for example Figure A.26). For tetraphenylporphyrins on Au(111) a bright species was found and identified as a molecule adsorbed on top of a Au adatom [292].
The difference between bright-bright and bright-dark species could then be similar as hypothesized in the 2H-Car-C1/Au(111) case, i.e. asymmetric position of the molecule on the Cu adatom or a tilt of the carpyridine. Under these assumption the switching from bright-bright to bright-dark would relate to repositioning of the adatom below or tilting of the molecule on top.
A higher concentration of Cu-metalated carpyridines might be achieved with moderate annealing of the sample. For Cu incorporation into porphyrins elevated temperatures are reported [304, 313].

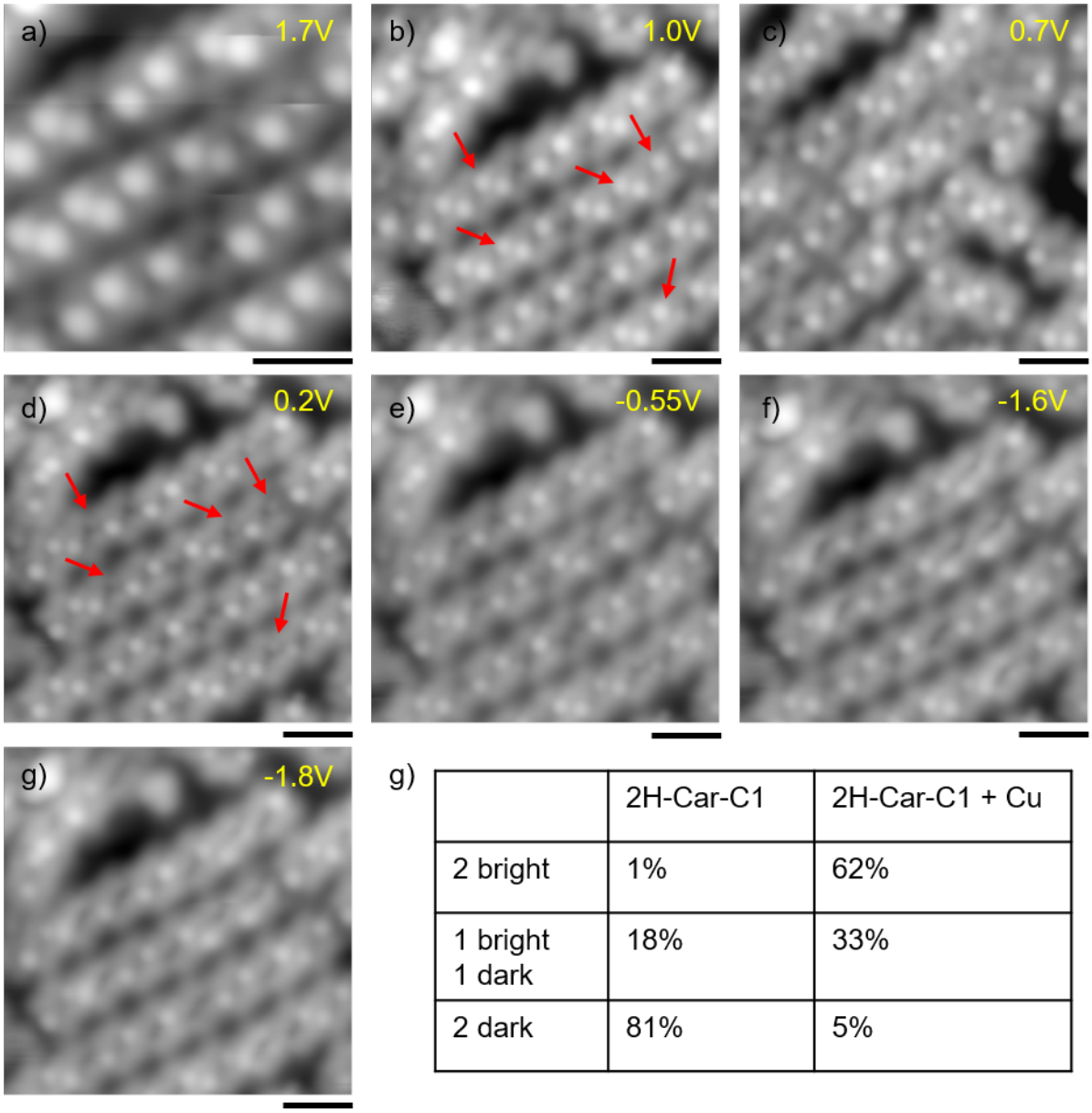

g)

	2H-Car-C1	2H-Car-C1 + Cu
2 bright	1%	62%
1 bright 1 dark	18%	33%
2 dark	81%	5%

Figure 5.21.: Bias dependent STM images of Cu/2H-Car-C1/Au(111). The molecular contrast remains constant over a wide bias range. Some molecules of the bright-bright species are converted during scanning into the bright-dark species (marked by red arrows in panel b) → d). The relative amounts of the three species before and after Cu dosing are given in table g). Imaging parameters, scale bar: a-c) 35 pA, 2 nm; d-g) 15 pA, 2 nm.

2H-Car-C1 and Fe

Inspired by the successful on-surface metalation of porphyrins, iron is chosen for metalation experiments with carpyridines. In STM experiments Fe-metalated porphyrin species show a bright protrusion in the center, allowing easy differentiation from unreacted species [305, 314–317]. For the metalation reaction the order of dosing molecules and iron is important. Procedures where the molecules are dosed on the surface prior to iron, report temperatures required for the metalation reaction around room temperature and below room temperature [85, 302, 314, 315, 318]. Recent studies on ethyl-substituted porphyrins reveal that temperatures up to 150°C are needed to metalate these species [319]. In inverted systems with porphyrin molecules dosed after iron, moderate annealing up to 277°C induces the metalation reaction [302, 320]. These experiments provide a starting point on the temperature ranges to probe the metalation reaction of carpyridines.

For the results presented in this section, iron is dosed on 2H-Car-C1/Au(111) held at room temperature and the sample is subsequently annealed up to 300°C. Additional preparation details are described in the methods section 2.5.

Figure 5.22 displays the XPS and STM results obtained on the Fe/2H-Car-C1/Au(111) system. The evolution of the N 1s signal with iron dosage and following annealing steps is shown in Figure 5.22 a), revealing a clear change in the signal. In the modeling process of the spectra, the position and separation of the NH in the carbazole group (green, 399.3 eV) and N in the pyridine group (brown, 398.3 eV) is fixed throughout the spectra. A new component at 398.2 eV, marked in blue correlates with iron addition and increases in intensity upon annealing. It is attributed to N coordinated to Fe. The respective area ratio of the N-Fe peak to the total signal starts at 17%, and increases at 100°C to 40% and saturates above 200°C at 63%. Possibly a similar reaction mechanism as for metalation of porphyrins is present, where the NH transfrom via a redox reaction to N and hydrogen is released [313].

STM images of samples corresponding to the 100°C and 200°C annealing steps are shown in Figure 5.22 b) and 5.22 c), respectively. In the 100°C-sample (panel 5.22 b) unreacted molecules (red arrows) are identified by their similar contrast to samples without Fe (see Figure 5.4 and Figure A.26). The bright species (marked by blue arrows) is tentatively attributed to Fe-modified carpyridines. It assembles in clusters, in contrast to the linear chains and islands of the unreacted species. In the clusters of three molecules, they arrange with their bright protrusions pointing towards the center. The brighter species keeps its contrast and increased intensity over a bias range between at least 1.7 V and -1.8 V, see also Figure A.27.

In the sample which was heated to 200°C (panel 5.22 c) the arrangement and appearance of the molecules changes. No cluster formation is observed anymore. Furthermore, the molecules present a more uniform apparent height distribution. At voltages < -1.5 V the protrusion at the pyridine position, changes from a spherical shape into a U-shape. For a bias series see Figure A.28, whereby the appearance resembles unreacted 2H-Car-C1/Au(111) in Figure 5.5.

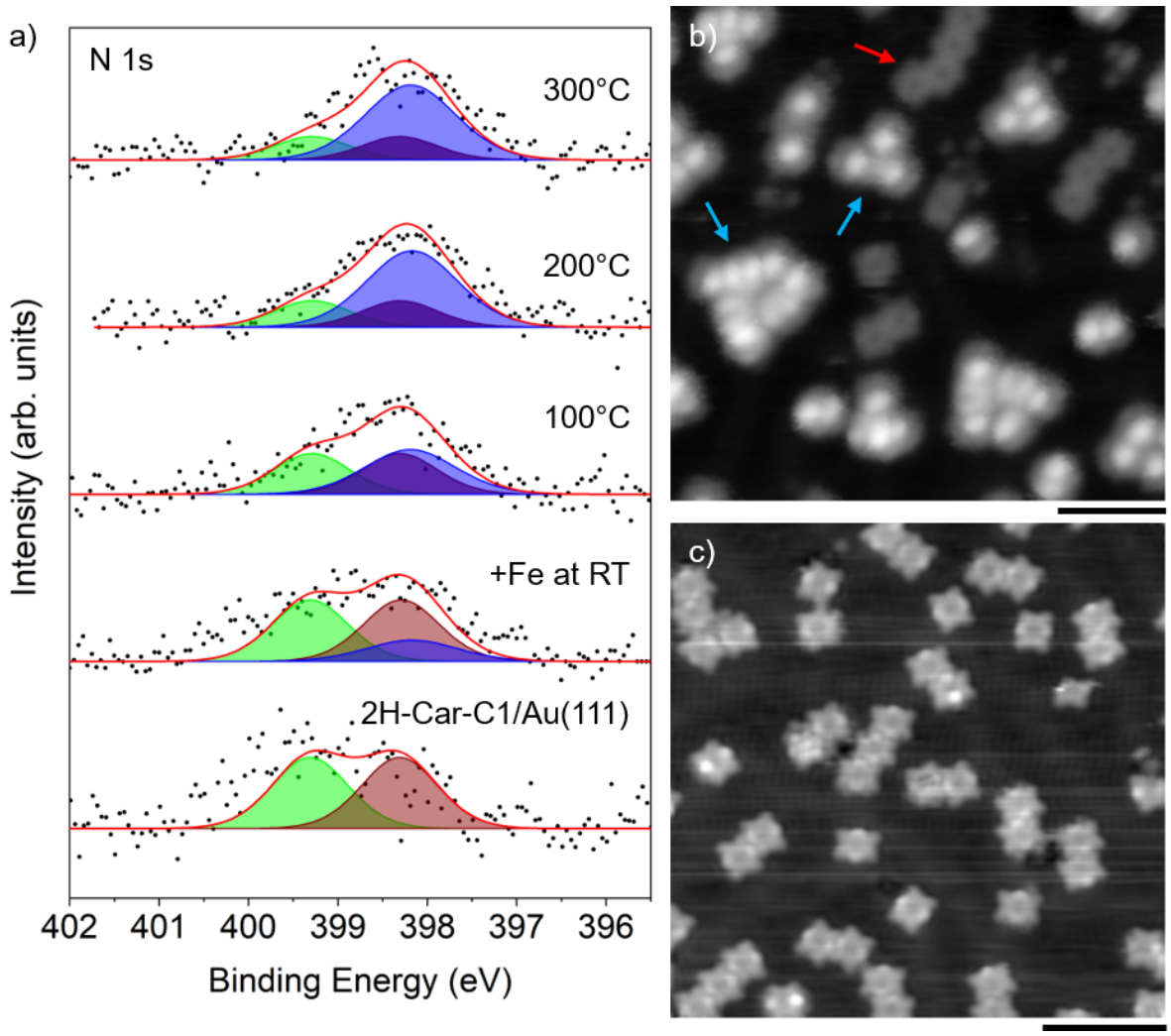

Figure 5.22.: XPS and STM data of the Fe/2H-Car-C1/Au(111) system. a) N 1s region after dosing Fe at room temperature and subsequent annealing steps to 300°C. b,c) STM images of samples heated to 100°C (b) and 200°C (c), respectively. In b) unreacted molecules are marked with a red arrow, while Fe-modified molecules are marked with blue arrows. After heating to 200°C (c) the molecules did not assemble in clusters and showed a more uniform contrast. Imaging parameters, scale bar: b) 20 pA, 50 mV, 5 nm; c) 100 pA, -1 V, 5 nm.

In summary, the 2H-Car-C1 molecules could be modified with iron on Au(111). The XPS data clearly show a change in the N 1s region with an additional component increasing in relative concentration with temperature. The identification of this modified species in STM images is challenging, as discussed below.
First, we focus on the XPS results. The binding energy of the new species (398.2 eV) lies close to that of the pyridine species (398.3 eV). In Fe metalated porphyrins the binding energy of the N-Fe species is found at 398.4 eV (Fe-TPP/Ag(111) [85]), 398.5 eV (Fe-OEP/Ag(111) [321]), 398.7 eV (Fe-TPP/Ag(111) [320]), 398.5 eV (Fe-TPP/Ag(100)

[322]), 398.5 eV (Fe-TPP/Fe(110) [323]). In iron phthalocyanine species the signal is observed at 398.8 eV (FePc/CoCu(100) [324]), 397.9-398.0 eV ($FePcF_x$/Au(111) x=0, 4, 16 [325]), 398.2 eV (FePc/Au(111) [326]), 398.7 eV (FePc/Cu(111) [327]), 398.8 eV (FePc/TiO2) [328]). In iron corroles it is located at 399.1 eV (Fe-HEDMC/Ag(111) [329]).
When comparing these macrocycles to the present carpyridine case, the binding energy of N 1s species in Fe-phthalocyanines at 398.2 eV matches with Fe/2H-Car-C1/Au(111). On the contrary, the N 1s positions in metalated porphyrin system are located at higher binding energies. A common feature between all three systems is that the N-Fe related peak is located close to the pyridinic/iminic nitrogen species. This is indicative of a removal of both hydrogens, resulting in four dehydrogenated nitrogen atoms providing the coordinating cavity. While it is possible to determine the Fe oxidation state from XPS measurements, in the present Fe/2H-Car-C1/Au(111) case, the small signal to noise ratio and the complex line shape of the Fe $2p_{3/2}$ signal does not allow a characterization of the Fe oxidation state.
In the Fe/2H-Car-C1/Au(111) XPS dataset the modeling starts from the unmodified species and a gradually increasing component related to metalation is observed. Interestingly, the data allows a model with a residual unreacted component up to temperatures of 300°C. For on-surface metalation of porphyrins with iron only moderate temperatures up to 150°C are needed [302, 319]. This higher reaction barrier in the carpyridines is tentatively related to their intrinsic saddle shape on the surface. The coordinating pocket deviates from the symmetric, planar shape of metalloporphyrins (compare Figure 5.17 d). For cyano-functionalized TPP on Cu(111) a increased reaction barrier for self metalation is observed, and partially related to the inverted saddle shape [275].
Next, the STM data is discussed. Several preparations are investigated in order to characterise the appearance of the iron-modified carpyridines by STM. The molecules on the sample with iron dosed at room temperature (compare Figure A.29) and the 100°C annealed sample (Figures 5.22 b, A.27) appear with a similar contrast. A striking feature is the formation of clusters. Note, in the clusters of three molecules, the bright protrusions point towards the center of the cluster. This could be related to iron atoms assembled in the center of the three molecules. For iron on Au(111), the formation of iron clusters at room temperature was reported in Ref. [330]. Upon annealing to 327°C they observed a coalescence of the cluster into large islands, due to the increased mobility. A similar effect could be related to the 200°C annealed Fe/2H-Car-C1/Au(111) samples, where no cluster of molecules are observed anymore. Iron atoms becoming mobile enough to diffuse onto the Au(111) step edges, could explain the lack of molecular clusters.
Furthermore, different Fe coverages were explored for the 200°C annealing series. Starting from nominally the same coverage as the 100°C experiment ($\text{flux} \cdot \text{time} = 520\text{nA} \cdot \text{s}$) lower coverages of $42\text{nA} \cdot \text{s}$ and finally $8.4\text{nA} \cdot \text{s}$ were investigated. Across these samples the molecules exhibit the same contrast. No indication for two different species, as expected for metalated and unmetalated molecules due to non-stoichiometric iron dosage, was observed. Moreover, the 100°C and 200°C annealed Fe/2H-Car-C1/Au(111) samples are compared to reference measurements of 2H-Car-C1/Au(111) annealed to 100°C (Figure A.26) and 200°C (Figure A.30), excluding thermally induced modifications in

the molecular appearance and assembly. Across these data sets we can identify a tendency of the molecules to assemble in irregular clusters and islands containing only few molecules with the increasing addition of iron (Figure A.31). This is in contrast to the reference samples, where the unmodified carpyridines predominantly assemble in linear islands containing typically more than ten molecules.
Interestingly, no clear indication for Fe-metalation is observed in the molecular contrast of carpyridines. For other Fe-metalated macrocycles, bright protrusions in the center are reported. In phthalocyanines such as FePc/Au(111) [331], FePc/Ag(110) [332], FePc/Au(110) [333] the position of the iron atom in the molecule correlates with a bright protrusion. In porphyrins such as FeTPP/Ag(111), FeTPyP/Ag(111) [314, 316], FeTPP/Au(111) [334] the molecules appear with a rod like enhanced intensity across the center. For the case on Au(111) even two distinct round protrusions are present at both ends of the rod. Also for the pyrphyrins FePyr/Cu(111) [335] and FePyr/Ag(111) [336] the metalated species appears with a bright protrusion. An exception is found in corroles. In an alkyl substituted corrol Fe-HEDMC/Ag(111) [329] only subtle contrast variations are observed in the center. For a triphenyl corrole Fe-TPC/Cu(111) [337] the molecules are characterized by an asymmetric appearance, but without a pronounced protrusion at the iron position. The differences in the Fe-HEDMC/Ag(111) system compared to FeOEP are attributed to additional molecular states in FeOEP near the Fermi edge, which are not present in Fe-HEDMC.
Summarizing the STM data, it is not possible to unequivocally identify the Fe-modified 2H-Car-C1 molecules by their contrast. However, indication for a disordered assembly upon Fe dosing is observed in the STM images. A next step for identification is to characterize the molecules via STS. Even though the bias series (Figures A.27, A.28) indicate a voltage independent contrast, subtle differences in the local density of states of the Fe-modified molecules may arise. For example, in STS measurements on Fe-TPP/Ag(111) and Fe-TPyP/Ag(111) an upshift of the LUMO is reported, compared to the respective free-base species 2H-TPP and 2H-TPyP [316, 338].

5.5. Conclusions and Outlook

This chapter provides the first high-resolution data set of carpyridines on surfaces in UHV. During this investigation several key characteristics were observed. For the case of 2H-Car-C1/Au(111) the molecules are found to adsorb parallel to the surface and keep a saddle shape, similar to bulk 2H-Car-C1. In the saddle shape geometry, the carbazole units are close to the surface and the pyridine groups are pointing upwards. In STS measurements the HOMO is found at -1.35 V and a broad feature in the unoccupied states region starts around 1 V. Typical self assembled structures on low-coverage samples are stripe-like patterns. On samples with coverages exceeding 1ML, no indication for vertical stacking, with locked-in positions due to the saddle shape, is found. Further modification of the 2H-Car-C1 molecules on the surface is achieved by dosing metal atoms such as Cu and Fe. While the XPS data points to a clear modification of the chemical environment of the nitrogen atoms, as for example due to a coordi-

nation of the metal atom, an unambiguous determination of the reaction product was not possible with the combined XPS and STM data at hand. Additional experiments with complementary techniques, such as STS measurements, are likely to reveal more insights. Specifically, Cu/2H-Car-C1/Au(111), where the majority of molecules exhibits two bright protrusions after Cu dosing, presents a promising system. NEXAFS and nc-AFM data could clarify changes to the geometry of the pyridine group, which in turn would help to identify the influence of metalation on configuration of the saddle shape. The reaction product is likely to be identifiable in combination with DFT calculations. For the structurally related 2H-Car-C2 species, a similar behaviour to 2H-Car-C1 is observed. The molecules adsorbed in a saddle-shape geometry. On low-coverage samples the 2H-Car-C2 molecules also form linear assemblies.

In general, the on-surface reactions of carpyridines are largely unexplored and offer a promising route to expand the synthetic efforts from solution chemistry. For example, low stability due to demetalation in alkyl chained metal-carpyridines such as Co-Car-tBu is observed by Woods [127]. Extrapolating from the versatility of metalated porphyrins, e.g. references [303, 339–341], metalated carpyridines might also find applications in areas such as catalysis, quantum information or harnessing magnetic interactions [264]. Another possible direction is the on-surface synthesis of non-planar structures by taking advantage of the inherent saddle shape. For example the established on-surface synthesis protocols, e.g. Ullmann-coupling [30, 342], could be extended by using functionalized carpyridines as monomers. In this way a controlled corrugation could be introduced in the resulting polymers.

6. Conclusions

This thesis reports on investigations of molecules on noble metal surfaces with a focus on systems that exhibit configurations protruding from the surface. The employed techniques are primarily based on scanning probe microscopy (STM, STS, AFM) at low temperatures in an UHV environment. Complementary methods such as XPS, NEXAFS and DFT provide additional insights into these systems. A total of four systems are characterized.

Chapter 3 describes the adsorption, single-molecule manipulation and self-assembly of borazine on Ag(111). Upon dosing borazine onto Ag(111) at 150 K, two phases are observed. A porous honeycomb like network is found for low exposures while higher exposures result in a dense packed stripe phase. Individual borazine molecules can be dehydrogenated via voltage pulses with the STM tip. The resulting main manipulation product is identified, in combination with DFT calculations, as an upright standing single dehydrogenated borazine species. The hydrogen is split from a boron position. The fragment adsorbs in fcc and hcp hollow sites, with the dehydrogenated boron atom pointing to the surface. Further translation and rotation of the fragment is achieved by voltage pulses. This control over the single molecule chemistry could lead to development of synthesis protocols for nanoflakes of hexagonal boron nitride.

Next, in chapter 4 two systems are described, that are aimed at the investigation of rotation on the single molecule level. First, hemithioindigo-based motor molecules are discussed. These motor molecules feature a light-driven unidirectional rotation in solution and are designed to keep this rotational behavior when anchored on a surface. To this end, an upright standing configuration on noble metal surfaces is envisioned by using -S-tBu groups as anchor points. An upright configuration is necessary for unrestricted azimuthal rotation. Experiments on these molecules, reported in a previous thesis [129], show an agglomeration of the molecules in a flat-lying adsorption geometry. In the present study, two methods are explored to guide the molecules into an upright standing geometry. On the one hand, co-adsorption with C_{60} results in phase separation of motor molecules and C_{60} molecules, resulting in a similar flat-lying adsorption geometry for the motor molecules as without C_{60}. On the other hand, we observed that a TBB-based COF influences the adsorption geometry of the motor molecules. The network features differently sized pores, such that pores of suitable size host single motor molecules. Even though this network successfully prevents island formation of the motor molecules, their flat-lying adsorption geometry remains largely unaffected inside the pores. An upright standing geometry may be achieved by a modification of the motor molecules to feature a tripodal base structure.

The second system for the investigation of rotation on the single molecule level are Thorium-Naphthalocaynine double-decker molecules (Th(NPc)2). An on-surface syn-

thesis protocol is successfully employed, resulting in Th(NPc)2 molecules embedded in a dense packed NPc monolayer on Ag(111). Tip-induced rotation of the top half in these Th(NPc)2 double-decker molecules proved challenging. A modified double-decker species, obtained through a voltage pulse, can be easily rotated with the AFM tip. Simultaneous acquisition of the frequency shift signal during the lateral manipulation procedure allowed to extract the tip-sample potential and consequently to determine the force in the manipulation direction. In combination with the distance to the center of rotation a minimum value of the torque for rotating the top half of the double-decker is calculated. Valuable conclusions are drawn for future experiments. A system suitable for quantifying torque on the molecular level via tip-induced rotation needs to have a rigid rotating unit which is unrestricted in its rotational movement. Furthermore, the rotated states need to be distinguishable in the STM images.
Finally in chapter 5, selected molecules of the carpyridine family are characterized in detail. Carpyridines are similar in size to porphyrins but feature an inherent saddle shape. Specifically, a high-resolution, multi-method study of 2H-Car-C1/Au(111) is presented in the main section of this chapter. The molecules adsorb with the carbazole units parallel to the surface and the pyridine moieties pointing away from the surface. Thus, the molecules keep a saddle shape on the surface with a tilt angle of 35° at the pyridines. This saddle shape is unambiguously characterized by AFM and NEXAFS measurements. Concerning the self-assembly on surfaces, chain-like structures are observed at low coverages and a dense-packed rectangular structure at higher coverages. On-surface metalation of carpyridines with Cu and Fe is probed with the 2H-Car-C1 species. A modification is clearly observed in STM and XPS data, however the precise nature of the metal binding to the molecule is not yet clear. Additional experiments with complementary techniques to STM/XPS such as STS/NEXAFS might elucidate the properties related to the metalated species. Furthermore, exploring parameters like type of metal atom, annealing temperatures and coverages, could pave the way for understanding the on-surface metalation of carpyridines. Compared to the already broad library of porphyrin-based metalated compounds, the inherent saddle-shape of the carpyridines would introduce another parameter to tune the desired properties of the resulting metalated species. Another promising route is using carpyridines in on-surface synthesis schemes, possibly introducing non-planar units which in turn results in precisely corrugated materials.
In summary, this thesis reports on protruding molecular species on surfaces, where the out-of-plane features are introduced by tip-induced single molecule chemistry, on-surface synthesis or carried over from the inherent saddle-shape of specific molecular species. These systems and their respective precursors are characterized in detail. Tailored molecular systems were used in experiments investigating tip-induced rotation of molecular units. Furthermore, the saddle-shaped molecules maintain their saddle shape on the surface and could provide a starting point for three-dimensional architectures on surfaces. The experiments showed that we have been able to augment one of the characteristic attributes of molecular assemblies on surfaces, i.e. restriction to two dimensions, to include vertical features, thus paving the way for research into exciting phenomena taking place beyond the immediate molecule-surface interface.

A. Appendix

A.1. Borazine

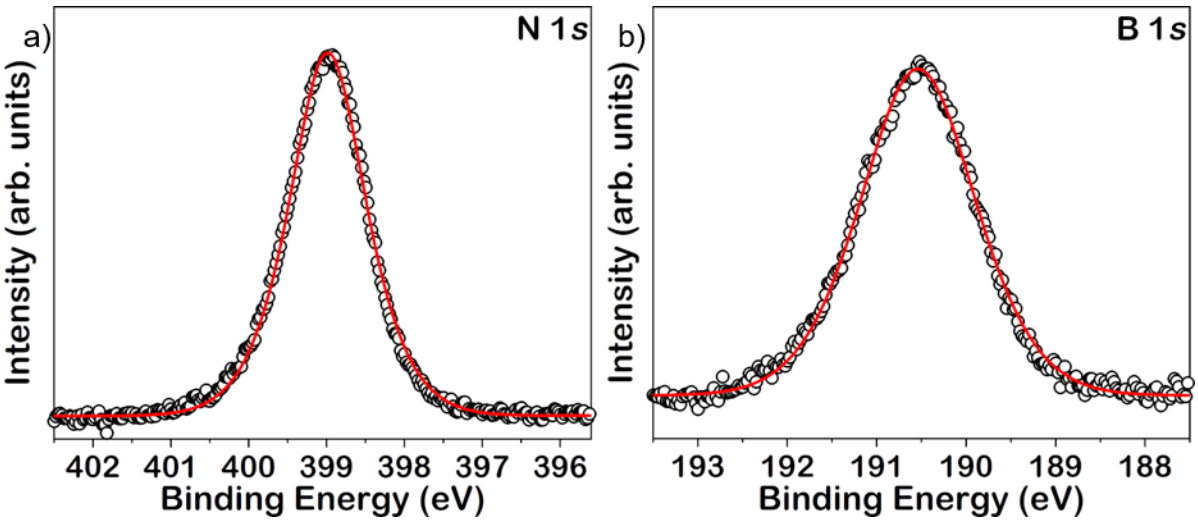

Figure A.1.: N 1s a) and B 1s b) XP spectra of borazine on Ag(111) recorded at 150 K. The peaks are located at 399.0 eV (FWHM 1.2 eV) and 190.5 eV (FWHM 1.5 eV), respectively. Dots represent experimental data and solid lines show the corresponding fits. The XP spectra are calibrated against the Ag 3d5/2 line at 368.27 eV and the peaks are fitted with Gaussian–Lorentzian line shape functions (N 1s: 65% Lorentzian, B 1s: 45% Lorentzian). For the N 1s region the Ag-plasmon background was modeled while in the B 1s region a Shirley background was subtracted. The XPS measurements were performed with a SPECS X-ray source (Mg K α, 1253.6 eV) and a SPECS PHOIBOS 100 electron analyzer, with a base pressure in the UHV chamber below $1 \cdot 10^{-9}$ mbar. The borazine/Ag(111) sample was prepared by exposing Ag(111) held at $\approx$ 150 K to 68 L of borazine. A nominal coverage close to one monolayer was estimated from the B 1s and Ag 3d peak intensities, adjusted for the respective photoionization cross-sections. This coverage exceeds the ones of the porous and dense packed phases. Accordingly, borazine molecules adsorbed in different configurations, including second layer components, might contribute to the XPS signal. The peak positions are comparable to multilayer components of intact borazine on Ni(111) (B 1s: 190.0-190.3 eV, N 1s: 399.2) [152] and Ir(111) (B 1s: 190.3-190.9 eV) [144]. No other reference data of weakly adsorbed borazine is available, as only strongly interacting systems (Ni(111), Ir(111)) are reported in literature [144, 152]. The peak widths fall well into the range of values measured in our experimental setup for regular assemblies of borazine derivatives, featuring a borazine core embedded in an all carbon environment and h-BN (1.2 -1.7 eV) [161]. Borazine dehydrogenation and decomposition was reported to induce pronounced binding energy shifts resulting in multiple peak structures [144, 152]. The rather symmetric N 1s and B1s line shapes here do not indicate such processes.

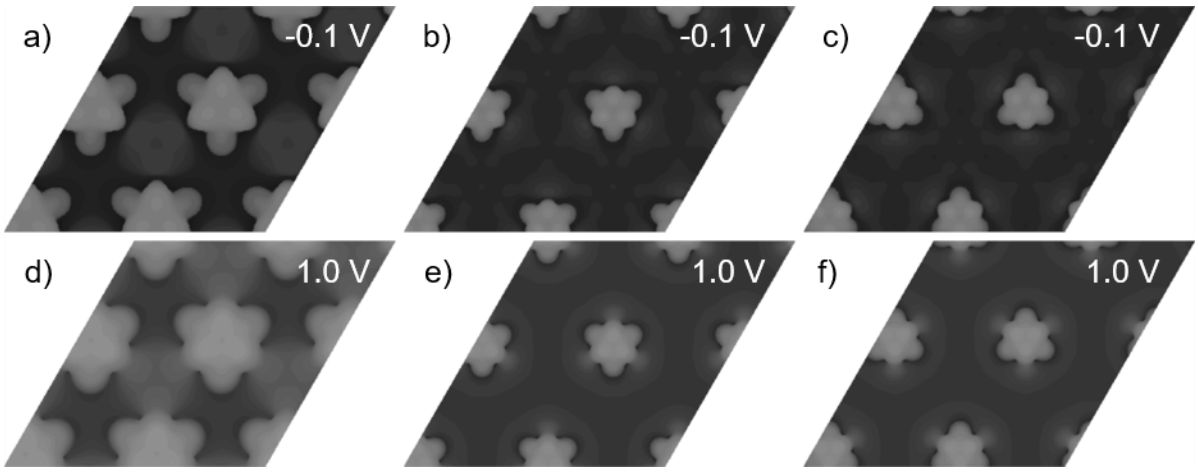

Figure A.2.: Tersoff-Haman simulation of a single borazine molecule at the fcc 30°a)-d) and hcp 90° e,f) sites on Ag(111). The STM images are obtained for bias values of -0.1 V a,c,e) and 1.0 V b,d,f), respectively. The molecules share similar contrast for denser arrangement and different adsorption sites.

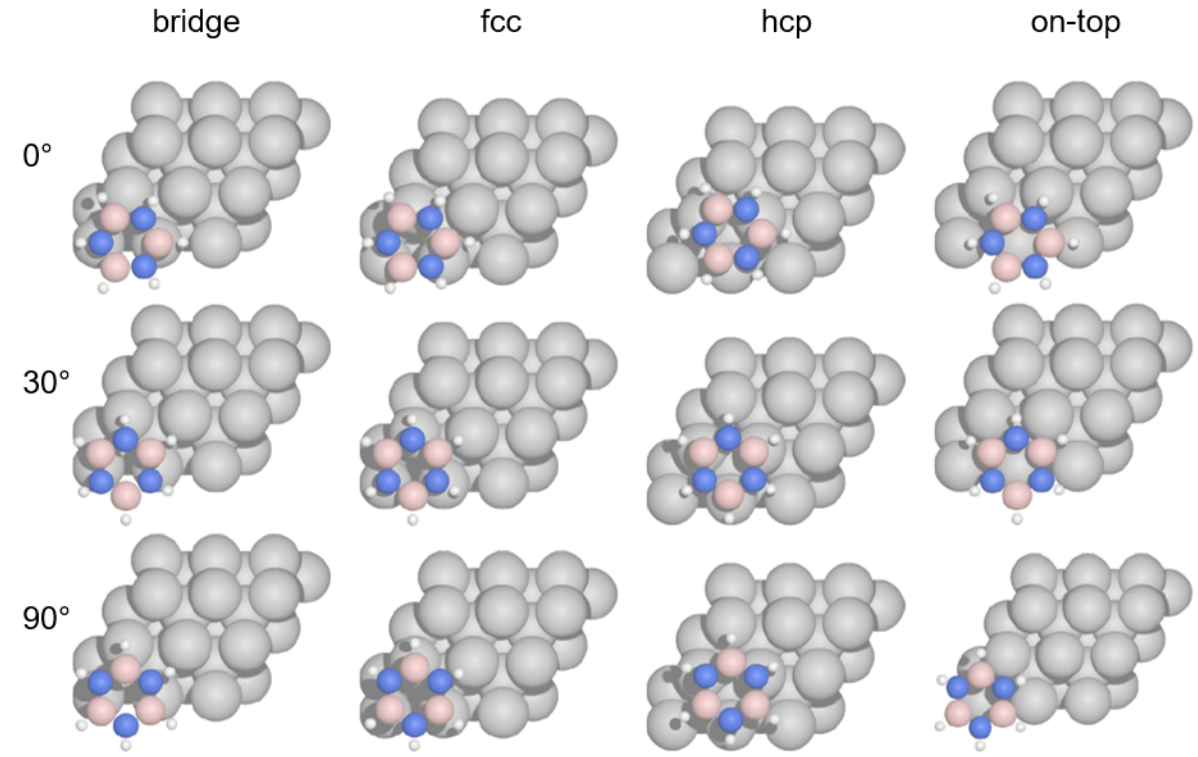

Figure A.3.: Distinct adsorption sites and azimuthal orientations for intact borazine adsorbed flat on a Ag(111) slab. Table A.1 lists the respective calculated adsorption heights and energies.

Species	Δ h (Å)	E_{ads} (eV)
fcc 0°	3.21	-0.87
fcc 30°	3.26	-0.86
fcc 90°	3.22	-0.81
hcp 0°	3.20	-0.86
hcp 30°	3.21	-0.81
hcp 90°	3.26	-0.86
on-top 0°	3.36	-0.83
on-top 30°	3.34	-0.81
on-top 90°	3.34	-0.81
bridge 0°	3.24	-0.86
bridge 30°	3.22	-0.84
bridge 90°	3.21	-0.84

Table A.1.: Adsorption distance and energy for different adsorption positions of borazine on the Ag(111) facet (compare Figure A.3).

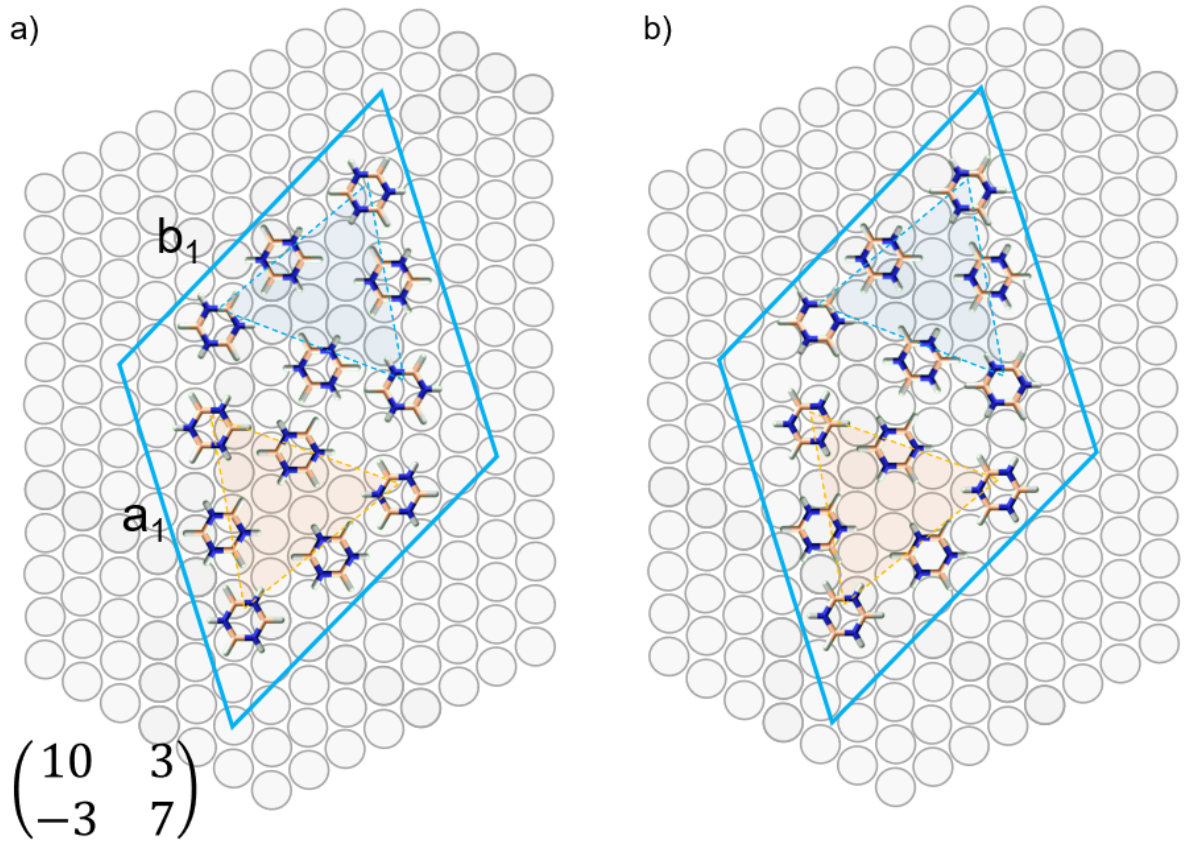

Figure A.4.: Tentative structural models of the porous borazine assembly on the Ag(111) lattice. The alignment and intermolecular distances are derived from the STM data, which were calibrated by atomic resolution of the Ag(111) lattice achieved in the same measurement run. a) shows a registry including fcc and hcp adsorption sites as discussed in the main text (see Figure 3.3 d). b) shows an alternative registry combining on top with hollow sites.

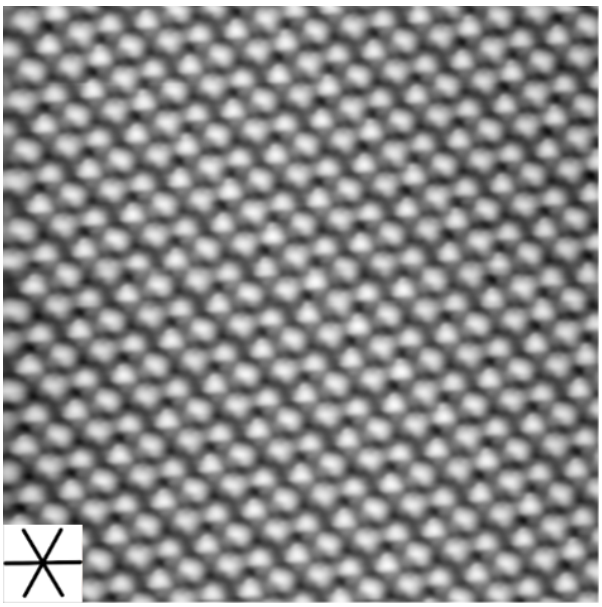

Figure A.5.: STM image revealing distinct orientations of the molecules in the dense packed phase. The black cross in the inset marks the dense packed Ag(111) directions. Imaging parameters: 11.0 x 11.0 nm^2, 0.2 V, 500 pA.

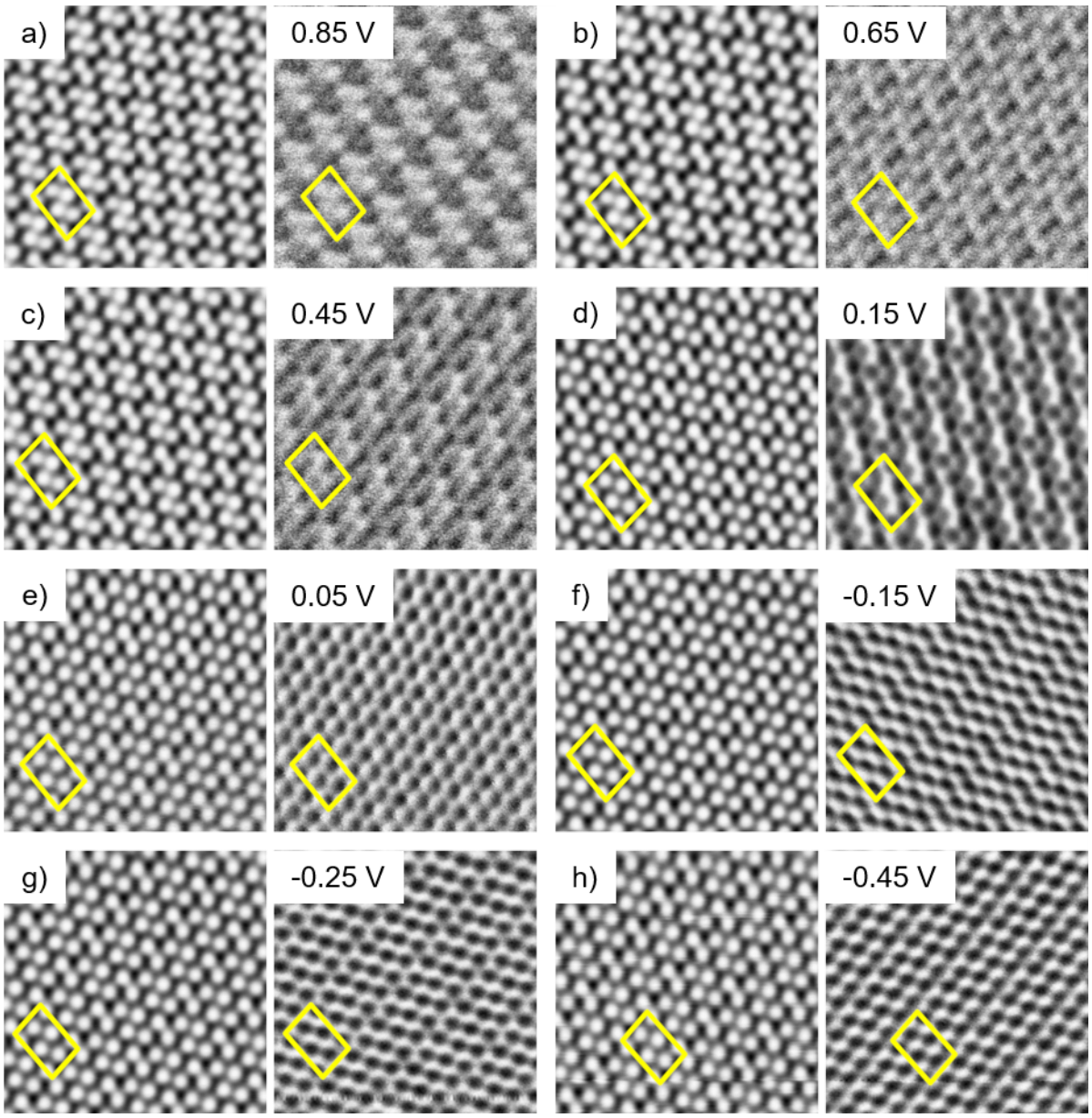

Figure A.6.: Scanning tunneling spectroscopy mapping on borazine molecules in the dense packed phase. Constant-current STM images (left sides) and dI/dV maps (right sides) were acquired simultaneously at different biases for the molecules assembled on Ag(111) in the three-stripe pattern (a-h). The dI/dV maps reveal electronic states of borazine molecules. The yellow frames mark the unit cell in the topographic image and the corresponding dI/dV map. Imaging parameters: 7.5 x 7.5 nm^2, 500 pA, a) 0.85 V, b) 0.65 V, c) 0.45 V, d) 0.15 V, e) 0.05 V, f) -0.15 V, g) -0.25 V, h) -0.45 V.

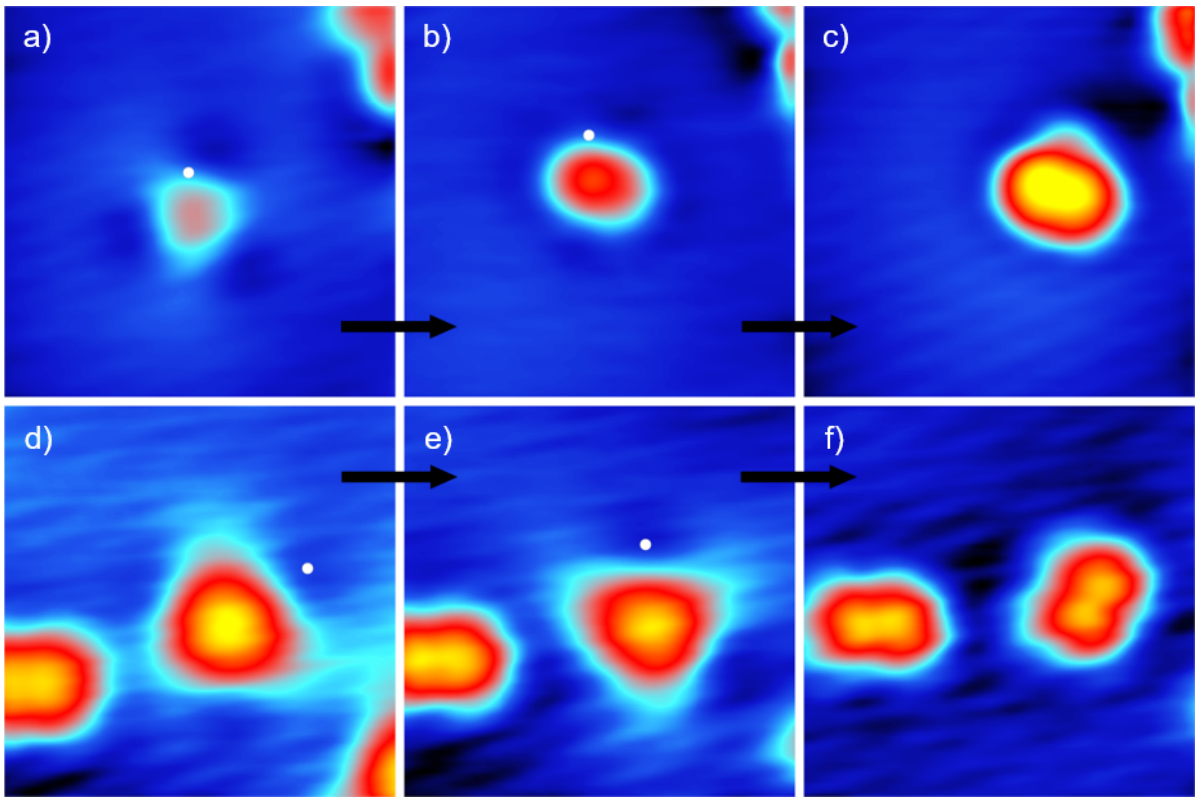

Figure A.7.: The series of STM images shows different states of borazine molecules, that are induced by manipulation via voltage pulses at positions marked by white dots. A pulse of 2.50 V is applied for 5 s to the molecule in image a), which is converted into the 2-fold symmetric intermediate state shown in image b). A subsequent pulse, with the same parameters, transforms it into the final manipulation product in image c), that is identified as upright standing species. The molecule in image d) experienced a pulse of 2.25 V for 5 s and thus is rotated by 60°, as displayed in image e). A further pulse transforms the molecule into the intermediate state f). Black arrows mark subsequent images after manipulation steps. Imaging parameters: a-f) 2.2 x 2.2 nm^2, a-c) -0.1 V, 500 pA, z-scale 0.0-1.9 Å d-f) 0.25 V, 500 pA, z-scale 0.0-0.6 Å.

DFT analysis of the adsorption of distinct borazine fragments on an Ag slab

As mentioned in the main text, for the single dehydrogenated and deprotonated species, diverse B-terminal adsorption sites are preferred over the N-termination. Additionally, for this N-terminal case stable geometries are only possible for on-top position, and for other adsorptions sites (hcp, fcc, or bridge) the reliable adsorption configuration was not able to be stabilized. Concerning the doubly dehydrogenated species, much fewer stable adsorption geometries were observed on the Ag(111) surface. Both ortho- and para-doubly dehydrogenated borazine molecules are optimized on all high-symmetry adsorption sites. Ortho-dehydrogenation leads to the exclusive formation of bridged

adsorption geometries (of slightly different energetics whether the adsorbed molecule tilts towards an fcc or hcp adsorption site), which share the same appearance in simulated STM images (Figure S10 a-b). Furthermore, para-dehydrogenation supports an upright adsorption position (B-terminal) on all high-symmetry sites with the on-top geometry being slightly favored over the others. However, this species is not stable with its plane oriented along the dense Ag-directions.

Species	E_{ads} (eV)
B-terminal, on-top 1 (Fig. A.8a)	3.08
B-terminal, on-top 2 (Fig. A.8b)	3.09
B-terminal, on-top 3 (Fig. A.8c)	3.09
B-terminal, bridge (Fig. A.8d)	3.04
B-terminal, fcc (Fig. 3.5g)	3.08
B-terminal, hcp (Fig. 3.5h)	3.08
N-terminal, on-top 1 (Fig. A.8e)	2.70
N-terminal, on-top 2 (Fig. A.8f)	2.60

Table A.2.: Adsorption energies of single dehydrogenated borazine molecules given relative to the optimized free molecule energies.

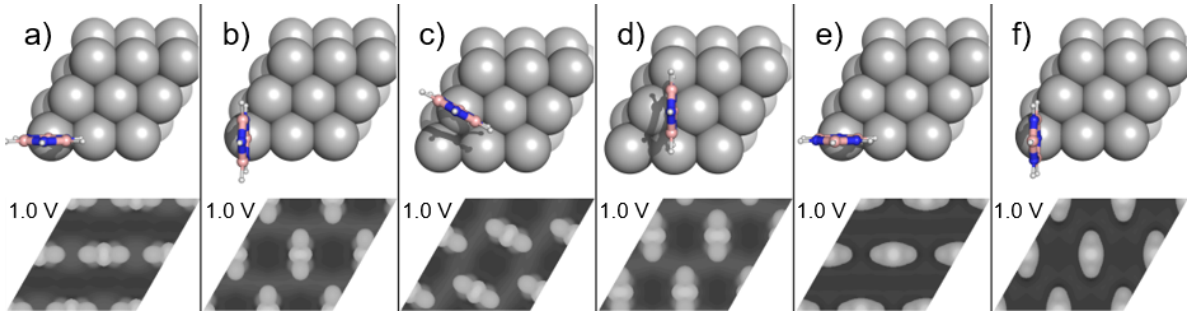

Figure A.8.: DFT optimized geometries and simulated STM signatures of single dehydrogenated borazine molecules at the following adsorption sites: a-c) B-terminal on-top, d) B-terminal bridge, e-f) N-terminal on top. STM simulations at 0.1V show nearly identical signature as at 1.0V.

Species	E_{ads} (eV)
B-terminal, on-top 1 (Fig. A.9a)	0.31
B-terminal, on-top 2 (Fig. A.9b)	0.31
B-terminal, on-top 3 (Fig. A.9c)	0.31
B-terminal, bridge (Fig. A.9d)	0.22
B-terminal, fcc	0.31
B-terminal, hcp	0.31
N-terminal, on-top 1 (Fig. A.9e)	0.14
N-terminal, on-top 2 (Fig. A.9f)	0.10

Table A.3.: Adsorption energies of single deprotonated borazine molecules given relative to the optimized free molecule energies. Fcc and hcp initialized geometries converged on on-top configurations with identical adsorption energies.

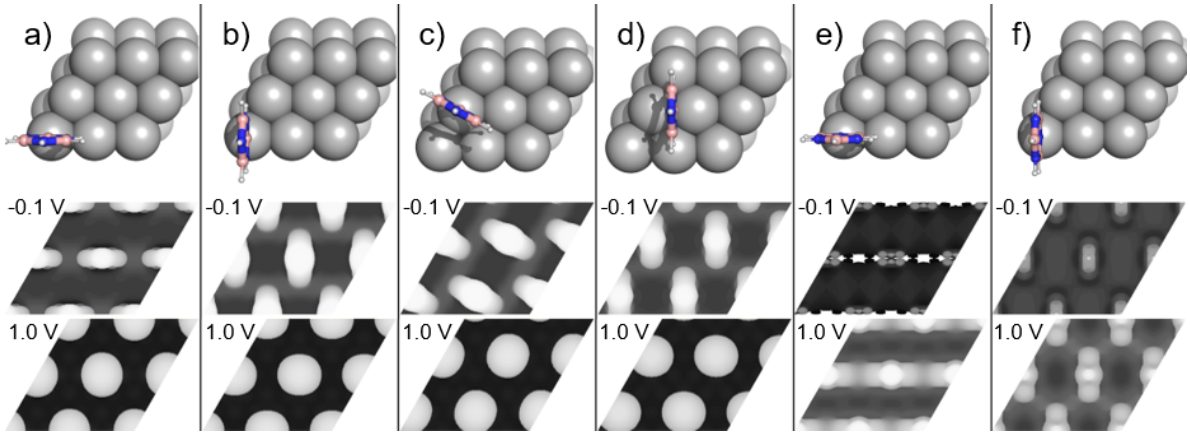

Figure A.9.: DFT optimized geometries and simulated STM signatures of single deprotonated borazine fragments at the following adsorption sites: a-c) B-terminal on-top, d) B-terminal bridge, e) N-terminal on top, f) N-terminal on top. Calculations set up for B-terminal fcc and hcp geometries converged in the on-top geometry.

Species	E_{ads} (eV)
Ortho, bridge, fcc (Fig. A.10a)	2.06
Ortho, bridge, hcp (Fig. A.10b)	2.04
Para, fcc (Fig. A.10c)	1.58
Para, bridge (Fig. A.10d)	1.58
Para, hcp (Fig. A.10e)	1.58
Para, on-top (Fig. A.10f)	1.58

Table A.4.: Adsorption energies of double dehydrogenated borazine molecules given relative to the optimized free molecule energies.

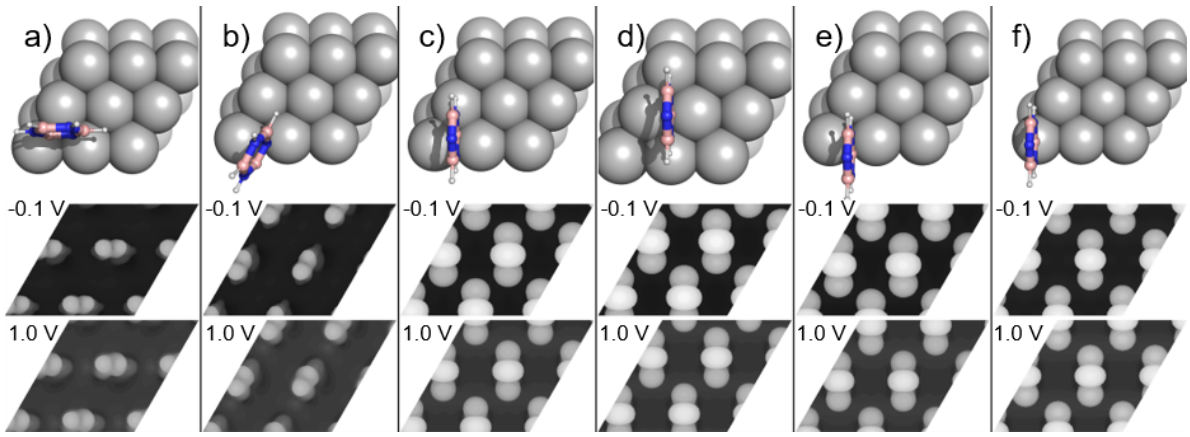

Figure A.10.: DFT optimized geometries and simulated STM signatures of double dehydrogenated borazine species. a-b): The ortho-dehydrogenated borazine molecule is adsorbed on the bridge position and is tilted towards either the fcc site a) or hcp site b). c-f): The para-dehydrogenated molecule is simulated for adsorption at the fcc c), bridge d), hcp e) and on-top f) position. The corresponding contrast in STM images is similar for the different adsorption sites within ortho- and para-species, respectively.

A.2. Motor and Torque

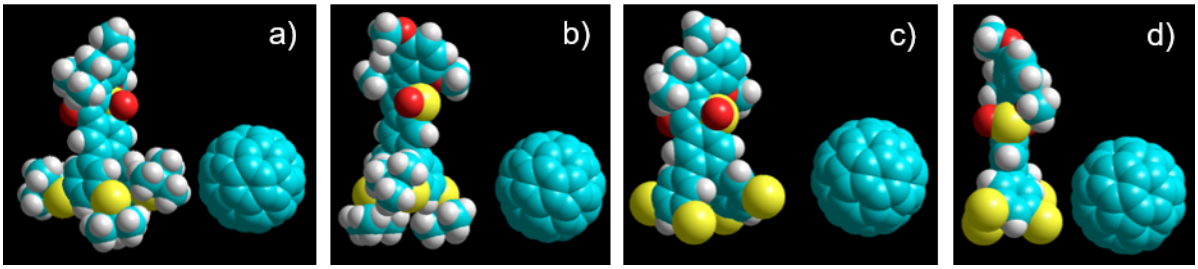

Figure A.11.: Comparison of van der Waals radii of motor 2 molecules and C_{60} molecules. a,b) Front and side view of motor 2 with butyl groups and C_{60}. c,d) Front and side view of motor 2 without butyl groups and C_{60}. Models are created with the Hyperchem 8 software package.

Figure A.12 and Figure A.13 show STM images after depositing Motor 1 at a sample temperature of 120 °C on C_{60}/Ag(111). The overview image A.12 a) shows that the Motor 1 molecules and C_{60} molecules form separated islands. The Motor 1 islands feature bright protrusions. The zoom-in images A.12 b) and c) reveal that the motor molecules appear similar to the species obtained after annealing Motor 1/Ag(111) to 200 °C. This indicates that the butyl groups can be cleaved already at lower temperatures. The large, bright protrusion visible in b) is attributed to residual adsorbate during sample preparation. In image A.12 c) a second type of protrusions is observed. They are located close to the position of the anchoring groups. Since the assembly of the

motor moleculse is unperturbed by the protrusion, they are assigned to butyl groups remaining on the molecule instead of upright standing motor molecules.

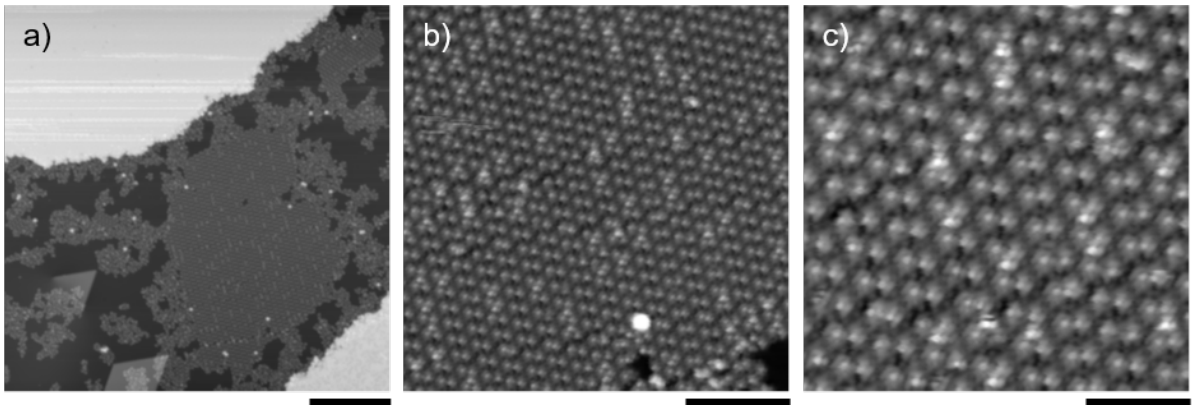

Figure A.12.: Motor 1 molecules on C_{60}/Ag(111). a) Motor molecules and C_{60} form separate islands. b) intermediate scale image showing some protrusions in the motor island. c) Zoom-in of the motor island. The protrusions are tentatively assigned to residual butyl groups at the anchoring groups. Imaging parameters, scale bar: a) 0.25 V, 100 pA, 30 nm b) 0.25 V, 100 pA, 10 nm c) -0.05 V, 100 pA, 5 nm.

An additional overview image of this system, shown in Figure A.13 a), reveals that there are few bright protrusions in the C_{60} islands. In image A.13 b) it can be seen, that the protrusions follow the periodicity given by the C_{60} molecules. The image series of the sample region in A.13 c)-e) shows the results from lateral manipulation of the protrusions along the red arrows. The protrusions can be easily removed with this procedure. Below the removed protrusion remains a C_{60} molecule, ruling out upright standing motor molecules as cause for the protrusions. Furthermore, their ellipse-like appearance changed during this process, attributed to changes to the tip apex. They are thus assigned to C_{60} molecules adsorbed in the second layer.

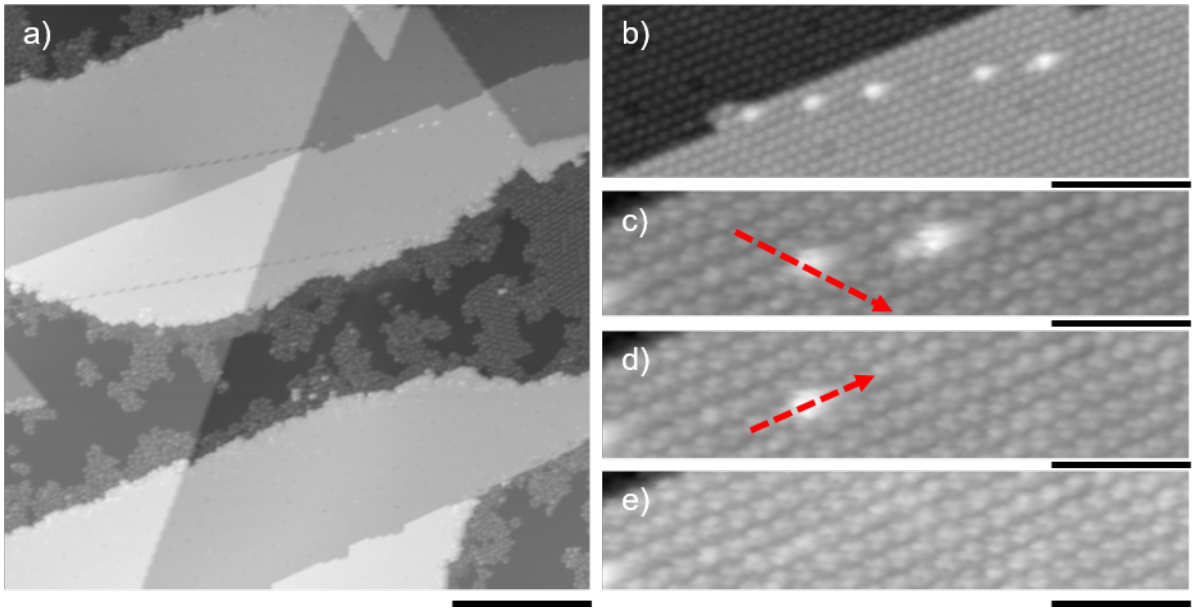

Figure A.13.: Motor 1 molecules on C_{60}/Ag(111). a) Overview image showing separated motor 1 and C_{60} islands. b) Zoom-in image of protrusions on the C_{60} islands, which are assigned to second layer C_{60} molecules. c)-e) Images before and after lateral manipulation show that a C_{60} molecule from the first layer is located below the protrusion. Imaging parameters, scale bar: a) 0.91 V, 93 pA, 40 nm b) 0.91 V, 93 pA, 10 nm c)-d) 0.3 V, 100 pA, 5 nm.

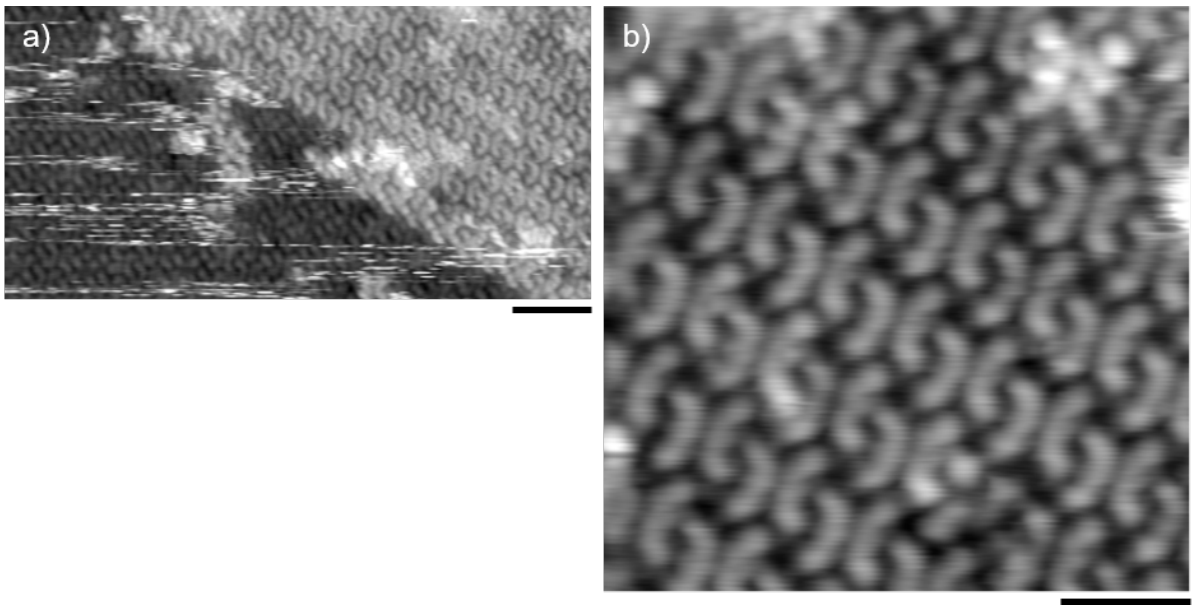

Figure A.14.: STM images of naphthalocyanine molecules on Ag(111) exceeding a coverage of one monolayer. a) The island in the right part of the image consists of molecules in the 2nd layer. b) Zoom-in image of the 2nd layer island. Imaging parameters, scale bar: a) 0.5 V, 5 pA, 4 nm; b) 0.3 V, 8 pA, 2 nm.

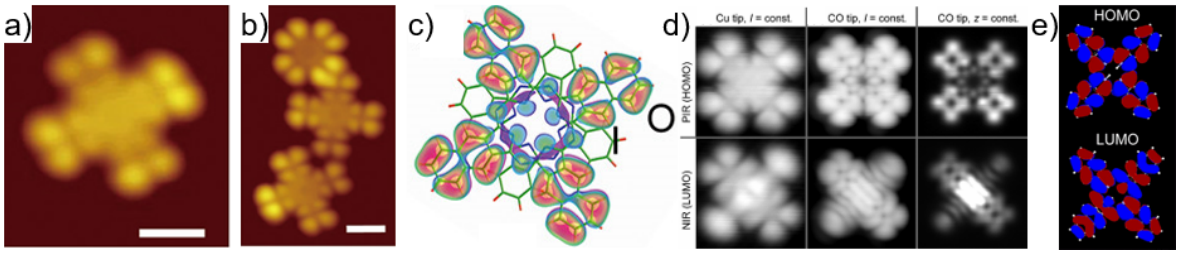

Figure A.15.: a,b) STM images of a heteroleptic phthalocyanine(Pc)-naphthalocyanine(NPc)-Terbium double decker. The NPc unit is pointing towards the vacuum side and the Pc unit is facing the surface, except in the top molecule in b) where Pc is pointing up and NPc is closer to the surface. c) Simulated STM contour of a NPc up TbPcNPc double-decker molecule. d) STM images of naphthalocyanine on 2 ML NaCl on Cu(111). e) Calculated HOMO and LUMO of naphthalocyanine. Panels a), b), c) adapted with permission from Tadahiro Komeda, Hironari Isshiki, Jie Liu, et al.; Variation of Kondo Peak Observed in the Assembly of Heteroleptic 2,3-Naphthalocyaninato Phthalocyaninato Tb(III) Double-Decker Complex on Au(111); ACS Nano; 2013. Copyright 2013 American Chemical Society [241]. Panel d), e) adapted from Leo Gross, Nikolaj Moll, Fabian Mohn, et al.; High-Resolution Molecular Orbital Imaging Using a p-Wave STM Tip; Physical Review Letters; 2011 [246].

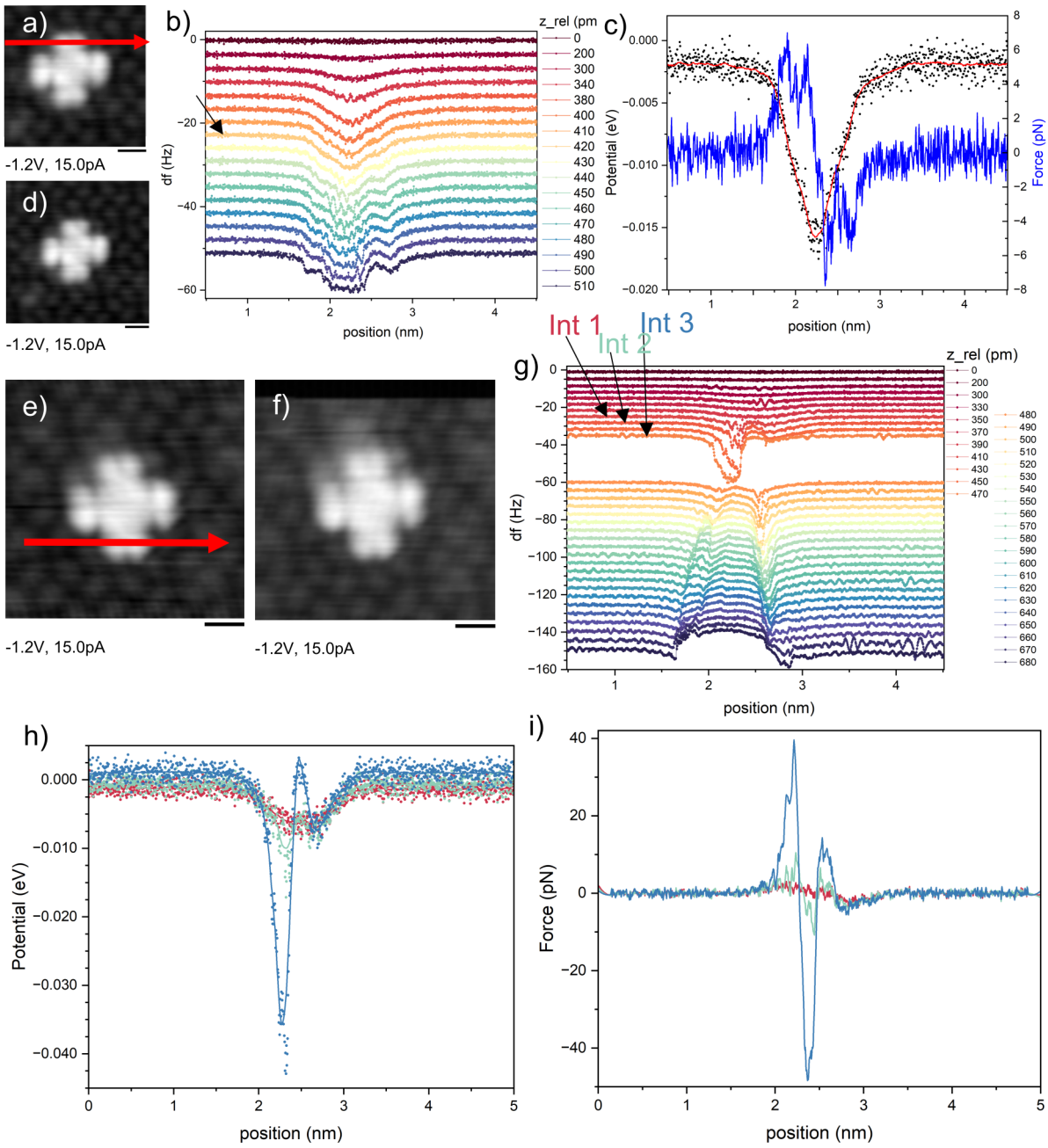

Figure A.16.: Rotation attempts on regular Th(NPc)2 doubledecker. In set a-d) the lower limit(black arrow) was chosen before a second minimum appears. In the lower set different lower limits are labeled with Int 1-3. The corresponding potential (h) and force (j) diagrams show increasing increasing values for closer tip-sample distances. Scale bar: 1 nm

A.3. Carpyridines

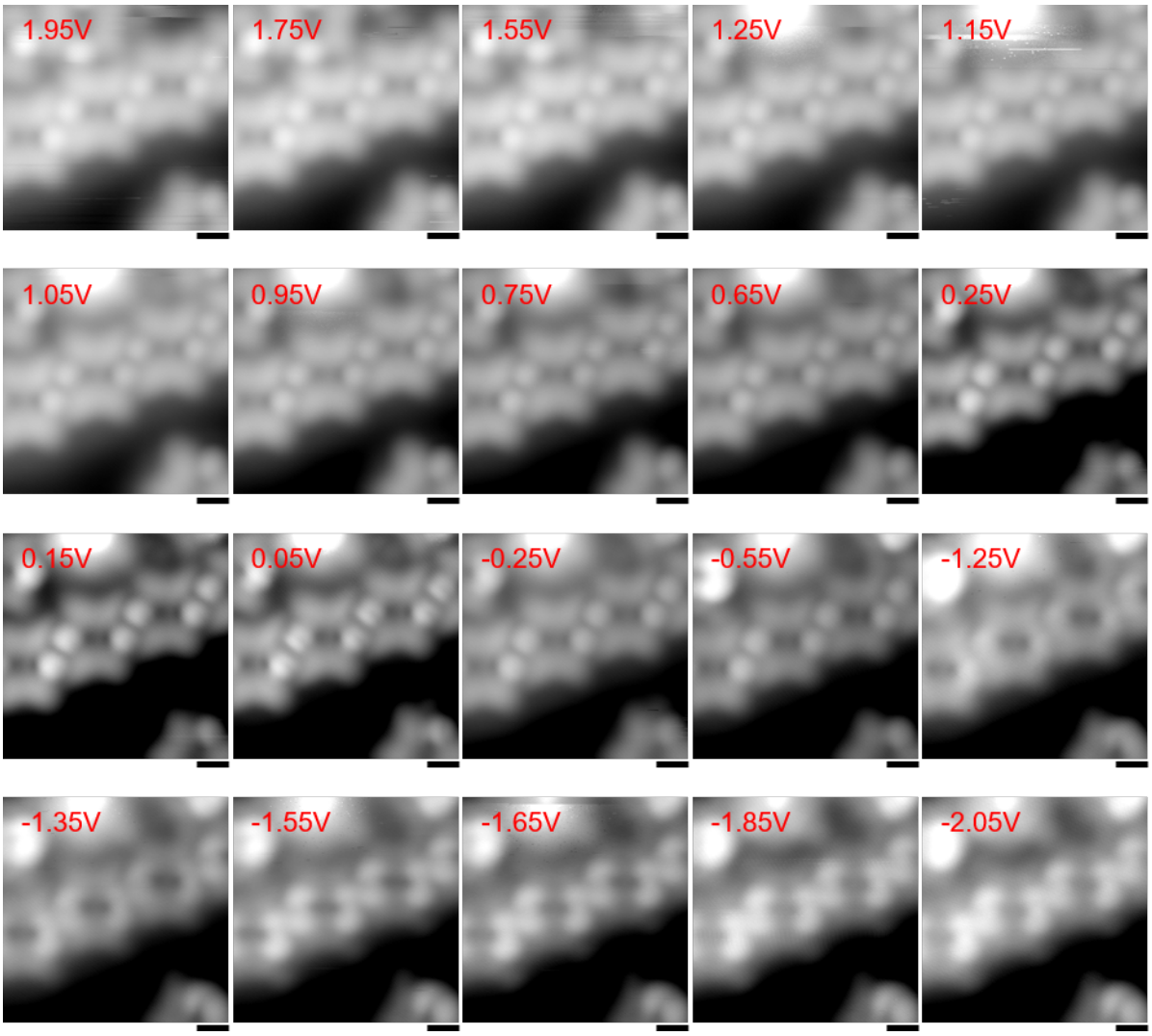

Figure A.17.: Bias series of self-assembled 2H-Car-C1 molecules on Au(111) imaged with a CO tip. Imaging parameters, scale bar: 10.0 pA, 0.5 nm.

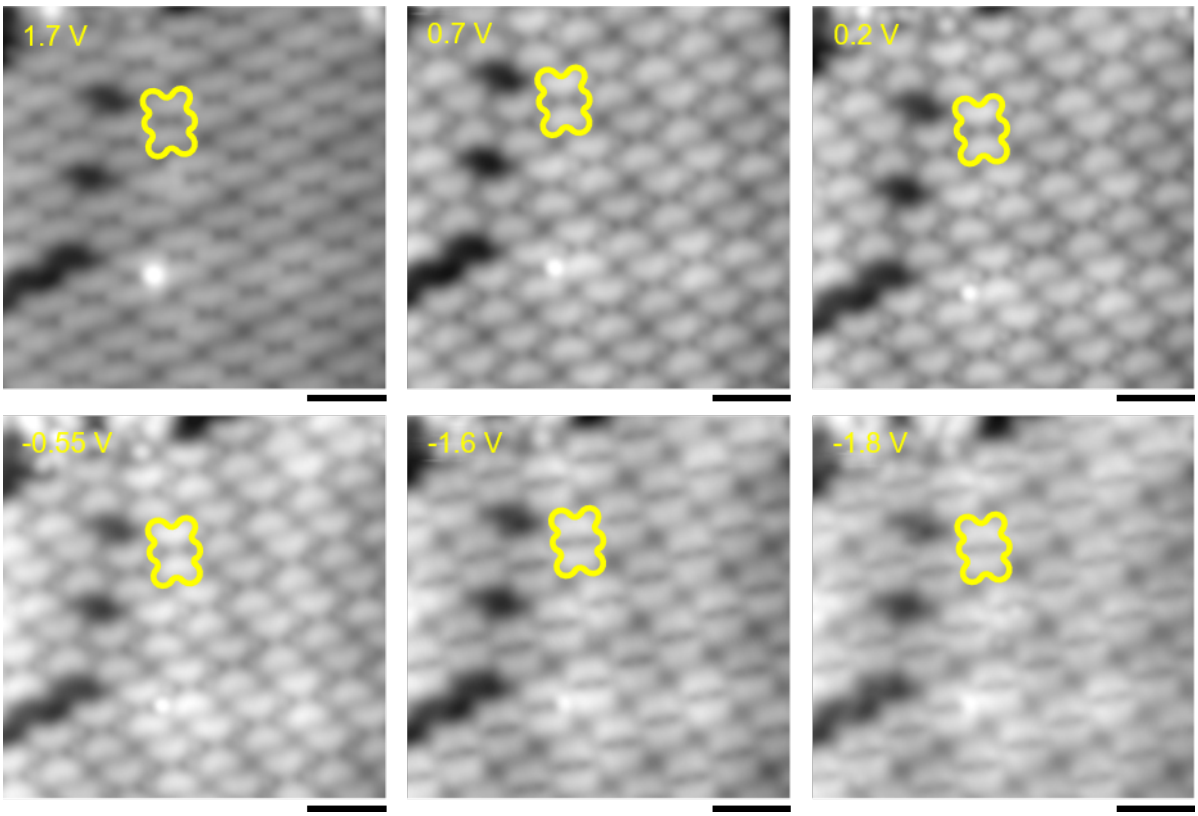

Figure A.18.: Bias series of 2H-Car-C1/Au(111) with a metal tip. The carbazole unit appears as rather straight at 1.7V, appears as a C shape in the intermediate bias region while at higher negative voltages (< -1.6V) the C shape becomes inverted. Imaging parameters, scale bar: 20 pA, 2 nm.

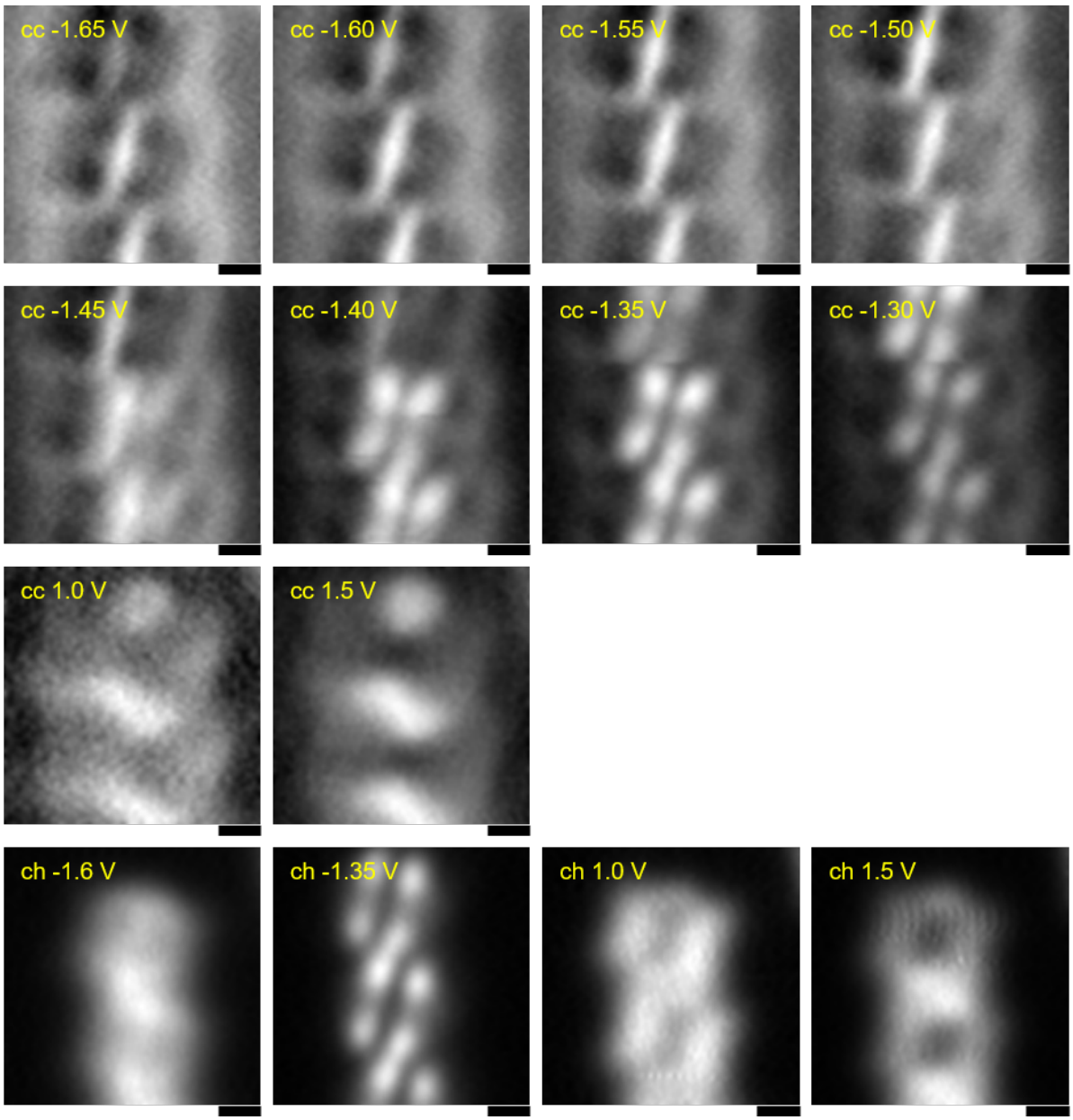

Figure A.19.: dI/dV maps of 2H-Car-C1/Au(111) in constant current (cc) and constant height (ch) mode. Imaging parameters: cc set point -1.65 V to -1.30 V: 10 pA, 1 V: 30 pA, 1.5 V, 50 pA. scale bar 0.5 nm

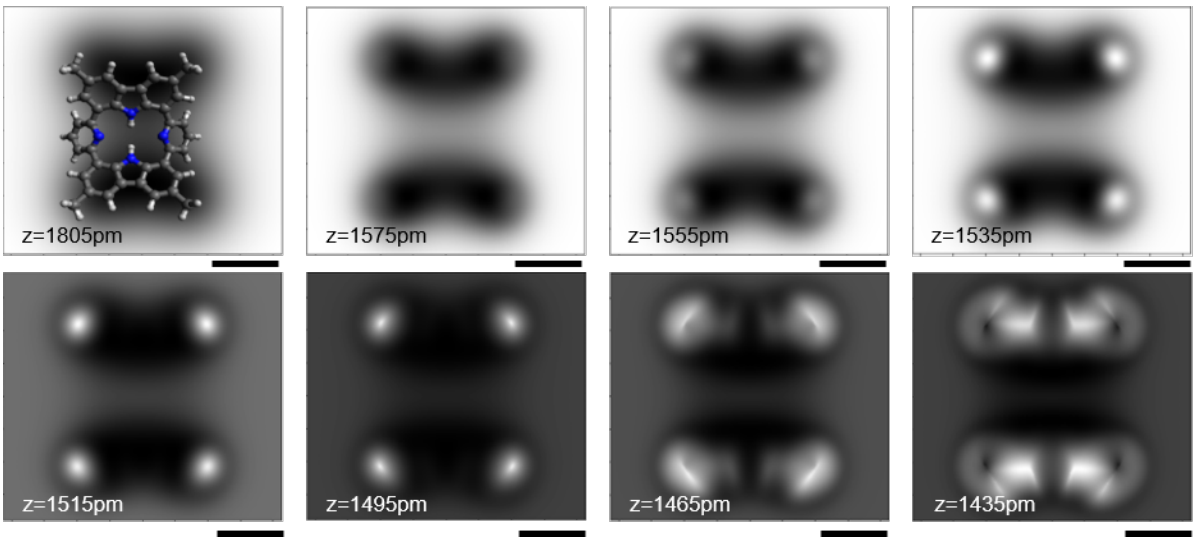

Figure A.20.: Probe-Particle model simulations of 2H-Car-C1 in the pyrdine-down geometry. Scale bar: 0.5 nm.

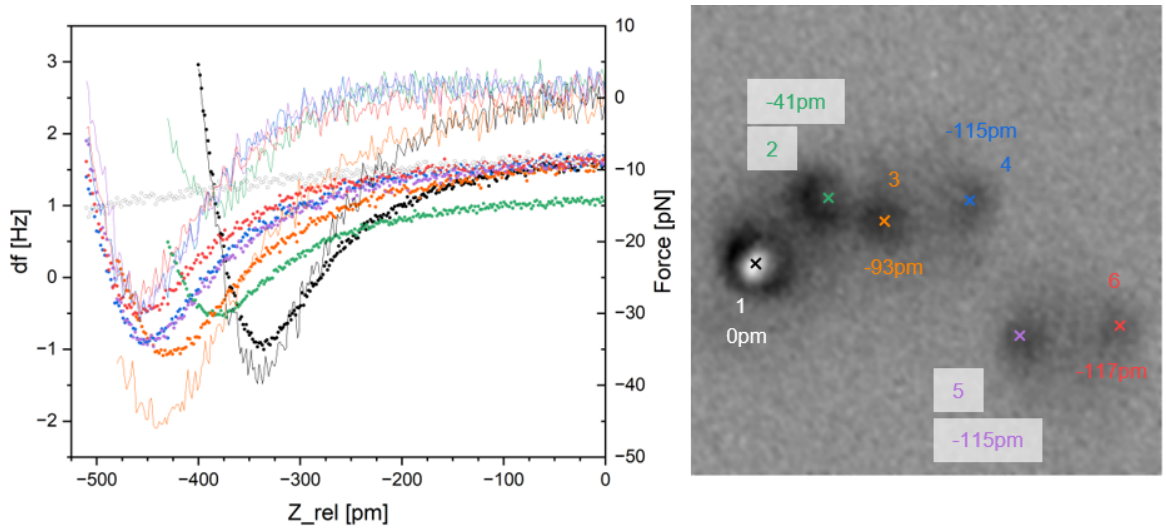

Figure A.21.: Comparison of pyridine group heights via frequency shift(df) and force vs z approach curves. Dotted lines represent the df signal above the pyridines groups marked in the corresponding color. The background corrected force vs z curves are plotted with solid lines. Empty circles mark the background df signal above bare Au(111). The distance of the minimum in the df curves of each pyridine group with respect to the brightest pyridine group (black curve) is given in the image.

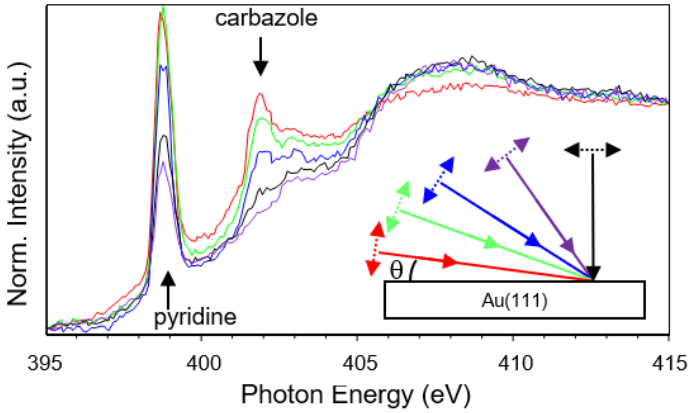

Figure A.22.: N K-edge NEXAFS spectra of 2H-Car-C2/Au(111) for varying incidence angles $\Theta = 30°, 42°, 53°, 70°, 90°$. The π^* resonance around 399 eV, originating from the nitrogen in the pyridine group, shows non-zero intensity at normal incidence. The signal of the carbazole group vanishes at normal incidence. The inset in the bottom right depicts the polarization direction (dashed lines) of the incoming light (solid lines).

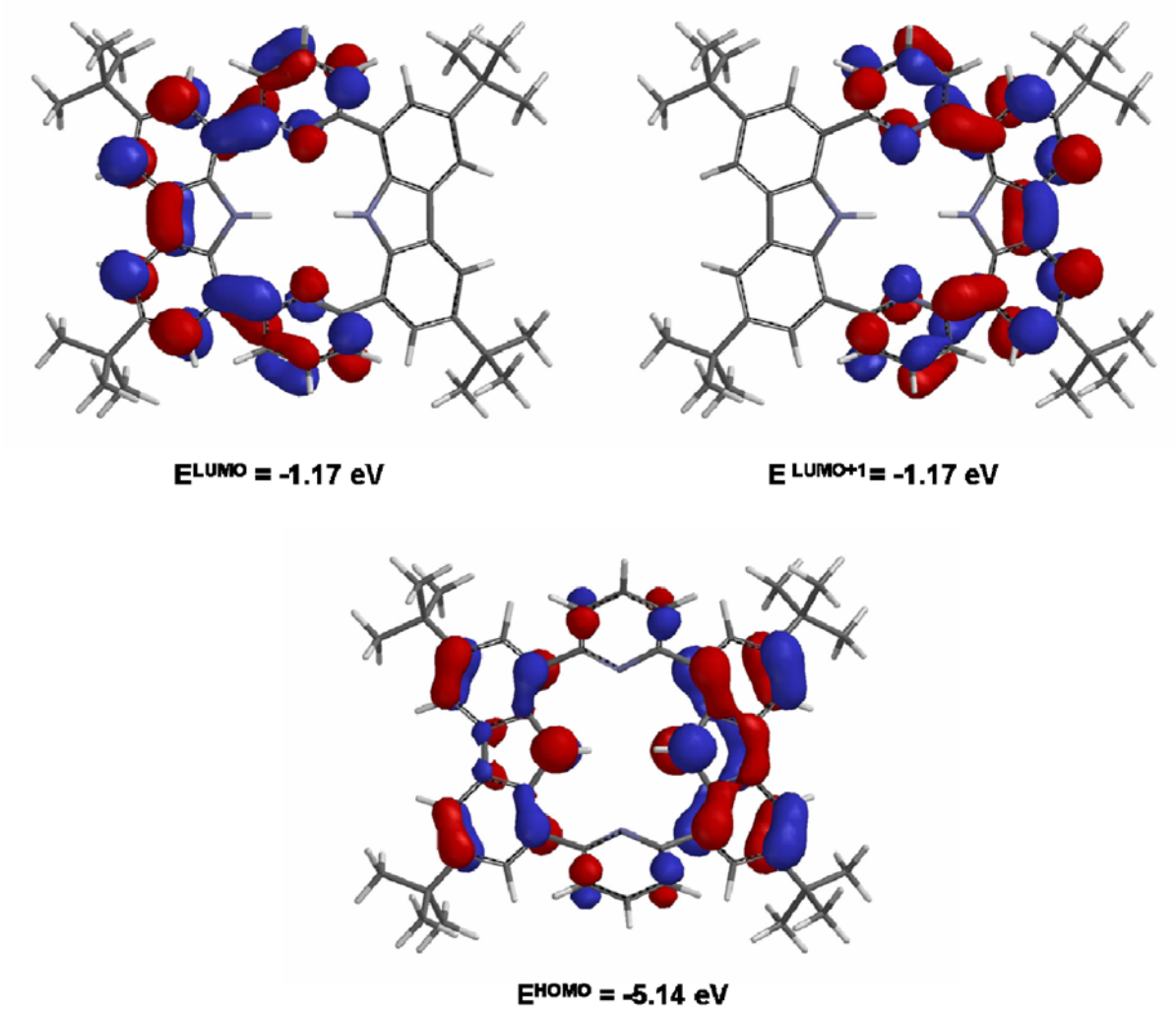

Figure A.23.: Calculated LUMO, LUMO+1 and HOMO orbitals of 2H-Car-tBu. Figure reproduced with permission from L. Arnold, H. Norouzi-Arasi, M. Wagner, V. Enkelmann and K. Müllen, Chem. Commun., 2011, 47, 970 [87].

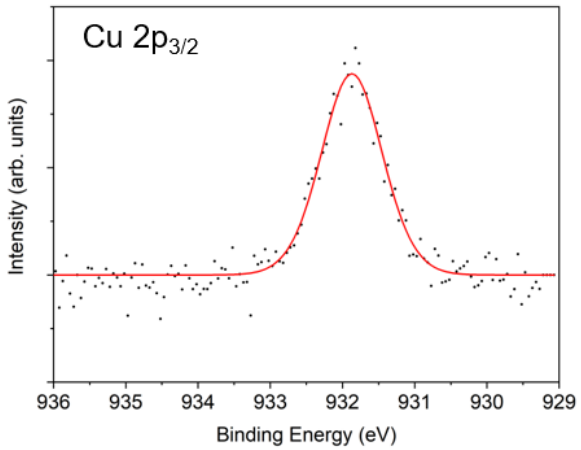

Figure A.24.: XPS of the Cu 2p 3/2 region corresponding to the Cu/2H-Car-C1/Au(111) sample.

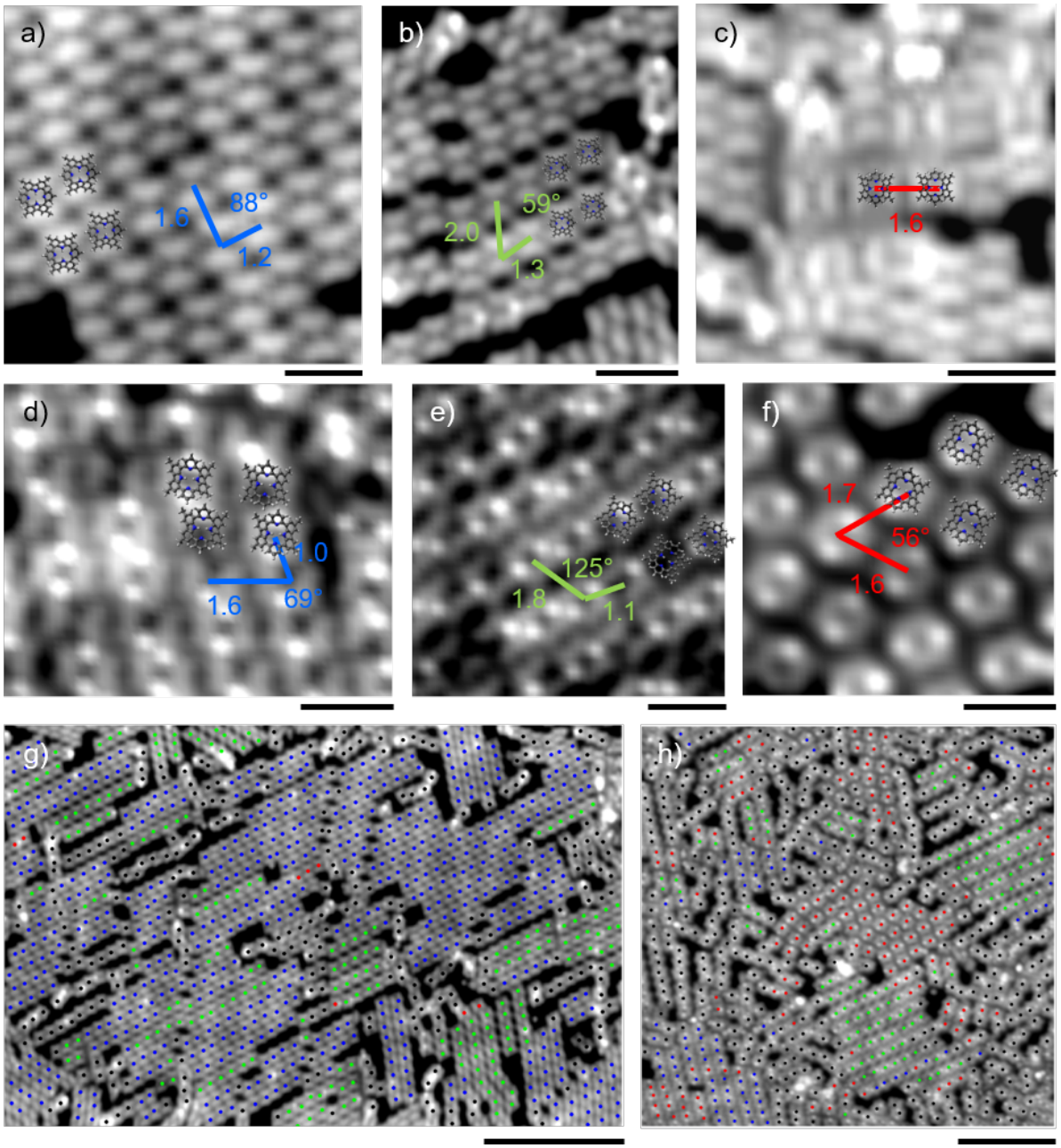

Figure A.25.: Changes in the self-assembly in Cu/2H-Car-C1/Au(111) compared to 2H-Car-C1/Au(111). For both self-assembled patterns, without Cu (a-c) and with Cu (d-f), molecular models are overlaid. In the overview images g (no Cu) and h (with Cu), the coloured dots mark the corresponding arrangements observed in a-f). Black dots mark single-molecule-wide chains and unordered structures. Imaging parameters, scale bar: a) 22 pA, 1 V, 2 nm b) 22 pA, 1 V, 3 nm c) 39 pA, 1 V, 3 nm d-f) 20 pA, 0.2 V, 2 nm g) 22 pA, 1 V, 15 nm h) 20 pA, 0.2 V, 10 nm.

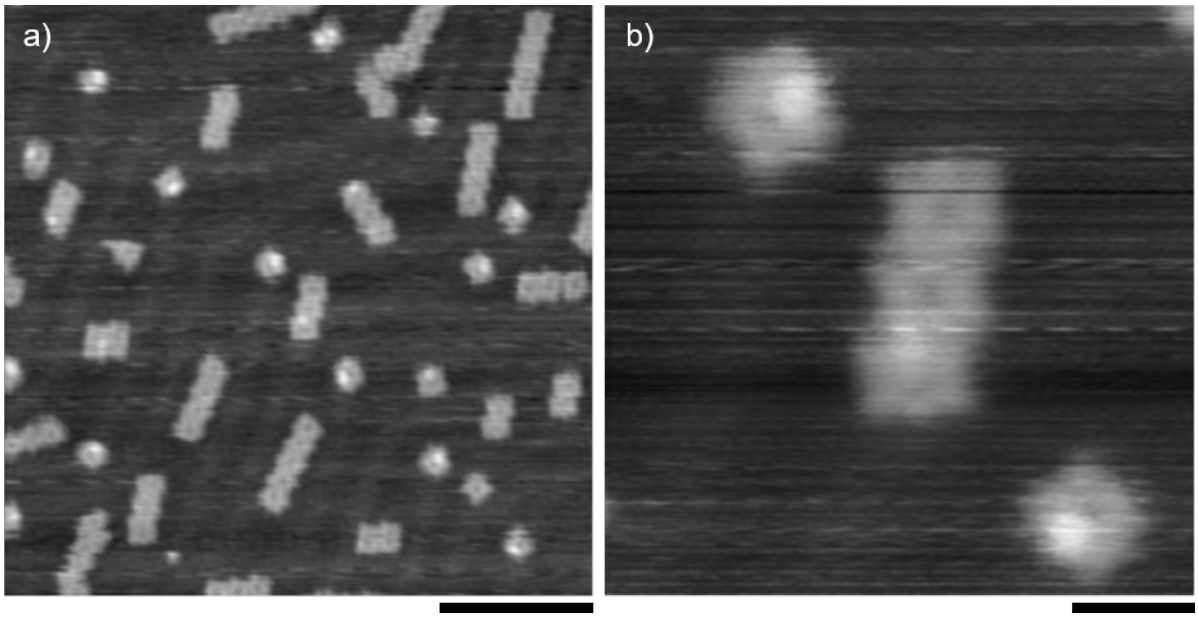

Figure A.26.: STM images of 2H-Car-C1/Au(111) annealed to 100°C. Imaging parameters, scale bar: a) 100 pA, 0.7 V, 10 nm; b) 100 pA, 0.7 V, 2 nm.

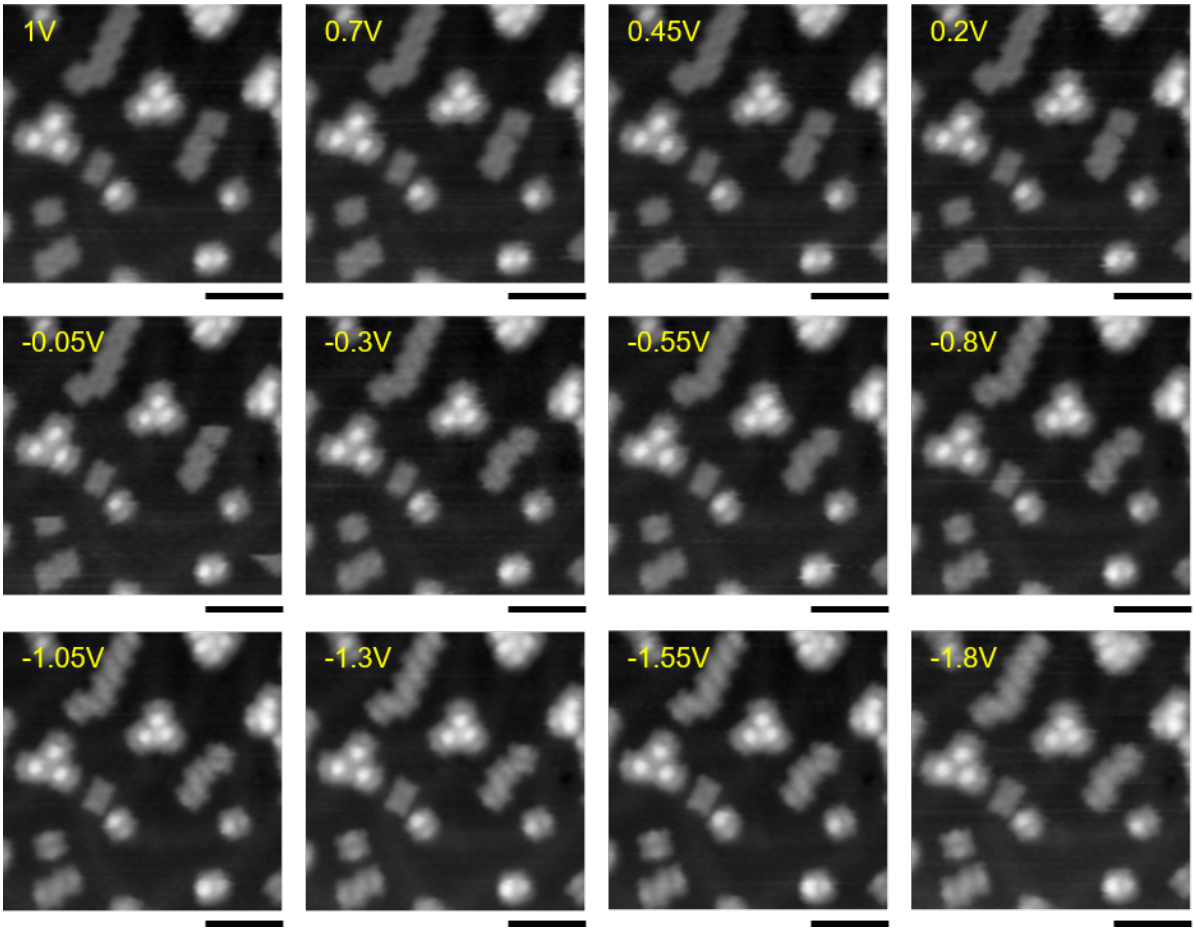

Figure A.27.: Bias sereis of Fe/2H-Car-C1/Au(111) annealed to 100°C. Imaging parameters, scale bar: CO-tip, 20 pA, 5 nm.

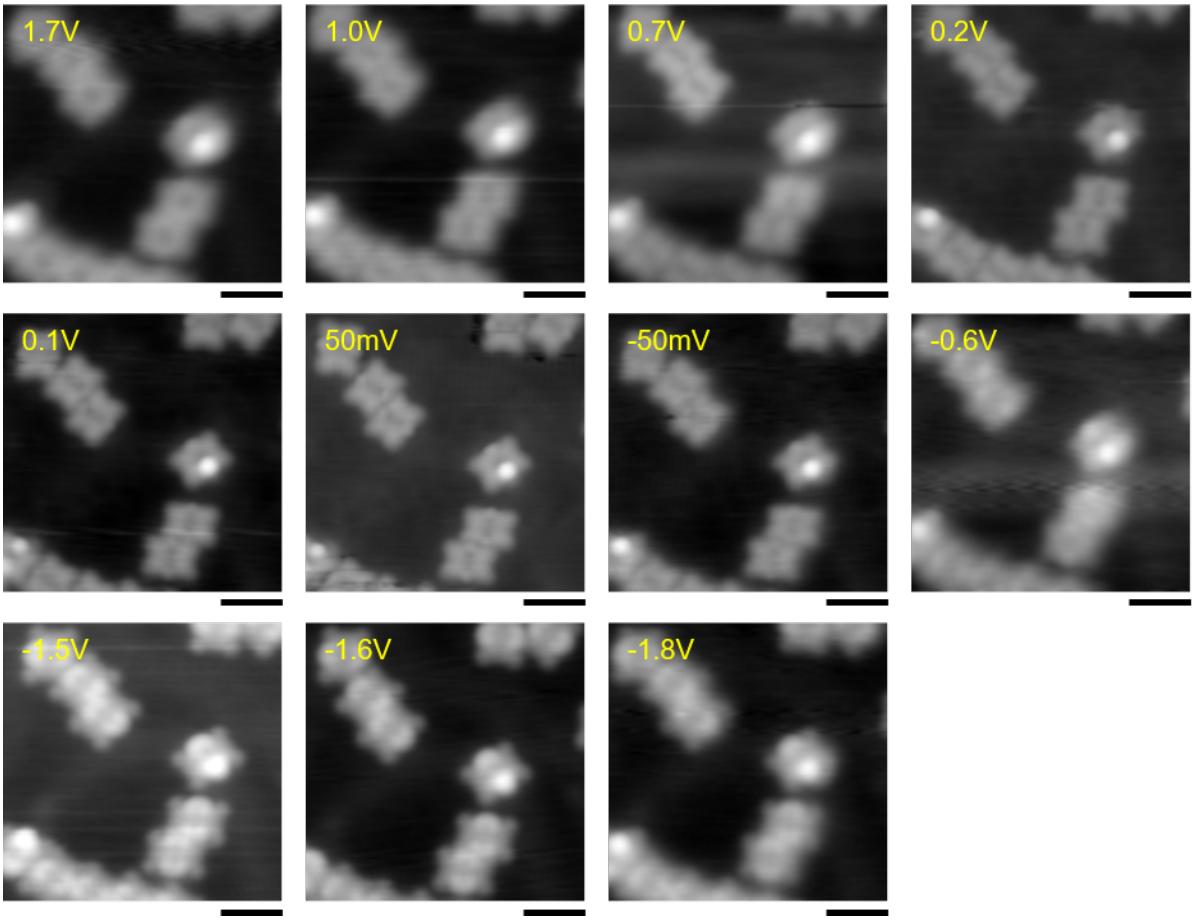

Figure A.28.: Bias sereis of Fe/2H-Car-C1/Au(111) annealed to 200°C. Imaging parameters, scale bar: 100 pA, 2 nm.

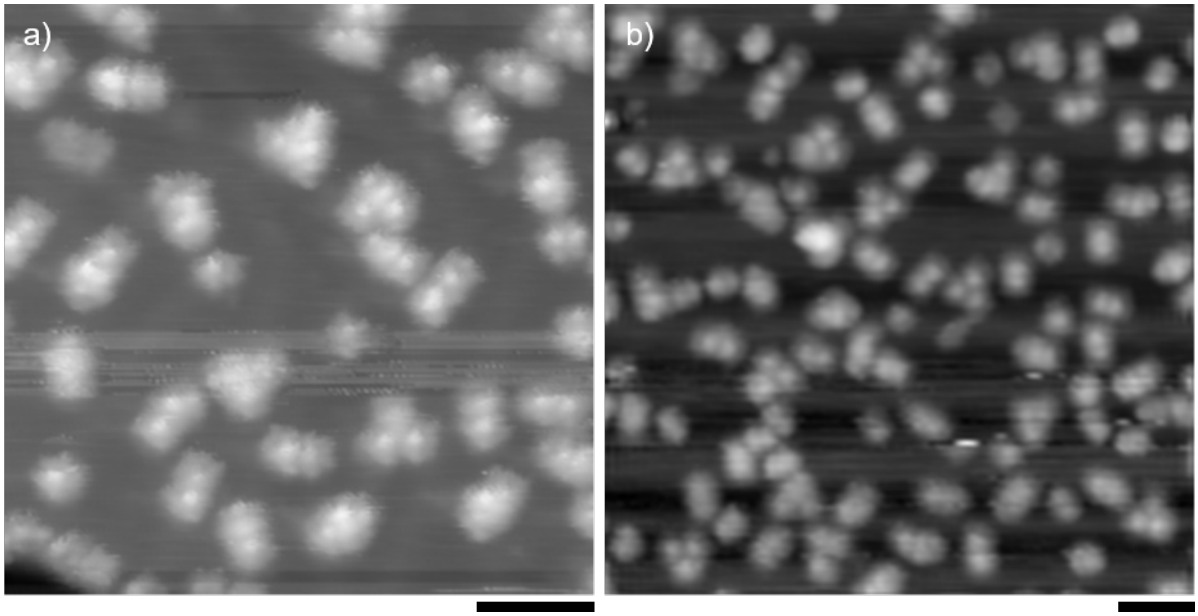

Figure A.29.: STM images of 2H-Car-C1/Au(111) after deposition of Fe at room temperature. Imaging parameters, scale bar: a) 75 pA, 50 mV, 5 nm; b) 55 pA, 1.2 V, 5 nm.

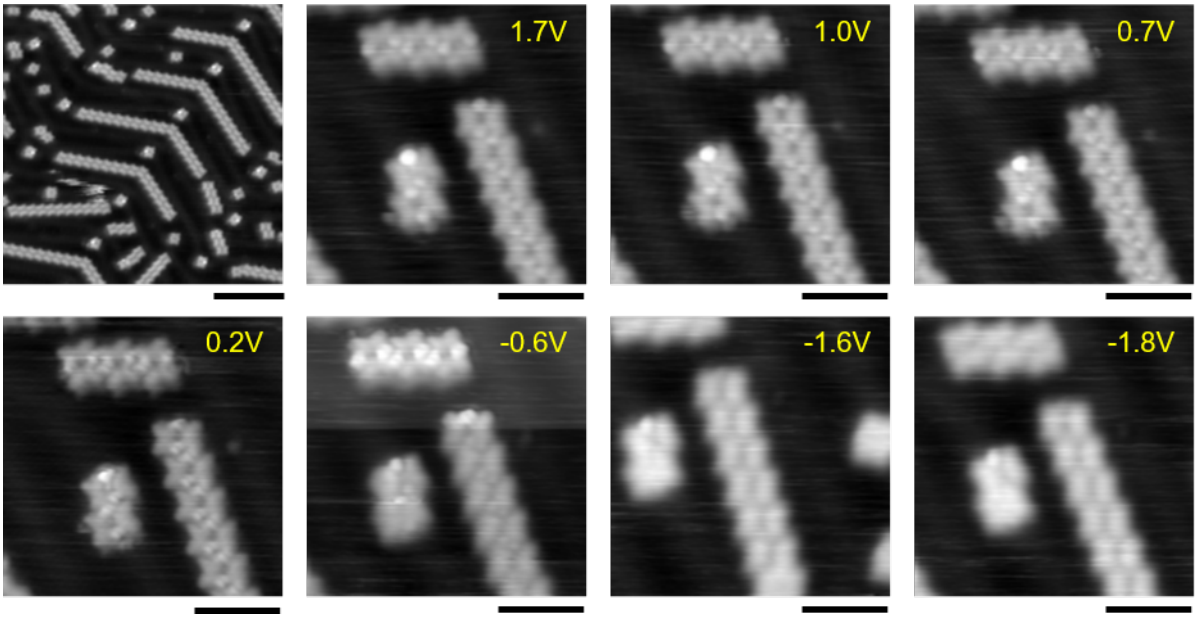

Figure A.30.: STM images of 2H-Car-C1/Au(111) annealed to 200°C. Imaging parameters, scale bar: overview: 100 pA, -1.6 V, 10 nm bias series: 100 pA, 2 nm.

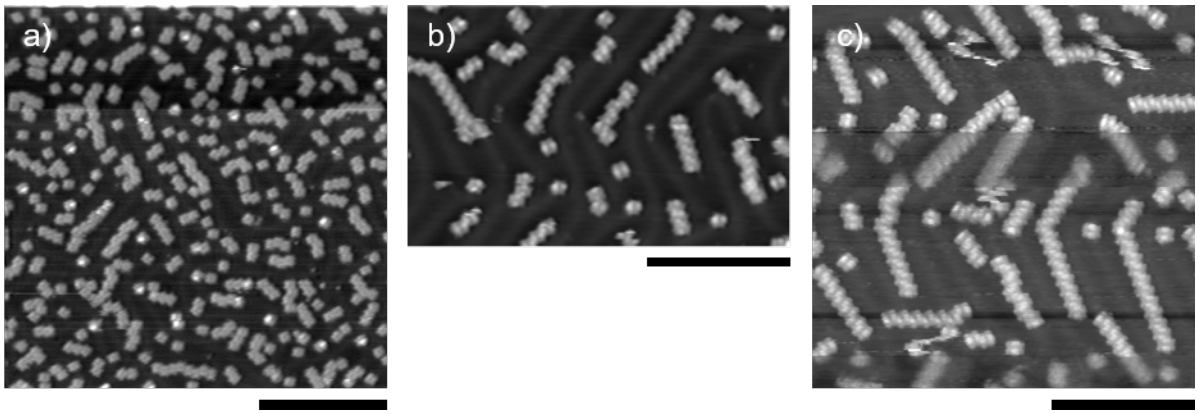

Figure A.31.: STM images of Fe/2H-Car-C1/Au(111) annealed to 200°C with decreasing Fe dosage in a to c. Fe flux · time = a): 520 nA · s, b): 42 nA · s and c): 8.4 nA · s. Imaging parameters, scale bar: a) 30 pA, 0.7 V, 20 nm b) 100 pA, -1.6 V, 15 nm c) 100 pA, -1.6 V, 15 nm .

B. Bibliography

[1] G. Binnig et al. "Surface Studies by Scanning Tunneling Microscopy." In: *Physical Review Letters* 49.1 (1982), pp. 57–61. DOI: 10.1103/physrevlett.49.57 (cit. on p. 7).

[2] P. Jelínek. "High resolution SPM imaging of organic molecules with functionalized tips." In: *Journal of Physics: Condensed Matter* 29.34 (2017), p. 343002. DOI: 10.1088/1361-648x/aa76c7 (cit. on p. 7).

[3] D. Wang et al. "Recent Progress of Imaging Chemical Bonds by Scanning Probe Microscopy: A Review." In: *ACS Nano* (2024). DOI: 10.1021/acsnano.4c10522 (cit. on p. 7).

[4] G. Binnig, C. F. Quate, and C. Gerber. "Atomic Force Microscope." In: *Physical Review Letters* 56.9 (1986), pp. 930–933. DOI: 10.1103/physrevlett.56.930 (cit. on p. 7).

[5] K. Bian et al. "Scanning probe microscopy." In: *Nature Reviews Methods Primers* 1.1 (2021), p. 36. DOI: 10.1038/s43586-021-00033-2 (cit. on pp. 7, 11, 14).

[6] L. Gross et al. "The Chemical Structure of a Molecule Resolved by Atomic Force Microscopy." In: *Science* 325.5944 (2009), pp. 1110–1114. DOI: 10.1126/science.1176210 (cit. on p. 7).

[7] K. Itaya and E. Tomita. "Scanning tunneling microscope for electrochemistry - a new concept for the in situ scanning tunneling microscope in electrolyte solutions." In: *Surface Science* 201.3 (1988), pp. L507–L512. DOI: 10.1016/0039-6028(88)90489-x (cit. on p. 7).

[8] Y. Liang et al. "Electrochemical Scanning Probe Microscopies in Electrocatalysis." In: *Small Methods* 3.8 (2018). DOI: 10.1002/smtd.201800387 (cit. on p. 7).

[9] L. Askadskaya and J. P. Rabe. "Anisotropic molecular dynamics in the vicinity of order-disorder transitions in organic monolayers." In: *Physical Review Letters* 69.9 (1992), pp. 1395–1398. DOI: 10.1103/physrevlett.69.1395 (cit. on p. 7).

[10] R. Wiesendanger et al. "Observation of vacuum tunneling of spin-polarized electrons with the scanning tunneling microscope." In: *Physical Review Letters* 65.2 (1990), pp. 247–250. DOI: 10.1103/physrevlett.65.247 (cit. on p. 7).

[11] S. Baumann et al. "Electron paramagnetic resonance of individual atoms on a surface." In: *Science* 350.6259 (2015), pp. 417–420. DOI: 10.1126/science.aac8703 (cit. on p. 7).

[12] J. K. Gimzewski et al. "Photon emission with the scanning tunneling microscope." In: *Zeitschrift fuer Physik B Condensed Matter* 72.4 (1988), pp. 497–501. DOI: 10.1007/bf01314531 (cit. on p. 7).

[13] R. Berndt et al. "Photon Emission at Molecular Resolution Induced by a Scanning Tunneling Microscope." In: *Science* 262.5138 (1993), pp. 1425–1427. DOI: 10.1126/science.262.5138.1425 (cit. on p. 7).

[14] J. H. K. Pfisterer et al. "Direct instrumental identification of catalytically active surface sites." In: *Nature* 549.7670 (2017), pp. 74–77. DOI: 10.1038/nature23661 (cit. on p. 7).

[15] J. K. H. Hörber and M. J. Miles. "Scanning Probe Evolution in Biology." In: *Science* 302.5647 (2003), pp. 1002–1005. DOI: 10.1126/science.1067410 (cit. on p. 7).

[16] Y. F. Dufrêne et al. "Imaging modes of atomic force microscopy for application in molecular and cell biology." In: *Nature Nanotechnology* 12.4 (2017), pp. 295–307. DOI: 10.1038/nnano.2017.45 (cit. on p. 7).

[17] R. Wiesendanger. "Spin mapping at the nanoscale and atomic scale." In: *Reviews of Modern Physics* 81.4 (2009), pp. 1495–1550. DOI: 10.1103/revmodphys.81.1495 (cit. on p. 7).

[18] H. Oka et al. "Spin-polarized quantum confinement in nanostructures: Scanning tunneling microscopy." In: *Reviews of Modern Physics* 86.4 (2014), pp. 1127–1168. DOI: 10.1103/revmodphys.86.1127 (cit. on p. 7).

[19] Y. Chen, Y. Bae, and A. J. Heinrich. "Harnessing the Quantum Behavior of Spins on Surfaces." In: *Advanced Materials* 35.27 (2022). DOI: 10.1002/adma.202107534 (cit. on p. 7).

[20] K. Kuhnke et al. "Atomic-Scale Imaging and Spectroscopy of Electroluminescence at Molecular Interfaces." In: *Chemical Reviews* 117.7 (2017), pp. 5174–5222. DOI: 10.1021/acs.chemrev.6b00645 (cit. on p. 7).

[21] R. Lindner and A. Kühnle. "On-Surface Reactions." In: *ChemPhysChem* 16.8 (2015), pp. 1582–1592. DOI: 10.1002/cphc.201500161 (cit. on p. 7).

[22] T. Wang and J. Zhu. "Confined on-surface organic synthesis: Strategies and mechanisms." In: *Surface Science Reports* 74.2 (2019), pp. 97–140. DOI: 10.1016/j.surfrep.2019.05.001 (cit. on p. 7).

[23] S. Clair and D. G. de Oteyza. "Controlling a Chemical Coupling Reaction on a Surface: Tools and Strategies for On-Surface Synthesis." In: *Chemical Reviews* 119.7 (2019), pp. 4717–4776. DOI: 10.1021/acs.chemrev.8b00601 (cit. on p. 7).

[24] Q. Fan et al. "Surface-Assisted Organic Synthesis of Hyperbenzene Nanotroughs." In: *Angewandte Chemie International Edition* 52.17 (2013), pp. 4668–4672. DOI: 10.1002/anie.201300610 (cit. on p. 7).

[25] L. Grill and S. Hecht. "Covalent on-surface polymerization." In: *Nature Chemistry* 12.2 (2020), pp. 115–130. DOI: 10.1038/s41557-019-0392-9 (cit. on p. 7).

[26] H.-Y. Gao et al. "Glaser Coupling at Metal Surfaces." In: *Angewandte Chemie International Edition* 52.14 (2013), pp. 4024–4028. DOI: 10.1002/anie.201208597 (cit. on p. 7).

[27] Q. Sun et al. "On-Surface Formation of One-Dimensional Polyphenylene through Bergman Cyclization." In: *Journal of the American Chemical Society* 135.23 (2013), pp. 8448–8451. DOI: 10.1021/ja404039t (cit. on p. 7).

[28] Q. Sun et al. "On-surface aryl–aryl coupling via selective C–H activation." In: *Chemical Communications* 50.80 (2014), pp. 11825–11828. DOI: 10.1039/c4cc05482b (cit. on p. 7).

[29] L. Grossmann et al. "On-surface photopolymerization of two-dimensional polymers ordered on the mesoscale." In: *Nature Chemistry* 13.8 (2021), pp. 730–736. DOI: 10.1038/s41557-021-00709-y (cit. on p. 7).

[30] M. Lackinger. "Surface-assisted Ullmann coupling." In: *Chemical Communications* 53.56 (2017), pp. 7872–7885. DOI: 10.1039/c7cc03402d (cit. on pp. 7, 115).

[31] J. A. Lipton-Duffin et al. "Synthesis of Polyphenylene Molecular Wires by Surface-Confined Polymerization." In: *Small* 5.5 (2009), pp. 592–597. DOI: 10.1002/smll.200801943 (cit. on p. 7).

[32] G. S. McCarty and P. S. Weiss. "Formation and Manipulation of Protopolymer Chains." In: *Journal of the American Chemical Society* 126.51 (2004), pp. 16772–16776. DOI: 10.1021/ja038930g (cit. on p. 7).

[33] J. Cai et al. "Atomically precise bottom-up fabrication of graphene nanoribbons." In: *Nature* 466.7305 (2010), pp. 470–473. DOI: 10.1038/nature09211 (cit. on p. 7).

[34] L. Lafferentz et al. "Controlling on-surface polymerization by hierarchical and substrate-directed growth." In: *Nature Chemistry* 4.3 (2012), pp. 215–220. DOI: 10.1038/nchem.1242 (cit. on p. 7).

[35] M. O. Blunt et al. "Templating molecular adsorption using a covalent organic framework." In: *Chemical Communications* 46.38 (2010), pp. 7157–7159. DOI: 10.1039/c0cc01810d (cit. on pp. 7, 52, 57).

[36] Z. Hao et al. "On-surface synthesis of one-type pore single-crystal porous covalent organic frameworks." In: *Chemical Communications* 55.72 (2019), p. 10800. DOI: 10.1039/c9cc04561a (cit. on pp. 7, 52).

[37] W. Auwärter et al. "A surface-anchored molecular four-level conductance switch based on single proton transfer." In: *Nature Nanotechnology* 7.1 (2011), pp. 41–46. DOI: 10.1038/nnano.2011.211 (cit. on pp. 8, 104).

[38] M. Fuechsle et al. "A single-atom transistor." In: *Nature Nanotechnology* 7.4 (2012), pp. 242–246. DOI: 10.1038/nnano.2012.21 (cit. on pp. 8, 42).

[39] G. Dujardin, R. E. Walkup, and P. Avouris. "Dissociation of Individual Molecules with Electrons from the Tip of a Scanning Tunneling Microscope." In: *Science* 255.5049 (1992), pp. 1232–1235. DOI: 10.1126/science.255.5049.1232 (cit. on p. 8).

[40] R. Martel, P. Avouris, and I.-W. Lyo. "Molecularly Adsorbed Oxygen Species on Si(111)-(7×7): STM-Induced Dissociative Attachment Studies." In: *Science* 272.5260 (1996), pp. 385–388. DOI: 10.1126/science.272.5260.385 (cit. on p. 8).

[41] S.-W. Hla et al. "Inducing All Steps of a Chemical Reaction with the Scanning Tunneling Microscope Tip: Towards Single Molecule Engineering." In: *Physical Review Letters* 85.13 (2000), pp. 2777–2780. DOI: 10.1103/physrevlett.85.2777 (cit. on p. 8).

[42] P. Maksymovych et al. "Collective Reactivity of Molecular Chains Self-Assembled on a Surface." In: *Science* 322.5908 (2008), pp. 1664–1667. DOI: 10.1126/science.1165291 (cit. on p. 8).

[43] K. Kaiser et al. "An sp-hybridized molecular carbon allotrope, cyclo[18]carbon." In: *Science* 365.6459 (2019), pp. 1299–1301. DOI: 10.1126/science.aay1914 (cit. on p. 8).

[44] F. Albrecht et al. "The odd-number cyclo[13]carbon and its dimer, cyclo[26]carbon." In: *Science* 384.6696 (2024), pp. 677–682. DOI: 10.1126/science.ado1399 (cit. on p. 8).

[45] F. Albrecht et al. "Selectivity in single-molecule reactions by tip-induced redox chemistry." In: *Science* 377.6603 (2022), pp. 298–301. DOI: 10.1126/science.abo6471 (cit. on p. 8).

[46] Y. Lin et al. "Steering Electron-Induced Surface Reaction via a Molecular Assembly Approach." In: *Journal of the American Chemical Society* 146.14 (2024), pp. 10150–10158. DOI: 10.1021/jacs.4c01623 (cit. on p. 8).

[47] Q. Zhong et al. "Constructing covalent organic nanoarchitectures molecule by molecule via scanning probe manipulation." In: *Nature Chemistry* 13.11 (2021), pp. 1133–1139. DOI: 10.1038/s41557-021-00773-4 (cit. on p. 8).

[48] D. M. Eigler and E. K. Schweizer. "Positioning single atoms with a scanning tunnelling microscope." In: *Nature* 344.6266 (1990), pp. 524–526. DOI: 10.1038/344524a0 (cit. on p. 8).

[49] M. F. Crommie, C. P. Lutz, and D. M. Eigler. "Confinement of Electrons to Quantum Corrals on a Metal Surface." In: *Science* 262.5131 (1993), pp. 218–220. DOI: 10.1126/science.262.5131.218 (cit. on p. 8).

[50] S. E. Freeney et al. "Electronic Quantum Materials Simulated with Artificial Model Lattices." In: *ACS Nanoscience Au* 2.3 (2022), pp. 198–224. DOI: 10.1021/acsnanoscienceau.1c00054 (cit. on p. 8).

[51] D. Civita et al. “Control of long-distance motion of single molecules on a surface.” In: *Science* 370.6519 (2020), pp. 957–960. DOI: 10.1126/science.abd0696 (cit. on p. 8).

[52] M. Ternes et al. “The Force Needed to Move an Atom on a Surface.” In: *Science* 319.5866 (2008), pp. 1066–1069. DOI: 10.1126/science.1150288 (cit. on pp. 8, 10, 16, 17, 43, 70, 74, 75).

[53] H.-Q. Mao et al. “Mechanical properties of H2Pc self-assembled monolayers at the single molecule level by noncontact atomic force microscopy.” In: *Journal of Physics: Condensed Matter* 24.8 (2012), p. 084004. DOI: 10.1088/0953-8984/24/8/084004 (cit. on pp. 8, 74).

[54] G. Langewisch et al. “Forces During the Controlled Displacement of Organic Molecules.” In: *Physical Review Letters* 110.3 (2013), p. 036101. DOI: 10.1103/physrevlett.110.036101 (cit. on pp. 8, 74).

[55] G. Langewisch et al. “Long Jumps of an Organic Molecule Induced by Atomic Force Microscopy Manipulation.” In: *Advanced Materials Interfaces* 1.2 (2013). DOI: 10.1002/admi.201300013 (cit. on p. 8).

[56] S. P. Jarvis et al. “Measuring the mechanical properties of molecular conformers.” In: *Nature Communications* 6.1 (2015). DOI: 10.1038/ncomms9338 (cit. on pp. 8, 74).

[57] R. Pawlak et al. “Single-molecule manipulation experiments to explore friction and adhesion.” In: *Journal of Physics D: Applied Physics* 50.11 (2017), p. 113003. DOI: 10.1088/1361-6463/aa599d (cit. on p. 8).

[58] K. Rothe et al. “Quantifying Force and Energy in Single-Molecule Metalation.” In: *Journal of the American Chemical Society* 144.16 (2022), pp. 7054–7057. DOI: 10.1021/jacs.2c00900 (cit. on p. 8).

[59] C. Musumeci. “Advanced Scanning Probe Microscopy of Graphene and Other 2D Materials.” In: *Crystals* 7.7 (2017), p. 216. DOI: 10.3390/cryst7070216 (cit. on p. 8).

[60] S. Su, J. Zhao, and T. H. Ly. “Scanning Probe Microscopies for Characterizations of 2D Materials.” In: *Small Methods* (2024). DOI: 10.1002/smtd.202400211 (cit. on p. 8).

[61] R. Cao, A. M. Díaz-García, and R. Cao. “Coordination compounds built on metal surfaces.” In: *Coordination Chemistry Reviews* 253.9–10 (2009), pp. 1262–1275. DOI: 10.1016/j.ccr.2008.08.010 (cit. on p. 9).

[62] R. Makiura et al. “Surface nano-architecture of a metal–organic framework.” In: *Nature Materials* 9.7 (2010), pp. 565–571. DOI: 10.1038/nmat2769 (cit. on p. 9).

[63] O. Shekhah et al. “Controlling interpenetration in metal–organic frameworks by liquid-phase epitaxy.” In: *Nature Materials* 8.6 (2009), pp. 481–484. DOI: 10.1038/nmat2445 (cit. on p. 9).

[64] R. Sakamoto et al. "π-Conjugated bis(terpyridine)metal complex molecular wires." In: *Chemical Society Reviews* 44.21 (2015), pp. 7698–7714. DOI: 10.1039/c5cs00081e (cit. on p. 9).

[65] B. H. Lee et al. "Growth and Properties of Hybrid Organic-Inorganic Metalcone Films Using Molecular Layer Deposition Techniques." In: *Advanced Functional Materials* 23.5 (2012), pp. 532–546. DOI: 10.1002/adfm.201200370 (cit. on p. 9).

[66] J.-L. Zhuang, A. Terfort, and C. Wöll. "Formation of oriented and patterned films of metal–organic frameworks by liquid phase epitaxy: A review." In: *Coordination Chemistry Reviews* 307 (2016), pp. 391–424. DOI: 10.1016/j.ccr.2015.09.013 (cit. on p. 9).

[67] Y.-H. Xiao, Z.-G. Gu, and J. Zhang. "Surface-coordinated metal–organic framework thin films (SURMOFs) for electrocatalytic applications." In: *Nanoscale* 12.24 (2020), pp. 12712–12730. DOI: 10.1039/d0nr03115a (cit. on p. 9).

[68] Y.-H. Xiao et al. "Surface-coordinated metal-organic framework thin films (SURMOFs): From fabrication to energy applications." In: *EnergyChem* 3.6 (2021), p. 100065. DOI: 10.1016/j.enchem.2021.100065 (cit. on p. 9).

[69] K. Oura et al. *Surface Science An Introduction*. Springer, 2003 (cit. on p. 9).

[70] *The Nobel Prize in Chemistry 2007*. https://www.nobelprize.org/prizes/chemistry/2007/press-release/ (cit. on p. 9).

[71] T. Kudernac et al. "Electrically driven directional motion of a four-wheeled molecule on a metal surface." In: *Nature* 479.7372 (2011), pp. 208–211. DOI: 10.1038/nature10587 (cit. on p. 9).

[72] S. Stolz et al. "Molecular motor crossing the frontier of classical to quantum tunneling motion." In: *Proceedings of the National Academy of Sciences* 117.26 (2020), pp. 14838–14842. DOI: 10.1073/pnas.1918654117 (cit. on p. 9).

[73] F. Eisenhut et al. "One-way rotation of a chemically anchored single molecule-rotor." In: *Nanoscale* 13.38 (2021), pp. 16077–16083. DOI: 10.1039/D1NR04583K (cit. on pp. 9, 76).

[74] M. Schied et al. "Chirality-Specific Unidirectional Rotation of Molecular Motors on Cu(111)." In: *ACS Nano* 17.4 (2023), pp. 3958–3965. DOI: 10.1021/acsnano.2c12720 (cit. on p. 9).

[75] T. Jasper-Toennies et al. "Rotation of Ethoxy and Ethyl Moieties on a Molecular Platform on Au(111)." In: *ACS Nano* 14.4 (2020), pp. 3907–3916. DOI: 10.1021/acsnano.0c00029 (cit. on p. 9).

[76] E. Moreno Pineda et al. "Surface confinement of TbPc2-SMMs: structural, electronic and magnetic properties." In: *Dalton Transactions* 45.46 (2016), pp. 18417–18433. DOI: 10.1039/c6dt03298b (cit. on p. 9).

[77] H. Tanaka et al. "Molecular Rotation in Self-Assembled Multidecker Porphyrin Complexes." In: *ACS Nano* 5.12 (2011), pp. 9575–9582. DOI: 10.1021/nn203773p (cit. on pp. 9, 42, 63).

[78] J. Otsuki et al. "Arrays of Double-Decker Porphyrins on Highly Oriented Pyrolytic Graphite." In: *Langmuir* 22.13 (2006), pp. 5708–5715. DOI: 10.1021/la0608617 (cit. on p. 9).

[79] J. Otsuki et al. "Rotational Libration of a Double-Decker Porphyrin Visualized." In: *Journal of the American Chemical Society* 132.20 (2010), pp. 6870–6871. DOI: 10.1021/ja907077e (cit. on pp. 9, 63).

[80] K. Miyake et al. "Molecular Motion of Surface-Immobilized Double-Decker Phthalocyanine Complexes." In: *Journal of the American Chemical Society* 131.49 (2009), pp. 17808–17813. DOI: 10.1021/ja904629d (cit. on pp. 9, 73).

[81] D. Écija et al. "Assembly and Manipulation of Rotatable Cerium Porphyrinato Sandwich Complexes on a Surface." In: *Angewandte Chemie International Edition* 50.17 (2011), pp. 3872–3877. DOI: 10.1002/anie.201007370 (cit. on pp. 9, 42, 43, 62, 63).

[82] W. Auwärter et al. "Porphyrins at interfaces." In: *Nature Chemistry* 7.2 (2015), pp. 105–120. DOI: 10.1038/nchem.2159 (cit. on pp. 9, 80).

[83] J. M. Gottfried. "Surface chemistry of porphyrins and phthalocyanines." In: *Surface Science Reports* 70.3 (2015), pp. 259–379. DOI: 10.1016/j.surfrep.2015.04.001 (cit. on pp. 9, 80, 82, 107).

[84] C. J. Kingsbury and M. O. Senge. "The shape of porphyrins." In: *Coordination Chemistry Reviews* 431 (2021), p. 213760. DOI: 10.1016/j.ccr.2020.213760 (cit. on pp. 9, 78, 80).

[85] G. Di Santo et al. "Conformational Adaptation and Electronic Structure of 2H-Tetraphenylporphyrin on Ag(111) during Fe Metalation." In: *The Journal of Physical Chemistry C* 115.10 (2011), pp. 4155–4162. DOI: 10.1021/jp111151n (cit. on pp. 9, 111, 112).

[86] F. Albrecht et al. "Direct Identification and Determination of Conformational Response in Adsorbed Individual Nonplanar Molecular Species Using Noncontact Atomic Force Microscopy." In: *Nano Letters* 16.12 (2016), pp. 7703–7709. DOI: 10.1021/acs.nanolett.6b03769 (cit. on pp. 9, 103).

[87] L. Arnold et al. "A porphyrin-related macrocycle from carbazole and pyridine building blocks: synthesis and metal coordination." In: *Chemical Communications* 47.3 (2011), pp. 970–972. DOI: 10.1039/c0cc03052j (cit. on pp. 9, 78, 104, 106, 107, 138).

[88] J. F. Woods et al. "Shape-assisted self-assembly." In: *Nature Communications* 13.1 (2022). DOI: 10.1038/s41467-022-31482-2 (cit. on pp. 9, 78–80, 102–105).

[89] J. F. Woods et al. "Saddles as rotational locks within shape-assisted self-assembled nanosheets." In: *Nature Communications* 14.1 (2023). DOI: 10.1038/s41467-023-40475-8 (cit. on pp. 9, 78, 80).

[90] L. Gallego et al. "Shape-Assisted Self-Assembly of Hexa-Substituted Carpyridines into 1D Supramolecular Polymers." In: *Angewandte Chemie International Edition* 63.11 (2024). DOI: 10.1002/anie.202318879 (cit. on pp. 9, 78, 80).

[91] C. G. Claessens et al. "Subphthalocyanines, Subporphyrazines, and Subporphyrins: Singular Nonplanar Aromatic Systems." In: *Chemical Reviews* 114.4 (2013), pp. 2192–2277. DOI: 10.1021/cr400088w (cit. on p. 9).

[92] G. Lavarda et al. "Recent advances in subphthalocyanines and related subporphyrinoids." In: *Chemical Society Reviews* 51.23 (2022), pp. 9482–9619. DOI: 10.1039/d2cs00280a (cit. on p. 9).

[93] J. Labella et al. "Preparation, Supramolecular Organization, and On-Surface Reactivity of Enantiopure Subphthalocyanines: From Bulk to 2D-Polymerization." In: *Journal of the American Chemical Society* 144.36 (2022), pp. 16579–16587. DOI: 10.1021/jacs.2c06377 (cit. on p. 9).

[94] J. Guilleme et al. "Non-Centrosymmetric Homochiral Supramolecular Polymers of Tetrahedral Subphthalocyanine Molecules." In: *Angewandte Chemie* 127.8 (2015), pp. 2573–2577. DOI: 10.1002/ange.201411272 (cit. on p. 9).

[95] W. Auwärter. "Hexagonal boron nitride monolayers on metal supports: Versatile templates for atoms, molecules and nanostructures." In: *Surface Science Reports* 74.1 (2019), pp. 1–95. DOI: 10.1016/j.surfrep.2018.10.001 (cit. on pp. 10, 26).

[96] K. Hoffmann, P. Mayer, and H. Dube. "A hemithioindigo molecular motor for metal surface attachment." In: *Organic & Biomolecular Chemistry* 17.7 (2019), pp. 1979–1983. DOI: 10.1039/C8OB02424C (cit. on pp. 10, 42).

[97] C. J. Chen. *Introduction to Scanning Tunneling Microscopy*. Oxford University Press, 2007. DOI: 10.1093/acprof:oso/9780199211500.001.0001 (cit. on p. 11).

[98] B. Voigtländer. *Scanning Probe Microscopy: Atomic Force Microscopy and Scanning Tunneling Microscopy*. Springer Berlin Heidelberg, 2015. DOI: 10.1007/978-3-662-45240-0 (cit. on pp. 11, 13–15).

[99] I. Horcas et al. "WSXM: A software for scanning probe microscopy and a tool for nanotechnology." In: *Review of Scientific Instruments* 78.1 (2007). DOI: 10.1063/1.2432410 (cit. on p. 11).

[100] D. Nečas and P. Klapetek. "Gwyddion: an open-source software for SPM data analysis." In: *Open Physics* 10.1 (2011), pp. 181–188. DOI: 10.2478/s11534-011-0096-2 (cit. on p. 11).

[101] M. Ruby. "SpectraFox: A free open-source data management and analysis tool for scanning probe microscopy and spectroscopy." In: *SoftwareX* 5 (2016), pp. 31–36. DOI: 10.1016/j.softx.2016.04.001 (cit. on p. 11).

[102] A. Riss. "SpmImage Tycoon: Organize and analyze scanning probe microscopy data." In: *Journal of Open Source Software* 7.77 (2022), p. 4644. DOI: 10.21105/joss.04644 (cit. on p. 11).

[103] F. J. Giessibl. "Advances in atomic force microscopy." In: *Reviews of Modern Physics* 75.3 (2003), pp. 949–983. DOI: 10.1103/revmodphys.75.949 (cit. on p. 14).

[104] J. E. Sader and S. P. Jarvis. "Accurate formulas for interaction force and energy in frequency modulation force spectroscopy." In: *Applied Physics Letters* 84.10 (2004), pp. 1801–1803. DOI: 10.1063/1.1667267 (cit. on pp. 14, 17, 71, 74).

[105] J. Welker, E. Illek, and F. J. Giessibl. "Analysis of force-deconvolution methods in frequency-modulation atomic force microscopy." In: *Beilstein Journal of Nanotechnology* 3.1 (2012), pp. 238–248. DOI: 10.3762/bjnano.3.27 (cit. on pp. 14, 17, 71, 74).

[106] P. Hapala et al. "Mechanism of high-resolution STM/AFM imaging with functionalized tips." In: *Physical Review B* 90.8 (2014), p. 085421. DOI: 10.1103/physrevb.90.085421 (cit. on pp. 15, 22).

[107] F. Bischoff. "Scanning probe microscopy studies of surface confined molecules and (metal-organic) nanostructures." PhD thesis. Technische Universität München, 2018, p. 192 (cit. on p. 15).

[108] F. A. Stevie and C. L. Donley. "Introduction to x-ray photoelectron spectroscopy." In: *Journal of Vacuum Science and Technology A: Vacuum, Surfaces, and Films* 38.6 (2020). DOI: 10.1116/6.0000412 (cit. on p. 19).

[109] S. Hüfner. *Photoelectron Spectroscopy*. Springer Berlin Heidelberg, 2003. DOI: 10.1007/978-3-662-09280-4 (cit. on p. 19).

[110] D. R. Penn. "Quantitative chemical analysis by ESCA." In: *Journal of Electron Spectroscopy and Related Phenomena* 9.1 (1976), pp. 29–40. DOI: 10.1016/0368-2048(76)85004-9 (cit. on p. 19).

[111] G. H. Major et al. "Practical guide for curve fitting in x-ray photoelectron spectroscopy." In: *Journal of Vacuum Science and Technology A* 38.6 (2020). DOI: 10.1116/6.0000377 (cit. on p. 19).

[112] D. Briggs and M. Seah, eds. *Practical Surface Analysis Volume 1 Auger and X-ray Photoelectron Spectroscopy*. Second edition. Wiley, 1990 (cit. on p. 19).

[113] J. Leiro, E. Minni, and E. Suoninen. "Study of plasmon structure in XPS spectra of silver and gold." In: *Journal of Physics F: Metal Physics* 13.1 (1983), pp. 215–221. DOI: 10.1088/0305-4608/13/1/024 (cit. on p. 19).

[114] G. Mercurio et al. "X-ray standing wave simulations based on Fourier vector analysis as a method to retrieve complex molecular adsorption geometries." In: *Frontiers in Physics* 2 (2014). DOI: 10.3389/fphy.2014.00002 (cit. on p. 19).

[115] S. Doniach and M. Sunjic. "Many-electron singularity in X-ray photoemission and X-ray line spectra from metals." In: *Journal of Physics C: Solid State Physics* 3.2 (1970), pp. 285–291. DOI: 10.1088/0022-3719/3/2/010 (cit. on p. 19).

[116] J. Stöhr. *NEXAFS Spectroscopy*. Springer Berlin Heidelberg, 1992. DOI: 10.1007/978-3-662-02853-7 (cit. on pp. 19–21).

[117] G. Hähner. "Near edge X-ray absorption fine structure spectroscopy as a tool to probe electronic and structural properties of thin organic films and liquids." In: *Chemical Society Reviews* 35.12 (2006), pp. 1244–1255. DOI: 10.1039/b509853j (cit. on pp. 19, 21).

[118] D. A. Outka and J. Stöhr. "Curve fitting analysis of near-edge core excitation spectra of free, adsorbed, and polymeric molecules." In: *The Journal of Chemical Physics* 88.6 (1988), pp. 3539–3554. DOI: 10.1063/1.453902 (cit. on pp. 20, 21, 88).

[119] J. Stöhr and D. A. Outka. "Determination of molecular orientations on surfaces from the angular dependence of near-edge x-ray-absorption fine-structure spectra." In: *Physical Review B* 36.15 (1987), pp. 7891–7905. DOI: 10.1103/physrevb.36.7891 (cit. on pp. 20, 21, 88).

[120] V. Blum et al. "Ab initio molecular simulations with numeric atom-centered orbitals." In: *Computer Physics Communications* 180.11 (2009), pp. 2175–2196. DOI: 10.1016/j.cpc.2009.06.022 (cit. on p. 22).

[121] A. Tkatchenko and M. Scheffler. "Accurate Molecular Van Der Waals Interactions from Ground-State Electron Density and Free-Atom Reference Data." In: *Physical Review Letters* 102.7 (2009), p. 073005. DOI: 10.1103/PhysRevLett.102.073005 (cit. on p. 22).

[122] V. G. Ruiz et al. "Density-Functional Theory with Screened van der Waals Interactions for the Modeling of Hybrid Inorganic-Organic Systems." In: *Physical Review Letters* 108.14 (2012), p. 146103. DOI: 10.1103/PhysRevLett.108.146103 (cit. on p. 22).

[123] J. P. Perdew, K. Burke, and M. Ernzerhof. "Generalized Gradient Approximation Made Simple." In: *Physical Review Letters* 77.18 (1996), pp. 3865–3868. DOI: 10.1103/physrevlett.77.3865 (cit. on p. 22).

[124] J. Tersoff and D. R. Hamann. "Theory of the Scanning Tunneling Microscope." In: *Physical Review B* 31.2 (1985), pp. 805–813. DOI: 10.1103/PhysRevB.31.805 (cit. on p. 22).

[125] P. Hapala et al. "Origin of High-Resolution IETS-STM Images of Organic Molecules with Functionalized Tips." In: *Physical Review Letters* 113.22 (2014), p. 226101. DOI: 10.1103/physrevlett.113.226101 (cit. on p. 22).

[126] N. Oinonen et al. "Advancing scanning probe microscopy simulations: A decade of development in probe-particle models." In: *Computer Physics Communications* 305 (2024), p. 109341. DOI: 10.1016/j.cpc.2024.109341 (cit. on p. 22).

[127] Woods, Joseph. "Shaping Saddles into 2D Sheets: On-Surface Self-Assembly and Structural Elucidation." PhD thesis. University of Zurich, 2024. DOI: 10.5167/UZH-258686 (cit. on pp. 22, 78, 106, 115).

[128] M. Muntwiler et al. "Surface science at the PEARL beamline of the Swiss Light Source." In: *Journal of Synchrotron Radiation* 24.1 (2017), pp. 354–366. DOI: 10.1107/s1600577516018646 (cit. on p. 23).

[129] K. Grill. "Hemithioindigo-basierte molekulare Motoren und deren supramolekulare Anwendungen." PhD thesis. Ludwig-Maximilians-Universität, 2023 (cit. on pp. 24, 44, 46, 48, 116).

[130] T. Weiss et al. "Adsorption, Single-Molecule Manipulation, and Self-Assembly of Borazine on Ag(111)." In: *Advanced Materials Interfaces* 11.4 (2023). DOI: 10.1002/admi.202300774 (cit. on p. 26).

[131] A. Stock and E. Pohland. "Borwasserstoffe, IX.: B3N3H6." In: *Berichte der deutschen chemischen Gesellschaft (A and B Series)* 59.9 (1926), pp. 2215–2223. DOI: 10.1002/cber.19260590907 (cit. on p. 26).

[132] R. Báez-Grez and R. Pino-Rios. "The hidden aromaticity in borazine." In: *RSC Advances* 12.13 (2022), pp. 7906–7910. DOI: 10.1039/D1RA06457F (cit. on p. 26).

[133] M. d. R. Merino-García et al. "Benzene and Borazine, so Different, yet so Similar: Insight from Experimental Charge Density Analysis." In: *Inorganic Chemistry* 61.18 (2022), pp. 6785–6798. DOI: 10.1021/acs.inorgchem.1c03923 (cit. on p. 26).

[134] D. Marchionni et al. "Synthesis and Applications of Organic Borazine Materials." In: *Advanced Functional Materials* 33.49 (2023), p. 2303635. DOI: 10.1002/adfm.202303635 (cit. on pp. 26, 27).

[135] A. E. Naclerio and P. R. Kidambi. "A Review of Scalable Hexagonal Boron Nitride (h-BN) Synthesis for Present and Future Applications." In: *Advanced Materials* 35.6 (2023), p. 2207374. DOI: 10.1002/adma.202207374 (cit. on p. 26).

[136] D. Golberg et al. "Boron Nitride Nanotubes and Nanosheets." In: *ACS Nano* 4.6 (2010), pp. 2979–2993. DOI: 10.1021/nn1006495 (cit. on p. 26).

[137] X. Wang, H. Wang, and J. Shi. "Synthesis, characterization, and ceramic conversion of a liquid polymeric precursor to SiBCN ceramic via borazine-modified polymethylsilane." In: *Journal of Materials Science* 53.16 (2018), pp. 11242–11252. DOI: 10.1007/s10853-018-2452-8 (cit. on p. 26).

[138] I. H. T. Sham et al. "Borazine materials for organic optoelectronic applications." In: *Chemical Communications* 28 (2005), pp. 3547–3549. DOI: 10.1039/B504510J (cit. on p. 26).

[139] S. Kervyn et al. "Polymorphism, Fluorescence, and Optoelectronic Properties of a Borazine Derivative." In: *Chemistry – A European Journal* 19.24 (2013), pp. 7771–7779. DOI: 10.1002/chem.201204598 (cit. on p. 26).

[140] J. W. He and D. W. Goodman. "Interaction of Borazine with a Re(0001) Surface, Studied by LEED, TDS, AES and ELS." In: *Surface Science* 232.1-2 (1990), pp. 138–148. DOI: /0039-6028(90)90594-X (cit. on p. 26).

[141] M. T. Paffett et al. "Borazine Adsorption and Decomposition at Pt(111) and Ru(001) Surfaces." In: *Surface Science* 232.3 (1990), pp. 286–296. DOI: 10.1016/0039-6028(90)90121-N (cit. on pp. 26, 40).

[142] A. P. Farkas et al. "Investigation of the adsorption properties of borazine and characterisation of boron nitride on Rh(111) by electron spectroscopic methods." In: *Applied Surface Science* 354 (2015), pp. 367–372. DOI: 10.1016/j.apsusc.2015.05.060 (cit. on pp. 26, 27).

[143] G. C. Dong et al. "How Boron Nitride Forms a Regular Nanomesh on Rh(111)." In: *Physical Review Letters* 104.9 (2010), p. 096102. DOI: 10.1103/PhysRevLett.104.096102 (cit. on pp. 26, 27).

[144] F. Orlando et al. "Epitaxial Growth of Hexagonal Boron Nitride on Ir(111)." In: *Journal of Physical Chemistry C* 116.1 (2012), pp. 157–164. DOI: 10.1021/jp207571n (cit. on pp. 26, 27, 119).

[145] R. J. Simonson and M. Trenary. "An Infrared Study of the Adsorption of Borazine, (BHNH)3, on the Pt(111) Surface." In: *Journal of Electron Spectroscopy and Related Phenomena* 54 (1990), pp. 717–728. DOI: 10.1016/0368-2048(90)80264-B (cit. on pp. 26, 37).

[146] R. J. Simonson et al. "A Vibrational Study of Borazine Adsorbed on Pt(111) and Au(111) Surfaces." In: *Surface Science* 254.1-3 (1991), pp. 29–44. DOI: 10.1016/0039-6028(91)90635-6 (cit. on pp. 26, 37, 38).

[147] L. Haug et al. "Precursor chemistry of h-BN: adsorption, desorption, and decomposition of borazine on Pt(110)." In: *Physical Chemistry Chemical Physics* 22.20 (2020), pp. 11704–11712. DOI: 10.1039/d0cp00112k (cit. on pp. 26, 27, 39, 40).

[148] R. H. Dong, T. Zhang, and X. L. Feng. "Interface-Assisted Synthesis of 2D Materials: Trend and Challenges." In: *Chemical Reviews* 118.13 (2018), pp. 6189–6235. DOI: 10.1021/acs.chemrev.8b00056 (cit. on p. 26).

[149] A. J. Mannix et al. "Synthesis and chemistry of elemental 2D materials." In: *Nature Reviews Chemistry* 1.2 (2017), p. 0014. DOI: 10.1038/s41570-016-0014 (cit. on p. 26).

[150] J. Sun et al. "Recent progress in the tailored growth of two-dimensional hexagonal boron nitride via chemical vapour deposition." In: *Chemical Society Reviews* 47.12 (2018), pp. 4242–4257. DOI: 10.1039/C8CS00167G (cit. on p. 26).

[151] K. Zhang et al. "Two dimensional hexagonal boron nitride (2D-hBN): synthesis, properties and applications." In: *Journal of Materials Chemistry C* 5.46 (2017), pp. 11992–12022. DOI: 10.1039/C7TC04300G (cit. on p. 26).

[152] P. Bachmann et al. "A HR-XPS study of the formation of h-BN on Ni(111) from the two precursors, ammonia borane and borazine." In: *Journal of Chemical Physics* 149.16 (2018), p. 164709. DOI: 10.1063/1.5051595 (cit. on pp. 27, 119).

[153] J. Felter et al. "In situ study of two-dimensional dendritic growth of hexagonal boron nitride." In: *2D Materials* 6.4 (2019), p. 045005. DOI: 10.1088/2053-1583/ab2926 (cit. on p. 27).

[154] A. Ruckhofer et al. "Evolution of ordered nanoporous phases during h-BN growth: controlling the route from gas-phase precursor to 2D material by in situ monitoring." In: *Nanoscale Horizons* 7.11 (2022), pp. 1388–1396. DOI: 10.1039/D2NH00353H (cit. on p. 27).

[155] I. Neogi and A. M. Szpilman. "Synthesis and Reactions of Borazines." In: *Synthesis* 54.08 (2022), pp. 1877–1907. DOI: 10.1055/a-1684-0031 (cit. on p. 27).

[156] C. A. Brown and A. W. Laubengayer. "B-Trichloroborazole1." In: *Journal of the American Chemical Society* 77.14 (1955), pp. 3699–3700. DOI: 10.1021/ja01619a007 (cit. on p. 27).

[157] D. Bonifazi et al. "Boron–nitrogen doped carbon scaffolding: organic chemistry, self-assembly and materials applications of borazine and its derivatives." In: *Chemical Communications* 51.83 (2015), pp. 15222–15236. DOI: 10.1039/C5CC06611E (cit. on p. 27).

[158] D. Marinelli et al. "Borazino-Doped Polyphenylenes." In: *Journal of the American Chemical Society* 139.15 (2017), pp. 5503–5519. DOI: 10.1021/jacs.7b01477 (cit. on p. 27).

[159] C. Chen et al. "Construction of Layered B3N3-Doped Graphene Sheets from an Acetylenic Compound Containing B3N3 by a Semisynthetic Strategy." In: *ACS Applied Materials and Interfaces* 11.36 (2019), pp. 33245–33253. DOI: 10.1021/acsami.9b10582 (cit. on p. 27).

[160] M. M. Lorenzo-Garcia and D. Bonifazi. "Renaissance of an Old Topic: From Borazines to BN-doped Nanographenes." In: *Chimia* 71.9 (2017), pp. 550–557. DOI: 10.2533/chimia.2017.550 (cit. on p. 27).

[161] M. Schwarz et al. "BN-Patterning of Metallic Substrates through Metal Coordination of Decoupled Borazines." In: *Chemistry - A European Journal* 24.38 (2018), pp. 9565–9571. DOI: 10.1002/chem.201800849 (cit. on pp. 27, 39, 119).

[162] A. Belser et al. "Visualization of the Borazine Core of B3N3-Doped Nanographene by STM." In: *ACS Applied Materials and Interfaces* 12.16 (2020), pp. 19218–19225. DOI: 10.1021/acsami.0c02324 (cit. on p. 27).

[163] N. Kalashnyk et al. "Self-Assembly of Decoupled Borazines on Metal Surfaces: The Role of the Peripheral Groups." In: *Chemistry – A European Journal* 20.37 (2014), pp. 11856–11862. DOI: 10.1002/chem.201402839 (cit. on p. 27).

[164] C. Sanchez-Sanchez et al. "On-Surface Synthesis of BN-Substituted Heteroaromatic Networks." In: *ACS Nano* 9.9 (2015), pp. 9228–9235. DOI: 10.1021/acsnano.5b03895 (cit. on p. 27).

[165] W. D. Xiao et al. "Self-assembly of chiral molecular honeycomb networks on Au(111)." In: *Journal of the American Chemical Society* 130.28 (2008), p. 8910. DOI: 10.1021/ja7106542 (cit. on pp. 27, 39).

[166] T. Jasper-Tonnies et al. "Coverage-Controlled Superstructures of C-3-Symmetric Molecules: Honeycomb versus Hexagonal Tiling." In: *Angewandte Chemie - International Edition* 59.18 (2020), pp. 7008–7017. DOI: 10.1002/anie.202001383 (cit. on pp. 27, 29, 39).

[167] F. Müller et al. "Epitaxial growth of hexagonal boron nitride on Ag(111)." In: *Physical Review B* 82.11 (2010), p. 113406. DOI: 10.1103/PhysRevB.82.113406 (cit. on pp. 31, 38).

[168] L. Merz and K.-H. Ernst. "Unification of the matrix notation in molecular surface science." In: *Surface Science* 604.11-12 (2010), pp. 1049–1054 (cit. on p. 32).

[169] I. Piquero-Zulaica et al. "Engineering quantum states and electronic landscapes through surface molecular nanoarchitectures." In: *Reviews of Modern Physics* 94.4 (2022), p. 045008. DOI: 10.1103/RevModPhys.94.045008 (cit. on pp. 34, 39).

[170] K. Müller, M. Enache, and M. Stöhr. "Confinement properties of 2D porous molecular networks on metal surfaces." In: *Journal of Physics: Condensed Matter* 28.15 (2016), p. 153003. DOI: 10.1088/0953-8984/28 (cit. on p. 34).

[171] J. I. Urgel et al. "Five-Vertex Lanthanide Coordination on Surfaces: A Route to Sophisticated Nanoarchitectures and Tessellations." In: *Journal of Physical Chemistry C* 118.24 (2014), pp. 12908–12915. DOI: 10.1021/jp502901z (cit. on p. 38).

[172] G. B. Grad et al. "Density functional theory investigation of the geometric and spintronic structure of h-BN/Ni(111) in view of photoemission and STM experiments." In: *Physical Review B* 68.8 (2003), p. 085404. DOI: 10.1103/physrevb.68.085404 (cit. on p. 38).

[173] R. Laskowski, P. Blaha, and K. Schwarz. "Bonding of hexagonal BN to transition metal surfaces: An ab initio density-functional theory study." In: *Physical Review B* 78.4 (2008), p. 045409. DOI: 10.1103/physrevb.78.045409 (cit. on p. 38).

[174] M. Bokdam et al. "Schottky barriers at hexagonal boron nitride/metal interfaces: A first-principles study." In: *Physical Review B* 90.8 (2014), p. 085415. DOI: 10.1103/PhysRevB.90.085415 (cit. on p. 38).

[175] K. Verma and K. S. Viswanathan. "The borazine dimer: the case of a dihydrogen bond competing with a classical hydrogen bond." In: *Physical Chemistry Chemical Physics* 19.29 (2017), pp. 19067–19074. DOI: 10.1039/C7CP04056C (cit. on p. 39).

[176] D. P. Malenov, A. J. Aladić, and S. D. Zarić. "Stacking interactions of borazine: important stacking at large horizontal displacements and dihydrogen bonding governed by electrostatic potentials of borazine." In: *Physical Chemistry Chemical Physics* 21.44 (2019), pp. 24554–24564. DOI: 10.1039/C9CP02966D (cit. on p. 39).

[177] Y. C. Ye et al. "A unified model: Self-assembly of trimesic acid on gold." In: *The Journal of Physical Chemistry C* 111.28 (2007), pp. 10138–10141. DOI: 10.1021/jp072726o (cit. on p. 39).

[178] J. Eichhorn et al. "Self-assembly of melem on Ag(111)-emergence of porous structures based on amino-heptazine hydrogen bonds." In: *CrystEngComm* 13.18 (2011), pp. 5559–5565. DOI: 10.1039/c1ce05342f (cit. on p. 39).

[179] M. Garnica et al. "Comparative study of the interfaces of graphene and hexagonal boron nitride with silver." In: *Physical Review B* 94.15 (2016), p. 155431. DOI: 10.1103/PhysRevB.94.155431 (cit. on p. 39).

[180] W. Liu et al. "Structure and energetics of benzene adsorbed on transition-metal surfaces: density-functional theory with van der Waals interactions including collective substrate response." In: *New Journal of Physics* 15 (2013), p. 053046. DOI: 10.1088/1367-2630/15/5/053046 (cit. on p. 40).

[181] W. Gao, W. T. Zheng, and Q. Jiang. "Dehydrogenation of benzene on Pt(111) surface." In: *Journal of Chemical Physics* 129.16 (2008), p. 164705. DOI: 10.1063/1.3001610 (cit. on p. 40).

[182] D. P. Miller et al. "Benzene derivatives adsorbed to the Ag(111) surface: Binding sites and electronic structure." In: *Journal of Chemical Physics* 142.10 (2015), p. 101924. DOI: 10.1063/1.4908267 (cit. on p. 40).

[183] J. A. G. Torres et al. "Adsorption energies of benzene on close packed transition metal surfaces using the random phase approximation." In: *Physical Review Materials* 1.6 (2017), p. 060803. DOI: 10.1103/PhysRevMaterials.1.060803 (cit. on p. 40).

[184] W. Liu et al. "Quantitative Prediction of Molecular Adsorption: Structure and Binding of Benzene on Coinage Metals." In: *Physical Review Letters* 115.3 (2015), p. 036104. DOI: 10.1103/PhysRevLett.115.036104 (cit. on p. 40).

[185] L. J. Lauhon and W. Ho. "Single-Molecule Chemistry and Vibrational Spectroscopy: Pyridine and Benzene on Cu(001)." In: *Journal of Physical Chemistry A* 104.11 (2000), pp. 2463–2467. DOI: 10.1021/jp991768c (cit. on p. 40).

[186] M. L. Bocquet, H. Lesnard, and N. Lorente. "Inelastic Spectroscopy Identification of STM-Induced Benzene Dehydrogenation." In: *Physical Review Letters* 96.9 (2006), p. 096101. DOI: 10.1103/physrevlett.96.096101 (cit. on p. 40).

[187] R. Feynman. "Plenty of Room at the Bottom." In: *Caltech's Engineering and Science* 23.5 (1960), pp. 22–36 (cit. on p. 42).

[188] S. Kassem et al. "Artificial molecular motors." In: *Chemical Society Reviews* 46.9 (2017), pp. 2592–2621. DOI: 10.1039/c7cs00245a (cit. on p. 42).

[189] R. Iino, K. Kinbara, and Z. Bryant. "Introduction: Molecular Motors." In: *Chemical Reviews* 120.1 (2020), pp. 1–4. DOI: 10.1021/acs.chemrev.9b00819 (cit. on p. 42).

[190] *The Nobel Prize in Chemistry 2016*. https://www.nobelprize.org/prizes/chemistry/2016/summary/ (cit. on p. 42).

[191] N. Koumura et al. "Light-driven monodirectional molecular rotor." In: *Nature* 401.6749 (1999), pp. 152–155. DOI: 10.1038/43646 (cit. on p. 42).

[192] Y. Deng et al. "Photo-responsive functional materials based on light-driven molecular motors." In: *Light: Science & Applications* 13.1 (2024), p. 63. DOI: 10.1038/s41377-024-01391-8 (cit. on p. 42).

[193] R. Eelkema et al. "Nanomotor rotates microscale objects." In: *Nature* 440.7081 (2006), pp. 163–163. DOI: 10.1038/440163a (cit. on p. 42).

[194] M. M. Pollard et al. "Controlled Rotary Motion in a Monolayer of Molecular Motors." In: *Angewandte Chemie International Edition* 46.8 (2007), pp. 1278–1280. DOI: 10.1002/anie.200603618 (cit. on p. 42).

[195] C. Stähler et al. "Highly Ordered Co-Assembly of Bisurea Functionalized Molecular Switches at the Solid-Liquid Interface." In: *Chemistry – A European Journal* 30.18 (2024), e202303994. DOI: 10.1002/chem.202303994 (cit. on pp. 42, 48).

[196] E. Rheinfrank et al. "Actinide Coordination Chemistry on Surfaces: Synthesis, Manipulation, and Properties of Thorium Bis(porphyrinato) Complexes." In: *Journal of the American Chemical Society* 143.36 (2021), pp. 14581–14591. DOI: 10.1021/jacs.1c04982 (cit. on pp. 42, 43, 62, 63, 65, 75).

[197] K. Katoh et al. "Direct Observation of Lanthanide(III)-Phthalocyanine Molecules on Au(111) by Using Scanning Tunneling Microscopy and Scanning Tunneling Spectroscopy and Thin-Film Field-Effect Transistor Properties of Tb(III)- and Dy(III)-Phthalocyanine Molecules." In: *Journal of the American Chemical Society* 131.29 (2009), pp. 9967–9976. DOI: 10.1021/ja902349t (cit. on p. 43).

[198] J. Granet et al. "Tuning the Kondo resonance in two-dimensional lattices of cerium molecular complexes." In: *Nanoscale* 10.19 (2018), pp. 9123–9132. DOI: 10.1039/c7nr08202a (cit. on p. 43).

[199] S. M. F. Shahed et al. "Observation of Yu–Shiba–Rusinov States and Inelastic Tunneling Spectroscopy for Intramolecule Magnetic Exchange Interaction Energy of Terbium Phthalocyanine (TbPc) Species Adsorbed on Superconductor NbSe2." In: *ACS Nano* 16.5 (2022), pp. 7651–7661. DOI: 10.1021/acsnano.1c11221 (cit. on p. 43).

[200] I. Saiful et al. “Ligand Rotation Induced Oxidation State Change and Spin Appearance of the Bis(phthalocyaninato)cerium (CePc2) Molecule on the Au(111) Surface.” In: *The Journal of Physical Chemistry C* 126.40 (2022), pp. 17152–17163. DOI: 10.1021/acs.jpcc.2c04234 (cit. on p. 43).

[201] J. I. Urgel et al. “In-Situ Growth of Gadolinium Phthalocyaninato Sandwich Complexes on the Ag(111) Surface.” In: *ChemPhysChem* 20.18 (2019), pp. 2301–2304. DOI: 10.1002/cphc.201900253 (cit. on pp. 43, 63).

[202] M. Guentner et al. “Sunlight-powered kHz rotation of a hemithioindigo-based molecular motor.” In: *Nature Communications* 6.1 (2015), p. 8406. DOI: 10.1038/ncomms9406 (cit. on p. 44).

[203] E. Uhl et al. “Transmission of Unidirectional Molecular Motor Rotation to a Remote Biaryl Axis.” In: *Angewandte Chemie International Edition* 57.34 (2018), pp. 11064–11068. DOI: 10.1002/anie.201804716 (cit. on p. 44).

[204] H. Häkkinen. “The gold–sulfur interface at the nanoscale.” In: *Nature Chemistry* 4.6 (2012), pp. 443–455. DOI: 10.1038/nchem.1352 (cit. on p. 45).

[205] J. A. Skolaut. “Molecular Motor Based on Single Chiral Tripodal Molecules Studied with STM.” PhD thesis. Karlsruher Institut für Technologie, 2022 (cit. on p. 47).

[206] E. I. Altman and R. J. Colton. *Determination of the orientation of C60 adsorbed on An(111) and Ag(111).* 1993. DOI: 10.1103/physrevb.48.18244 (cit. on p. 49).

[207] D. Kühne et al. “Rotational and constitutional dynamics of caged supramolecules.” In: *Proceedings of the National Academy of Sciences* 107.50 (2010), pp. 21332–21336. DOI: 10.1073/pnas.1008991107 (cit. on p. 57).

[208] L. Gerhard and M. Valášek. “Switching Behavior of Tripodal Molecules on Au(111) Studied With STM.” In: *Encyclopedia of Interfacial Chemistry: Surface Science and Electrochemistry* (2018), pp. 271–280. DOI: 10.1016/B978-0-12-409547-2.14156-3 (cit. on p. 61).

[209] J. Homberg et al. “Six state molecular revolver mounted on a rigid platform.” In: *Nanoscale* 11.18 (2019), pp. 9015–9022. DOI: 10.1039/C9NR00259F (cit. on p. 61).

[210] M. Valášek, M. Lindner, and M. Mayor. “Rigid multipodal platforms for metal surfaces.” In: *Beilstein Journal of Nanotechnology* 7.1 (2016), pp. 374–405. DOI: 10.3762/BJNANO.7.34 (cit. on p. 61).

[211] M. Valášek and M. Mayor. “Spatial and Lateral Control of Functionality by Rigid Molecular Platforms.” In: *Chemistry – A European Journal* 23.55 (2017), pp. 13538–13548. DOI: 10.1002/CHEM.201703349 (cit. on p. 61).

[212] S. E. Zhu et al. “Self-decoupled porphyrin with a tripodal anchor for molecular-scale electroluminescence.” In: *Journal of the American Chemical Society* 135.42 (2013), pp. 15794–15800. DOI: 10.1021/ja4048569 (cit. on p. 61).

[213] F. L. Otte et al. "Ordered monolayers of free-standing porphyrins on gold." In: *Journal of the American Chemical Society* 136.32 (2014), pp. 11248–11251. DOI: 10.1021/ja505563e (cit. on p. 61).

[214] F. Matino et al. "Electronic decoupling of a cyclophane from a metal surface." In: *Proceedings of the National Academy of Sciences of the United States of America* 108.3 (2011), pp. 961–964. DOI: 10.1073/pnas.1006661107 (cit. on p. 61).

[215] N. Balzer et al. "Synthesis and Surface Behaviour of NDI Chromophores Mounted on a Tripodal Scaffold: Towards Self-Decoupled Chromophores for Single-Molecule Electroluminescence." In: *Chemistry – A European Journal* 27.47 (2021), pp. 12144–12155. DOI: 10.1002/CHEM.202101264 (cit. on p. 61).

[216] V. Rai et al. "Hot luminescence from single-molecule chromophores electrically and mechanically self-decoupled by tripodal scaffolds." In: *Nature Communications* 14.1 (2023), pp. 1–10. DOI: 10.1038/s41467-023-43948-y (cit. on pp. 61, 77).

[217] W. Xiao et al. "Formation of a Regular Fullerene Nanochain Lattice." In: *The Journal of Physical Chemistry B* 110.43 (2006), pp. 21394–21398. DOI: 10.1021/jp065333i (cit. on p. 61).

[218] A. J. Mäkinen et al. "Sexithiophene Adlayer Growth on Vicinal Gold Surfaces." In: *The Journal of Physical Chemistry B* 109.12 (2005), pp. 5790–5795. DOI: 10.1021/jp044921y (cit. on p. 61).

[219] J. Kröger et al. "Molecules on vicinal Au surfaces studied by scanning tunnelling microscopy." In: *Journal of Physics: Condensed Matter* 18.13 (2006), S51–S66. DOI: 10.1088/0953-8984/18/13/s04 (cit. on p. 61).

[220] N. Merino-Díez et al. "Switching from Reactant to Substrate Engineering in the Selective Synthesis of Graphene Nanoribbons." In: *The Journal of Physical Chemistry Letters* 9.10 (2018), pp. 2510–2517. DOI: 10.1021/acs.jpclett.8b00796 (cit. on p. 61).

[221] M. Corso et al. "Electronic states in faceted Au(111) studied with curved crystal surfaces." In: *Journal of Physics: Condensed Matter* 21.35 (2009), p. 353001. DOI: 10.1088/0953-8984/21/35/353001 (cit. on p. 62).

[222] F. Cicoira et al. "Ordered Assembly of α-Quinquethiophene on a Copper Oxide Nanotemplate." In: *Small* 2.11 (2006), pp. 1366–1371. DOI: 10.1002/smll.200600057 (cit. on p. 62).

[223] R. Otero et al. "One-Dimensional Assembly and Selective Orientation of Lander Molecules on an O–Cu Template." In: *Angewandte Chemie International Edition* 43.16 (2004), pp. 2092–2095. DOI: 10.1002/anie.200353586 (cit. on p. 62).

[224] F. Cicoira et al. "Molecular Assembly of Rubrene on a Metal/Metal Oxide Nanotemplate." In: *The Journal of Physical Chemistry A* 111.49 (2007), pp. 12674–12678. DOI: 10.1021/jp076090c (cit. on p. 62).

[225] M. Oehzelt et al. "α-Sexithiophene on Cu(110) and Cu(110)–(2×1)O: An STM and NEXAFS study." In: *Surface Science* 603.2 (2009), pp. 412–418. DOI: 10.1016/j.susc.2008.12.005 (cit. on p. 62).

[226] A. Timmer et al. "Site-Specific Adsorption of Aromatic Molecules on a Metal/Metal Oxide Phase Boundary." In: *Nano Letters* 18.7 (2018), pp. 4123–4129. DOI: 10.1021/acs.nanolett.8b00855 (cit. on p. 62).

[227] Q. Fan et al. "Confined Synthesis of Organometallic Chains and Macrocycles by Cu–O Surface Templating." In: *ACS Nano* 10.3 (2016), pp. 3747–3754. DOI: 10.1021/acsnano.6b00366 (cit. on p. 62).

[228] P. Jacobson et al. "Adsorption and Motion of Single Molecular Motors on TiO2(110)." In: *The Journal of Physical Chemistry C* 124.45 (2020), pp. 24776–24785. DOI: 10.1021/acs.jpcc.0c07065 (cit. on p. 62).

[229] S. Forth et al. "Torque Measurement at the Single-Molecule Level." In: *Annual Review of Biophysics* 42 (2013), pp. 583–604. DOI: 10.1146/annurev-biophys-083012-130412 (cit. on p. 62).

[230] W. Huang et al. "Single Molecule Study of Force-Induced Rotation of Carbon–Carbon Double Bonds in Polymers." In: *ACS Nano* 11.1 (2017), pp. 194–203. DOI: 10.1021/acsnano.6b07119 (cit. on p. 62).

[231] C. Loppacher et al. "Direct Determination of the Energy Required to Operate a Single Molecule Switch." In: *Physical Review Letters* 90.6 (2003), p. 066107. DOI: 10.1103/PhysRevLett.90.066107 (cit. on p. 62).

[232] R. Pawlak et al. "Directed Rotations of Single Porphyrin Molecules Controlled by Localized Force Spectroscopy." In: *ACS Nano* 6.7 (2012), pp. 6318–6324. DOI: 10.1021/nn301774d (cit. on p. 62).

[233] A. J. Weymouth et al. "Lateral Force Microscopy Reveals the Energy Barrier of a Molecular Switch." In: *ACS Nano* 15.2 (2021), pp. 3264–3271. DOI: 10.1021/acsnano.0c09965 (cit. on pp. 62, 74).

[234] D. Lensen and J. A. A. W. Elemans. "Artificial molecular rotors and motors on surfaces: STM reveals and triggers." In: *Soft Matter* 8.35 (2012), p. 9053. DOI: 10.1039/c2sm26235e (cit. on p. 62).

[235] C. Ni and J.-Z. Wang. "STM Studies on Molecular Rotors and Motors." In: *Surface Review and Letters* 25.Supp01 (2018), p. 1841004. DOI: 10.1142/s0218625x18410044 (cit. on p. 62).

[236] A. G. Martynov et al. "Rare-earth based tetrapyrrolic sandwiches: chemistry, materials and applications." In: *Chemical Society Reviews* 51.22 (2022), pp. 9262–9339. DOI: 10.1039/d2cs00559j (cit. on p. 62).

[237] Y. Pan et al. "Scanning tunnelling spectroscopy and manipulation of double-decker phthalocyanine molecules on a semiconductor surface." In: *Journal of Physics: Condensed Matter* 29.36 (2017), p. 364001. DOI: 10.1088/1361-648x/aa7dc4 (cit. on p. 62).

[238] J. Otsuki, M. Taka, and D. Kobayashi. "Rotational Libration of a Porphyrin /Phthalocyanine Double-decker Complex with Ce(IV) as Revealed by 1H NMR and STM." In: *Chemistry Letters* 40.7 (2011), pp. 717–719. DOI: 10.1246/cl.2011.717 (cit. on p. 63).

[239] Y. Zhang et al. "Simultaneous and coordinated rotational switching of all molecular rotors in a network." In: *Nature Nanotechnology* 11.8 (2016), pp. 706–712. DOI: 10.1038/nnano.2016.69 (cit. on p. 63).

[240] J. D. Subramaniam et al. "Synthesis of Ce(IV) Heteroleptic Double-Decker Complex with a New Helical Naphthalocyanine as a Potential Gearing Subunit." In: *Chemistry – A European Journal* (2024). DOI: 10.1002/chem.202402470 (cit. on p. 63).

[241] T. Komeda et al. "Variation of Kondo Peak Observed in the Assembly of Heteroleptic 2,3-Naphthalocyaninato Phthalocyaninato Tb(III) Double-Decker Complex on Au(111)." In: *ACS Nano* 7.2 (2013), pp. 1092–1099. DOI: 10.1021/nn304035h (cit. on pp. 63, 65, 131).

[242] J. Jiang, W. Liu, and D. P. Arnold. "Sandwich complexes of naphthalocyanine with the rare earth metals." In: *Journal of Porphyrins and Phthalocyanines* 07.07 (2003), pp. 459–473. DOI: 10.1142/s1088424603000598 (cit. on p. 63).

[243] T. V. Dubinina et al. "Novel near-IR absorbing phenyl-substituted phthalo- and naphthalocyanine complexes of lanthanide(iii): synthesis and spectral and electrochemical properties." In: *Dalton Trans.* 43.7 (2014), pp. 2799–2809. DOI: 10.1039/c3dt52726c (cit. on p. 63).

[244] V. E. Pushkarev, L. G. Tomilova, and V. N. Nemykin. "Historic overview and new developments in synthetic methods for preparation of the rare-earth tetrapyrrolic complexes." In: *Coordination Chemistry Reviews* 319 (2016), pp. 110–179. DOI: 10.1016/j.ccr.2016.04.005 (cit. on p. 63).

[245] R. Wu et al. "Direct Visualization of Hydrogen-Transfer Intermediate States by Scanning Tunneling Microscopy." In: *The Journal of Physical Chemistry Letters* 11.4 (2020), pp. 1536–1541. DOI: 10.1021/acs.jpclett.0c00046 (cit. on pp. 64, 73).

[246] L. Gross et al. "High-Resolution Molecular Orbital Imaging Using a p-Wave STM Tip." In: *Physical Review Letters* 107.8 (2011), p. 086101. DOI: 10.1103/PhysRevLett.107.086101 (cit. on pp. 65, 131).

[247] A. Zhao et al. "Controlling the Kondo Effect of an Adsorbed Magnetic Ion Through Its Chemical Bonding." In: *Science* 309.5740 (2005), pp. 1542–1544. DOI: 10.1126/science.1113449 (cit. on p. 73).

[248] J. Schaffert et al. "Imaging the dynamics of individually adsorbed molecules." In: *Nature Materials* 12.3 (2013), pp. 223–227. DOI: 10.1038/nmat3527 (cit. on p. 74).

[249] A. Shiotari, T. Odani, and Y. Sugimoto. "Torque-Induced Change in Configuration of a Single NO Molecule on Cu(110)." In: *Physical Review Letters* 121.11 (2018), p. 116101. DOI: 10.1103/physrevlett.121.116101 (cit. on p. 74).

[250] B. J. Albers et al. "Three-dimensional imaging of short-range chemical forces with picometre resolution." In: *Nature Nanotechnology* 4.5 (2009), pp. 307–310. DOI: 10.1038/nnano.2009.57 (cit. on p. 74).

[251] D. Yesilpinar et al. "Mechanical and Chemical Interactions in Atomically Defined Contacts." In: *Small* 17.35 (2021). DOI: 10.1002/smll.202101637 (cit. on p. 75).

[252] J. Berwanger et al. "Atomically Resolved Chemical Reactivity of Small Fe Clusters." In: *Physical Review Letters* 124.9 (2020), p. 096001. DOI: 10.1103/physrevlett.124.096001 (cit. on p. 75).

[253] A. J. Weymouth, T. Hofmann, and F. J. Giessibl. "Quantifying Molecular Stiffness and Interaction with Lateral Force Microscopy." In: *Science* 343.6175 (2014), pp. 1120–1122. DOI: 10.1126/science.1249502 (cit. on p. 75).

[254] T. Komeda et al. "Observation and electric current control of a local spin in a single-molecule magnet." In: *Nature Communications* 2.1 (2011), p. 217. DOI: 10.1038/ncomms1210 (cit. on p. 75).

[255] F. Moresco et al. "Conformational Changes of Single Molecules Induced by Scanning Tunneling Microscopy Manipulation: A Route to Molecular Switching." In: *Physical Review Letters* 86.4 (2001), pp. 672–675. DOI: 10.1103/PhysRevLett.86.672 (cit. on p. 75).

[256] W.-H. Soe, S. Srivastava, and C. Joachim. "Train of Single Molecule-Gears." In: *The Journal of Physical Chemistry Letters* 10.21 (2019), pp. 6462–6467. DOI: 10.1021/acs.jpclett.9b02259 (cit. on p. 75).

[257] K. H. Au Yeung et al. "Transmitting Stepwise Rotation among Three Molecule-Gear on the Au(111) Surface." In: *The Journal of Physical Chemistry Letters* 11.16 (2020), pp. 6892–6899. DOI: 10.1021/acs.jpclett.0c01747 (cit. on p. 75).

[258] W.-H. Soe et al. "Mechanics of Molecule-Gears with Six Long Teeth." In: *The Journal of Physical Chemistry C* 124.41 (2020), pp. 22625–22630. DOI: 10.1021/acs.jpcc.0c08194 (cit. on pp. 75, 76).

[259] K. H. Au-Yeung et al. "Thermal with Electronic Excitation for the Unidirectional Rotation of a Molecule on a Surface." In: *The Journal of Physical Chemistry C* 127.34 (2023), pp. 16989–16994. DOI: 10.1021/acs.jpcc.3c04990 (cit. on p. 76).

[260] W.-S. Wong and M. Stępień. "Emerging applications of curved aromatic compounds." In: *Trends in Chemistry* 4.7 (2022), pp. 573–576. DOI: 10.1016/j.trechm.2022.04.005 (cit. on p. 78).

[261] R. Kumar, H. Aggarwal, and A. Srivastava. "Of Twists and Curves: Electronics, Photophysics, and Upcoming Applications of Non-Planar Conjugated Organic Molecules." In: *Chemistry – A European Journal* 26.47 (2020), pp. 10653–10675. DOI: 10.1002/chem.201905071 (cit. on p. 78).

[262] T. Jasper-Toennies et al. "Robust and Selective Switching of an FeIII Spin-Crossover Compound on Cu2N/Cu(100) with Memristance Behavior." In: *Nano Letters* 17.11 (2017), pp. 6613–6619. DOI: 10.1021/acs.nanolett.7b02481 (cit. on p. 78).

[263] S. Johannsen et al. "Spin-Crossover and Fragmentation of Fe(neoim)2 on Silver and Gold." In: *The Journal of Physical Chemistry Letters* 14.35 (2023), pp. 7814–7823. DOI: 10.1021/acs.jpclett.3c01551 (cit. on p. 78).

[264] C. Wäckerlin et al. "Magnetic exchange coupling of a synthetic Co(II)-complex to a ferromagnetic Ni substrate." In: *Chemical Communications* 49.91 (2013), p. 10736. DOI: 10.1039/c3cc45401k (cit. on pp. 78, 105, 106, 115).

[265] P. Muller. "Glossary of terms used in physical organic chemistry (IUPAC Recommendations 1994)." In: *Pure and Applied Chemistry* 66.5 (1994), pp. 1077–1184. DOI: 10.1351/pac199466051077 (cit. on p. 78).

[266] G. P. Moss. "Basic terminology of stereochemistry (IUPAC Recommendations 1996)." In: *Pure and Applied Chemistry* 68.12 (1996), pp. 2193–2222. DOI: 10.1351/pac199668122193 (cit. on p. 78).

[267] M. Rickhaus, M. Mayor, and M. Juríček. "Chirality in curved polyaromatic systems." In: *Chemical Society Reviews* 46.6 (2017), pp. 1643–1660. DOI: 10.1039/c6cs00623j (cit. on p. 78).

[268] Gallego, Lucía. "Carpyridines as Versatile Platforms for Shape-Assisted Self-Assembly and for Energy Transfer." PhD thesis. 2024. DOI: 10.5167/UZH-259333 (cit. on pp. 78, 106, 107).

[269] L. Gallego, J. F. Woods, and M. Rickhaus. "Recent Concepts for Supramolecular 2D Materials." In: *Organic Materials* 4.03 (2022), pp. 137–145. DOI: 10.1055/a-1932-0463 (cit. on p. 78).

[270] F. Buchner et al. "Ordering aspects and intramolecular conformation of tetraphenylporphyrins on Ag(111)." In: *Physical Chemistry Chemical Physics* 12.40 (2010), p. 13082. DOI: 10.1039/c004551a (cit. on p. 80).

[271] J. Brede et al. "Dynamics of molecular self-ordering in tetraphenyl porphyrin monolayers on metallic substrates." In: *Nanotechnology* 20.27 (2009), p. 275602. DOI: 10.1088/0957-4484/20/27/275602 (cit. on p. 80).

[272] W. Auwärter et al. "Site-specific electronic and geometric interface structure of Co-tetraphenyl-porphyrin layers on Ag(111)." In: *Physical Review B* 81.24 (2010), p. 245403. DOI: 10.1103/physrevb.81.245403 (cit. on p. 80).

[273] W. Auwärter et al. "Conformational Adaptation and Selective Adatom Capturing of Tetrapyridyl-porphyrin Molecules on a Copper (111) Surface." In: *Journal of the American Chemical Society* 129.36 (2007), pp. 11279–11285. DOI: 10.1021/ja071572n (cit. on p. 80).

[274] T. Yokoyama et al. "Nonplanar adsorption and orientational ordering of porphyrin molecules on Au(111)." In: *The Journal of Chemical Physics* 115.8 (2001), pp. 3814–3818. DOI: 10.1063/1.1389276 (cit. on p. 80).

[275] M. Lepper et al. "Controlling the Self-Metalation Rate of Tetraphenylporphyrins on Cu(111) via Cyano Functionalization." In: *Angewandte Chemie International Edition* 57.32 (2018), pp. 10074–10079. DOI: 10.1002/anie.201803601 (cit. on pp. 80, 113).

[276] A. Berdonces-Layunta et al. "Order from a Mess: The Growth of 5-Armchair Graphene Nanoribbons." In: *ACS Nano* 15.10 (2021), pp. 16552–16561. DOI: 10.1021/acsnano.1c06226 (cit. on p. 82).

[277] L. Scudiero, D. E. Barlow, and K. W. Hipps. "Scanning Tunneling Microscopy, Orbital-Mediated Tunneling Spectroscopy, and Ultraviolet Photoelectron Spectroscopy of Nickel(II) Octaethylporphyrin Deposited from Vapor." In: *The Journal of Physical Chemistry B* 106.5 (2002), pp. 996–1003. DOI: 10.1021/jp012436m (cit. on p. 82).

[278] K. Diller et al. "Temperature-dependent templated growth of porphine thin films on the (111) facets of copper and silver." In: *The Journal of Chemical Physics* 141.14 (2014). DOI: 10.1063/1.4896605 (cit. on pp. 82, 83).

[279] K. Diller et al. "Investigating the molecule-substrate interaction of prototypic tetrapyrrole compounds: Adsorption and self-metalation of porphine on Cu(111)." In: *The Journal of Chemical Physics* 138.15 (2013). DOI: 10.1063/1.4800771 (cit. on p. 82).

[280] A. C. Papageorgiou et al. "Self-Terminating Protocol for an Interfacial Complexation Reaction in Vacuo by Metal–Organic Chemical Vapor Deposition." In: *ACS Nano* 7.5 (2013), pp. 4520–4526. DOI: 10.1021/nn401171z (cit. on p. 82).

[281] F. Buchner et al. "Diffusion, Rotation, and Surface Chemical Bond of Individual 2H-Tetraphenylporphyrin Molecules on Cu(111)." In: *The Journal of Physical Chemistry C* 115.49 (2011), pp. 24172–24177. DOI: 10.1021/jp206675u (cit. on pp. 82, 83).

[282] J. Homberg et al. "Enhanced conductance of molecular states at interstitial sites." In: *New Journal of Physics* 25.1 (2023), p. 013029. DOI: 10.1088/1367-2630/acb4b6 (cit. on p. 86).

[283] X. Lu et al. "Spatially Mapping the Spectral Density of a Single C60 Molecule." In: *Physical Review Letters* 90.9 (2003), p. 096802. DOI: 10.1103/physrevlett.90.096802 (cit. on p. 86).

[284] W. Krenner et al. "Assessment of Scanning Tunneling Spectroscopy Modes Inspecting Electron Confinement in Surface-Confined Supramolecular Networks." In: *Scientific Reports* 3.1 (2013). DOI: 10.1038/srep01454 (cit. on p. 86).

[285] A. Vairavamurthy and S. Wang. "Organic Nitrogen in Geomacromolecules: Insights on Speciation and Transformation with K-edge XANES Spectroscopy." In: *Environmental Science and Technology* 36.14 (2002), pp. 3050–3056. DOI: 10.1021/es0155478 (cit. on p. 88).

[286] C. Kolczewski et al. "Detailed study of pyridine at the C 1s and N 1s ionization thresholds: The influence of the vibrational fine structure." In: *The Journal of Chemical Physics* 115.14 (2001), pp. 6426–6437. DOI: 10.1063/1.1397797 (cit. on p. 88).

[287] G. Vall-llosera et al. "The C 1s and N 1s near edge x-ray absorption fine structure spectra of five azabenzenes in the gas phase." In: *The Journal of Chemical Physics* 128.4 (2008). DOI: 10.1063/1.2822985 (cit. on p. 88).

[288] P. Leinweber et al. "Nitrogen K-edge XANES – an overview of reference compounds used to identify 'unknown' organic nitrogen in environmental samples." In: *Journal of Synchrotron Radiation* 14.6 (2007), pp. 500–511. DOI: 10.1107/s0909049507042513 (cit. on p. 88).

[289] Q. Zhu et al. "Determination of the Fate of Nitrogen Functionality in Carbonaceous Materials during Pyrolysis and Combustion Using X-ray Absorption Near Edge Structure Spectroscopy." In: *Langmuir* 13.7 (1997), pp. 2149–2157. DOI: 10.1021/la961027s (cit. on p. 88).

[290] S. Mitra-Kirtley et al. "Determination of the nitrogen chemical structures in petroleum asphaltenes using XANES spectroscopy." In: *Journal of the American Chemical Society* 115.1 (1993), pp. 252–258. DOI: 10.1021/ja00054a036 (cit. on p. 88).

[291] P. Maksymovych, D. C. Sorescu, and J. T. Yates. "Gold-Adatom-Mediated Bonding in Self-Assembled Short-Chain Alkanethiolate Species on the Au(111) Surface." In: *Physical Review Letters* 97.14 (2006), p. 146103. DOI: 10.1103/physrevlett.97.146103 (cit. on p. 103).

[292] J. Mielke et al. "Adatoms underneath Single Porphyrin Molecules on Au(111)." In: *Journal of the American Chemical Society* 137.5 (2015), pp. 1844–1849. DOI: 10.1021/ja510528x (cit. on pp. 103, 109).

[293] D. A. Duncan et al. "Local adsorption structure and bonding of porphine on Cu(111) before and after self-metalation." In: *The Journal of Chemical Physics* 150.9 (2019). DOI: 10.1063/1.5084027 (cit. on p. 103).

[294] P. T. P. Ryan et al. "Validation of the inverted adsorption structure for free-base tetraphenyl porphyrin on Cu(111)." In: *Chemical Communications* 56.25 (2020), pp. 3681–3684. DOI: 10.1039/c9cc09638h (cit. on pp. 103, 104).

[295] M. Lepper et al. ""Inverted" porphyrins: a distorted adsorption geometry of free-base porphyrins on Cu(111)." In: *Chemical Communications* 53.58 (2017), pp. 8207–8210. DOI: 10.1039/c7cc04182a (cit. on p. 103).

[296] S. Joshi et al. "Control of Molecular Organization and Energy Level Alignment by an Electronically Nanopatterned Boron Nitride Template." In: *ACS Nano* 8.1 (2013), pp. 430–442. DOI: 10.1021/nn406024m (cit. on p. 104).

[297] G. Rojas et al. "Surface state engineering of molecule–molecule interactions." In: *Physical Chemistry Chemical Physics* 14.14 (2012), p. 4971. DOI: 10.1039/c2cp40254h (cit. on pp. 104, 105).

[298] F. Bischoff et al. "Metalation of Porphyrins by Lanthanide Atoms at Interfaces: Direct Observation and Stimulation of Cerium Coordination to 2H-TPP/Ag(111)." In: *The Journal of Physical Chemistry C* 122.9 (2018), pp. 5083–5092. DOI: 10.1021/acs.jpcc.7b10363 (cit. on p. 104).

[299] G. Rojas et al. "Self-Assembly and Properties of Nonmetalated Tetraphenylporphyrin on Metal Substrates." In: *The Journal of Physical Chemistry C* 114.20 (2010), pp. 9408–9415. DOI: 10.1021/jp1012957 (cit. on p. 105).

[300] J. I. Wu, I. Fernández, and P. v. R. Schleyer. "Description of Aromaticity in Porphyrinoids." In: *Journal of the American Chemical Society* 135.1 (2012), pp. 315–321. DOI: 10.1021/ja309434t (cit. on p. 105).

[301] N. Cao et al. "The role of aromaticity in the cyclization and polymerization of alkyne-substituted porphyrins on Au(111)." In: *Nature Chemistry* 15.12 (2023), pp. 1765–1772. DOI: 10.1038/s41557-023-01327-6 (cit. on p. 105).

[302] K. Diller et al. "In vacuo interfacial tetrapyrrole metallation." In: *Chemical Society Reviews* 45.6 (2016), pp. 1629–1656. DOI: 10.1039/c5cs00207a (cit. on pp. 106, 111, 113).

[303] F. Santanni and A. Privitera. "Metalloporphyrins as Building Blocks for Quantum Information Science." In: *Advanced Optical Materials* (2024). DOI: 10.1002/adom.202303036 (cit. on pp. 106, 115).

[304] Y. Li et al. "Coordination and Metalation Bifunctionality of Cu with 5,10,15,20-Tetra(4-pyridyl)porphyrin: Toward a Mixed-Valence Two-Dimensional Coordination Network." In: *Journal of the American Chemical Society* 134.14 (2012), pp. 6401–6408. DOI: 10.1021/ja300593w (cit. on pp. 107, 109).

[305] T. Lin et al. "Two-Dimensional Lattice of Out-of-Plane Dinuclear Iron Centers Exhibiting Kondo Resonance." In: *ACS Nano* 8.8 (2014), pp. 8310–8316. DOI: 10.1021/nn502765g (cit. on pp. 107, 111).

[306] J. Nowakowski et al. "Porphyrin metalation providing an example of a redox reaction facilitated by a surface reconstruction." In: *Chemical Communications* 49.23 (2013), p. 2347. DOI: 10.1039/c3cc39134e (cit. on p. 107).

[307] M. Röckert et al. "Abrupt Coverage-Induced Enhancement of the Self-Metalation of Tetraphenylporphyrin with Cu(111)." In: *The Journal of Physical Chemistry C* 118.3 (2014), pp. 1661–1667. DOI: 10.1021/jp412121b (cit. on p. 107).

[308] M. Röckert et al. "Coverage- and Temperature-Dependent Metalation and Dehydrogenation of Tetraphenylporphyrin on Cu(111)." In: *Chemistry – A European Journal* 20.29 (2014), pp. 8948–8953. DOI: 10.1002/chem.201402420 (cit. on p. 107).

[309] K. Diller et al. "Self-metalation of 2H-tetraphenylporphyrin on Cu(111): An x-ray spectroscopy study." In: *The Journal of Chemical Physics* 136.1 (2012). DOI: 10.1063/1.3674165 (cit. on p. 107).

[310] J. Xiao et al. "Temperature-Dependent Chemical and Structural Transformations from 2H-tetraphenylporphyrin to Copper(II)-Tetraphenylporphyrin on Cu(111)." In: *The Journal of Physical Chemistry C* 116.22 (2012), pp. 12275–12282. DOI: 10.1021/jp301757h (cit. on p. 107).

[311] C. M. Doyle et al. "Evidence for the formation of an intermediate complex in the direct metalation of tetra(4-bromophenyl)-porphyrin on the Cu(111) surface." In: *Chemical Communications* 47.44 (2011), p. 12134. DOI: 10.1039/c1cc15241f (cit. on p. 107).

[312] M. Chen et al. "Coordination Reactions and Layer Exchange Processes at a Buried Metal–Organic Interface." In: *The Journal of Physical Chemistry C* 118.16 (2014), pp. 8501–8507. DOI: 10.1021/jp5019235 (cit. on p. 107).

[313] T. E. Shubina et al. "Principle and Mechanism of Direct Porphyrin Metalation: Joint Experimental and Theoretical Investigation." In: *Journal of the American Chemical Society* 129.30 (2007), pp. 9476–9483. DOI: 10.1021/ja072360t (cit. on pp. 109, 111).

[314] L. Zotti et al. "Ab-initio calculations and STM observations on tetrapyridyl and Fe(II)-tetrapyridyl-porphyrin molecules on Ag(111)." In: *Surface Science* 601.12 (2007), pp. 2409–2414. DOI: 10.1016/j.susc.2007.03.040 (cit. on pp. 111, 114).

[315] F. Buchner et al. "Microscopic Evidence of the Metalation of a Free-Base Porphyrin Monolayer with Iron." In: *ChemPhysChem* 8.2 (2007), pp. 241–243. DOI: 10.1002/cphc.200600698 (cit. on p. 111).

[316] W. Auwärter et al. "Controlled Metalation of Self-Assembled Porphyrin Nanoarrays in Two Dimensions." In: *ChemPhysChem* 8.2 (2007), pp. 250–254. DOI: 10.1002/cphc.200600675 (cit. on pp. 111, 114).

[317] W. Wang et al. "Intramolecularly resolved Kondo resonance of high-spin Fe(II)-porphyrin adsorbed on Au(111)." In: *Physical Review B* 91.4 (2015), p. 045440. DOI: 10.1103/physrevb.91.045440 (cit. on p. 111).

[318] F. Buchner et al. "Modification of the Growth of Iron on Ag(111) by Predeposited Organic Monolayers." In: *Zeitschrift für Physikalische Chemie* 223.1–2 (2009), pp. 131–144. DOI: 10.1524/zpch.2009.6028 (cit. on p. 111).

[319] F. Rüth. "On-Surface Metalation of Ethyl-Functionalized 5,10,15,20-Tetraphenylporphyrins (2H-TPP) on Ag(111) and Cu(111)." BA thesis. TUM School of Natural Sciences, 2023 (cit. on pp. 111, 113).

[320] F. Buchner et al. "Coordination of Iron Atoms by Tetraphenylporphyrin Monolayers and Multilayers on Ag(111) and Formation of Iron-Tetraphenylporphyrin." In: *The Journal of Physical Chemistry C* 112.39 (2008), pp. 15458–15465. DOI: 10.1021/jp8052955 (cit. on pp. 111, 112).

[321] P. Borghetti et al. "Adsorption geometry, conformation, and electronic structure of 2H-octaethylporphyrin on Ag(111) and Fe metalation in ultra high vacuum." In: *The Journal of Chemical Physics* 138.14 (2013). DOI: 10.1063/1.4798934 (cit. on p. 112).

[322] M. Röckert et al. "Evidence for a precursor adcomplex during the metalation of 2HTPP with iron on Ag(100)." In: *Chemical Physics Letters* 635 (2015), pp. 60–62. DOI: 10.1016/j.cplett.2015.05.031 (cit. on p. 113).

[323] A. Goldoni et al. "Room Temperature Metalation of 2H-TPP Monolayer on Iron and Nickel Surfaces by Picking up Substrate Metal Atoms." In: *ACS Nano* 6.12 (2012), pp. 10800–10807. DOI: 10.1021/nn304134q (cit. on p. 113).

[324] F. Schmitt et al. "Characterization of the interface interaction of cobalt on top of copper- and iron-phthalocyanine." In: *Analytical and Bioanalytical Chemistry* 400.3 (2011), pp. 665–671. DOI: 10.1007/s00216-011-4691-2 (cit. on p. 113).

[325] K. Greulich et al. "Interfaces between Different Iron Phthalocyanines and Au(111): Influence of the Fluorination on Structure and Interfacial Interactions." In: *The Journal of Physical Chemistry C* 126.1 (2021), pp. 716–727. DOI: 10.1021/acs.jpcc.1c08826 (cit. on p. 113).

[326] M. Schmid et al. "Interfacial Interactions of Iron(II) Tetrapyrrole Complexes on Au(111)." In: *The Journal of Physical Chemistry C* 115.34 (2011), pp. 17028–17035. DOI: 10.1021/jp204524s (cit. on p. 113).

[327] O. Snezhkova et al. "Iron phthalocyanine on Cu(111): Coverage-dependent assembly and symmetry breaking, temperature-induced homocoupling, and modification of the adsorbate-surface interaction by annealing." In: *The Journal of Chemical Physics* 144.9 (2016). DOI: 10.1063/1.4942121 (cit. on p. 113).

[328] R. Karstens et al. "FePc and FePcF16 on Rutile TiO2(110) and (100): Influence of the Substrate Preparation on the Interaction Strength." In: *Molecules* 24.24 (2019), p. 4579. DOI: 10.3390/molecules24244579 (cit. on p. 113).

[329] M. Schmid et al. "On-Surface Synthesis and Characterization of an Iron Corrole." In: *The Journal of Physical Chemistry C* 122.19 (2018), pp. 10392–10399. DOI: 10.1021/acs.jpcc.8b00067 (cit. on pp. 113, 114).

[330] W.-C. Lin et al. "Dimensionality Control and Magnetism of Fe on Nanopatterned Au(111) Surface." In: *IEEE Transactions on Magnetics* 45.10 (2009), pp. 4037–4040. DOI: 10.1109/tmag.2009.2025183 (cit. on p. 113).

[331] Z. H. Cheng et al. "Epitaxial Growth of Iron Phthalocyanine at the Initial Stage on Au(111) Surface." In: *The Journal of Physical Chemistry C* 111.6 (2007), pp. 2656–2660. DOI: 10.1021/jp0660738 (cit. on p. 114).

[332] M. Casarin et al. "Coverage-Dependent Architectures of Iron Phthalocyanine on Ag(110): a Comprehensive STM/DFT Study." In: *The Journal of Physical Chemistry C* 114.5 (2010), pp. 2144–2153. DOI: 10.1021/jp904260p (cit. on p. 114).

[333] M. G. Betti et al. "Structural Phases of Ordered FePc-Nanochains Self-Assembled on Au(110)." In: *Langmuir* 28.37 (2012), pp. 13232–13240. DOI: 10.1021/la302192n (cit. on p. 114).

[334] C. Rubio-Verdú et al. "Orbital-selective spin excitation of a magnetic porphyrin." In: *Communications Physics* 1.1 (2018). DOI: 10.1038/s42005-018-0015-6 (cit. on p. 114).

[335] A. Rieger et al. "Ranking the Stability of Transition-Metal Complexes by On-Surface Atom Exchange." In: *The Journal of Physical Chemistry Letters* 8.24 (2017), pp. 6193–6198. DOI: 10.1021/acs.jpclett.7b02834 (cit. on p. 114).

[336] A. Rieger et al. "Identification of On-Surface Reaction Mechanism by Targeted Metalation." In: *The Journal of Physical Chemistry C* 121.49 (2017), pp. 27521–27527. DOI: 10.1021/acs.jpcc.7b10019 (cit. on p. 114).

[337] S. Kuck et al. ""Naked" Iron-5,10,15-triphenylcorrole on Cu(111): Observation of Chirality on a Surface and Manipulation of Multiple Conformational States by STM." In: *Journal of the American Chemical Society* 130.43 (2008), pp. 14072–14073. DOI: 10.1021/ja8059478 (cit. on p. 114).

[338] A. Weber-Bargioni et al. "Interaction of Cerium Atoms with Surface-Anchored Porphyrin Molecules." In: *The Journal of Physical Chemistry C* 112.10 (2008), pp. 3453–3455. DOI: 10.1021/jp076961i (cit. on p. 114).

[339] I. Mochida et al. "Enhanced catalytic activity of cobalt tetraphenylporphyrin on titanium dioxide by evacuation at elevated temperatures for intensifying the complex-support interaction." In: *The Journal of Physical Chemistry* 87.9 (1983), pp. 1524–1529. DOI: 10.1021/j100232a015 (cit. on p. 115).

[340] A. Rezaeifard and M. Jafarpour. "The catalytic efficiency of Fe-porphyrins supported on multi-walled carbon nanotubes in the heterogeneous oxidation of hydrocarbons and sulfides in water." In: *Catalysis Science and Technology* 4.7 (2014), p. 1960. DOI: 10.1039/c3cy00554b (cit. on p. 115).

[341] L.-L. Li and E. W.-G. Diau. "Porphyrin-sensitized solar cells." In: *Chemical Society Reviews* 42.1 (2013), pp. 291–304. DOI: 10.1039/c2cs35257e (cit. on p. 115).

[342] T. Niu, C. Hua, and M. Zhou. "On-Surface Synthesis toward Two-Dimensional Polymers." In: *The Journal of Physical Chemistry Letters* 13.34 (2022), pp. 8062–8077. DOI: 10.1021/acs.jpclett.2c01481 (cit. on p. 115).

C. List of Publications

Adsorption, Single-Molecule Manipulation, and Self-Assembly of Borazine on Ag(111)
Tobias Weiss, Aleksandr Baklanov, Georg S. Michelitsch, Karsten Reuter, Martin Schwarz, Manuela Garnica and Willi Auwärter
Advanced Materials Interfaces 11.4 (2023), p. 2300774, DOI: 10.1002/admi.202300774

Holistic structural understanding of epitaxially-grown Bi/Au(111) moiré superstructures
Pablo Vezzoni Vicente, Tobias Weiss, Dennis Meier, Wenchao Zhao, Birce Sena Tömekçe, Marc G. Cuxart, Benedikt P. Klein, David A. Duncan, Tien-Lin Lee, Anthoula C. Papageorgiou, Matthias Muntwiler, Ari Paavo Seitsonen, Willi Auwärter, Peter Feulner, Johannes V. Barth, and Francesco Allegretti
Physical Review Materials 8 (2024), p.104001, DOI: 10.1103/PhysRevMaterials.8.104001

D. Acknowledgements

Over the past years, numerous people contributed, directly or indirectly, to this work.
Mainly, I want to thank Prof. Willi Auwärter for allowing me to perform this thesis in his group. Starting in 2019 with the master's thesis, I could participate in many different projects and gain insights using many exciting and advanced techniques. Thank you for the supervision and support throughout all the years.
Moreover, I am also thankful to the collaborators Dr. Georg Michelitsch, Dr. Kerstin Grill, and the group of Prof. Michel Rickhaus for providing clarifying calculations and interesting molecules.
I also want to thank the colleagues at E20, Willi Auwärter, Knud Seufert, Aleksandr Baklanov, Alexander Riss, Joel Deyerling, Ignacio Piquero-Zulaica, who taught me the details in the daily lab work, supported measurements, engaged in fruitful discussions, and motivated me to work hard. I'm also grateful to all the office colleagues and E20 members who were part of the thriving but still relaxed atmosphere at E20.
A big thanks also goes to the various teams of the beamtimes at the SLS, making working long shifts enjoyable. I also thank Patrick Ascher and Matthias Muntwiler for their support.
I'm also thankful to the staff at E20, Viktoria Blaschek, Karl Eberle, Reinhold Schneider, and Fabian Strunk, for dealing with bureaucratic hurdles and lab equipment repairs. Specifically, I also want to thank Prof. Peter Feulner for his ingenious ideas their realization and help on all technical matters.
I also had a blast with recovery breaks, including but not limited to: ice cream, conferences, Summer/Christmas parties, climbing, playing cards with Joel, Pablo, Patrick, Dennis, Iñaki, Mathias, Miguel and many more.
Finally, I want to thank my parents, family, and friends who helped me through times of misery and were present to share happy memories. Your continuous support throughout all my studies made this journey possible.